

Characterisation and modelling of additively manufactured polymeric tpms lattices for structural application

Stepinac, Lucija

Doctoral thesis / Disertacija

2024

Degree Grantor / Ustanova koja je dodijelila akademski / stručni stupanj: **University of Zagreb, Faculty of Civil Engineering / Sveučilište u Zagrebu, Građevinski fakultet**

Permanent link / Trajna poveznica: <https://um.nsk.hr/um:nbn:hr:237:559881>

Rights / Prava: [In copyright](#)/[Zaštićeno autorskim pravom.](#)

Download date / Datum preuzimanja: **2024-11-29**

Repository / Repozitorij:

[Repository of the Faculty of Civil Engineering,
University of Zagreb](#)





TPMS University of Zagreb

Faculty of Civil Engineering

Lucija Stepinac

**CHARACTERISATION AND MODELLING
OF ADDITIVELY MANUFACTURED
POLYMERIC TPMS LATTICES FOR
STRUCTURAL APPLICATION**

DOCTORAL DISSERTATION

Supervisors:

Associate professor Ana Skender, Ph.D.

Full professor Josip Galić, Ph.D.

Zagreb, 2024



Sveučilište u Zagrebu

Građevinski fakultet

Lucija Stepinac

**KARAKTERIZACIJA I MODELIRANJE
ADITIVNO PROIZVEDENIH POLIMERNIH
TPMS REŠETKI ZA PRIMJENU U
KONSTRUKCIJAMA**

DOKTORSKI RAD

Mentori:

izv. prof. dr. sc. Ana Skender

prof. dr. sc. Josip Galić

Zagreb, 2024.

DECLARATION OF ORIGINALITY

I declare that my thesis is the original result of my work and that I have used no sources other than those indicated in the thesis.

IZJAVA O IZVORNOSTI

Izjavljujem da je moj doktorski rad izvorni rezultat mojeg rada te da se u izradi istoga nisam koristila drugim izvorima osim onih koji su u njemu navedeni.

Lucija Stepinac, mag.ing.aedif.

ACKNOWLEDGMENTS / ZAHVALE

First, a thank you to my mentors, Assoc. Prof. Ana Skender and Prof. Josip Galić. Your support and the freedom you gave me to develop and pursue my ideas were invaluable.

To my wonderful husband and my two amazing boys, Gustav and Pavel – you were and remain my biggest motivation and inspiration. Thank you for being my constant support and source of happiness.

A huge thanks to my parents and family for taking care of the kids and preparing all those delicious gluten-free meals. Your help kept me nourished and sane through this journey.

Thank you all for being part of this adventure!

THESIS SUMMARY

The tendency in structural engineering and architecture is that prototypes of the future will resemble biological and natural cellular structures. By observing many objects in nature, it was found that the TPMS (triply periodic minimal surface) pattern is an optimal geometry in terms of minimal surface that separates space into equal volume domains. The mechanical principle that prevails in bioinspired TPMS structures is implemented into the topology optimization of structural elements, resulting in minimal material consumption to resist the applied load. The use of TPMS geometries in structures can be a great improvement in its structural properties while increasing visual attractiveness. Combining additive manufacturing (AM) with topology optimization principles into structural design production of complex but optimal forms will result in time and cost reduction while the whole process will be fully controlled.

This research unfolds across several stages: a preliminary investigation into composite bridge decks with lattice structures featuring 2D and 3D core geometries; mechanical characterization of 3D printed materials; parametric design, experimental and numerical analysis of 1) five TPMS unit morphologies with two different relative densities (20% and 40%); 2) topology-optimized load-bearing sandwich panel with tempered glass face sheets, and 3) topology-optimized load-bearing sandwich panel with GFRP face sheets. Furthermore, the analysis approaches of complex TPMS geometries suitable only for 3D printing were investigated. Using the Homogenization Finite Element Analysis (FEA) in Abaqus and the nTopology software, the mechanical properties were calculated using Hooke's law and analytical formulations were determined. These formulations served as inputs for a calculation algorithm tailored for beams and slabs to quickly estimate the bending stiffness. Fracture analysis in Abaqus was conducted on several TPMS units and two main sandwich composite structures utilizing an elastoplastic material model. Finally, the research proposes advanced methodologies for detailed thermal-mechanical analysis and fracture analysis within the Abaqus framework and GENOA software.

Key words: TPMS, cellular lattice, bridge deck, fracture analysis, topology optimization, homogenization analysis, polymers, fibre reinforced polymers, additive manufacturing, 3D printing

EXTENDED ABSTRACT IN CROATIAN

Ključne riječi: TPMS, ćelijasta rešetka, kolnička konstrukcija, analiza loma, topološka optimizacija, analiza homogenizacije, polimeri, polimeri ojačani vlaknima, aditivna tehnologija, 3D printanje

1. Uvod i pregled stanja područja

Razvoj suvremenih načina brzog prototipiziranja i računalnog projektiranja olakšao je i ubrzao istraživanje biološki inspiriranih struktura za konstruktivnu primjenu. Tako je, promatrajući mnoge prirodne modele, otkriveno da trostruko periodične minimalne plohe (TPMS) predstavljaju optimalnu geometriju koja omogućuje ispunjavanje prostora strukturama minimalne površine. Ovaj biološki nadahnut princip ugrađen je u postupke za topološku optimizaciju konstrukcijskih elemenata kojom se postiže minimalna potrošnja materijala potrebna za zadana opterećenja. Korištenjem TPMS geometrija u projektiranju konstrukcija mogu se istovremeno postići poboljšana mehanička svojstva i poželjno oblikovanje. Združivanje principa topološke optimizacije s tehnikama aditivne proizvodnje (eng. *additive manufacturing* - AM) omogućit će kontrolirani proces oblikovanja i proizvodnje konstrukcija uz očekivano smanjenje potrebnog vremena i troškova.

Istraživanje opisano u ovom radu provedeno je u nekoliko koraka. Prvo je provedeno preliminarno istraživanje na kompozitnim kolničkim konstrukcijama s rešetkastom ravninskom i prostornom ispunom. Zatim je provedena mehanička karakterizacija 3D ispisanih uzoraka, nakon čega je provedeno parametarsko projektiranje te eksperimentalna i numerička analiza na: 1) uzorcima pet različitih morfologija TPMS jedinica u dvije izvedbe (s 20% i 40%-tnom ispunom), 2) uzorku sendvič panela s topološki optimiziranom 3D ispisanom ispunom ugrađenom između staklenih ploča te 3) uzorku sendvič panela s topološki optimiziranom 3D ispisanom ispunom ugrađenom između dvije ploče od polimera ojačanih vlaknima (eng. *glass fibre reinforced polymer* - GFRP). Nadalje, istražene su i ispitane prikladne metode proračuna složenih TPMS geometrija izvedivih jedino u tehnici 3D ispisa. Koristeći metodu homogenizacije za analizu konačnih elemenata (eng. *finite element analysis* - FEA) u računalnim programima Abaqus i nTopology, pomoću Hookeovog zakona dobivene su

vrijednosti za mehanička svojstva TPMS struktura kao materijala te su za njih predloženi analitički izrazi. Ti izrazi su poslužili kao ulazni parametri za programski algoritam za preliminarnu procjenu krutosti na savijanje greda i ploča od polimera s TPMS ispunom. Analiza loma u računalnom programu Abaqus provedena je za modele nekoliko TPMS jedinica i dva sendvič sustava sa zadanim elasto-plastičnim ponašanjem materijala. Na kraju, predložene su napredne numeričke metode za detaljnu analizu loma i termodinamičku analizu za računalne programe Abaqus i GENOA.

U sklopu ove doktorske disertacije predložene su sljedeće hipoteze:

H1: TPMS strukture Diamond and Gyroid su najprimjenjivije za nosive konstrukcijske elemente.

H2: Topološki optimizirana TPMS struktura dovodi do ravnomjerne raspodjele naprezanja unutar konstrukcije, što rezultira u uštedi materijala i troškova proizvodnje.

Pregled stanja područja

Protekla dva do tri desetljeća došlo je do ubrzanog informatičkog razvoja i posljedično do povećane prilagodljivosti računalnih programa i mogućnosti računalno potpomognutog projektiranja (CAD). To je nadalje projektantski fokus usmjerilo na mogućnosti integracije digitalnog projektiranja s postojećim i novim proizvodnim procesima [1]. Jedan takav proizvodni proces u ubrzanom razvoju je aditivna proizvodnja (AM) ili 3D ispis koja svoju učinkovitost potvrđuje u brojnim industrijama, od medicinske [2], automobilske [3, 4], zrakoplovne [5] do svemirske [6]. Međutim, prodor i primjena aditivne proizvodnje je u građevinarstvu i arhitekturi znatno sporiji pa su tako i primjeri konstrukcija proizvedenih tehnikom 3D ispisa rijetki, bilo da se radi o betonu, metalu, umjetnim i drugim materijalima. Često se ove nove tehnike računalnog projektiranja i (aditivne) proizvodnje testiraju i demonstriraju na tipologiji (pješačkih) mostova [7, 8]. Smatra se da je prvi 3D ispisani most od kompozitnih materijala na bazi polimera (u daljnjem tekstu kompozita) proizveden u Kini 2020. g. [9]. Dimenzija 15,5 x 3,8 m, ovaj most ima proračunatu ukupnu nosivost od 250 kg/m² i očekivani vijek trajanja od 30 godina. Načinjen je od akrilonitril-stiren-akrilata (ASA) ojačanog staklenim vlaknima s udjelom vlakana od 12,5 % te je težak 5,8 tona. Proizvodnja na 3D pisaču s kapacitetom ispisa od 8 kg/h i radnim volumenom od 24 x 4 x 1,5 m je trajala 30 dana što je relativno sporo u usporedbi s tradicionalnim načinima gradnje.

Recentna istraživanja robotske proizvodnje usmjerena su na mogućnosti dobivanja intrigantnih arhitektonskih oblika uz istodobno smanjenje troškova proizvodnje i ugradnje [10, 11], a brzi napredak informacijskih tehnologija i robotike podržava aditivnu proizvodnju i trodimenzionalni ispis velikih predmeta [12]. Kako su polimeri najzastupljenija vrsta materijala za 3D ispis, a svojom malom težinom i jednostavnošću obrade omogućuju proizvodnju elemenata složenih geometrija, privlače interes istraživača za nove mogućnosti primjene ove vrste proizvodnje.

Prvotna primjena AM-a u gradnji bila je za proizvodnju oplata i kalupa za tradicionalne materijale i proizvodne postupke [14], a svoju prikladnost i učinkovitost kao neovisne građevinske tehnologije demonstrirala je upravo na pojavi inovativnih oblika, materijala i konstrukcijskih rješenja - osobito onih koji sadrže geometrije koje nijedna druga tradicionalna tehnologija do tada nije mogla proizvesti. Aditivne proizvodne tehnologije, posebno FDM (eng. *fused deposition modelling*) nude jedinstvene mogućnosti kako proizvodnje konstrukcija u različitim veličinama i materijalima [15-18] tako i projektantske slobode kombiniranja i gradacije materijala i samim time olakšanu proizvodnju predmeta funkcionalno složenih geometrija (FGM) [19].

Zahvaljujući pomacima u proizvodnji i znanostima o materijalima, kao i u softverskim mogućnostima [88], istraživanja su sve više usmjerena ka postizanju što laganijih konstrukcija. To uključuje razne strategije, primjerice zamjenu punih dijelova volumena elemenata šupljim jediničnim geometrijama, a za materijal izrade se - u skladu sa strategijama održivog razvoja - primjećuju sve češći pokušaji korištenja materijala prirodnog podrijetla ili potpuno reciklabilnih termoplastičnih materijala [83, 84].

Uvođenje i primjena metamaterijala u graditeljstvu i arhitekturi zahtijeva standardizaciju kako mehaničkih ispitivanja, tako i analize nosivih konstrukcija [38]. Iako je interes za sendvič panele s TPMS ispunom u inženjerskim poljima sve veći, oni su u glavnom manjeg mjerila (od onog potrebnog za konstrukcijsku primjenu) [62] te osim jezgre, imaju i pojaseve ispisane u istom materijalu [105].

Kombiniranjem parametarskog projektiranja i aditivne proizvodnje u jedan povezan proces, inženjeri arhitektonske i građevinske struke mogu precizno odrediti željeni tip, veličinu i svojstva osnovne gradbene jedinice - ćelije - što pruža do sada neviđenu kontrolu nad projektiranjem konstrukcije [29]. Ova inovacija obećava sinergiju

građevinarstva, arhitekture i znanosti o materijalima - cilj dostižan aditivnom proizvodnjom i korištenjem visoko funkcionalnih materijala [104].

Uz izazove koje primjena 3D ispisa i aditivnih tehnologija u arhitekturi i građevinarstvu predstavlja, ona istovremeno nosi i veliki potencijal ostvariv kroz daljnji razvoj i istraživanje. Prvenstveno su to mogućnost revolucionariziranja načina projektiranja i proizvodnje suvremenih konstrukcija, veća sloboda oblikovanja, učinkovitija uporaba materijala i ekonomičnije građenje. Da bi se što prije nadišli problemi koji stoje na putu ostvarenja tog potencijala, neophodno je ulagati napor u daljnja istraživanja i razvoj ovih tehnologija kao i njihovu integraciju u sektor projektiranja i gradnje konstrukcija.

2. Preliminarno istraživanje kolničkih konstrukcija s rešetkastim strukturama

Preliminarno istraživanje provedeno je kroz analizu 24 modela sendvič panela s ravninskom (2D) geometrijom ispune ekstrudiranom uzduž elemenata. Njih 12 definirano je kao anizotropni GFRP materijal s orijentacijom vlakana u dva ortogonalna smjera [0/90/0/90], dok je ostalih 12 definirano kao materijal kvazi-izotropnih svojstava: usitnjena staklena vlakna su u raznim smjerovima unutar polimerne matrice. Očekivano je kako će kvazi-izotropni materijal rezultirati većom deformacijom i manjom nosivosti. Također je očekivano kako će zakrivljena geometrija mosta rezultirati manjom deformacijom i većom krutosti. Glavni cilj ovog preliminarnog istraživanja je kvantificirati smanjenje nosivosti u odnosu na smanjenu količinu materijala i smanjenje deformacije u odnosu na geometriju. Mnogi aspekti FRP kolničkih konstrukcija utječu na rezultate poput materijala (GFRP, CFRP), konfiguracije i nagiba unutarnjih šupljina i debljina stijenki zidova. U ovoj preliminarnoj analizi predložena je jednostavno oslonjena greda raspona 5 m, visine presjeka 200 mm i širine presjeka 1,8 m. Ploče su oblikovane tako da im masa bude međusobno što je moguće sličnija kako bi se usporedba svela na odnos geometrije ispune i čvrstoće materijala.

Rezultati pokazuju da je maksimalna deformacija zabilježena na ravnim mostovima s kvazi-izotropnim svojstvima materijala, za sendvič panel s trokutastom ispunom. Najniže deformacije izmjerene su na Superdeck-u (konfiguracija šesterostrane ćelije) i EZ Span-u (konfiguracija trokutaste ćelije). U prethodnim istraživanjima [127], uzorci sa Superdeck (šesterostrana ćelija) i ASSET (trokutasta ćelija, slična EZ Span-u) ispunama bili su krući od drugih, što se poklapa s rezultatima ove preliminarne analize.

Predviđanje mehaničkih svojstava TPMS ispunske geometrije dosad je provedena u brojnim studijama i pokazalo se da su efektivna svojstva uglavnom definirana odabirom morfologije [129]. TPMS jedinica matematički je definirana implicitnom funkcijom, a postoje beskrajne mogućnosti za inovaciju novih i hibridnih geometrija. Neke od najčešćih su: Gyroid, Schwarz, Diamond, Split i Neovius. U ovom preliminarnom istraživanju fokus je bio na Gyroid i Schwarz Primitive strukturama. Sve geometrije analizirane su u ravnim i zakrivljenim oblicima. Različite dimenzije TPMS jedinica uspoređene su na istom postotku gustoće odnosno konačne mase konstrukcije. Uspoređena je standardna dvodimenzionalna geometrija ispune kolničkih konstrukcija

(Superdeck, Duraspan, EZSpan, Strongwell i sendvič paneli sa saćastom i trokutastom ispunom) s novom trodimenzionalnom TPMS strukturom (Gyroid i Schwarz). Za sve tipologije definirana je gornja i donja pojasnica debljine 10 mm. Pretpostavljeno je da je pojasnica kruto vezana za geometriju ispune, koja se može 3D ispisati u jednom komadu. Rezultati za sendvič panele 2D ispune su uspoređeni s novim sustavom s geometrijom jezgre od TPMS-a.

Uspoređujući saćasti sendvič panel i TPMS strukturu s istom gustoćom i materijalnim svojstvima, trodimenzionalna struktura Gyroid TPMS-a ima 50% manje deformacije od saćastog 2D sendvič panela, 45% manje deformacije od Duraspan-a, 40% manje deformacije od EZSpan-a, 48% manje deformacije od Strongwell-a, 41% manje deformacije od Superdeck-a i 60% manje deformacije od trokutastog sendvič panela. Rezultati pokazuju veliki potencijal za sendvič panele s TPMS ispunskom geometrijom u usporedbi s tradicionalnim sustavima.

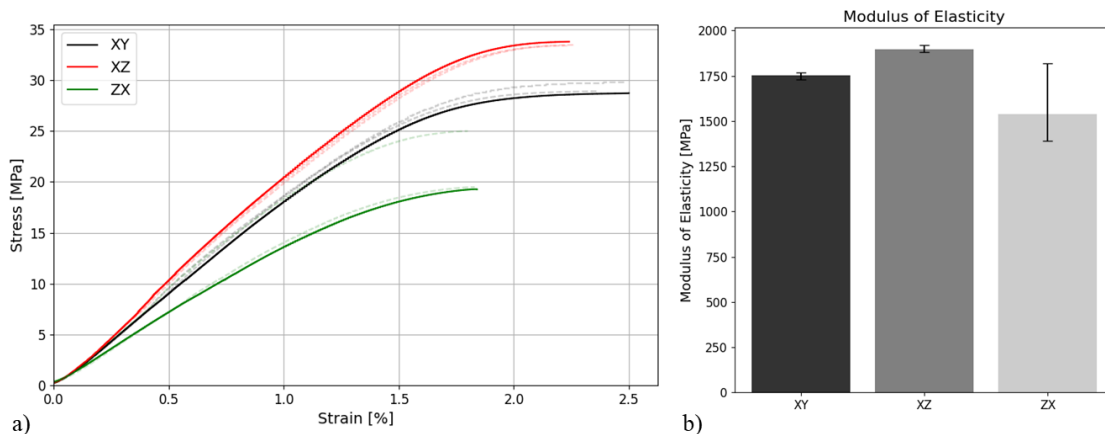
3. Određivanje mehaničkih karakteristika 3D ispisanog materijala

FDM tehnologija u kojoj se materijal nanosi sloj na sloj nosi i mnoga ograničenja i probleme, poput slabije međusobne veze i stvaranja mikro i makro šupljina. Sve to uvodi dodatnu anizotropiju u materijal u usporedbi s tradicionalnim proizvodnim procesima poput pultruzije. Ovo anizotropno ponašanje utječe na prijevremeno otkazivanje 3D ispisanih polimernih dijelova.

Definiranje svojstava 3D ispisanih materijala izazovno je zbog brojnih faktora, poput putanje ispisa, visine sloja, materijala podloge, kvalitete materijala potpore, temperaturnih prijelaza, formiranja mikro i makro pukotina, brzine ispisa, okolne temperature i drugih. Prisutnost praznina i defekata unutar ispisane konstrukcije može povećati koncentraciju naprezanja, smanjujući ukupnu čvrstoću i potičući prijevremeno otkazivanje. Preostala naprezanja generirana tijekom procesa ispisa mogu utjecati na mehanizme otkazivanja i propagacije pukotina.

Osim toga, znanstvenici su otkrili da se mehanička svojstava 3D ispisanih elemenata mogu poboljšati dodavanjem vlakana u korištene polimere te da ugljična i staklena vlakna povećavaju njihovu mehaničku otpornost. Dva su materijala ispitana u sklopu ovog doktorskog rada: termoplastika ASA i karbonskim vlaknima ojačana termoplastika (HI_TEMP CF).

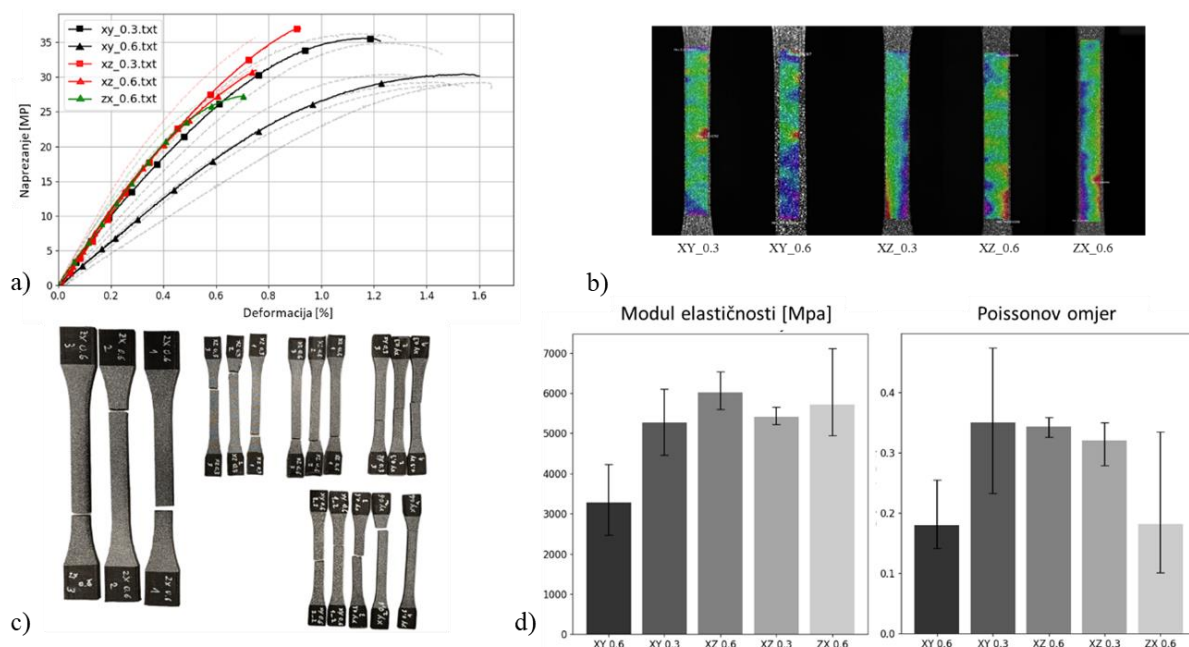
Za 3D ispisani ASA materijal, modul elastičnosti (odnosi se na sekantni) je različit u tri glavna smjera, što je posljedica slojevitog načina ispisivanja. Tako je on najslabiji za smjer ZX kada je opterećenje okomito na slojeve (Slika 3.3b).



Slika 3.3: a) Dijagram naprezanja i deformacije za smjerove ispisa XY, XZ i ZX; b) Modul elastičnosti

Kalibracija materijalnog modela za HI_TEMP CF materijal prikazana je na slici 3.8. za tri različita smjera ispisa i dvije različite rezolucije ispisa. Modul elastičnosti i Poissonov omjer izračunati su koristeći podatke iz DIC-a (eng. *Digital Image Correlation*) i izmjerene površine poprečnog presjeka za svako ispitivanje provedeno u različitim smjerovima 3D ispisa. Modul elastičnosti odnosi se na sekantni modul, izračunat unutar intervala deformacije između $\varepsilon_1 = 0,05\%$ i $\varepsilon_2 = 0,25\%$ prema ISO 527-1.

Rezultati ukazuju da uzorci ispisani u smjeru XY pokazuju najveće odstupanje (isprekidane linije) u deformaciji ovisno o rezoluciji ispisa. Suprotno tome, svi ostali smjerovi ispisa i rezolucije pokazuju slične nagibe krivulje naprezanja/deformacije. Međutim, spomenuto je da su mehanička svojstva za ovu relativno nisku rezoluciju ispisa (0,3 mm i 0,6 mm) izmjerena niža za otprilike 30% u usporedbi s vrijednostima navedenim u tehničkom listu proizvođača.

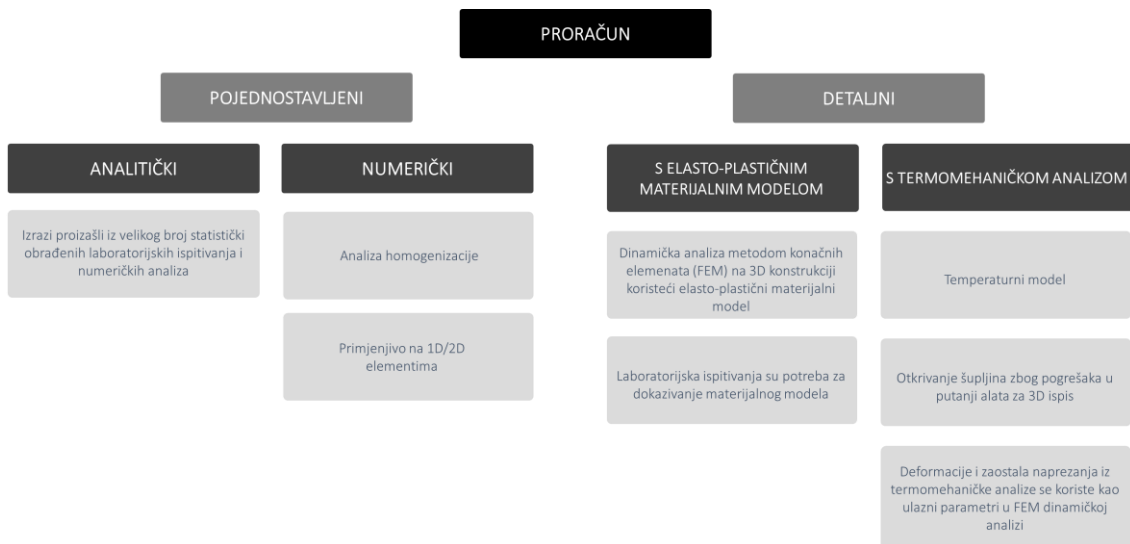


Slika 3.8 Materijalni model: a) krivulje naprezanja-deformacije s raspršenjem prikazanim isprekidanim linijama; b) rezultati DIC-a; c) vizualni prikaz uzoraka nakon ispitivanja; d) modul elastičnosti i Poissonov omjer s 'I profilima' koje označavaju raspršenje rezultata

4. Metode izračuna složenih TPMS geometrija

Modeliranje naprednih geometrija i naprednih materijala može imati i pojednostavljene i detaljnije proračunske pristupe (Slika 5.1). Različite analitičke i numeričke metode su prezentirane s ciljem implementacije tih pristupa u proračun nosivih elemenata. Svi proračunski modeli su potvrđeni za 3D printane TPMS rešetkaste konstrukcije. Primijenjeno je nekoliko alata za implicitno modeliranje 3D ćelijskih strukturalnih objekata, koji se mogu razlikovati po tipu, veličini i materijalnim svojstvima.

Metoda proračuna razvijena u ovom istraživanju uključuje kombinaciju analize homogenizacije reprezentativnih volumenskih elemenata (RVE) i analitičke formulacije savojne krutosti višeslojnih kompozitnih greda. Prvo je korištena analiza homogenizacije RVE-a kako bi se odredila efektivna svojstva TPMS konstrukcija. Izračunate su matrice krutosti za pet različitih geometrija TPMS-a, poput Gyroida, Schwarza, Diamonda, Splita i Neoviusa. Osim toga, provedena su različita eksperimentalna ispitivanja kako bi se te metode i potvrdile.



Slika 5.1 Proračunski pristupi od pojednostavljenih do detaljnih FEM analiza

Rezultati dobiveni ovim analizama pokazali su značajno podudaranje s FEM (eng. *finite element method*) analizom, potvrđujući točnost predloženog algoritma. Predstavljeni algoritam pokazuje se kao vrijedan alat za brzu procjenu kompozitnih sendvič panela i greda. Uključivanjem TPMS jezgre i različitih materijala pojasnica, ovaj pristup nudi nove mogućnosti za dizajn i optimizaciju kompozitnih sendvič panela s TPMS ispunskim geometrijama. Ovakva kombinacija sendvič panela omogućuje istraživanje različitih kombinacija materijala, debljina slojeva, odabira TPMS-a i strukturnih sustava, pružajući brze rezultate u postizanju željenog omjera krutosti i mase sendvič panela. Istraženi su i različiti pristupi parametarskom modeliranju rešetkastih struktura. Različite konfiguracije ulaznih parametara mogu rezultirati uniformnim i neuniformnim rešetkastim strukturama, promjenjive i hibridne geometrije. Hibridna Diamond/Neovius geometrija pokazuje neutralnu distribuciju naprezanja, iako s neizbježnim koncentracijama naprezanja u prijelaznim zonama. S druge strane, Gyroid geometrija postiže neutralnu distribuciju naprezanja kako debljina zida raste u zonama većeg naprezanja.

Detaljni numerički modeli su razvijeni u računalnom programu Abaqus s uvidom u termomehničko ponašanje korištenjem računalnog programa GENOA. GENOA [170] omogućava definiranje različitih parametara kako bi se okarakteriziralo ponašanje 3D printanih kompozita. Ti parametri uključuju svojstva vlakana i matrice, udio volumena vlakana i šupljina, geometriju vlakana, prisutnost proizvodnih nedostataka te kriterije za otkazivanje.

Problem šupljina u 3D printanim materijalima predstavlja značajne izazove u postizanju optimalne kvalitete ispisa i čvrstoće materijala. Šupljine se odnose na prazne prostore unutar ispisanog materijala, što može ugroziti njegovu čvrstoću, funkcionalnost i opću estetiku. Uz problem šupljina tu su i zaostala naprezanja koja nastaju uslijed proizvodnog procesa po principu sloj po sloj te uslijed temperaturnih promjena koje se odvijaju unutar materijala u tijeku 3D ispisa.

5. Parametarsko modeliranje

U ovom poglavlju fokus je na parametarskom algoritamskom modeliranju konstrukcija koje se temelji na principima inspiriranim prirodom. Parametarska studija TPMS metamaterijala uključuje sustavnu varijaciju i analizu fizičkih i mehaničkih parametara. Istraživanjem niza parametara, istraživači mogu identificirati optimalne konfiguracije koje ispunjavaju željenu funkcionalnost budućih nosivih elemenata. Rešetkaste strukture općenito se kategoriziraju u dva tipa: uniformne i neuniformne.

Pet različitih geometrija TPMS jedinica uz dvije vrijednosti relativne gustoće (20% i 40%) definirane su korištenjem različitih matematičkih funkcija $\emptyset(x, y, z)$. Mehanička svojstva TPMS strukture izravno su povezana s udjelom volumena rešetke, tj. relativnom gustoćom ρ_r (omjer volumena rešetke prema volumenu jedinične ćelije, $\rho_r=1$ -poroznost).

Parametarsko modeliranje prve varijante sendvič panela s pojasnicama od kaljenog stakla generiran je korištenjem računalnog programa nTopology [130]. Prvo je izvršena statička analiza na punom volumenu dimenzija jezgre od 0,81 x 0,30 x 0,06 m, podvrgnuta koncentriranom opterećenju u sredini ploče. Rezultati naprezanja dobiveni iz statičke analize korišteni su kao ulazni parametri za topološku optimizaciju ispunske jezgre TPMS-a. Geometrija Gyroida generirana je korištenjem periodičnog pravokutnog bloka rešetke s veličinom ćelije od 100 x 70 x 60 mm. Za topološku optimizaciju, raspodjela materijala postignuta je variranjem veličine ćelija Gyroida i debljinom njegovih zidova. Debljina zidova varirala je između 3.5 i 5.5 mm.

Geometrijski parametri druge varijante sendvič panela s GFRP pojasnicama predstavlja prototip mosta inspiriran geometrijom Da Vinci mosta. Cilj je bio dodijeliti veću visinu presjeka područjima većeg momenta savijanja i veću širinu poprečnog presjeka tamo gdje prevladava posmična sila. Gradbena jedinica, dimenzija 60×60×60

mm, pokazala se prikladna za stvaranje krute, ujedno lagane konstrukcije. Ove su dimenzije odabrane da bi se uklopile unutar okvira dimenzija $900 \times 240 \times 220$ mm.

6. Eksperimentalno istraživanje

U prvom redu izrađeno je pet različitih jedinica TPMS-a (Gyroid, Schwarz, Diamond, Split i Neovius) za dvije različite relativne gustoće (20% i 40%). Priprema za 3D ispis STL datoteke provedena je u GrabCAD sliceru. Uzorci su ispisani sivim ASA materijalom s debljinom slojeva od 0,15 mm i 100%-nom ispunom na stroju Stratasys F123 s mlaznicom širine 0,4 mm. Vizualnim pregledom nakon ispisa nisu utvrđeni nedostaci. Zbog trodimenzionalnosti svih geometrija, postoje dijelovi koji zahtijevaju upotrebu dodatnog potpornog materijala. Ti potporni dijelovi se ispisuju istodobno s glavnom konstrukcijom, ali od materijala koji se naknadno otapa u posebnoj tekućini. Provedeno je ukupno 30 tlačnih ispitivanja jedinica TPMS-a. Korištena je stanična TPMS struktura, definirana kao minimalna površina unutar volumena $50 \times 50 \times 50$ mm. Svi uzorci izrađeni su u uspravnom položaju i podvrgnuti tlačnom opterećenju u smjeru konstrukcije korištenjem univerzalnog statičkog ispitnog stroja (Zwick/Roell Z600E) s kapacitetom opterećenja ± 50 kN. Tlačno opterećenje ravnomjerno je primijenjeno na gornju površinu jedinice preko čelične pločice. Tijekom opterećenja mjerena su sila i vertikalni pomak. Sve jedinice TPMS-a ispitane su do sloma. Primijenjena je brzina prirasta deformacije od 1 mm/min uz kontrolu pomaka.

Varijanta sendvič panela s pojasnicama od kaljenog stakla i topološki optimizirane 3D ispune od ASA materijala podvrgnuta je savijanju u tri točke korištenjem univerzalnog ispitnog stroja Shimadzu AGS-X 100 kN u skladu s normom ASTM C393 za savijanje na sendvič panelima. Dimenzije uzorka uključivale su ukupnu duljinu od 810 mm, širinu od 300 mm i visinu 66 mm. Valjci na osloncima imali su promjer od 35 mm, dok je metalni šuplji valjak promjera 40 mm korišten za linearni unos sile. Kako bi se izbjegao izravan kontakt cilindra sa staklenom pojasnicom, guma je postavljena na kontaktne zone. Pomak je bio zadan pri konstantnoj brzini od 2 mm/min.

Varijanta sendvič panela s pojasnicama od GFRP-a ispitana je na savijanje u četiri točke za ravni oblik uzorka dimenzija $440 \times 60 \times 60$ mm i na savijanje u tri točke za formu u luku dimenzija $900 \times 240 \times 220$ mm. Također je ispitana i sama 3D printana jezgra sendvič panela dimenzija $440 \times 60 \times 60$ mm. Laminati gornje i donje pojasnice izrađeni su

korištenjem tkanine od staklenih vlakana težine 430 g/m^2 proizvedenih od strane tvrtke GIVIDI FABRIC S.R.L. Za matricu je korištena epoksidna smola, Biresin® CR83-2, razvijena od strane tvrtke Sika Technology AG. Laminati s orijentacijom staklenih vlakana $[90/0]_s$ proizvedeni su vakuumskom infuzijom i ostavljeni su da se stvrdnu na sobnoj temperaturi tijekom 24 sata. Ista smola korištena je kao ljepilo za spajanje jezgre s pojasnicama. Za element grede dimenzija $440 \times 60 \times 60 \text{ mm}$ proizvedeno je ukupno četiri sloja laminata, što rezultira ukupnom debljinom od 1,2 mm gornje i donje pojasnice. Dodatno, za gredu u luku proizvedeni su laminati s pet slojeva, s ukupnom debljinom pojasnica od 1,5 mm. Preliminarni izračuni za višeslojne kompozitne materijale provedeni su kako bi se osiguralo da gornji slojevi imaju dovoljnu krutost za kontrolu deformacije jezgre. Eksperimenti na 3D ispisanim uzorcima od materijala pojačanog ugljičnim vlaknima (HI_TEMP CF) mogu se podijeliti u tri grupe: prvo, ispitivanje savijanjem grede same jezgre dimenzija $440 \times 60 \times 60 \text{ mm}$; drugo, ispitivanje savijanjem kompozitnih uzoraka sastavljenih od 3D ispisanje jezgre $440 \times 60 \times 60 \text{ mm}$ s gornjim i donjim GFRP pojasnicama debljine 1,2 mm; i naposljetku, kompozitna greda u luku s 3D ispisanom jezgrom i gornjim i donjim pojasnicama debljine 1,5 mm. Kako bi se održala homogenost kroz cijelu staničnu rešetkastu strukturu jezgre, veličina jedinice i debljina zidova ostaju fiksni na 6 mm, što osigurava konstantnu relativnu gustoću od 20% kroz cijeli volumen. Jedan uzorak samo jezgre i dva uzorka kompozitnih sendvič greda $440 \times 60 \times 60 \text{ mm}$ podvrgnuti su prirastu pomaka od 5 mm/min korištenjem elektromehaničkog stroja Walter + Bai AG kapaciteta 50 kN. Podaci o sili i pomaku su zabilježeni, a vrijednosti deformacijama iz DIC mjerenja su korišteni za detaljnu obradu podataka.

7. Numeričko modeliranje

Za numeričku analizu TPMS jedinica koristi se ista geometrija i rubni uvjeti kao za uzorke ispitane u laboratoriju s dimenzijama $50 \times 50 \times 50 \text{ mm}$. Početni korak u numeričkoj analizi bio je stvaranje mreže konačnih elemenata korištenjem programskog paketa nTopology. Razlučivost mreže jedinične dimenzije $1 \times 1 \text{ mm}$ prihvaćena je kao prikladna za postizanje dostatne preciznosti rezultata za numeričku analizu. Rezultirajuća STEP datoteka zatim je uvezena u Abaqus gdje je podvrgnuta dinamičkoj analizi. Krute ploče postavljene su na vrhu i na dnu modela, pri čemu su njihove referentne točke imale

ograničene translacijske i rotacijske stupnjeve slobode. Prirast konstantnog vertikalnog pomaka implementiran je na gornjoj referentnoj točki. Kako bi se spriječilo samoprodiranje, definirane su postavke kontakta svih dodirnih površina unutar modela. Osim toga, zadana je svojstvena interakcija bez trenja između ploča i jedinice TPMS kako bi se omogućilo klizanje. Materijalni model definiran je kao elasto-plastični izotropni te su definirana svojstva materijala pri lomu kako bi se identificirale potencijalne zone otkazivanja. Uspoređene su krivulje sila-pomak i naprezanje-deformacija s eksperimentalnim podacima iz laboratorijskih ispitivanja.

Potrebna visina jezgre prve varijante sendvič panela sa staklenim pojasnicama je preliminarno izračunata analitički. Nakon toga, u softveru nTopology generirani su 3D model i mreža konačnih elemenata. Mreža konačnih elemenata definirana je na temelju minimalne debljine zida od 3×3 mm te je kao takva uvezena u Abaqus kako bi se provela analiza loma. U svrhu istraživanja utjecaja geometrijskih parametara na karakteristike savijanja sendvič ploče s jezgrom od 3D ispisane TPMS konstrukcije, provedena je FEA analiza koristeći ABAQUS/Explicit, s ciljem simulacije ispitivanja savijanjem u tri točke. U FEA-u, elasto-plastični konstitutivni model primijenjen je na jezgri Gyroida s ASA materijalom, dok je za ploče od kaljenog stakla korišten linearno-elastični konstitutivni model. U definiciji Abaqusa za kontakt između pojasnica od kaljenog stakla i 3D printane jezgre, definiran je koeficijent trenja 1 (što označava puni kontakt) i 'čvrsti kontakt' (eng. *hard contact*). Rubni uvjeti zadani su tako da se ograniče samo vertikalni pomaci dok se dopušta slobodno horizontalno klizanje ležajeva. Opterećenje je primijenjeno kroz vertikalni prirast pomaka od 2 mm/min na sredini gornje pojasnice od kaljenog stakla. Alternativno, mehaničke karakteristike Gyroid jezgre mogu se odrediti putem metode homogenizacije. Razmatrajući topološki optimizirani dizajn ove specifične sendvič jezgre, jezgra je podijeljena u pet segmenata. Veličina jedinice od 100×70×60 mm (prikazana kao Material_01 i Material_01_R*) je primijenjena na rubovima i središnjem poprečnom presjeku, dok je veličina jedinice od 130×70×60 mm (prikazana kao Material_02 i Material_02_R*) korištena za preostala dva segmenta.

FEM modeli sendvič panela s GFRP pojasnicama su provedeni u Abaqusu. Prvi model simulira ponašanje samo 3D printane jezgre pri savijanju. Ovaj model poslužio je za validaciju izotropnog elasto-plastičnog materijalnog modela koji je kalibriran na temelju rezultata vlačnog ispitivanja materijala HI_TEMP CF. Drugi model simulira

sendvič gredu, dok treći simulira gredu u luku. Pretpostavlja se da se ovaj materijalni model može primijeniti za analizu većih 3D ispisanih komponenti sa zadovoljavajućim rezultatom. Svi 3D modeli kreirani su u računalnom programu nTopology korištenjem parametarskog modeliranja. Naknadno je mreža konačnih elemenata definirana s dimenzijama 3×3 mm, te je izvezena u Abaqus za provjeru analize loma. Rubni uvjeti za slobodno oslonjene grede zadani su tako da ograniče samo vertikalne pomake dok dopuštaju horizontalno klizanje ležajeva. Savijanje u četiri točke postignuto je postavljanjem dva valjka udaljena 50 mm od sredine raspona grede. Korišten je materijalni model koji uzima u obzir promjenu brzine deformiranja od 5 mm/min, te tako oponaša uvjete promatrane tijekom laboratorijskih ispitivanja. Rubni uvjeti za gredu u luku postavljeni su ograničavanjem svih horizontalnih i rotacijskih pomaka na oba ruba. Brzina pomaka od 5 mm/min primijenjena je u jednoj točki na sredini gornje GFRP pojasnice.

8. Usporedba eksperimentalnih rezultata i rezultata numeričkih analiza

Tlačno ispitivanje na TPMS jedinicama, pod jednolikim prirastom deformacije otkrilo je više pojedinosti. Gotovo svi modeli otkazuju s početnom pojavom pukotina na mjestu spoja dva sloja. Pretpostavlja se da je lom tijekom tlačnog opterećenja posljedica oslabljenih zona između slojeva materijala, između kojih se otvaraju pukotine. Njihovo međusobno povezivanje na kraju dovodi do posmičnog sloma zidova TPMS-a. Numerička analiza loma iz Abaqusa s prilično velikom točnosti reproducira stvarne rezultate ispitivanja za sve TPMS geometrije, osim Schwarz_40, gdje je došlo do vertikalnog loma umjesto horizontalnog. Kod anizotropnih modela poput Schwarza i Neoviusa, uočeno je otkazivanje koje je nenajavljeno i katastrofalno (fragmentacija u slučaju Schwarza). Suprotno tome, više izotropni modeli (Gyroid, Diamond i Split) pokazuju da nakon početnog otkazivanja (u horizontalnoj ravnini), zidovi se dalje drobe bez iznenadne fragmentacije dijelova konstrukcije, što povećava njihovu sigurnost za upotrebu u nosivim sustavima. U elastičnoj zoni, sve TPMS geometrije pokazale su jednolik prirast sile i deformacije. Kako je i očekivano, Diamond geometrija pokazala se superiornom u pogledu tlačne otpornosti, s maksimalnim vrijednostima od 8.36 kN pri relativnoj gustoći od 20% i 20.10 kN pri relativnoj gustoći od 40%. Najmanju otpornost

na tlačnu silu pokazala je Schwarz geometrija, s minimalnim vrijednostima od 1.55 kN i 9.48 kN, prije krtog loma koji se dogodio i pri relativnoj gustoći od 20% i 40%. Neovius geometrija iako anizotropna, pokazala se kao druga najbolja geometrija slijedeći Diamond sa 7.78 kN i 18.75 kN, za relativne gustoće od 20% i 40%. Diamond je također pokazao najveće produljenje pri slomu. Gyroid i Split, oba izotropna modela, pokazuju prednosti za primjenu u nosivim konstrukcijama, pri čemu Gyroid više podsjeća na organičke strukture kao što su pronađene u strukturi ljudskih kostiju. Iako Split ima superiorna svojstva, njegova relativno razvedena površina možda nije najbolji izbor za primjenu u konstrukcijama zbog dužeg vremena potrebnog za 3D ispis. Gyroid, s druge strane, razmatran je u sendvič panelima zbog svojih obećavajućih mehaničkih karakteristika i privlačne vizualne prirode.

Promatrajući krivulju sile i pomaka kod kompozitne ploče s 3D geometrijom TPMS jezgre i pojasnicama od kaljenog stakla, očito je da je opterećenje brzo doseglo maksimum pri relativnoj maloj deformaciji sustava. Pad sile dovodi do produljenog platoa deformacije pri konstantnoj sili. Stoga se krivulja sile i pomaka može podijeliti na tri faze:

1. Faza prije otkazivanja: Ova faza predstavlja dio krivulje sile/pomaka od početka do prvog vrhunca sile, tijekom kojeg opterećenje postupno raste.
2. Faza otkazivanja: Određeni zidovi s manjom gustoćom materijala razvijaju otvorene pukotine u horizontalnoj ravnini.
3. Faza nakon otkazivanja: Nakon što se otkazivanje dogodilo, kompozit pokazuje ponovni rast sile, a i pomaka sve do naglog i krtog loma koji se događa na gornjoj staklenoj pojasnici uslijed tlačnog opterećenja uslijed kojeg dolazi do posmičnog otkazivanja zidova jezgre po cijeloj visini poprečnog presjeka.

Kruta veza između staklenih pojasnica i jezgre s Gyroid ispunom spriječila je deformaciju stakla. Kako se povećavalo tlačno naprezanje, rezultiralo je drobljenjem stakla, što je dovelo do trenutnog posmičnog otkazivanja zidova jezgre. Ponašanje do sloma 3D sendvič panela pod opterećenjem na savijanje učinkovito je simulirano korištenjem elasto-plastičnog izotropnog materijalnog model unutar FEA.

Zbog složenosti 3D geometrije jezgre unutar sendvič strukture, rezultati za sendvič panele s GFRP pojasnicama su detaljno analizirani koristeći podatke dobivene iz DIC mjerenja. Za statističko tumačenje dobivenih rezultata modeli prostih greda

podijeljeni su u tri zone po visini grede (gore, dolje i sredina), te u tri zone po rasponu grede (oslonac, sredina i ostalo). Kod grede u luku, područje interesa predstavljala je sredina raspona grede. Stoga su se zone po visini podijelile na gornju i donju, zajedno s dvije srednje zone. Podaci o pomacima iz mjerenja DIC metodom prikazani su za točke prema lokaciji na rasponu grede, pri čemu su različite boje dodijeljene čvorovima na vrhu (plava), dnu (siva) i u sredini (zelena). Različiti markeri koristili su se za razlikovanje čvorova na osloncima (kvadrat), u sredini (kružnica) i za ostale (trokut). Rezultati su prikazani za ukupno 39 čvorova tijekom svih vremenskih intervala ispitivanja, pri čemu je transparentnost u bojama uvedena kako bi se predstavili različiti vremenski intervali. Krivulje deformacije prikazane su za trenutak otkazivanja i nakon faze otkazivanja. Materijalni model potvrđen je kroz FEM analizu na gredi sa samo 3D printanom jezgrom, pri čemu je utvrđeno da je smjer ispisa XY s rezolucijom visine ispisa sloja od 0,6 mm bio najprikladniji. Ovaj odabir također je usklađen s parametrima 3D ispisa u smjeru XY i debljinom sloja od 0,6 mm. Sendvič greda analizirana je i uspoređena s dva uzorka sendviča ispitana savijanjem. Analiza i laboratorijska ispitivanja pokazali su da je krutost sendvič grede i grede u luku povećana zbog proizvodnog procesa kompozita, koji uključuje lijepljenje TPMS jezgre na pojasnice s Biresin® CR83-2, koji se zatim impregnira u zonu gornjih i donjih presjeka. Ovi modeli uspješno su detektirali krutost sustava i identificirali zone otkazivanja. Analiza je pokazala dosljednost s početnim analitičkim izračunima, koji su pokazali da pojasnice imaju dovoljnu krutost za kontrolu deformacije jezgre. Impresivno je otkriće da sendvič nosač, u usporedbi sa jezgrom koja je samostalno ispitana, pokazuje gotovo sedmerostruko veću nosivost i četiri puta veću krutost. S relativno malim povećanjem od 25% ukupne težine konstrukcije. Ispitivanje na savijanje grede u luku koji ima uniformnu periodičnost jezgre izazvao je koncentraciju naprezanja samo lokalno u gornjoj zoni, što je rezultiralo drobljenjem tankih zidova TPMS rešetke. Ipak, potencijal topološki optimiziranih konstrukcija u luku korištenjem metamaterijala zahtijeva daljnje istraživanje. FEA model uspješno je identificirao fenomene poput drobljenja i delaminacije gornje pojasnice. Međutim, nedostatak ponašanja nakon otkazivanja i otvaranje pukotina unutar modela jezgre je preporučeno s detaljnijom analizom koja uključuje termomehanički model za 3D ispis.

TABLE OF CONTENT

THESIS SUMMARY	I
EXTENDED ABSTRACT IN CROATIAN	III
LIST OF FIGURES	XXII
LIST OF TABLES	XXV
1 INTRODUCTION AND STATE OF THE ART.....	1
1.1 Objective and hypotheses of research	7
1.2 Methodology and plan of research	8
2 PRELIMINARY INVESTIGATION OF COMPOSITE BRIDGE DECKS WITH LATTICE STRUCTURES	11
2.1 FRP bridge decks with two-dimensional core geometry.....	12
2.1.1 Materials and methods	13
2.1.2 Results	16
2.2 FRP bridge decks with three-dimensional core geometry	18
2.2.1 Materials and methodology	18
2.2.2 Results	20
3 MECHANICAL CHARACTERIZATION OF 3D PRINTED MATERIAL	23
3.1 ASA material.....	24
3.1.1 Specimen design and experimental setup.....	24
3.1.2 Calibration of the material model	25
3.2 HI_TEMP CF material	28
3.2.1 Specimen design and experimental setup.....	28
3.2.2 Calibration of the material model	31
4 PARAMETRIC DESIGN	33
4.1 TPMS units.....	35
4.2 Composite sandwich panel with tempered glass face sheets	36
4.3 Composite sandwich panel with GFRP face sheets	39
5 ANALYSIS APPROACHES	42
5.1 Homogenization analysis	43
5.1.1 Numerical analysis of TPMS units	46

5.1.2	Analytical analysis of TPMS units	50
5.2	Multilayer composite analysis.....	51
5.3	Thermo-mechanical analysis.....	58
6	SPECIMEN DESIGN AND EXPERIMENTAL CAMPAIGN.....	66
6.1	TPMS units.....	66
6.2	Composite sandwich panel with tempered glass face sheets	68
6.3	Composite sandwich panel with GFRP face sheets	69
7	NUMERICAL MODELLING	74
7.1	TPMS units.....	74
7.2	Composite sandwich panel with tempered glass face sheets	75
7.3	Composite sandwich panel with GFRP face sheets	78
8	COMPARISON OF EXPERIMENTAL AND NUMERICAL RESULTS	80
8.1	TPMS units.....	80
8.2	Composite sandwich panel with tempered glass face sheets	86
8.3	Composite sandwich panel with GFRP sheets.....	90
8.3.1	Core only	91
8.3.2	Sandwich beam.....	94
8.3.3	Arch beam	97
8.3.4	Finite element models	100
9	DISCUSSION	103
9.1	PRELIMINARY INVESTIGATION OF COMPOSITE BRIDGE DECKS WITH LATTICE STRUCTURES	103
9.2	MECHANICAL CHARACTERIZATION OF 3D PRINTED MATERIAL 104	
9.3	ANALYSIS APPROACHES	105
9.4	TPMS UNITS.....	105
9.5	COMPOSITE SANDWICH WITH TEMPERED GLASS FACE SHEETS 106	
9.6	COMPOSITE SANDWICH WITH GFRP FACE SHEETS	107
10	CONCLUSIONS	109
10.1	Research hypothesis verification.....	111

10.2	Scientific contribution of proposed research.....	114
10.3	Recommendations for future research.....	115
	REFERENCES	117
	CURRICULUM VITAE	134
	LIST OF PUBLISHED WORKS BY THE AUTHOR	135

LIST OF FIGURES

Figure 1.1 First 3d printed bridge in China, Shanghai [9]	1
Figure 1.2 Robotic arms at the EPFL University	2
Figure 1.3 Cellular structures found in nature: butterfly wings, weevils and the structure of the human bone [39,46]	3
Figure 1.4 From 3D solid to porous TPMS structure	4
Figure 2.1 GFRP plate, adhesively bonded pultruded profiles: (a) Superdeck; (b) Superdeck in an arch; (c) EZSpan; (d) EZSpan in an arch; (e) DuraSpan; (f) DuraSpan in an arch; (g) Strongwell; (h) Strongwell in an arch. Sandwich panels: (i) triangular-shaped infill; (j) triangular-shaped infill in an arch; (k) honeycomb-shaped infill; (l) honeycomb-shaped infill in an arch.	15
Figure 2.2 Modulus of elasticity for glass fibre reinforced polymers [129]	16
Figure 2.3 Geometry of: (a) Superdeck and (b) Superdeck in an arch. Deformation for: (c) Superdeck (laminated); (d) Superdeck (laminated) in an arch; (e) Superdeck (quasi-isotropic); (f) Superdeck (quasi-isotropic) in an arch.	17
Figure 2.4 Results for displacements.	17
Figure 2.5: TPMS deck infill: a) Gyroid (500 mm grid) 20% densification, b) Gyroid (500 mm grid) 20% densification in an arch, c) Gyroid (500 mm grid) 35% densification, d) Gyroid (500 mm grid) 35% densification in an arch, e) Gyroid (200 mm grid) 35% densification, f) Gyroid (200 mm grid) 35% densification in an arch, g) Schwarz Primitive (200 mm grid) 35% densification, h) Schwarz Primitive (200 mm grid) 35% densification..	19
Figure 2.6: Topology optimization with Gyroid structure	20
Figure 2.7: Comparison of Gyroid TPMS deck with traditional deck system	21
Figure 2.8 Topology optimized Gyroid core with 20% densification based on stress distribution	22
Figure 3.1: Dogbone ASA specimens for the tensile test	25
Figure 3.2 Nine 3D-printed specimens displaying various fracture zones (1, 2 and 3 represent the XY, XZ and ZX print direction, respectively).....	26
Figure 3.3: a) Stress-strain diagram for the XY, XZ and ZX print direction; b) Modulus of elasticity	26
Figure 3.4 Scanning electron micrographs of (a) ASA XY print direction showing when a strut at 0° direction is printed on a bottom 90° direction strut (b) Printing in the XZ direction displays layers of elliptical shape in the cross-section, revealing irregularities and visible open cavities between 0 and 90° c) The ASA ZX print orientation exhibits a localized thickening effect by placing a strut at a 0° angle over a strut at a lower 90° direction.....	28
Figure 3.5 Voids from 3D printed part vs. void prediction from the toolpath error.....	28
Figure 3.6 Tensile test specimens - HI_TEMP CF material	29
Figure 3.7 Tensile test setup.....	30
Figure 3.8 Material model: a) stress strain curves with scatter illustrated with dashed lines; b) DIC results; c) visual representation of failed tensile test specimens; d) modulus of elasticity and Poisson's ratio with 'I bars' indicating scatter	32
Figure 4.1 Parametric generative design of TPMS: a) Gyroid and b) Diamond structures	33
Figure 4.2 Five different TPMS unit cells derived from the iso-surface: Gyroid, Schwarz, Diamond, Split and Neovius (from left to right)	36

Figure 4.3 Design of Gyroid core	37
Figure 4.4 Final part of the composite TPMS bridge deck with tempered glass face sheets.....	39
Figure 4.5 Geometry definition in Rhinoceros and Grasshopper	40
Figure 4.6 Cellular structures for the proposed bridge geometry: a) Periodic homogeneous cellular structure; b) Periodic heterogeneous structures; c) Pseudo-periodic homogenous structure; d) Pseudo-periodic heterogeneous structure.....	41
Figure 4.7 Final composite bridge model	41
Figure 5.1 Analysis approaches from simplified to more detailed.....	42
Figure 5.2 RVE Homogenization analysis set of 6 load cases	44
Figure 5.3 Polynomial regression curve for determination of mechanical properties for each TPMS type.....	44
Figure 5.4 Calculated expression from curve fitting for each TPMS type; a) Gyroid, b) Schwarz, c) Diamond, 45	
Figure 5.5 Parametric design of: a) Gyroid Unit Cell: Math Algorithm (1 cell), b) Gyroid Unit Cell: Topology Optimization (5×5 raster), c) Gyroid Non-Uniform Lattice: Structural Optimization (5×5 raster), d) Gyroid Non-Uniform Lattice: Functional Gradient Design e) Gyroid with Neovius Hybrid Geometry; f) Diamond Unit Cell: Math Algorithm (1 cell), g) Diamond Unit Cell: Topology Optimization (5×5 raster), h) Diamond Non-Uniform Lattice: Structural Optimization (5×5 raster), i) Diamond Non-Uniform Lattice: Functional Gradient Design and j) Diamond with Neovius Hybrid Geometry.....	47
Figure 5.6 Anisotropy properties of sheet TPMS: a) Gyroid Unit Cell: Math Algorithm (1 cell), b) Gyroid Unit Cell: Topology Optimization (5×5 raster), c) Gyroid Non-Uniform Lattice: Structural Optimization (5×5 raster), d) Gyroid Non-Uniform Lattice: Functional Gradient Design e) Gyroid with Neovius Hybrid Geometry; f) Diamond Unit Cell: Math Algorithm (1 cell), g) Diamond Unit Cell: Topology Optimization (5×5 raster), h) Diamond Non-Uniform Lattice: Structural Optimization (5×5 raster), i) Diamond Non-Uniform Lattice: Functional Gradient Design and j) Diamond with Neovius Hybrid Geometry.....	48
Figure 5.7 Software interface	52
Figure 5.8 Design flowchart.....	53
Figure 5.9 Comparison of results from FEM analysis and novel application for composite beams with TPMS infill	54
Figure 5.10 left: graph displacement to TPMS infill density ratio; right: Total weight of structural system vs. TPMS infill density ratio.....	56
Figure 5.11 Optimised composite plate with 15% gyroid core - FEM and results from quick estimation algorithm: a) 200 mm core and top and bottom 10 mm flange from 3D printed unfilled plastic; b) 110 mm core from 3D printed filled plastic and 1 mm top and bottom glass flange; c) 120 mm core from 3D printed unfilled plastic, 10 mm top concrete and 1 mm bottom FRP flange; d) 100 mm core from 3D printed filled plastic and 0.5 mm top and bottom steel flange.....	58
Figure 5.12 Flowchart of simulation approach.....	60
Figure 5.13: a) ASA filament tension test setup; b) Microscopic view of the fracture zone; c) stress-strain relationship obtained from the tensile test performed on the ASA filament specimen	62
Figure 5.14 Virtual simulation flowchart.....	63

Figure 5.15 Mechanical analysis from Abaqus UMAT: a) Stress – von Mises XY print direction; b) Magnitude of displacement XY print direction; c) Stress – von Mises ZX print direction; d) Magnitude of displacement ZX print direction.....	63
Figure 5.16 Boundary conditions for the tensile test simulation.....	64
Figure 5.17 Strain concentration and potential fracture zones.....	64
Figure 5.18 Dogbone brittle fracture: a) ASA XY print direction; b) ASA XZ print direction.....	64
Figure 5.19 Comparison of Virtual Simulation Dynamic Analysis with the 3D printed tensile test in the XY print direction.....	65
Figure 5.20 Comparison of Virtual Simulation Dynamic Analysis with the 3D printed tensile test in the ZX print direction.....	65
Figure 6.1 Five TPMS units (Gyroid, Schwarz, Neovius, Diamond and Split from left to right) with 20% relative density: a) Model preparation; b) 3D-printed part after removal of support material; c) laboratory test setup.....	67
Figure 6.2 Five TPMS units (Gyroid, Schwarz, Neovius, Diamond and Split from left to right) with 40% relative density: a) Model preparation; b) 3D-printed part after removal of support material; c) laboratory test setup.....	68
Figure 6.3 Three-point bending test – setup.....	69
Figure 6.4 4-point bending test of beam samples.....	70
Figure 6.5 Bigrep PRO printer built print space of 1005 x 1005 x 1005 mm.....	72
Figure 6.6 Production of the composite sandwich arch.....	73
Figure 7.1 Material model set for FEM analysis of the sandwich panel with 3D printed core.....	76
Figure 7.2 Design process flow.....	77
Figure 7.3 Finite element models: a) Core only; b) Sandwich beam; c) Arch beam.....	78
Figure 8.1 TPMS unit cells (Gyroid, Schwarz, Neovius, Diamond and Split from left to right) with 20% relative density: a) Thermal analysis; b) Void from toolpath error; c) Compression test failure modes; d) Abaqus dynamic failure analysis.....	82
Figure 8.2 TPMS unit cells (Gyroid, Schwarz, Neovius, Diamond and Split from left to right) with 40% relative density: a) Thermal analysis; b) Void from toolpath error; c) Compression test failure modes; d) Abaqus dynamic failure analysis.....	83
Figure 8.3 Failure modes of TPMS units under compressive load (Gyroid, Schwarz, Diamond, Split and Neovius from left to right).....	84
Figure 8.4 Compressive load-displacement diagrams for five TPMS geometries.....	85
Figure 8.5 Three-point bending test results and comparison with the FEA.....	87
Figure 8.6 3D printing toolpath from GrabCAD slicer.....	88
Figure 8.7 Snapshots from bending test by phases.....	89
Figure 8.8 Detail finite element analysis in GENOA AlphaSTAR software: a) Thermal analysis– temperature; b) Macro-void resulting from toolpath errors; c) Mechanical analysis – von Mises; d) Mechanical analysis – displacements.....	90
Figure 8.9 Core only: Displacement.....	92
Figure 8.10 Core only: Shear stress vs. strain.....	92
Figure 8.11 Core Only: First principal stress vs. strain, second principal stress vs. strain, stress vs. strain in x direction (parallel to material deposition), stress vs. strain in y direction (orthogonal to material deposition).....	93

Figure 8.12 Sandwich beam: Displacement	95
Figure 8.13 Sandwich beam: Shear stress vs. strain	95
Figure 8.14 Sandwich beam: First principal stress vs. strain, second principal stress vs. strain, stress vs. strain in x direction (parallel to material deposition), stress vs. strain in y direction (orthogonal to material deposition).....	96
Figure 8.15 Arch beam: Displacement	98
Figure 8.16 Arch beam: Shear stress vs. strain	98
Figure 8.17 Arch beam: First principal stress vs. strain, second principal stress vs. strain, stress vs. strain in x direction (parallel to material deposition), stress vs. strain in y direction (orthogonal to material deposition).....	99
Figure 8.18 Comparison of load vs. displacement: FEM and experimental data for “core-only”, “sandwich beam”, and “arch beam”	101
Figure 8.19 Failure modes detected for: “core only”, “sandwich beam”, “arch beam”	102
Figure 10.1 Panel wall with non-uniform lattice structure based on structural optimization	115

LIST OF TABLES

Table 2.1 Physical properties of plate systems from adhesively bonded pultruded profiles [111].	13
Table 2.2 Composite layup material properties for Glass Fiber Epoxy resin	16
Table 3.1 Material properties of ASA and Process parameters for Stratasys F123	24
Table 3.2 Measured dimensions of the specimens before the test.....	25
Table 3.3 Tensile test dimensions.....	30
Table 3.4 Material properties HI-TEMP CF and Process parameters for BigRep PRO.....	31
Table 4.1 Mathematical function of each TPMS type	34
Table 4.2 Material properties and process parameters.....	37
Table 4.3 Tempered glass and Adhesive material properties.....	38
Table 5.1 Mechanical properties obtained from Homogenization Analysis	49
Table 5.2 Results for C_1 and n constants for each TPMS	51
Table 5.3 Values for density and Young’s modulus of chosen materials.....	52
Table 5.4 Comparison of results for different TPMS, density of TPMS infill and for 4 models.....	55
Table 6.1 Properties of the 3D-printed TPMS samples	66
Table 6.2 Mechanical properties obtained from Homogenization Analysis.....	71
Table 6.3 Process parameters for BigRep PRO	72

1 INTRODUCTION AND STATE OF THE ART

In the last two to three decades, there has been a tremendous increase in the power of computers and the adaptability of software packages for computer-aided design (CAD). In the 21st century, the focus is on linking digital design with production processes [1].

Additive manufacturing (AM) has demonstrated its efficacy in numerous sectors including medicine [2], automotive [3,4], aerospace [5], and space industry [6]. However, its utilization in structural engineering and architecture remains limited, with the most common application being in pedestrian bridges [7] [8]. There are few examples of 3D printed concrete, steel, and some promising projects of printing bridges with composites. The first example of a 3D-printed composite pedestrian bridge with overall dimensions of 15.5 x 3.8 m was produced in China in 2020 [9]. The total load-bearing capacity was analysed for 250 kg/m² and an expected service life of 30 years (Figure 1.1). The material is ASA (acrylonitrile styrene acrylate) reinforced with glass fibres. The total weight of the bridge is 5.8 t with 12.5 % of fibre content. The entire production took 30 days on a 3D printer with a printing capacity of 8 kg/h and a volume of 24 x 4 x 1.5 m. The problem is still a relatively slow process of 3D printing compared to the traditional material bridge construction techniques.



Figure 1.1 First 3d printed bridge in China, Shanghai [9]

Recent research describes how industrial robots (Figure 1.2) can handle complex architectural forms, reducing the cost of custom design, manufacturing, and assembly [10,11]. Rapid advances in information technologies and robotics have greatly favoured the use of 3D printing in large-scale manufacturing [12]. The use of lighter polymer materials in 3D printing technologies is of great interest to researchers today, as they can be used to produce complex geometries. Additive manufacturing (AM) has evolved over the years, with various production methods to choose from: Selective Laser Melting (SLM), Selective Laser Sintering (SLS), Stereolithography (SLA), Direct Light Processing (DLP) and the technology used in this research - Fused Deposition Modelling (FDM) [13].



Figure 1.2 Robotic arms at the EPFL University

AM primary role was the production of formworks for traditional building materials and techniques [14]. To demonstrate its effectiveness as an independent construction technique, new designs, materials, and structural systems should be employed, with a focus on forms that no other production method is capable of satisfying.

An AM technique, FDM offers unique possibilities for the production of structures in various sizes and materials [15–18]. This method offers design freedom by allowing the combination and variation of raw materials and facilitating the production of objects with functionally graded materials (FGM) [19]. This capability results in increased strength, particularly in highly stressed areas. However, it requires special attention to geometric deviations during the printing process, especially in the case of 3D lattices [20]. The layer-by-layer technique has some disadvantages that affect the quality of the finished part. Specifically, the staircase effect cannot be completely avoided [21]. More sophisticated objects can be produced using 6-axis machining with a robotic arm. Once the basic computer-aided design (CAD) model is created, different materials and production processes can be selected [22,23].

While some 3D printing solutions are still in the experimental stage, there is a challenge in successfully adapting and implementing 3D printing within the construction industry [10,24]. Research [25] suggests that technologies such as artificial intelligence (AI), remote sensing (RS), and 3D printing (3DP) can enhance reliability, sustainability, and automation in civil construction.

Through systematic observation, advanced computer programming and precise calculations, it is possible to strategically manipulate the behaviour of the material to achieve the desired geometry of the structural elements [26–31]. The emerging trend is that the forthcoming prototypes will exhibit resemblances to biological and natural structures, mirroring the intricate formations found in bones, plants, tissues, sponges and corals [32]. The idea of simulating forms found in nature is a new facilitation method in construction. Such technology

transfer is called bionics, biomimetics, or biognosis [33–35]. Cellular organisms provide us with examples of how material is concentrated where it is most needed to create optimized structures [36].

Lighter materials offer the advantage of building complex geometries, as costs are primarily influenced by material consumption rather than geometric complexity [37,38]. The application of additive manufacturing ranges from nano, micro, meso and macro-scale to large-scale applications [22,39–42].

The development of high-performance, lightweight structures mirrors the principles observed in metamaterials, known as triply periodic minimal surfaces (TPMS) [43]. By observing many objects in nature, such as the scaled biphotonic structure of butterfly wings, weevils and a human bone structure (Figure 1.3) - a great example of symmetric and optimized physical properties of the TPMS pattern was found [32,44,45]. Cellular organisms provide us with examples of how material is concentrated where it is needed most to create optimized structures [36] as many biological structures are porous but with great interconnectivity [32].

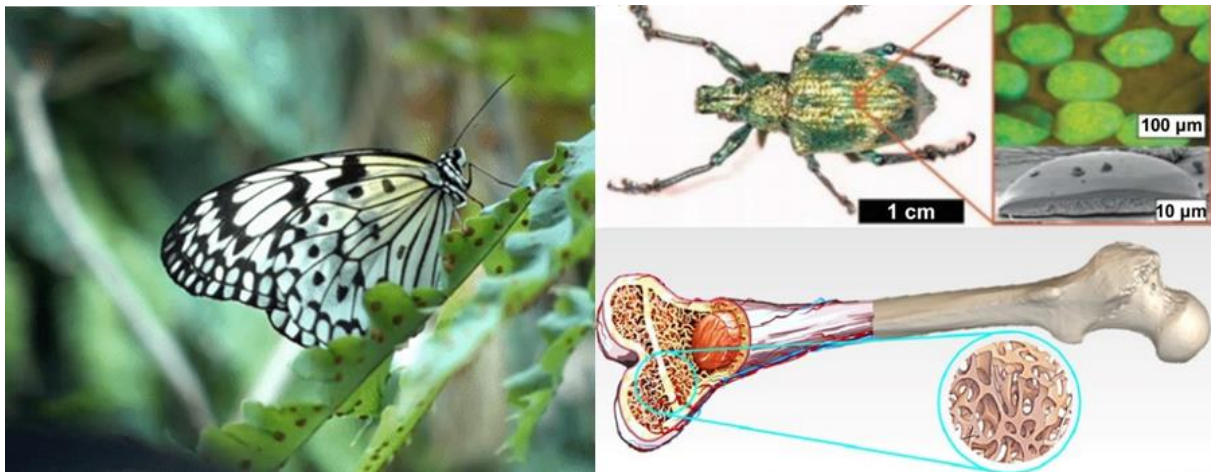


Figure 1.3 Cellular structures found in nature: butterfly wings, weevils and the structure of the human bone [39,46]

The application of TPMS in topology optimization has been used in many fields of mechanical engineering [47]. TPMS is considered to be the optimal geometry in terms of minimum surface area dividing the space into equal volume domains [44] accompanied by the superior mechanical properties [48]. The lattice structures derived from TPMS consist of repeating unit cells with a high degree of porosity (Figure 1.4). The challenges of 3D printing on a larger scale were studied in [49], where compressive and flexural properties across different specimen sizes of 3D printed parts were examined. The experiments revealed substantial reductions in compression strength and bending strength for polymeric material as the specimen size increased.

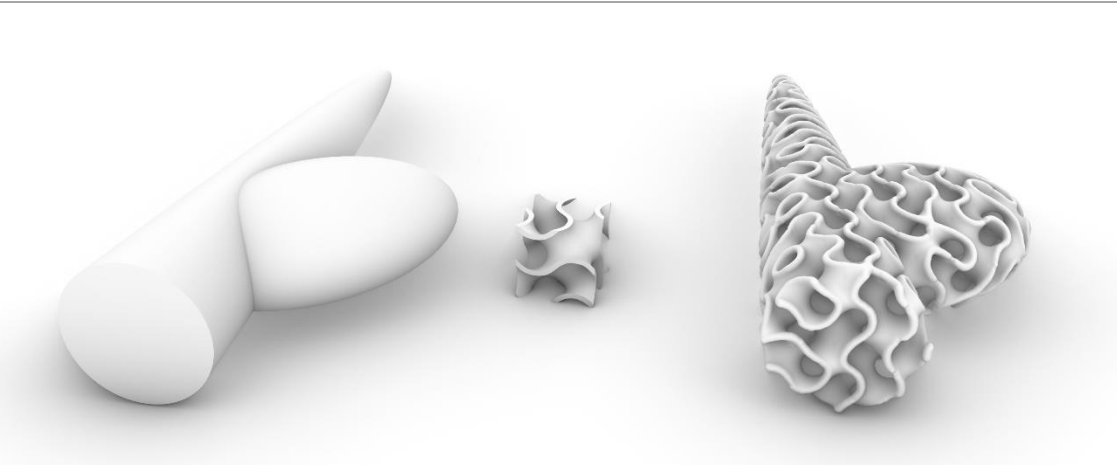


Figure 1.4 From 3D solid to porous TPMS structure

Cellular structures can be observed on micro, meso and macro scale [50]. Mesoscale cellular structures can generally be classified into stochastic and non-stochastic types. Non-stochastic structures can be observed in 2D and 3D lattice configurations, with current research focusing on 3D lattices categorized as strut and cell lattices [51]. 2D and 3D cellular lattices can be classified as either periodic, with uniform and homogeneous features within their 2D planes or 3D space, or pseudo-periodic with uniform but heterogeneity achieved by variations in strut and cell thickness. In non-stochastic cellular structures, the properties of unit cells represent those of the entire structure. In contrast, stochastic structures allow for variations in unit cell shape and size.

The TPMS are also topology optimized structures, characterised by cost and weight efficiency, improved mechanical properties in compression and crushing, and excellent energy absorption and vibration characteristics [52,53]. TPMS are considered auxetic materials or structures that expand in all directions when stretched and contract when compressed, resulting in a negative Poisson's ratio [54–56]. This unique behaviour is often beneficial for applications such as impact absorption [57], aeronautic applications [47], engineering materials [58], medical devices [59] and many more.

Some of the most popular TPMS are Gyroid, Schwarz, Diamond, Split and Neovius. Structures based on the Diamond surface demonstrate superior absorption capacity under compressive loading compared to structures based on Schwarz and Gyroid surfaces [60]. It has been shown that the absorption coefficient is influenced by the volume fraction and the unit cell size, while the height of the structures can be adjusted to change the effective frequency ranges [61]. An increase in compressive modulus and strength was observed at higher volume fractions [60]. Valuable insights into the mechanical properties and structural characteristics of the Neovius structure, indicating potential applications in material science and engineering, can be found in [62]. A similar study was conducted by Khan et al [63]. The failure mechanism of

FDM-based polymer and composite materials has been investigated for various properties including tensile strength [64], flexural strength [65], impact strength [66], compressive strength [60] and thermo-mechanical behaviour [67] under static loading conditions.

Existing lattice structures are primarily constructed using uniform or graded units. Han and Lu [29] proposed a novel method for gradient design of non-uniform lattice structures based on additive manufacturing technology, namely the size gradient method (SGM). Nguyen et al [68] utilized the Size Matching and Scaling (SMS) method and simplified the optimization process by concentrating on two variables: the maximum and minimum strut diameter or in the case of TPMS - cell thickness. Some research has focused on hybrid lattice structures that contain two or more types of units [69].

The design freedom of cellular 3D structures, especially heterogeneous lattices and pseudo-periodic lattices, has increased with AM and 3D printing [51,70]. This advancement allows for more cost-effective and sustainable options, as there are no additional costs for materials and production. The structural optimization method [71] employs size optimization to utilize displacement or Von-Mises stress points obtained from structural analysis as input parameters for the parametric design of lattice structures known as load-adaptive pseudo-periodic lattice by changing shape and size in areas of higher stress, thereby providing a more efficient structure while saving material. To enhance design efficiency and reduce computational time, various topology optimization methods can be employed. Some of the most commonly used methods include ground structure optimization [72], Solid Isotropic Material with Penalization (SIMP) [73], and Bidirectional Evolutionary Structural Optimization (BESO) [74].

Cellular structures with controllable topology are called Metamaterials [20,75]. Metamaterials, known as TPMS, are iso-surfaces defined by the mathematically implicit functions [2,42,60,76–80]. Following the concept of functional gradation observed in microstructures, the Functionally Graded Triply Periodic Minimal Surfaces (FG-TPMS) [81] were developed. Through the graded topology, greater control over properties such as elastic modulus, shear modulus, bulk modulus, and Poisson's ratio can be achieved.

Sandwich structures can be made of numerous materials depending on the application [82]. In aerospace structures high-tech components such as metal and polymer foams can be found [47]. According to the current strategy of sustainable development the attempts to use materials of natural origin [83] and fully recyclable thermoplastics [84] can be observed. The mathematical tools for predicting the behaviour of sandwiches make it easy to provide the desired results in the shortest possible time [85]. A generalization of the analytical model of

sandwich structures was presented in [86], where the authors proposed a continuous and symmetric variation of the mechanical properties in the thickness direction. They mentioned that another improvement of their theory is to introduce thin layers connecting the faces and the core. The study by Stepinac et al. [87] aims to analyse different fibre-reinforced polymer (FRP) sandwich configurations, comparing their material properties and the impact of their geometry on stiffness, finding that the bridge shape geometry and infill configuration have a significant effect on increasing stiffness, more so than improving material properties.

Driven by the recent advancements in production and material sciences [58], as well as in software capabilities [88], researchers have focused more on achieving lightweight structures. This involves substituting solid volumes with intricately designed cellular structures that can be only produced by the AM techniques.

TPMS structures are used as a core structure in sandwich panels. Compared to other lattice core structures, TPMS structures show much better performance [89,90]. Due to the porosity of its structure, TPMS structure can be used wherever energy absorption is required, e.g. connections in structure. Sengsri et al. [91] studied the mechanical properties and energy-absorption capabilities of TPMS sandwich lattice for the purpose of bridge bearing applications. The findings of the study revealed that the structure demonstrated promising potential for effective utilization in bridge bearing applications.

The following study [90] investigated seven 3D printed core structures. The cores of sandwich panels were made as honeycomb and re-entrant honeycomb (both with small and large cell sizes), Pyramid and Hierarchical Pyramid lattices and TPMS core known as Gyroid. The 3D printed core structures were coupled with CFRP composite face sheets and tested for strength and stiffness using three-point bending test. The results showed that Gyroid structure had the highest specific stiffness and strength. The application of TPMS geometry as a core of a sandwich structure is widely investigated for purposes of sound insulation, energy absorption and blast resistance [57,92–96].

Sandwich panels are widely used in the construction sector as secondary elements for roofs and wall isolation panels. In bridge construction they are used as deck systems [66]. The panels are constructed with thin and rigid flanges bonded to a lightweight core [89]. Optimal sandwich design involves the use of thin, high-modulus flanges over a low-density core with high shear modulus [97]. Factors that influence the shear strength of sandwich panels listed in test standard ASTM C393 are flanges and core materials, core geometry (cell size) and density, adhesive thickness [98]. Different topological shapes for core structures have been researched

and used, including honeycomb, foam, lattice, corrugated core and face centred cubic core [99–103].

By combining AM and parametric design, architects and structural engineers can precisely specify the desired unit cell type, size and features, giving them unprecedented control over the structural intricacies of their designs [29]. This innovation promises to bring metamaterials to the forefront of structural engineering and architecture, where the convergence of materials science and cutting-edge design methods promises to redefine the possibilities in construction and structural innovation. In the field of structural engineering, reducing the weight of structures is a top priority. This goal can be achieved through the optimization of additive manufacturing and the use of high-performance mechanical metamaterials [104]. The integration of metamaterials into structural engineering on the other hand requires the standardization of mechanical tests for cellular metamaterial structures [38]. While sandwich panels with TPMS core are gaining more interest across various engineering fields, they often remain limited to smaller scales [62] with flanges typically 3D printed from the same material as the core [105]. In this thesis, the TPMS core was 3D printed on a large scale for architectural and structural reasons and to maximize bending stiffness, and then laminated with thin GFRP face sheets. Furthermore, numerous challenges hinder the standardization of 3D-printed components in general, especially for structural and architectural applications, making extensive laboratory testing imperative.

1.1 Objective and hypotheses of research

The possibilities of additive manufacturing for future large-scale implementation of metamaterials are investigated, especially for use in load-bearing architectural components and the following goals have been defined:

- Calibration of the material model of solid 3D-printed material for the FEA of TPMS (Gyroid, Schwarz, Diamond, Split, Neovius) unit cells
- Homogenization FEA of bioinspired TPMS (Gyroid, Schwarz, Diamond, Split, Neovius) structures
- Determining the correlation between the mechanical properties of TPMS structures and their relative density by curve fitting based on compression tests and numerical modelling.
- Generate topological optimal structures with graded TPMS depending on the primary stress distribution.

Based on the defined goals the following hypotheses are proposed:

- Diamond and Gyroid TPMS structures are the most applicable for load-bearing structural elements.
- A topology-optimized structure using a TPMS structure leads to uniform stress distribution, resulting in material and cost savings.

1.2 Methodology and plan of research

The research within this doctoral dissertation was carried out in nine phases:

Phase 1: Preliminary investigation of composite bridge decks with lattice structures

A preliminary investigation of composite bridge decks with lattice core structures was first carried out on well-known 2D core geometries, simulating pultruded deck systems and sandwich deck systems. Afterward, 3D geometries were introduced into bridge deck systems using similar outer dimensions but with reduced material properties, as it was assumed that the only possible production process was additive manufacturing.

Phase 2: Mechanical characterization of 3D printed material

The two 3D printed materials investigated within this doctoral thesis are ASA material and carbon-fibre-reinforced high-temperature 3D printed material, HI_TEMP CF. Defining the properties of 3D printed materials is challenging due to numerous factors, such as print path, layer height, substrate material, support material quality, transition temperatures, formation of micro and macro cracks, printing speed, ambient temperature, and more. The presence of voids and defects within the printed structure can increase stress concentration, reducing the overall strength and promoting premature failure. The residual stresses generated during the printing process can affect crack initiation and propagation mechanisms. As a result, the biggest challenge in the design of 3D printed structures is defining the material model.

Phase 3: Parametric design

The parametric design and optimization of both uniform and non-uniform unit cells and the exploration of various design approaches for the structural application of metamaterials were analysed. The methods used are unit cell design based on a mathematical algorithm, unit cell design based on topology optimization [80], the design of non-uniform lattice structures based on structural optimization and functional gradation, and the design with a hybrid geometry.

Phase 4: Analysis approaches

Based on the statistically derived data from both the laboratory tests and the FEM analysis, a two-stage structural design approach was proposed: simplified and detailed. The preliminary (simplified) design stage, utilizing statistically determined data, aims to identify the optimal physical and geometrical parameters for the desired application. In this stage, the analysis process is optimized to reduce trial-and-error iterations in the development of complex TPMS structures. To validate the analytical methodology at a less detailed level, a 1D/2D/3D design methodology was proposed, based on orthotropic material properties calculated using RVE (Representative Volume Element) homogenization analysis. In addition, the thermomechanical analysis of the 3D printing process and the void detection based on toolpath considerations were explored for potential integration into future FEM analyses.

Phase 5: Specimen design and experimental campaign

First, laboratory tests on 3D TPMS units were conducted. Five different TPMS geometries (Gyroid, Schwarz, Diamond, Split and Neovius) at two relative densities (20% and 40%) were analysed for this purpose. The additively manufactured TPMS cell units were subjected to compressive tests in the laboratory and the test results were compared with numerical simulations in Abaqus.

Implementation of TPMS structure in sandwich panels is proposed for the secondary structural elements – the pedestrian bridge decks. The mechanical principle that prevails in natural structures is implemented in the topology optimization of structural elements, using the minimum amount of material to resist the applied load. The first sandwich panel prototype is designed using thin glass flanges and a 3D-printed ASA TPMS non-uniform gyroid core, parametrically designed utilizing structural optimization and functional gradation. Second sandwich panel prototype incorporates a TPMS core consisting of uniform Gyroid structure. The entire core geometry was 3D printed using a Carbon fibre (CF) reinforced polymer. Merging of the traditional da Vinci bridge geometry with the core structure derived from TPMS architecture represents the integration of traditional design principles with bionics [35], resulting in the development of a novel structural system.

Phase 6: Numerical modelling

The same geometry as the laboratory-tested samples, is employed for the numerical analysis and identical boundary conditions are simulated. The initial step in the analysis process was to create the geometry using the nTopology software. To ensure accurate results while

maintaining computational efficiency, a convergence study was conducted to determine the appropriate mesh resolution. This involved analysing both denser and coarser meshes until a satisfactory convergence of results and computational efficiency was achieved.

Fracture analysis in Abaqus was conducted on several TPMS units and two sandwich systems using an elastoplastic material model. Finally, the research proposes advanced methods for detailed thermo-mechanical analysis and fracture analysis within Abaqus and GENOA software.

Phase 7: Comparison of experimental and numerical results

Based on the calculated Root Mean Squared Error (RMSE) in the linear region of the curve from the compression test on TPMS units, strain range from approximately 0.1 to 0.2, it is evident that the Abaqus numerical analysis with the Plasticity Material Model can accurately predict the measured data. Additionally, the bending stiffness of the sandwich panels was tested in the laboratory and compared to FEM analysis results. The material properties were determined through tension tests conducted for three orthogonal print directions, which were then used to calibrate the Plasticity Material Model. A simply supported beam test was conducted for the sandwich panel with flat configuration, while both sides were fixed for the sandwich panel in an arch configuration. These results underscore the significant potential for future lightweight 3D-printed bridge structures employing bioinspired metamaterials.

Phase 8: Discussion of results

In this section, the main findings of the dissertation are interpreted. It begins with discussing preliminary studies on bridge decks, covering both 2D and 3D core geometries. Following promising results with 3D core geometries, FDM materials were chosen, and mechanical properties were determined through tensile tests. Detailed experimental and numerical investigations included compression tests on TPMS unit samples with varying morphologies and densities. After validation, further analysis and design approaches for load-bearing elements were explored. Finally, the results of two novel structural systems tested in the laboratory are discussed.

Phase 9: Conclusion and recommendations for future research

At the end of the dissertation, a comprehensive comparison of numerical, analytical, and experimental results is provided, along with a critical review of the obtained results. Additionally, guidelines for future research are proposed.

2 PRELIMINARY INVESTIGATION OF COMPOSITE BRIDGE DECKS WITH LATTICE STRUCTURES

The parts of this chapter were published in the paper: Stepinac, Lucija; Skender, Ana; Damjanović, Domagoj; Galić, Josip. FRP pedestrian bridges—analysis of different infill configurations. Buildings, (2021), DOI: <https://doi.org/10.3390/buildings11110564>.

Henry Ford, a great innovator in the auto industry, introduced FRP material to the world under the motto “Ten times stronger than steel” [106]. However, even though it is not a novelty in developed countries, it is still not widely used in developing countries.

FRP is a two-component material whose volume consists of 30–70% fibre, with 50% of its total weight incorporated into a polymer matrix. With regard to the mechanical characteristics of FRP, fibres are the ones in charge of carrying the load and providing strength, stiffness, and thermal stability. The matrix wraps the fibres and protects them during the production process and during the exploitation time, ensuring an even load distribution to each fibre. It is also crucial in providing composite durability [107].

At this point, the market is full of various fibres. Glass fibres (GF) are the most common choice for investors, architects, and structural engineers due to their good mechanical and physical properties and low price compared to carbon fibres (CF), aramid fibres (AF), and basalt fibres (BF).

There are many applications of FRP in bridge engineering, mostly with pedestrian bridges. FRP material is a good alternative to traditional materials that will extend the life of the structure or enable the usage of pedestrian bridges for a longer period. The replacement of parts in existing bridges, such as concrete decks, or even replacing the whole structure, can be performed without significantly disturbing the structure. Even though there are alternatives, such as composites with wood and steel, polymer composites excel because of their high modulus of elasticity, ultimate load capacity, and low density, making them ideal for strengthening existing girders and decks, as well as for use in new, fully composite or hybrid bridge structures [108]. Some of this material’s other beneficial properties include rapid construction, anticorrosive properties, water resistance, pleasant appearance, lasting colour, overloading resistance, good dynamic performance [109], and the potential to build bridges with a greater span [110]. In addition, research by Mara [111] shows that less energy is needed for the production and maintenance of FRP bridges than for construction based on other materials.

FRP is promising in terms of its durability, but its high price makes it difficult for it to compete with traditional materials. Insufficient building codes and poor knowledge of the benefits of anisotropic materials are the reasons why architects and structural engineers often choose traditional materials over FRP.

2.1 FRP bridge decks with two-dimensional core geometry

Plate bridge deck systems have not changed much since 1991 [112]. The most common systems are sandwich panels and pultruded profiles that are adhesively connected. The technology of pultrusion is the most commonly used in the FRP production process, and for those reasons, the most common plate systems available on the market are EZSpan (Atlantic Research), Superdeck (Creative Pultrusions), DuraSpan (Martin Marietta Materials), and Strongwell. Sandwich panels consist of top and bottom flanges that carry the load and a low-weight infill that connects them and transmits the load but does not contribute to the panel's stiffness [113].

In a recent review paper [114], a summary of FRP pultruded deck and sandwich panel failure modes has been provided [115–118]. It can be concluded that FRP decks demonstrate linear elastic behaviour up until failure. Some pseudo-ductility could be achieved through the structural system and cell configuration [114].

An example of a temporary bridge structure [119] shows that after eight years of service, some visible damages were: flange crushing, longitudinal cracks, visible fibres due to top-surface blooming, and some local damages. Despite these flaws, structural stability was not yet jeopardized, and all of the damages were easily repaired, for the connections stayed in perfect condition.

It has been reported [120] that for triangular cell configurations in a pultruded deck (EZ Span and Asset deck), only around 20% of the material compression strength is utilized. This is caused by local buckling and delamination between the web and flanges, which are the symptoms of deck failure. Local deformation or cracking of the top surface or wear surface will occur under patch load, well before the compression strength limit of the material is reached. For this reason, many parameters of FRP decks should be considered during the design to obtain a more optimal, cost-acceptable, attractive, and sustainable solution.

The pultruded plate systems that are currently available on the market vary in depth from 80 to 225 mm depending on the production process (Table 2.1). Sandwich panels, on the other hand, are more flexible in terms of production dimensions, and can also be inclined. An

FRP composite structural system with FRP sandwich decking laying on a U-box girder with a bridge span of 15–25 m has recently been proposed and examined in Poland [121,122].

Table 2.1 Physical properties of plate systems from adhesively bonded pultruded profiles [111].

System	Production process	Thickness [mm]	Weight per m ² [kN/m ²]
Superdeck	Pultrusion	203	1.00
DuraSpan	Pultrusion	195	1.05
EZSpan	Pultrusion	216	0.96
Strongwell	Pultrusion	170	-

2.1.1 Materials and methods

Research has been conducted to see how the inclination and shape of the bridge, its infill geometry, and its material can affect stiffness. It was assumed that the type of material is known. Twenty-four models were made. Twelve of them have been modelled with an anisotropic GFRP material and a layup orientation in two orthogonal directions (0/90/0/90). Another 12 models have quasi-isotropic material properties, including apropos matrix mixes with chopped fibres. Quasi-isotropic material will result in a higher deformation and a lower load-bearing capacity due to its lower modulus of elasticity and strength. A curved bridge geometry will result in lower deformation and higher stiffness. The main aim of this preliminary research is to quantify the level of this reduction according to material and geometry. The reason for the use of quasi-isotropic material (even though its modulus of elasticity is much lower than laminated alternatives) is because of the application of FRP in more advanced production processes, such as 3D printing.

After defining the material properties, it is necessary to define a cross-section of the element. The infill geometry is based on established plate systems that can be found on the market. Four of them have longitudinally oriented cells with different web inclinations, and two have orthogonally oriented cells, known as sandwich panels. Designing a bridge in the form of an arch enabled us to quantify an increase in stiffness and, consequently, a deflection reduction.

The FRP's load-bearing shell structure can be flat or curved. A shell in arch has a higher stiffness and a smaller deformation. The problem with forming the elements in an arch is that additional material is required at the area where the bending moment is significant. A bridge made in cooperation with the FiberCore company [123] is a good example where each bridge structure's design fulfils the required, ultimate serviceability limit states for every member within the allocated costs. Lately, optimization with additional software, such as Grasshopper, Karamba, and Kangaroo, has been of great help [124].

Many aspects of FRP decks affect the final results, such as material (e.g., GFRP or CFRP), the configuration and inclination angle of the internal cavities, and thicknesses, etc. It is shown [125,126] that a triangular configuration in pultruded decks has a higher in-plane shear stiffness (G_{xz}) compared to a rectangular configuration. In sandwich panels, the density of the cavities will influence stiffness more than geometry. Sandwich panels can be filled with polymeric foam in order to increase stiffness [111]. Sandwich decks usually have sufficient shear stiffness to transfer these strains, whereas pultruded FRP decks have lower shear stiffness.

In this preliminary analysis, a bridge deck with two fixed supports and a span of 5 m was used. The depth of all of the decks was uniform at 200 mm, while the width was 1.8 m. Uniform wall thicknesses of 6 mm were used in all cross-sections (four layers of 1.5 mm in two orthogonal directions (0/90/0/90)). The main aim was to have a similar depth and mass for all decks. Thus, the stiffness would be primarily influenced by the cell configuration.

Different infill geometries and web inclinations were analysed using Abaqus software. Panel depth was taken as 200 mm according to the available standard panel systems (Figure 2.1): (a,b) EZ-Span (49.91 kg/m²), (c,d) Superdeck (50.48 kg/m²), (e,f) DuraSpan (50.74 kg/m²), and (g,h) Strongwell (41.08 kg/m²), which are made of pultruded profiles, and sandwich panels: (i,j) with a profiled triangular infill (74.84 kg/m²) and (k,l) honeycomb sandwich panels (54.19 kg/m²). The geometry of the deck cross-sections (rectangular, triangular, trapezoidal, and honeycomb) was taken from the different FRP cell units available in the market. Each plate system weighs approximately 50 kg/m². Future research will be performed for 3D cell configuration [127].

The geometry was defined using the Rhinoceros software package. The serviceability load combination was applied to the top of each deck according to the British code [128]. A distributed live load of 5 kN/m² and a dead load of 1 kN/m² was applied (in case of wearing, the surface is applied).

A simple arch with a height of 30 cm at the middle of the span was developed. With innovative production processes, such as 3D printing, more design freedom is possible. Optimal structures, based on internal forces, could be created. The selection of bridge geometry would not be determined by the location of the bridge.

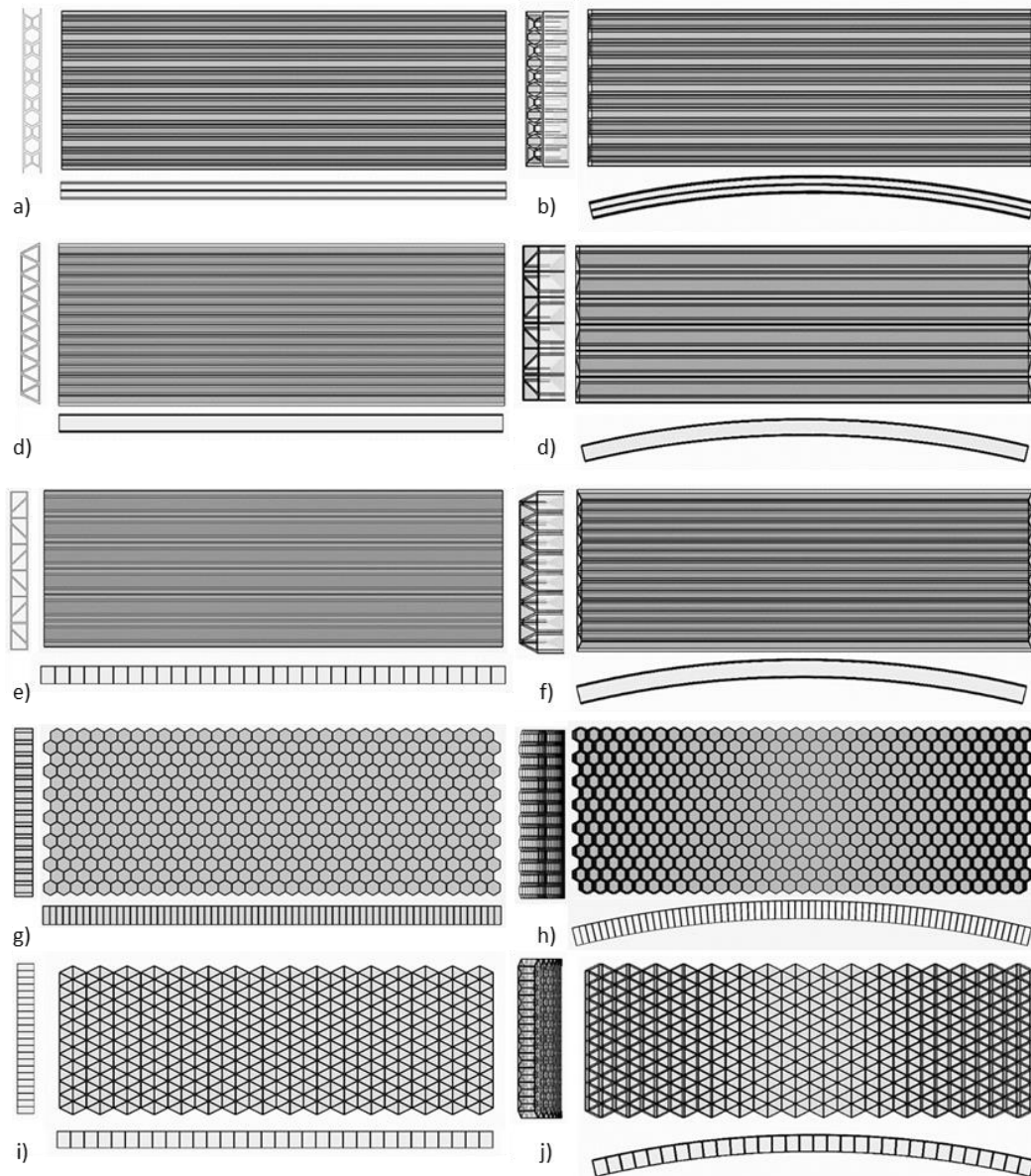


Figure 2.1 GFRP plate, adhesively bonded pultruded profiles: **(a)** Superdeck; **(b)** Superdeck in an arch; **(c)** EZSpan; **(d)** EZSpan in an arch; **(e)** DuraSpan; **(f)** DuraSpan in an arch; **(g)** Strongwell; **(h)** Strongwell in an arch. Sandwich panels: **(i)** triangular-shaped infill; **(j)** triangular-shaped infill in an arch; **(k)** honeycomb-shaped infill; **(l)** honeycomb-shaped infill in an arch.

Additionally, a comparison was made between a composite fibre layup (0/90/0/90) material and a quasi-isotropic material. The composite layup consists of four orthogonally positioned fibre layers, each 1.5 mm thick, with their material properties shown in Table 2.2. On the other hand, one modulus of elasticity is defined for the quasi-isotropic material. The modulus of elasticity for composites reinforced with glass fibres can vary from 5 GPa to 50 GPa [129]. For a resin reinforced with 40% of chopped strand mat by weight, a modulus of elasticity of 10 GPa was chosen (Figure 2.2). Three-dimensional models were imported from Rhinoceros software into Abaqus software as surface shell parts. Tie constraints connected the

top and bottom surfaces to infill surfaces, thus simulating the rigid behaviour of all composite panel board instances. The pedestrian bridge was analysed as a clamped supported beam and a clamped arch. Finite element modelling was performed with quadratic mesh size elements of $50 \text{ mm} \times 50 \text{ mm}$.

Table 2.2 Composite layup material properties for Glass Fiber Epoxy resin

E_1 [MPa]	E_2 [MPa]	ν_{12}	G_{12} [MPa]	G_{13} [Mpa]	G_{23} [Mpa]	ρ [kg/m ³]
34412	6531	0.217	2433	1698	2433	2000

E_1 : Young's modulus in longitudinal (fibre) direction. E_2 : Young's modulus in transverse. ν_{12} : Minor Poisson ratio. G_{12} : In-plane shear modulus. G_{13} : Out of plane shear modulus. G_{23} : Out of plane shear modulus. ρ : Density.

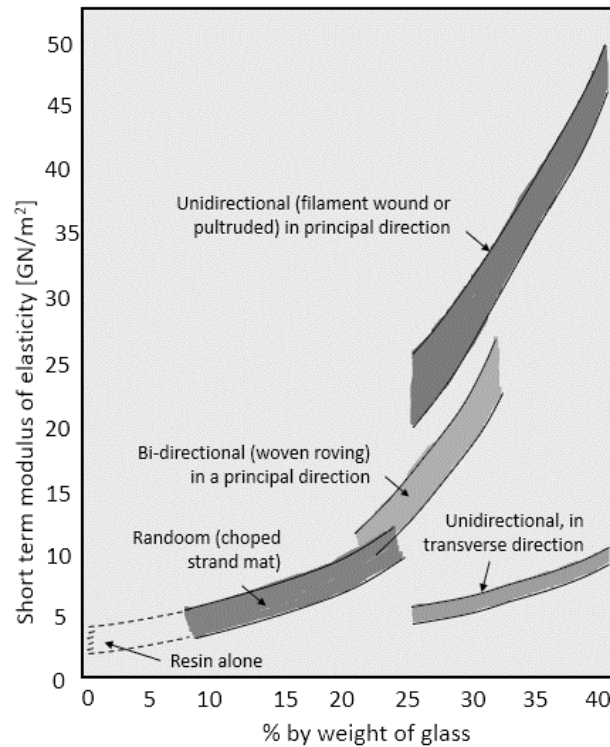


Figure 2.2 Modulus of elasticity for glass fibre reinforced polymers [129]

2.1.2 Results

The most effective cell unit configuration was determined based on the serviceability design criteria as governed by deflections. According to the British code [128], a deformation limitation of $L/300$ (16.6 mm) was compared to the maximum deformation at the middle of the span. To obtain the deformations, the complex numerical modelling of several FRP decks (Table 2.2) was performed in Abaqus. The results are shown in Figure 2.3 and Figure 2.4.

The study showed that the lowest deflections of about 1.75 mm were obtained in the arched Superdeck (which has a hexagonal cell configuration) and EZ Span (with a triangular cell configuration) bridge decks. The decks made of pultruded profiles were stiffer overall than the sandwich panels. In previous research by [130], the authors found that Superdeck (hexagonal cell) and ASSET (triangular cell, similar to EZ Span) were stiffer than others, which is in accordance with the results of this research.

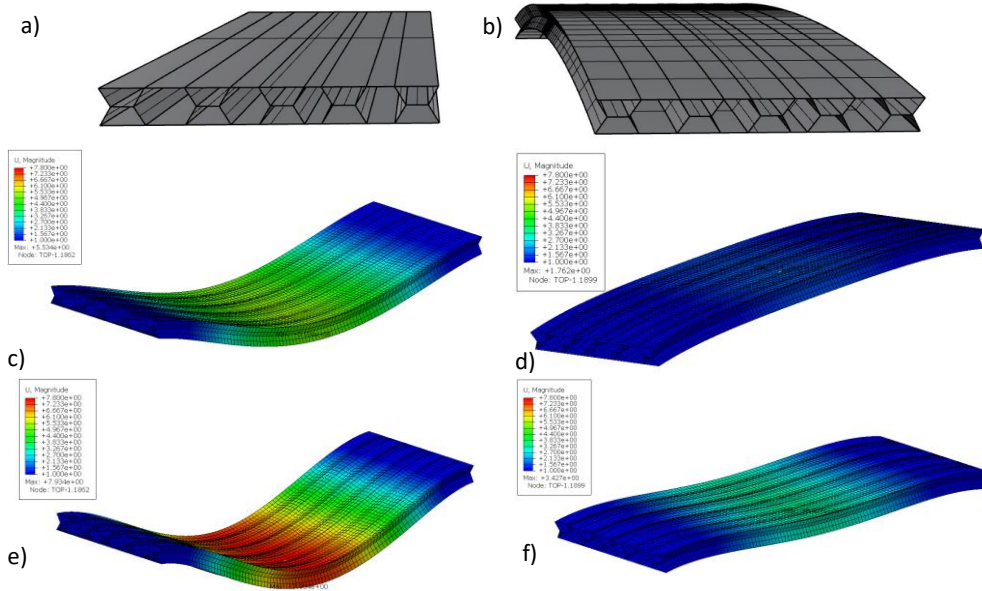


Figure 2.3 Geometry of: (a) Superdeck and (b) Superdeck in an arch. Deformation for: (c) Superdeck (laminated); (d) Superdeck (laminated) in an arch; (e) Superdeck (quasi-isotropic); (f) Superdeck (quasi-isotropic) in an arch.

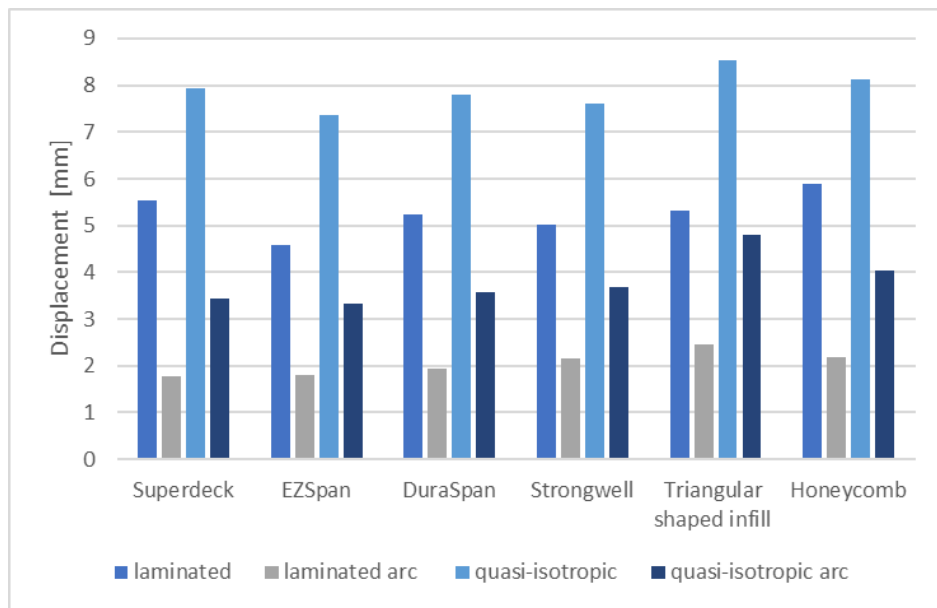


Figure 2.4 Results for displacements.

2.2 FRP bridge decks with three-dimensional core geometry

The prediction of the mechanical properties of TPMS cellular material has been carried out in numerous studies so far and it has been shown that the effective properties are mainly influenced by their morphology [131]. The TPMS unit is mathematically defined by the implicit function and there are endless possibilities for the innovation of new and hybrid formulations. Some of the most common are: Gyroid, Schwarz, Diamond, Split, and Neovius. In this preliminary analysis, the focus was on Gyroid and Schwarz Primitive Structure. All geometries were analysed in flat and arched form. Different unit cell dimensions were compared at the same densification percentage.

A comparison is made between the typical two-dimensional web infill geometry in popular FRP deck panels (Superdeck, Duraspan, EZSpan, Strongwell and sandwich panels with honeycomb and triangular infill) and the novel three-dimensional TPMS structure (Gyroid and Schwarz). A 10 mm thick top and bottom flange is defined for all typologies. It is assumed that the flange is tie-constrained with the infill geometry, which can be 3D printed in one piece or additionally glued to a sheet made of glass, FRP, metal or other materials. The results for the sandwich panels were taken from the study [8] and compared with the novel deck system with TPMS geometry. The TPMS structures used are Gyroid and Schwarz Primitive. For all types, the analysis is performed in flat and curved plate geometry.

2.2.1 Materials and methodology

The dimensions of the deck are $5.0 \times 1.8 \times 0.2$ m for all slabs. FEA is performed with solid 3D elements and nTopology software [132] is used to create the TPMS geometries with a periodic grid block (Figure 2.5). For the Gyroid structure, two different grids are used: $500 \times 500 \times 500$ mm and $200 \times 200 \times 200$ mm, and for Schwarz structure, a grid of $200 \times 200 \times 200$ mm was used. Since the deck height is 200 mm, the gyroid structure is shortened by 150 mm at the top and bottom with the larger grid. The meshing is done separately for the flanges and TPMS lattice, with a uniform size of 10 mm. The connection between the top flange and lattice, and between lattice and the flange is assumed to be fully constrained. The pressure is assumed to be 6 kN/m^2 for the serviceability load combination (1 kN/m^2 for dead load and 5 kN/m^2 for live load). The supports are defined as displacement restraints in three orthogonal directions on both slab sides.

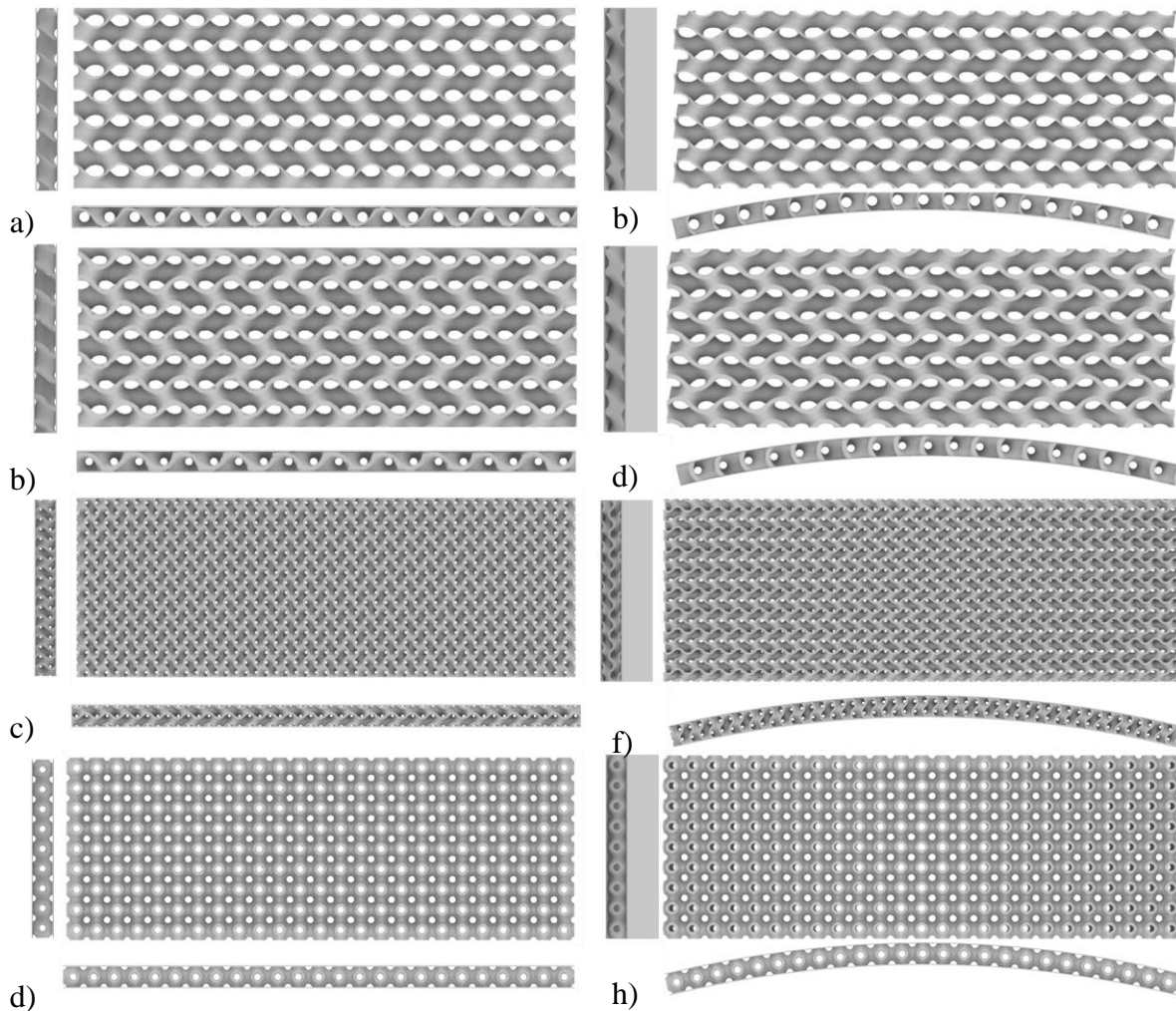


Figure 2.5: TPMS deck infill: a) Gyroid (500 mm grid) 20% densification, b) Gyroid (500 mm grid) 20% densification in an arch, c) Gyroid (500 mm grid) 35% densification, d) Gyroid (500 mm grid) 35% densification in an arch, e) Gyroid (200 mm grid) 35% densification, f) Gyroid (200 mm grid) 35% densification in an arch, g) Schwarz Primitive (200 mm grid) 35% densification, h) Schwarz Primitive (200 mm grid) 35% densification

The FRP material with a 40% chopped glass fibre content was used for standard sandwich deck systems. The quasi-isotropic properties are defined, and the modulus of elasticity is assumed to be 10 GPa. Theoretical assumptions were made for the proposed new TPMS decks since no specific material was selected. The proposed new TPMS decks were calculated for the quasi-isotropic material to compare with the filled 3D-printed composite material with a modulus of elasticity of 5 GPa. Similar properties can be achieved for filled ASA or bio-composites PHBV with natural fillers such as hemp, flax or wood fibres [133], [134]. The potential of green additive manufacturing can become even more sustainable through the use of bio composites [135] and topology optimization based on structural analysis (Figure 2.6).

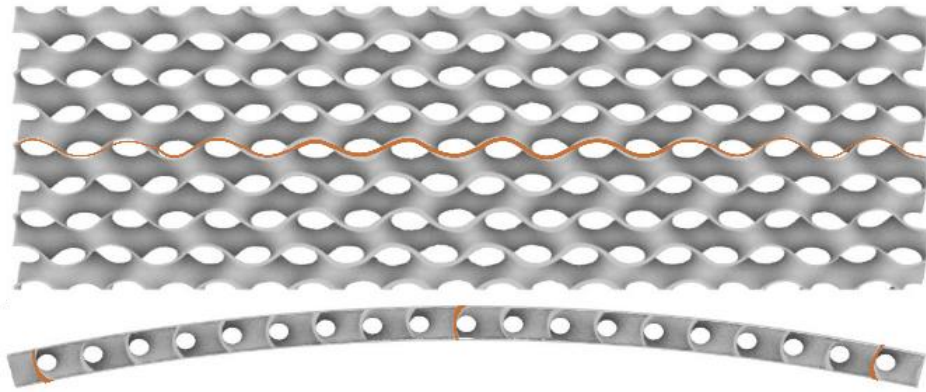


Figure 2.6: Topology optimization with Gyroid structure

2.2.2 Results

The results are presented graphically and the potential of additively manufactured TPMS decks is explained. The comparison is made based on weight and stiffness. 3D printing of polymers with a robotic arm uses a pellet filler, at the end of which is a nozzle of about 5 mm that can pump about 8 kg of material per hour. To produce one deck, this would result in about 2 printing days. In the production of the 3D printed component, less material waste, energy consumption, and gas emissions from the machines are considered. Therefore, the environmental impact of additive manufacturing is demonstrably lower than other production methods.

The unit cell morphology for each TPMS structure was periodically repeated in two orthogonal directions. For a 500×500 mm grid, the number of unit cells is about 40 and for a 200×200 mm grid, the total number is 225 units.

For the comparison of the results, the density of the FRP material is assumed to be 2000 kg/m^3 and that of the 3D printed material (ASA or bio-composite) is assumed to be 1079 kg/m^3 . For each TPMS geometry, the volume and weight were determined. Finally, the static analysis was performed based on the serviceability design criteria. The displacement results were used to quantify the stiffness of each novel deck system and compare it to the conventional FRP decks.

The results show a deck with a smaller gyroid TPMS unit and a deck with a larger (incomplete height) TPMS unit. The results show almost the same stiffness with a 2% difference in deformation for the same global deck density. This proves that the structural properties are mainly influenced by the densification after morphology is defined. Comparison of two TPMS morphologies: Gyroid and Schwarz Primitive, generated with the same dimensions $200 \times 200 \times 200$ mm and the same total densification of 30%, the results are within a 3% difference in favour of Gyroid TPMS. Compared to the honeycomb sandwich panel and

TPMS structure with the same density and material properties, the Gyroid three-dimensional structure has 50% less deflection than the honeycomb 2D sandwich panel, 45% less deflection than Duraspan, 40% less deflection than EZSpan, 48% less deflection than Strongwell, 41% less deflection than Superdeck and 60% less deflection than the triangular sandwich panel. The results show great potential for TPMS deck compared to the traditional deck systems (Figure 2.7).

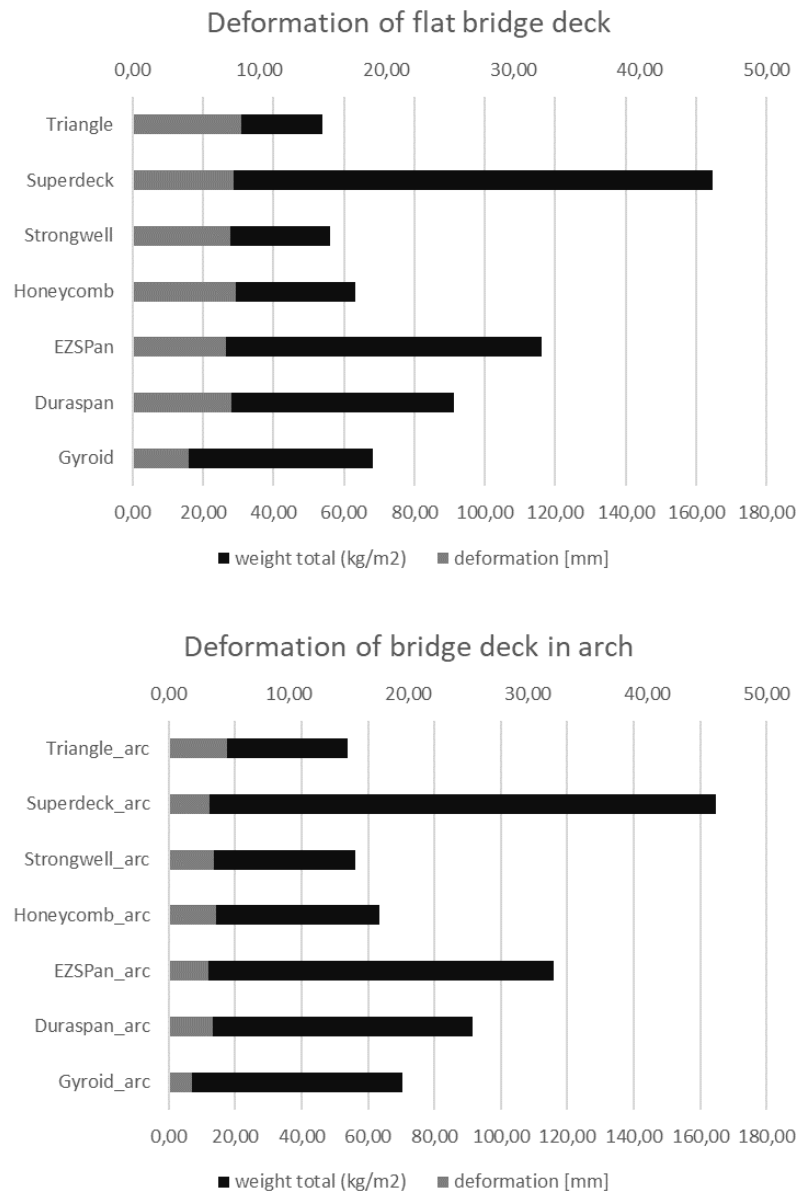


Figure 2.7: Comparison of Gyroid TPMS deck with traditional deck system

Topology optimization was applied to the gyroid deck in an arch. To reduce the overall weight of the structure, the gyroid unit was modelled with a grid of $500 \times 500 \times 500$ mm, changing the wall thickness from 10 to 50 mm depending on the von Mises stress values measured from the static analysis of the solid (Figure 2.8). The parallel can be drawn based on

weight reduction and reduction in material properties. The optimized TPMS gyroid deck results in an 80% lighter structure compared to the solid body. The optimized geometry is even 57% lighter than the uniform TPMS gyroid deck with only 18% higher deformation. Another comparison can be made based on the material - with the same total volume of the structure (almost double the total weight of the structure) and a 50% degradation of modulus of elasticity the stiffness increases by 23% in favour of the optimized structure and nearly neutral stress distribution within the whole deck.

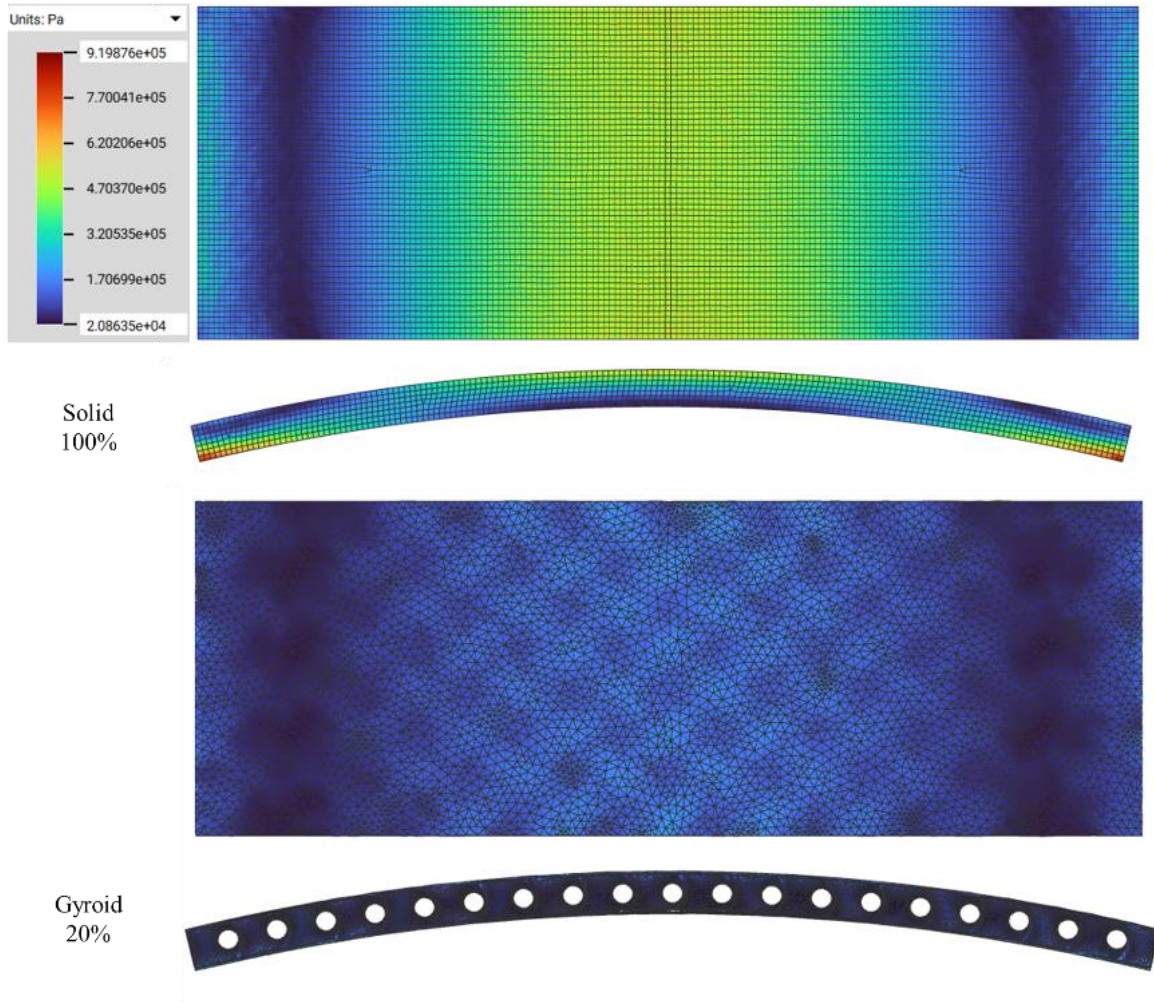


Figure 2.8 Topology optimized Gyroid core with 20% densification based on stress distribution

3 MECHANICAL CHARACTERIZATION OF 3D PRINTED MATERIAL

Understanding FDM prints requires comprehending the bonding between plastic lines (raster) and their limitations, such as weaker inter-raster entanglement and void formation [136]. All this introduces an additional anisotropy to composite materials [137–139] compared to traditional production processes such as pultrusion [140]. The printing direction in FDM mitigates anisotropy in the XY printing plane, but does not eliminate it entirely [141] [142]. The ZX direction, corresponding to the layer-by-layer build, still exhibits inherent weaknesses due to weaker inter-layer bonding. In print planes, the first letter shows the orientation of the specimen's main axis relative to the build platform, while the combination of the first and second letters identifies the plane of the largest surface [143]. This anisotropic behaviour affects the fracture toughness and fatigue resistance of 3D printed polymer parts [144,145].

Defining the properties of 3D printed materials is challenging due to numerous factors, such as print path, layer height, substrate material, support material quality, transition temperatures, formation of micro and macro cracks, printing speed, ambient temperature, and more [146–148]. The presence of voids and defects within the printed structure can increase stress concentration, reducing the overall strength and promoting premature failure [149]. The residual stresses generated during the printing process can affect the crack initiation and propagation mechanisms [150,151]. The comparison between neat material, final 3D printed material, and compression moulded composite was presented in [152].

Furthermore, researchers have explored the use of reinforcing fillers or fibres to improve the mechanical properties and fracture toughness of 3D printed polymers [16,146,153,154]. The incorporation of fillers such as carbon or glass fibres can enhance the strength and toughness by providing reinforcement and bridging effects across cracks or interfaces [155]. Additionally, fibre orientation optimization techniques can be employed to maximize the load-bearing capacity in specific directions.

The growing interest in Large Format Additive Manufacturing (LFAM) technologies is driven by the ability to produce large format parts. To support these technologies, optimized materials are needed that have both functional capabilities and good printability [156–160]. Acrylonitrile styrene acrylate (ASA) is also particularly promising as a thermoplastic material for LFAM due to its favourable wettability and mechanical properties [146].

3.1 ASA material

3.1.1 Specimen design and experimental setup

A common test for determining stress-strain relationships is the uniaxial tension test. The tensile test was performed on 3D printed ASA specimens. 3D printing was performed on an industrial Stratasys F123, FDM printer. The CAD models were prepared for the GrabCAD slicer, to generate G-Code for the 3D printer. Modelling was performed in Rhinoceros software. Each of the specimens printed with FDM was printed with the same nozzle diameter of 0.4 mm, a layer resolution of 0.15 mm and path design 0-90°. ASA material properties defined by the manufacturer and process parameters for Stratasys F123 are presented in Table 3.1.

Table 3.1 Material properties of ASA and Process parameters for Stratasys F123

Density [kg/m ³]	1080	Printing speed [mm/s]	70
Filament Diameter	1.75 mm +/- 0.05	Layer height [mm]	0.15
Colour	Grey	Line width [mm]	0.4
Tensile Strength [MPa]	31.9	Infill angle	0-90°
Tensile Modulus [MPa]	2140		
Elongation at Break [%]	2.5		
Flexural Strength [MPa]	61.5		
Flexural Modulus [MPa]	1980		
Melting Temperature (T _g)	103.55 °C		

The tensile tests were performed according to EN ISO 527-2 [161]. Test specimens were printed in three different printing directions (XY, XZ and ZX) as shown in Figure 3.1. XY plane represents the largest face area lying on the printing bed. XZ specimen is rotated around the x axis and ZX specimen is rotated around the y axis. The measured dimensions of the specimens are given in Table 3.2. The first number (1, 2, or 3) next to ASA represents the printing direction, with 1, 2 and 3 indicating XY, XZ and ZX, respectively. The second number denotes the specimen number, with three specimens for each printing direction. A total of nine tensile tests were conducted, to determine the elastic plastic isotropic material model for each printing direction and perform fracture analysis. During the experiment, the tensile load was applied at a displacement rate of 0.3 mm/min with a gauge length of 50 mm. The calibration of the material models was performed based on the experimental results.

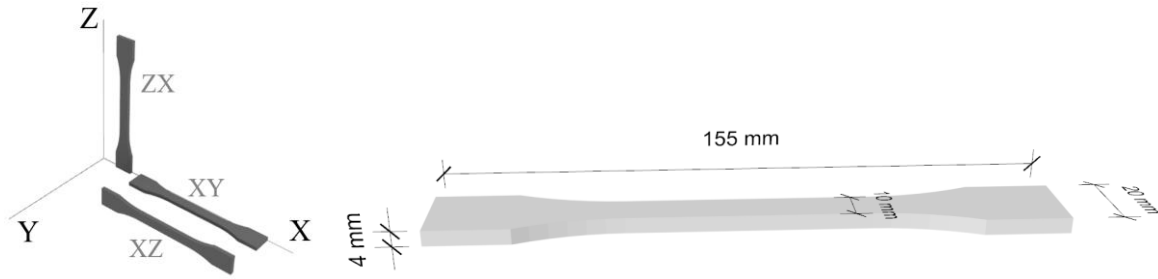


Figure 3.1: Dogbone ASA specimens for the tensile test

Table 3.2 Measured dimensions of the specimens before the test

specimens	b_1 (mm)	h (mm)	m (g)	L_0 (mm)
ASA 1-1	9.9	4.0	8.5	50
ASA 1-2	9.9	4.0	8.7	50
ASA 1-3	10.0	4.0	8.3	50
ASA 2-1	10.0	4.0	8.4	50
ASA 2-2	10.1	4.0	8.4	50
ASA 2-3	10.1	4.0	8.3	50
ASA 3-1	10.0	4.0	8.0	50
ASA 3-2	9.9	3.9	8.1	50
ASA 3-3	10.0	4.0	8.0	50

b_1 - width of the specimen at narrow portion

L_0 - gauge length

h - thickness

m - mass of the specimen.

3.1.2 Calibration of the material model

The following section presents the results of laboratory tests on 3D-printed ASA material, with specimens printed in three orthogonal directions. The different fracture modes are shown in Figure 3.2. The fracture surfaces occur predominantly at the edge of the gauge length, while two specimens failed in the middle of the specimen. The results demonstrate variability, indicating that the cause of fractures can be attributed to certain parameters such as material defects or errors in the tool path.



Figure 3.2 Nine 3D-printed specimens displaying various fracture zones (1, 2 and 3 represent the XY, XZ and ZX print direction, respectively)

Stress and strain diagrams for each print direction are plotted in Figure 3.3a. Furthermore, Figure 3.3b presents the modulus of elasticity for different 3D printing directions, with error bars indicating the maximum and minimum values. Modulus of elasticity is calculated as the slope of the tangent line on the initial linear portion of the stress-strain curve for each print direction. As the load is aligned perpendicular to the layers, the printed models in ZX are the weakest of the specimens, but also show the greatest deviation in the test results (dashed lines).

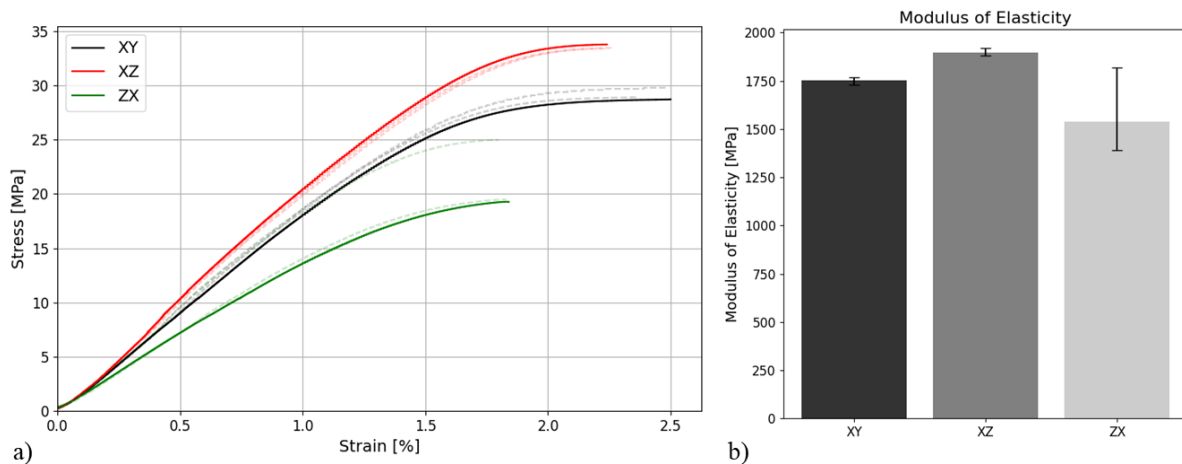
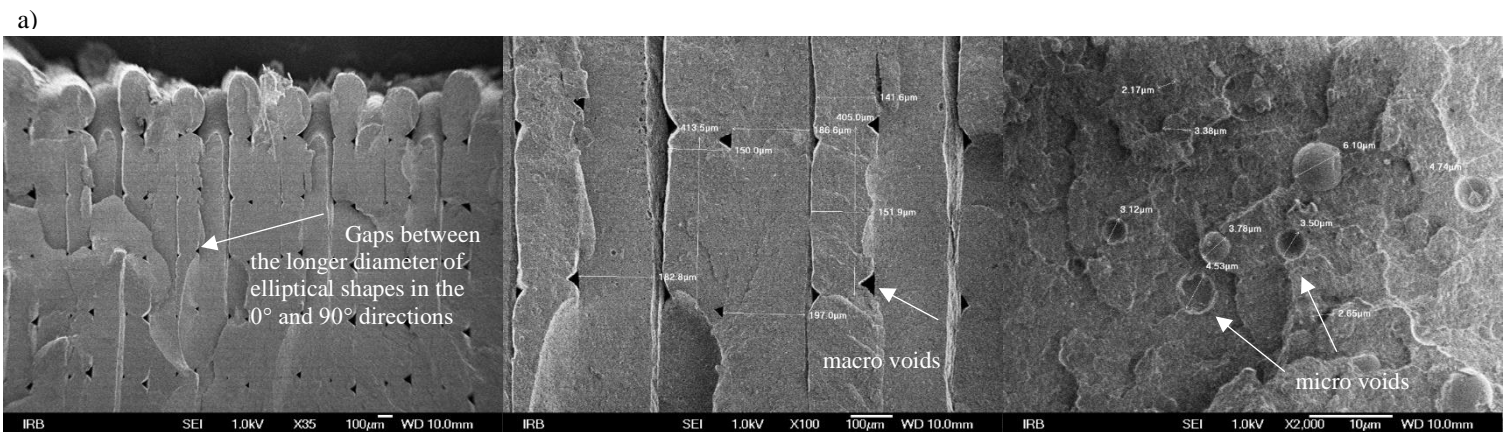
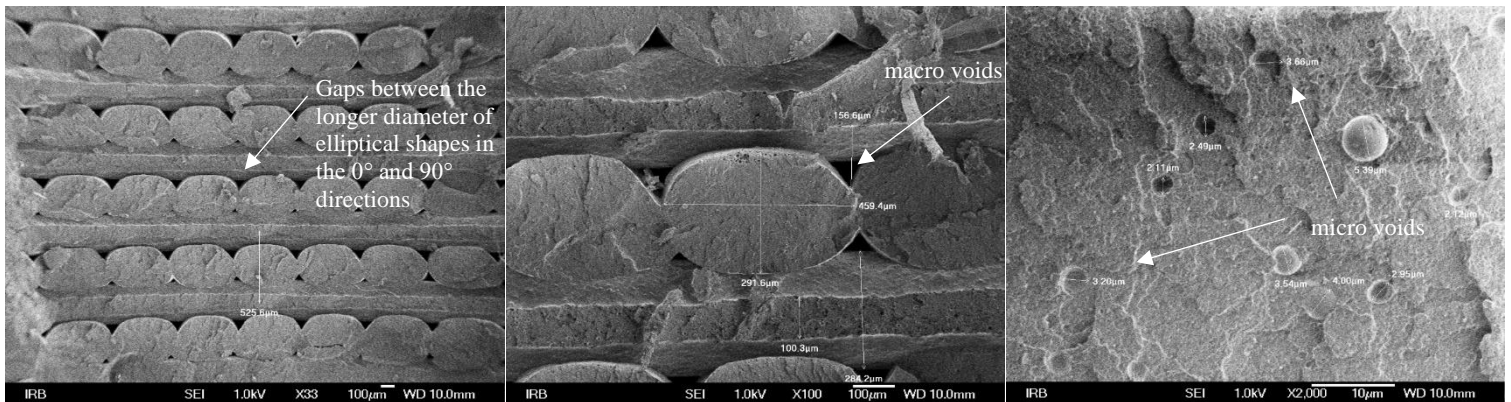


Figure 3.3: a) Stress-strain diagram for the XY, XZ and ZX print direction; b) Modulus of elasticity

Furthermore, photos from the Scanning Electron Microscope (SEM) are provided for each printing direction in Figure 3.4. In the SEM images, the section where the cutting failure

occurred is prominently observed. This area indicates the point at which the specimen failed during testing. The images reveal the presence of both micro and macro pores within the ASA 3D printed specimens. These pores vary in size and are distributed throughout the material. Moreover, the layer thicknesses of the 3D printed ASA specimens are not uniform, which could have implications for the material's mechanical properties. There are areas where the bond between adjacent layers is not well-established, more prominently visible in the XY print direction than in the XZ print direction (Figure 3.4). This incomplete bonding can be a critical factor affecting the overall strength and integrity of the specimens, potentially leading to premature fracture. Specifically, the outer layers, along with the infill layers, exhibit gaps and open voids. Gaps exceeding $100\ \mu\text{m}$ are evident between the longer diameter of elliptical shapes in the 0° and 90° directions. Gaps between the outer layers and infill layers in the virtual model are identified as voids resulting from toolpath errors (Figure 3.5). These pores may act as stress concentrators during testing, likely compromising the durability of the specimens.



b)



c)

Figure 3.4 Scanning electron micrographs of (a) ASA XY print direction showing when a strut at 0° direction is printed on a bottom 90° direction strut (b) Printing in the XZ direction displays layers of elliptical shape in the cross-section, revealing irregularities and visible open cavities between 0 and 90° c) The ASA ZX print orientation exhibits a localized thickening effect by placing a strut at a 0° angle over a strut at a lower 90° direction

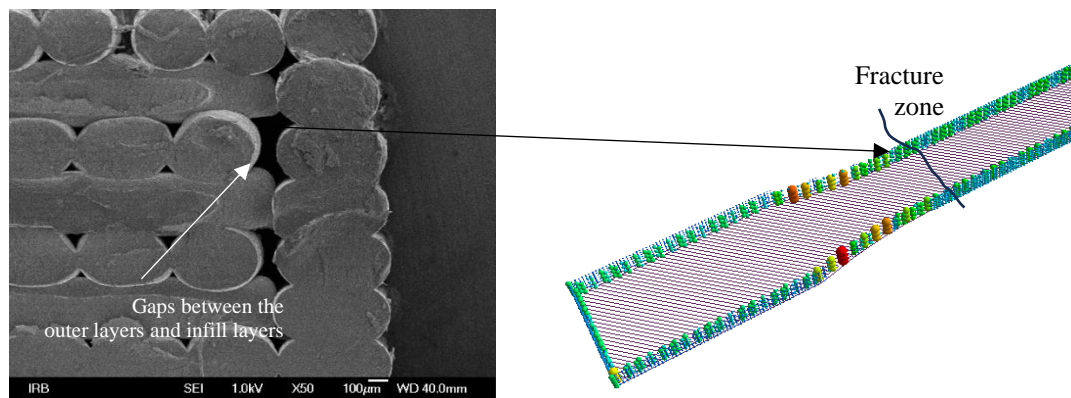


Figure 3.5 Voids from 3D printed part vs. void prediction from the toolpath error

3.2 HI_TEMP CF material

3.2.1 Specimen design and experimental setup

The second material used is temperature-resistant polymer (HI_TEMP) with Carbon Fibers (CF). The mechanical properties were investigated on HI_TEMP CF 3D printed samples (Figure 3.6) with respect to the print direction (XY, XZ, and ZX) and the print resolution (layer thickness of 0.3 mm and 0.6 mm). Three samples were printed for each print direction and resolution. The aim was to achieve high-quality prints as quickly as possible using the 3D BigRep PRO printer, which has a built print space of 1005 x 1005 x 1005 mm.

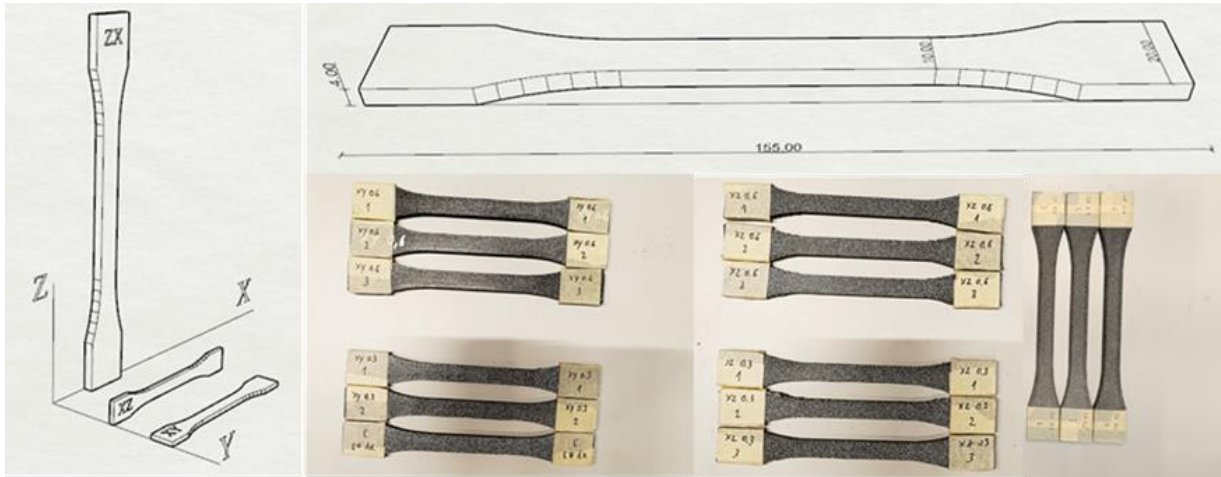


Figure 3.6 Tensile test specimens - HI_TEMP CF material

The uniaxial tensile test was used along with Digital Image Correlation (DIC) to measure surface displacement and strain over the area of interest to determine the stress-strain relationship and subsequently calibrate the material model.

Following the EN ISO 527-2 standard, fifteen tensile tests were conducted using a universal testing machine (Walter + Bai AG, Switzerland) equipped with a 50 kN load cell, ensuring a load accuracy of $\pm 0.5\%$ (Figure 3.7). The tests were performed at a constant deformation rate of 0.3 mm/min. Deformation was monitored using a two-dimensional Digital Image Correlation (DIC) system. Before testing, a DIC pattern was applied to one side of the specimens by spraying. Side cross-sectional pictures for thickness measurements were collected using an optical microscope (Keyence VHX-5000).

Due to the large nozzle diameter, the ZX print direction failed to produce quality prints for the standard sample dimensions approximately $155 \times 40 \times 4$ mm (see Table 3.3. for measured dimensions of each specimen). Consequently, the samples were scaled by a factor of 2. For this reason, only three samples were produced and tested for the ZX direction at a resolution of 0.6 mm. This comparison aimed to assess the impact of changes in material characteristics resulting from an increase in nozzle diameter and, consequently, layer thickness. The CAD models in STL format were imported into BLADE, BigRep's slicer software, where all printing parameters were configured. G-Code was generated and exported to initiate the printing process.

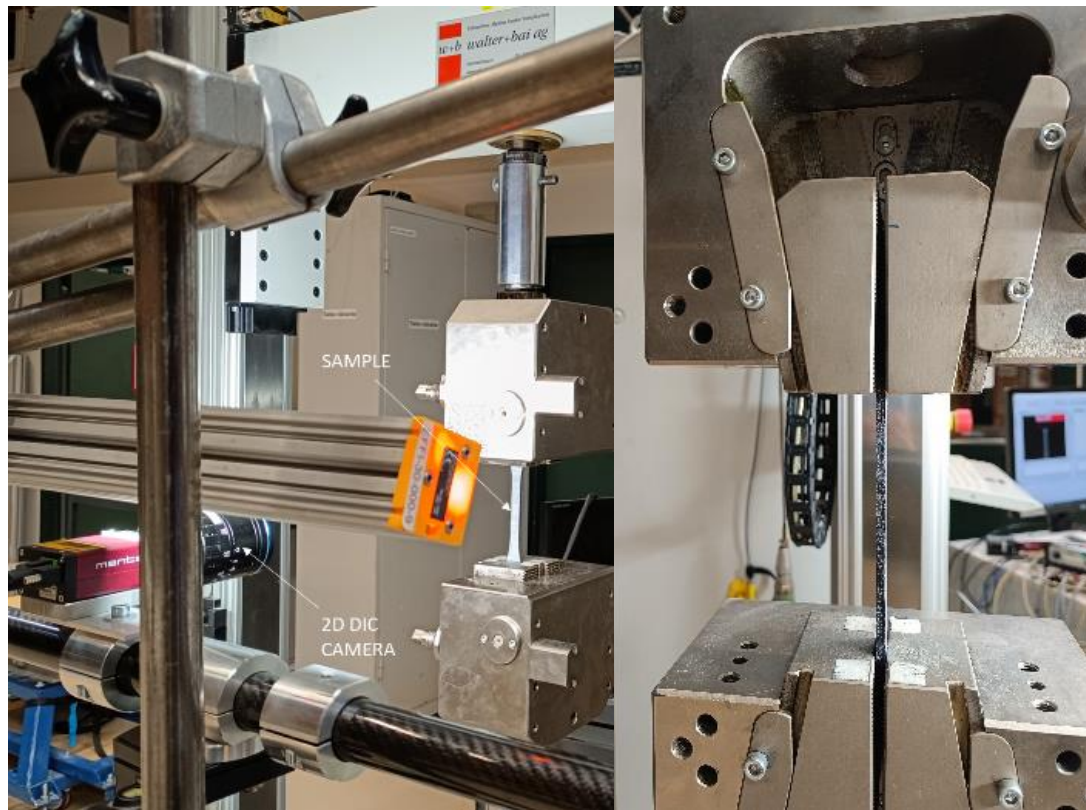


Figure 3.7 Tensile test setup

Table 3.3 Tensile test dimensions

Sample	Print Direction	Resolution [mm]	b [mm]	h [mm]	m [g]
S1	XY	0.6	10.63	4.39	11.63
S2	XY	0.6	10.66	4.41	11.78
S3	XY	0.6	10.66	4.34	11.72
S4	XY	0.3	10.67	3.89	11.22
S5	XY	0.3	10.57	3.85	11.2
S6	XY	0.3	10.66	3.83	11.21
S7	XZ	0.6	10.49	4.49	11.72
S8	XZ	0.6	10.31	4.43	11.66
S9	XZ	0.6	10.42	4.29	11.76
S10	XZ	0.3	9.94	4.54	11.69
S11	XZ	0.3	10.13	4.51	12.11
S12	XZ	0.3	10.12	4.52	11.74
S13	ZX	0.6	21.05	9.44	92.63
S14	ZX	0.6	21.38	9.33	91.54
S15	ZX	0.6	21.22	9.31	92.46

The properties of the 3D printed carbon-reinforced polymer material, sourced from the manufacturer's technical data sheet [162] and 3D printed process parameters are presented in Table 3.4.

Table 3.4 Material properties HI-TEMP CF and Process parameters for BigRep PRO

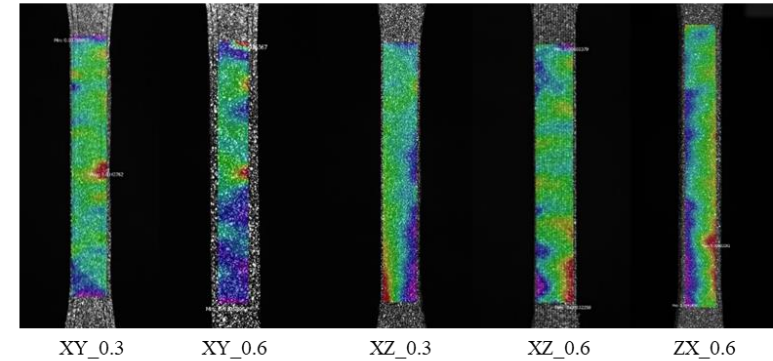
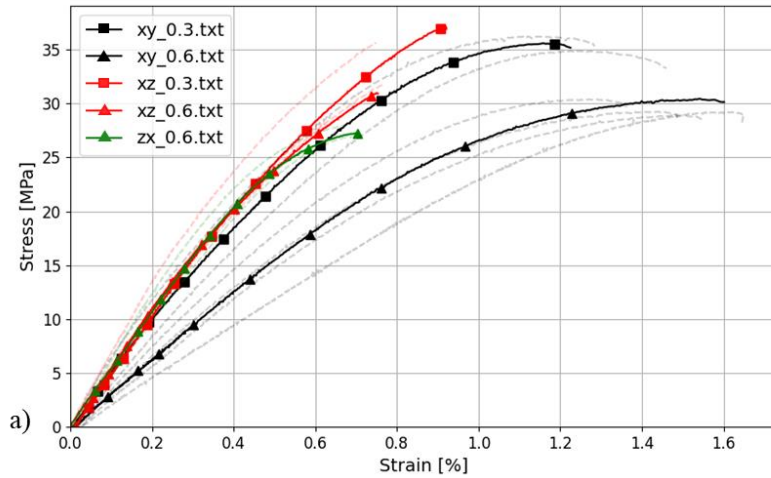
Density [kg/m ³]	1200	Printing speed [mm/s]	300
Filament Diameter	2.85 mm +/- 0.05	Layer height [mm]	0.3 and 0.6
Colour	Dark grey	Line width [mm]	1.0
Tensile Strength [MPa]	65	Infill angle	45°
Tensile Modulus [MPa]	7000		
Elongation at Break [%]	2.5		
Flexural Strength [MPa]	70		
Flexural Modulus [MPa]	7200		
Melting Temperature (T _m)	170 – 180 °C		

3.2.2 Calibration of the material model

The tensile tests serve to define the material properties of an isotropic elastic-plastic material model, crucial for finite element modelling of the 3D cellular structure. The calibration of material models for the HI_TEMP CF material is illustrated in Figure 3.8. for three distinct printing directions and two print resolutions. The modulus of elasticity and Poisson's ratio are calculated using data from the DIC and the measured cross-sectional dimensions for each test conducted in different 3D printing directions. The modulus of elasticity is calculated as the slope of the tangent line on the initial linear portion of the stress-strain curve for each print direction, within the strain interval between $\varepsilon_1 = 0.05\%$ and $\varepsilon_2 = 0.25\%$ according to ISO 527-1 [163].

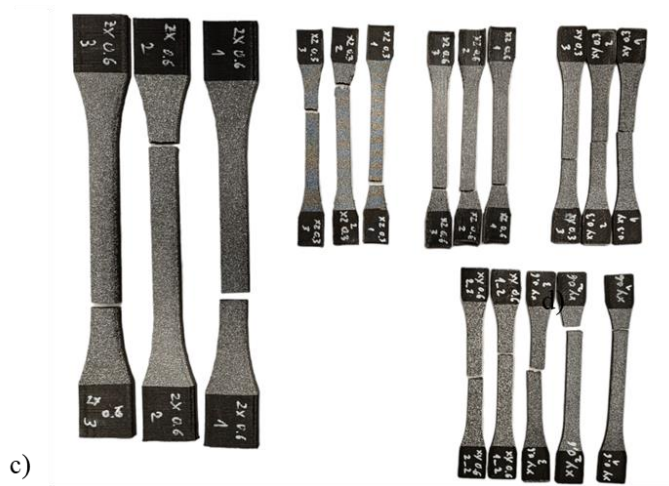
The results are presented for two print resolutions: 0.3 mm and 0.6 mm layer height. This allows for the observation of mechanical properties, illustrating the dependency on material quality at a meso-scale (material deposition), while the material at the micro-scale remains unchanged. It can be observed that fracture modes occur similarly for different print resolutions within the same print direction. Specifically, it is noted that damage predominantly occurs near the mechanical clamps in almost all specimens in the XZ direction, while in the XY print direction, most specimens fail in the middle area.

The results indicate that the specimens printed in the XY direction demonstrate the greatest deviation (dashed lines) in strain depending on the print resolution. Conversely, all other print directions and resolutions exhibit similar slopes of the stress/strain curve. However, it should be noted that the mechanical properties for this relatively low print resolution (0.3 mm and 0.6 mm) were measured to be approximately 30% lower than the values given in the technical data sheet shown in Table 3.4.

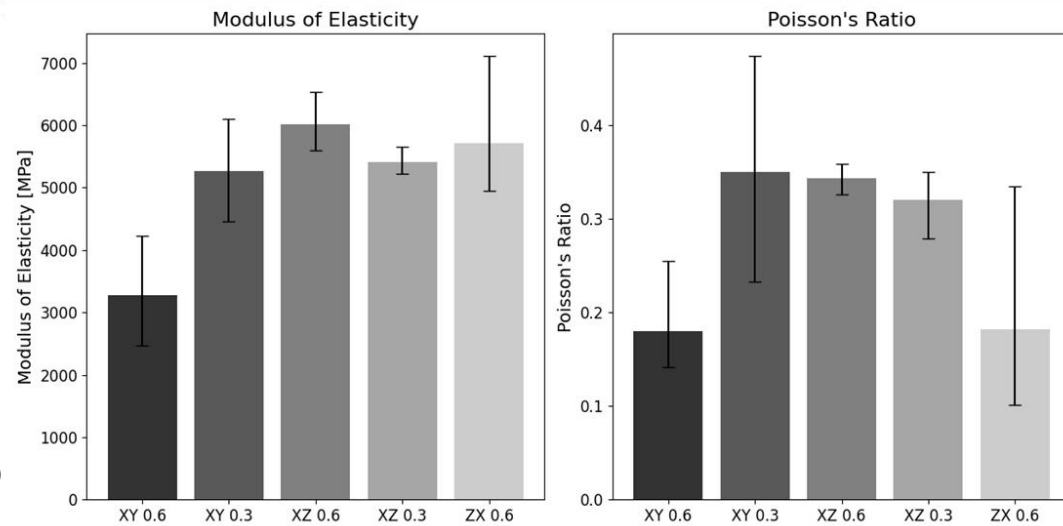


a)

b)



c)



d)

Figure 3.8 Material model: a) stress strain curves with scatter illustrated with dashed lines; b) DIC results; c) visual representation of failed tensile test specimens; d) modulus of elasticity and Poisson's ratio with 'I bars' indicating scatter

4 PARAMETRIC DESIGN

In this section, the focus is on the parametric algorithmic design of structures based on principles inspired by nature [164]. A parametric study of TPMS metamaterials involves the systematic variation and analysis of physical and mechanical parameters within the structural design. By investigating a range of design parameters, researchers can identify optimal configurations that fulfil the desired functionality of the part. The definition of TPMS geometries is categorized as parametric design as they are defined by a mathematical implicit function that determines the iso-surface, together with the adjustment of the wall thickness to determine the relative density. Parameters such as wave amplitudes can be adjusted to generate different variations of TPMS structures.

Structural lattice designs are generally categorized into two types: uniform and non-uniform. The different methods of parametric generative design are illustrated in Figure 4.1. The TPMS unit size, density, wall thickness, graded design and hybrid structure were investigated for two types of TPMS, Gyroid and Diamond.

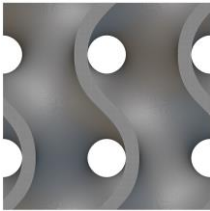
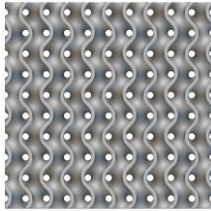
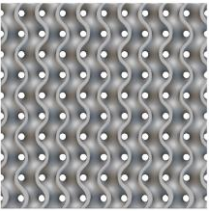
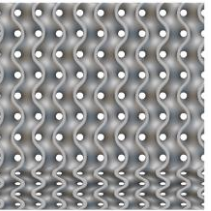
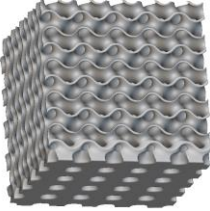

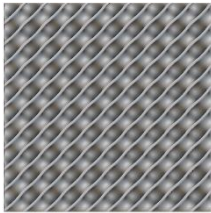
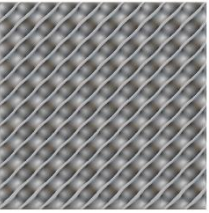
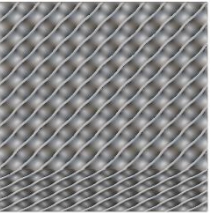
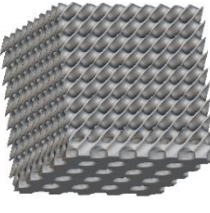
PARAMETRIC GENERATIVE DESIGN				
Design and Optimization of Uniform Lattice Structures	Design and Optimization of Non-Uniform Lattice Structures		Design and Optimization of Hybrid Lattice Structures	
Unit Cell Design Based on Mathematical Algorithm	Uniform Lattice Design Based on Topology Optimization	Non-Uniform Lattice Design Based on Structural Optimization	Non-Uniform Lattice Design Based on Functional Gradient Design	Design with Hybrid Geometry
a) 				
b) 				

Figure 4.1 Parametric generative design of TPMS: a) Gyroid and b) Diamond structures

Unit Cell Design Based on Mathematical Algorithm

Taking advantage of the inherent periodicity in various lattice metamaterials, some studies [54,165] have characterized the mechanical properties by simulating just one unit cell, which provides an insight into the properties of the entire structure. TPMS geometries are defined by simple mathematical implicit functions (Table 4.1). The sheet TPMS porous structures are created by offsetting TPMS surfaces with a constant wall thickness. Mesh models generated using the MC algorithm are subsequently utilized for visualizing or manufacturing these geometries.

Table 4.1 Mathematical function of each TPMS type

Gyroid	$\sin(x)\cos(y) + \sin(y)\cos(z) + \sin(z)\cos(x)$
Schwarz	$\cos(x) + \cos(y) + \cos(z)$
Diamond	$\sin(x)\sin(y)\sin(z) + \sin(x)\cos(y)\cos(z) + \cos(x)\sin(y)\cos(z) + \cos(x)\cos(y)\sin(z)$
Split	$1.1(\sin(2x)\sin(z)\cos(y) + \sin(2y)\sin(x)\cos(z) + \sin(2z)\sin(y)\cos(x)) - 0.2(\cos(2x)\cos(2y) + \cos(2y)\cos(2z) + \cos(2z)\cos(2x)) - 0.4(\cos(2x) + \cos(2y) + \cos(2z))$
Neovius	$3(\cos(x) + \cos(y) + \cos(z)) + 4\cos(x)\cos(y)\cos(z)$

In contrast to conventional truss or strut structures, which are prone to stress concentrations and defects at the joints, TPMS structures exhibit a continuous and integrated surface, providing zero mean curvature. The absence of joints and nodes in TPMS structures contributes significantly to their superior structural integrity and performance, mirroring natural structures such as butterfly wings and human bone structures [39].

Unit cell design based on topology optimization

Topology optimization, which dictates morphological parameters like pore size and volume fraction of lattice structures, is a well-established method for achieving uniform lattice structures [80]. The optimization can be configured for various physical and geometric parameters to achieve specific performance goals.

Non-Uniform Lattice Structure Based on Structural Optimization

In this method, the cell structure and cell thickness are determined based on the local stress state within a solid structure, targeting both minimum and maximum stress conditions. Initially, a static analysis is performed on a box to determine stress points, which are then used as an input parameter for the parametric design of the TPMS. Software tools facilitate a seamless adjustment in the lattice cell's wall thickness, transitioning smoothly from regions of lower stress to those with higher stress levels.

Non-Uniform Lattice Structures Based on Functional Gradient Design

The gradually changing porosity, present in the highly efficient natural architecture of human bones, integrates adjustments in unit size dimensions to enhance design functionality and save material [39]. A similar approach can be employed to create TPMS geometries where the porosity and TPMS type can be tailored for different structural applications with advanced property requirements.

Design with hybrid geometry

To achieve a more targeted control of mechanical performance, special hybrid TPMS structures have been developed so that the advantages of different TPMS units can be utilized together [166]. The findings indicate distinct strengths and weaknesses for each structure [167]. A reasonable selection of units and weight ratio is helpful to control the mechanical performances and produce isotropic porous structures.

4.1 TPMS units

Lattice structures are generated by repeating unit cells with a high degree of porosity. TPMS lattices are selected for this application because they offer the smallest possible surface area for a given volume, with an average curvature of zero at any point on the surface. As an iso-surface, TPMS can be visualized using the marching cubes (MC) algorithm, a 3D technique developed by Lorensen and Cline [168]. The TPMS structures are defined using different mathematical functions $\phi(x, y, z)$. The TPMS iso-surface is defined when the function $\phi(x, y, z)$ equals c , where c is the parameter that controls the iso-value offset from the zero level. There are two ways to develop the TPMS structure, depending on the material distribution. In the case of skeletal TPMS, the iso-surface divides the volume into two sub-volumes, one filled with material and the other one void (Figure 4.2). In the case of sheet TPMS, the material is distributed around the minimal surface on both sides, providing two separate void volumes. The mechanical properties of the TPMS structure are directly related to the volume fraction of the lattice, i.e. the relative density ρ_r (ratio of the lattice volume to the unit cell volume, $\rho_r = 1 - porosity$). The threshold constant c , the periodic parameter ω and the offset thickness t have a considerable influence on the value of the relative density. This scientific framework integrates visualization, iso-surface extraction, and distance field techniques for characterizing TPMS in diverse applications.

Different TPMS structures exhibit different deformation behaviour under compressive load. Failure modes observed in the study by Maskery et al [15] led to the conclusion that cell unit size plays a crucial role in early localized failure and crack propagation. Although a smaller

unit size is recommended, it should be consistent with the recommended quality of the manufacturing process.

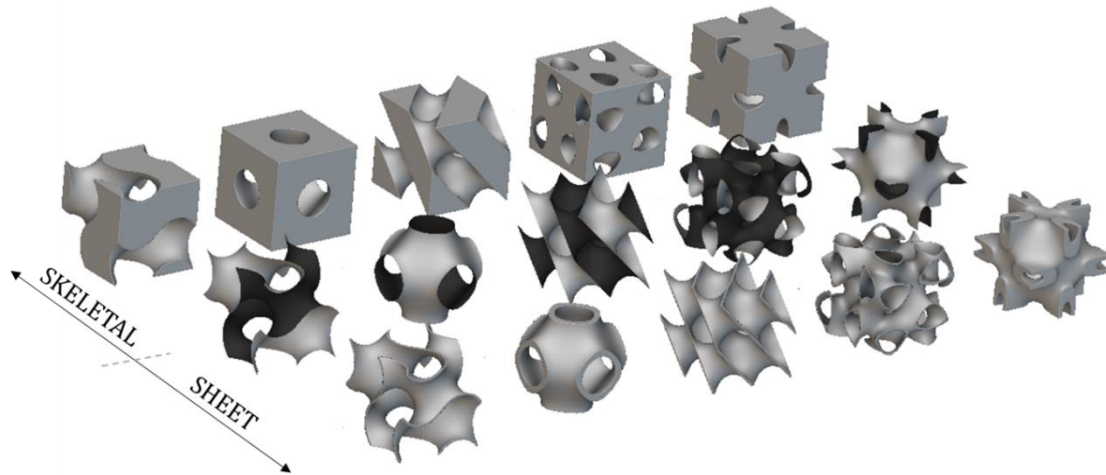


Figure 4.2 Five different TPMS unit cells derived from the iso-surface: Gyroid, Schwarz, Diamond, Split and Neovius (from left to right)

4.2 Composite sandwich panel with tempered glass face sheets

Parametric generative design was performed using software programme nTopology [132]. Initially, a static analysis was performed on a solid with core dimensions of 0.81 x 0.30 x 0.06 m, subjected to a concentrated load in the middle. The supports were defined with displacement restraints in three orthogonal directions on one side and a sliding constraint in the longitudinal direction on the other side. The von Mises stress points derived from the static analysis results (Figure 4.3) were utilized as input parameters for the parametric design of the TPMS core. Scalar ramp enabled a smooth variation in the size of the lattice cell map from areas of lower stress to those with higher stress values. The Gyroid geometry of the deck was generated using a periodic rectangular lattice block with a cell size of 100 x 70 x 60 mm. To optimize the deck's weight, material distribution was achieved by varying the cell size of the Gyroid and the thickness of its walls. A ramp function facilitated a gradual transition based on the stress distribution in the solid deck. Wall thickness varied between 3.5 and 5.5 mm, with the cell size approximately twice as dense in regions of higher stresses (in the middle of the deck and above supports).

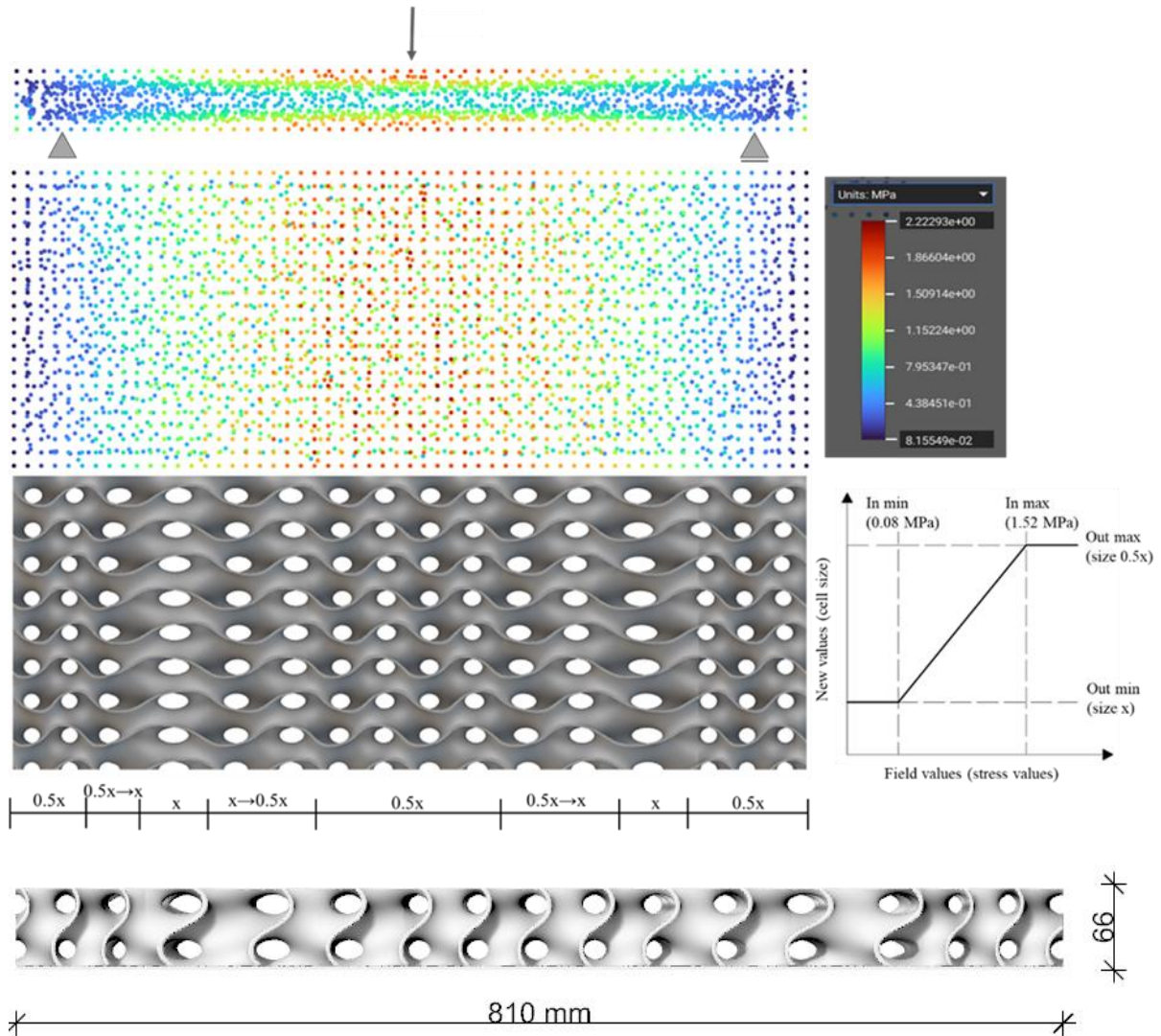


Figure 4.3 Design of Gyroid core

The 3D printing parameters for the non-uniform 3D printed plate are presented in the Table 4.2. To enhance time and material cost efficiency, successful printability was achieved through the optimization of print time and material consumption by increasing layer height and bead width (refers to wall thickness). Additionally, support material was minimized by adhering to the maximum angle required for support generation. The 3D printing process was executed using the Stratasys F770 machine.

Table 4.2 Material properties and process parameters

Material properties		Process parameters	
Printing material	ASA	3D printer used:	Stratasys F770
Specimens' dimensions [mm]	155×40×4	Printing speed [mm/s]	2
Density [kg/m ³]	1080	Layer height [mm]	0.33
Young's elastic modulus [MPa]	1438.21	Body thickness [mm]	0.4
Poisson coefficient	0.4	Infill angle	45°

Tension strength (ZX) [MPa]	19.54	Printing direction	xy plane
Compression strength [MPa]	75	Support material	SR30
Shear strength [MPa]	10.96	Printing temperature [°C]	260
Duration of print:	100 hours and 24 minutes		
Material consumption	1373 cm ³		
Support material consumption	627 cm ³		

After the support material was removed, the 3D-printed core underwent gluing to the 3 mm flanges of tempered glass using Bohle Verifix UV-Klebstoff MV 760 to achieve full contact (Table 4.3). The adhesive thickness was manually applied along the top and bottom curved lines of the Gyroid part using a 1.37 mm needle. This method may vary in consistency, so the suggestion for future larger-scale production is to automate the adhesive application process for consistency and precision. These systems may include robotic arms equipped with nozzles, ensuring uniformity and accuracy in adhesive application. The final part is presented in Figure 4.4.

Table 4.3 Tempered glass and Adhesive material properties

Tempered glass		Adhesive	
Density [kg/m ³]	2500	UV Adhesive	Verifix® MV 760
Young's elastic modulus [MPa]	70000	Viscosity [mPa·s]	1500
Poisson ratio [-]	0.22	Shear strength [MPa]	25
Shear modulus [MPa]	28000	Temperature range	-40 - +120 °C
Failure stress [MPa]	120	Colour	crystal clear
		Viscoelastic properties	Impact resistant

The adhesive thickness was manually applied along the top and bottom curved lines of the Gyroid part using a 1.37 mm needle.

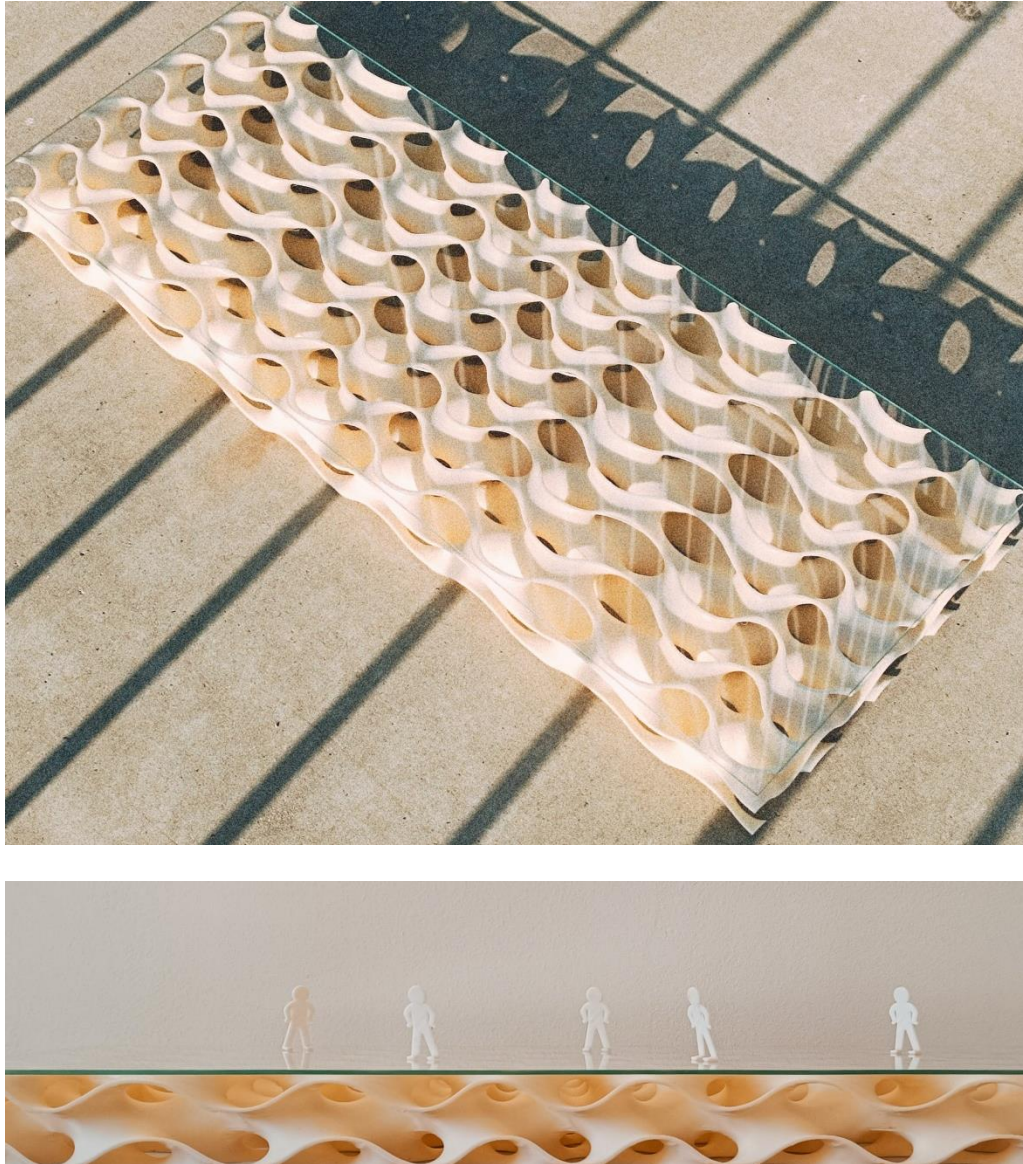


Figure 4.4 Final part of the composite TPMS bridge deck with tempered glass face sheets

4.3 Composite sandwich panel with GFRP face sheets

The geometric parameters of the bridge, such as the height and width in the middle section and at both edge supports, were parameterized using Rhinoceros and Grasshopper software. Inspired by the Da Vinci bridge geometry and internal load distribution, the goal was to allocate greater height to regions experiencing high bending moments and wider support areas where shear force predominates. The mathematical relationships established for the scaled bridge prototype with a total span of 90 cm are presented in Figure 4.5

The parameters of the macrostructure core were established by examining the micro and macro-scale metamaterial found in natural forms [34] specifically the TPMS structures. Gyroid morphology was chosen due to its bending-dominated structure [169] and isotropic properties

[131,160,170]. Gyroid was selected for its visual appeal as well, enabling full transparency through the voids within the lattice structure.

The macro building block, measuring $60 \times 60 \times 60$ mm, proved to be suitable for creating a stiff yet lightweight structure, with only 2 kg of core material, 0.377 kg of top flange, and 0.292 kg for the bottom flange. These dimensions were chosen to fit within a bounding box measuring $900 \times 240 \times 220$ mm.

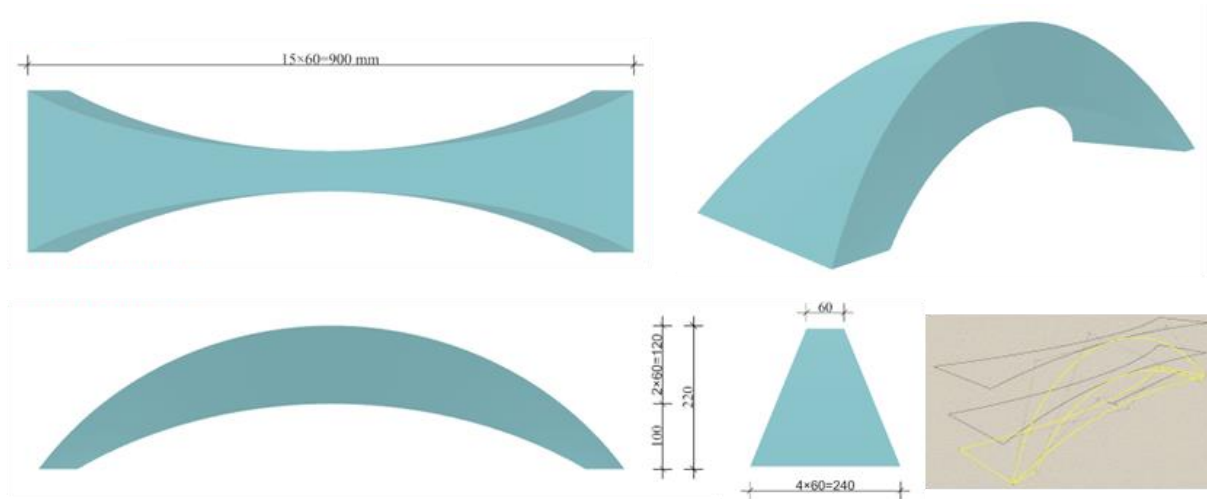


Figure 4.5 Geometry definition in Rhinoceros and Grasshopper

The parametric representation of the potential cellular structures described in the Introduction section is illustrated in the Figure 4.6a, presenting a uniform periodic homogeneous cellular structure with the arch bottom surface serving as a reference plane. This structure is also homogeneous, with uniform density due to the constant wall thickness across all building blocks. Figure 4.6b illustrates a periodic but heterogeneous structure. Through structural optimization, the thickness varies based on higher stresses, resulting in a load-adaptive structure. Figure 4.6c showcases a pseudo-periodic cellular structure, where the cell mapping between the top and bottom faces leads to alterations in the shape and size of the building blocks to conform to the specified volume. Similar to Figure 4.6b structural optimization was implemented in Figure 4.6d, resulting in a heterogeneous pseudo-periodic structure.

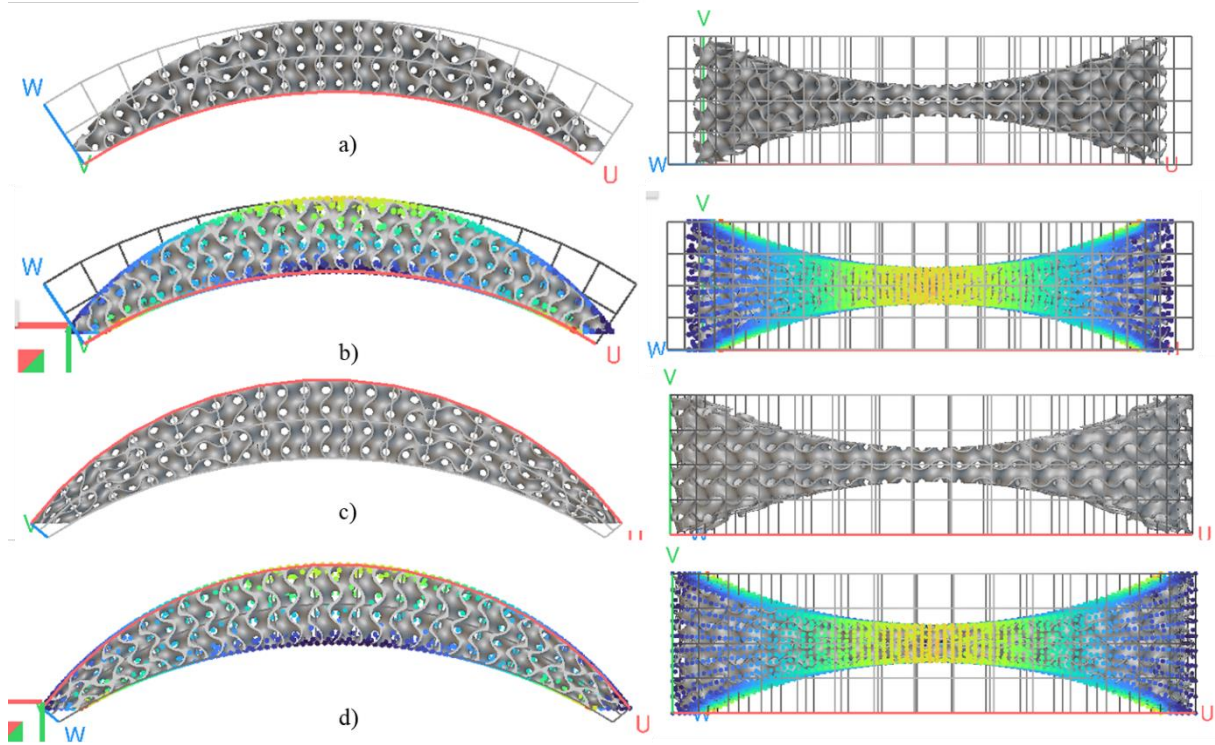


Figure 4.6 Cellular structures for the proposed bridge geometry: a) Periodic homogeneous cellular structure; b) Periodic heterogeneous structures; c) Pseudo-periodic homogenous structure; d) Pseudo-periodic heterogeneous structure

The potential variations in geometry and cellular structure definition are numerous, including additional gradations [34] or even hybrid structures [167]. However, for the purpose of this work, where the final product is a sandwich composite consisting of the cellular core with top and bottom GFRP face sheets (Figure 4.7), it is crucial to establish control over this novel system with the least number of unknown input variables. This involves managing the interaction between the core and the face sheets, as well as comprehending the behaviour of the 3D printed material, which introduces additional anisotropy into the system. Therefore, a uniform and periodic cellular structure was initially manufactured and experimentally investigated (Figure 4.6a).

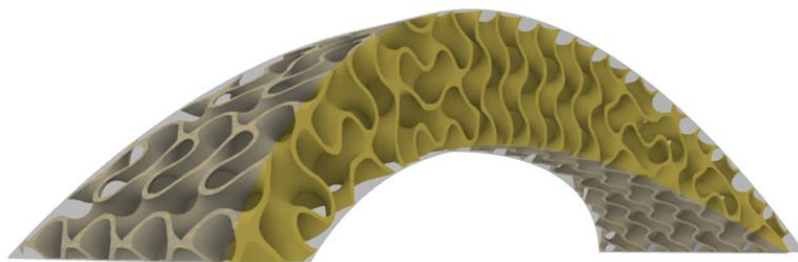


Figure 4.7 Final composite bridge model

5 ANALYSIS APPROACHES

The parts of this chapter were published in the paper: Stepinac, Lucija; Galić, Josip; Binički, Marin. Fast estimation of bending stiffness in sandwich- structured composites with 3D printed TPMS core. Mechanics of Advanced Materials and Structures, (2023), DOI: <https://doi.org/10.1080/15376494.2023.2267551>.

The modelling of advanced geometries and advanced materials can have both simplified and more detailed approaches (Figure 5.1). Different analytical and numerical methods were presented with the aim of implementing these design approaches in the calculation of load-bearing elements. The solidification in all models was performed for the sheet TPMS structures. There are several tools for the implicit modelling of 3D cellular structural objects, which can vary in type, size and properties.

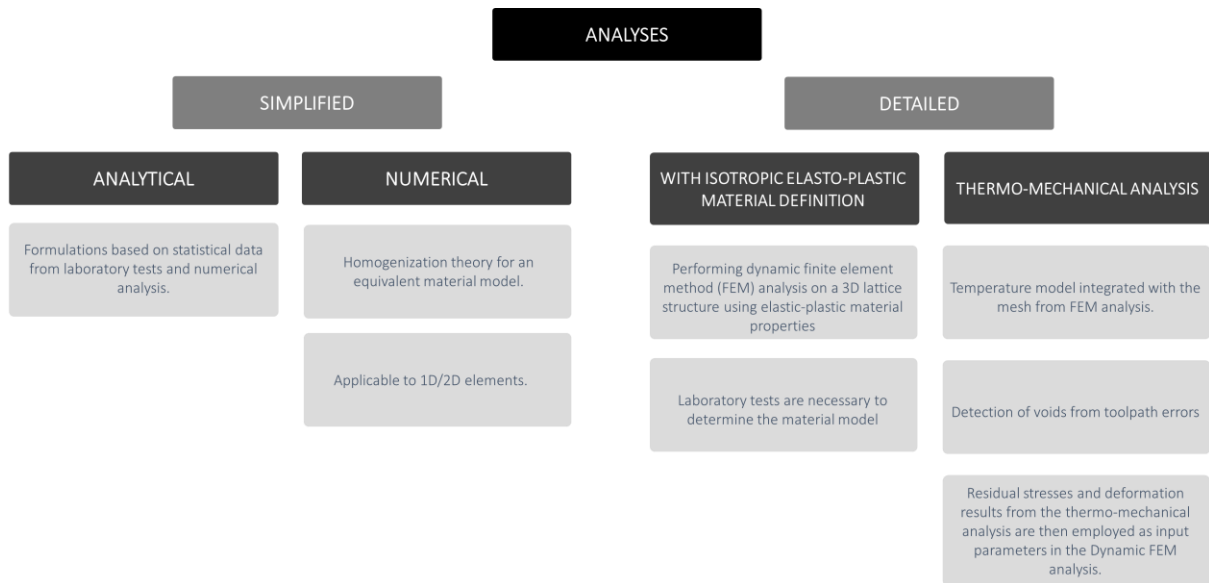


Figure 5.1 Analysis approaches from simplified to more detailed

The design method developed in this research involves a combination of representative volume element (RVE) homogenization analysis and analytical formulation of the flexural stiffness of multilayer composite beams. Firstly, the RVE homogenization analysis was used to determine the effective stiffness properties of TPMS structures. It calculated stiffness matrices for five different TPMS geometries, such as Gyroid, Schwarz, Diamond, Split and Neovius and the RVE homogenization method allowed the investigation of mechanical properties of other materials. In addition, different experimental designs were used to determine the flexural stiffness of the multilayer composite beams made of top and bottom sheets and TPMS core.

5.1 Homogenization analysis

Homogenization process was done in nTopology software [132] and checked within Abaqus plug-in Micromechanics [171]. RVE Homogenization analysis was conducted for five different TPMS types (Gyroid, Schwarz, Diamond, Split and Neovius) and at eight different densities (10%, 15%, 20%, 25%, 30%, 35%, 40%). The RVE Homogenization analysis sets up a set of six load cases (Figure 5.2). In each load case, it applies a unit perturbation of one component of the volume-averaged engineering strain, holding all other components constant at zero. For each of these load cases, the resulting perturbation of the volume-averaged stress forms a column of the Hooke's stiffness tensor (McLendon, 2016). Using data from FEM analysis the polynomial regression curve is used for determination of mechanical properties of each TPMS type. The identification of anisotropy of the elasticity tensor can easily be made for different TPMS types based on their stiffness matrix. The ratio factor that defines the anisotropy index, the Zener factor Z can be expressed.

According to the generalized Hooke's law ((5.1) and Lamé constants in stiffness matrix form of 6 rows and 6 columns in Eq. (5.2), both elastic modulus (5.3) and anisotropy properties (Zener ratio) (5.4) can be obtained [165].

$$\{\sigma\} = [C]\{\varepsilon\}$$

$$[C] = \begin{bmatrix} C_{11} & C_{12} & C_{12} & 0 & 0 & 0 \\ C_{12} & C_{11} & C_{12} & 0 & 0 & 0 \\ C_{12} & C_{12} & C_{11} & 0 & 0 & 0 \\ 0 & 0 & 0 & C_{44} & 0 & 0 \\ 0 & 0 & 0 & 0 & C_{44} & 0 \\ 0 & 0 & 0 & 0 & 0 & C_{44} \end{bmatrix} \quad (5.1)$$

$$\begin{bmatrix} \sigma_{11} \\ \sigma_{22} \\ \sigma_{33} \\ \sigma_{12} \\ \sigma_{13} \\ \sigma_{23} \end{bmatrix} = \begin{bmatrix} \lambda + 2\mu & \lambda & \lambda & 0 & 0 & 0 \\ \lambda & \lambda + 2\mu & \lambda & 0 & 0 & 0 \\ \lambda & \lambda & \lambda + 2\mu & 0 & 0 & 0 \\ 0 & 0 & 0 & 2\mu & 0 & 0 \\ 0 & 0 & 0 & 0 & 2\mu & 0 \\ 0 & 0 & 0 & 0 & 0 & 2\mu \end{bmatrix} \begin{bmatrix} \varepsilon_{11} \\ \varepsilon_{22} \\ \varepsilon_{33} \\ \varepsilon_{12} \\ \varepsilon_{13} \\ \varepsilon_{23} \end{bmatrix} \quad (5.2)$$

$$E = \frac{C_{11}^2 + C_{12}C_{11} - 2C_{12}^2}{C_{11} + C_{12}} \quad (5.3)$$

$$Z = \frac{E}{2G(1 + \nu)} = \frac{2C_{44}}{C_{11} - C_{12}} \quad (5.4)$$

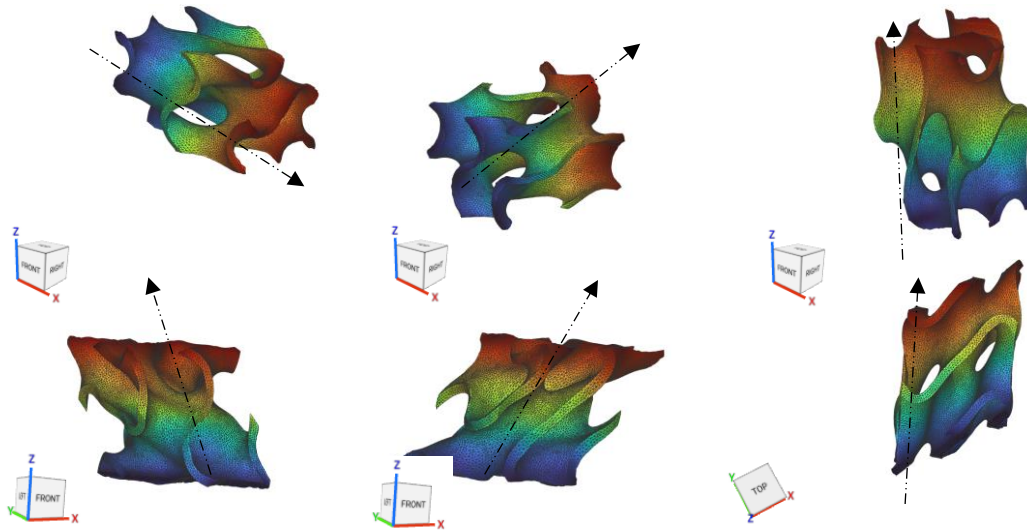


Figure 5.2 RVE Homogenization analysis set of 6 load cases

Figure 5.3 illustrates the relationship between the ratio of the modulus of elasticity of TPMS unit to that of a solid material (E/E_s) and the density of TPMS relative to a solid (ρ/ρ_s). The data points were fitted with curve-fitting approaches to obtain mathematical formulations for each TPMS type (Figure 5.4).

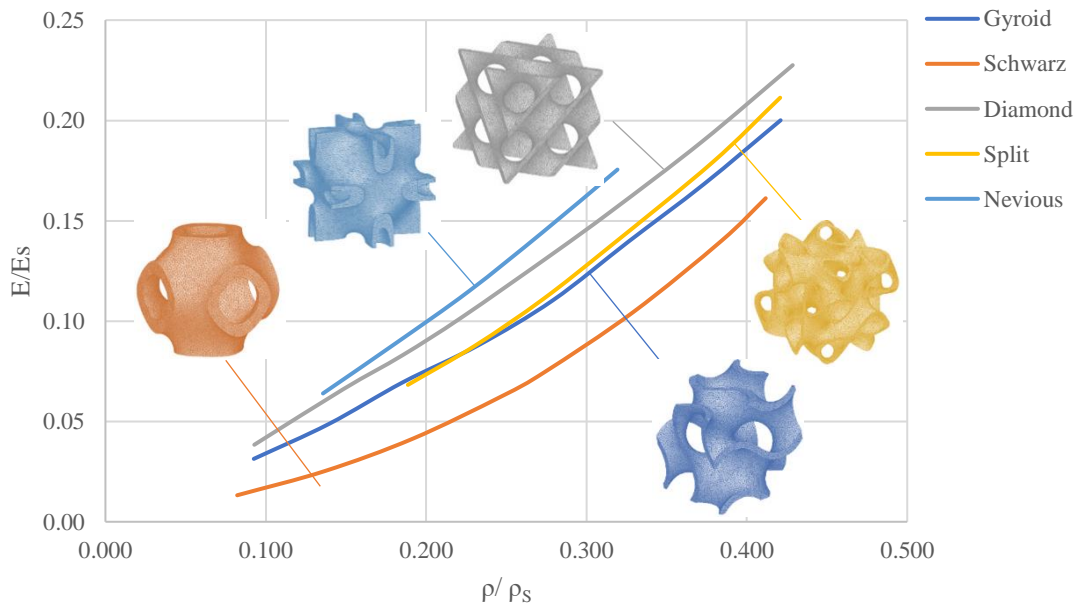


Figure 5.3 Polynomial regression curve for determination of mechanical properties for each TPMS type

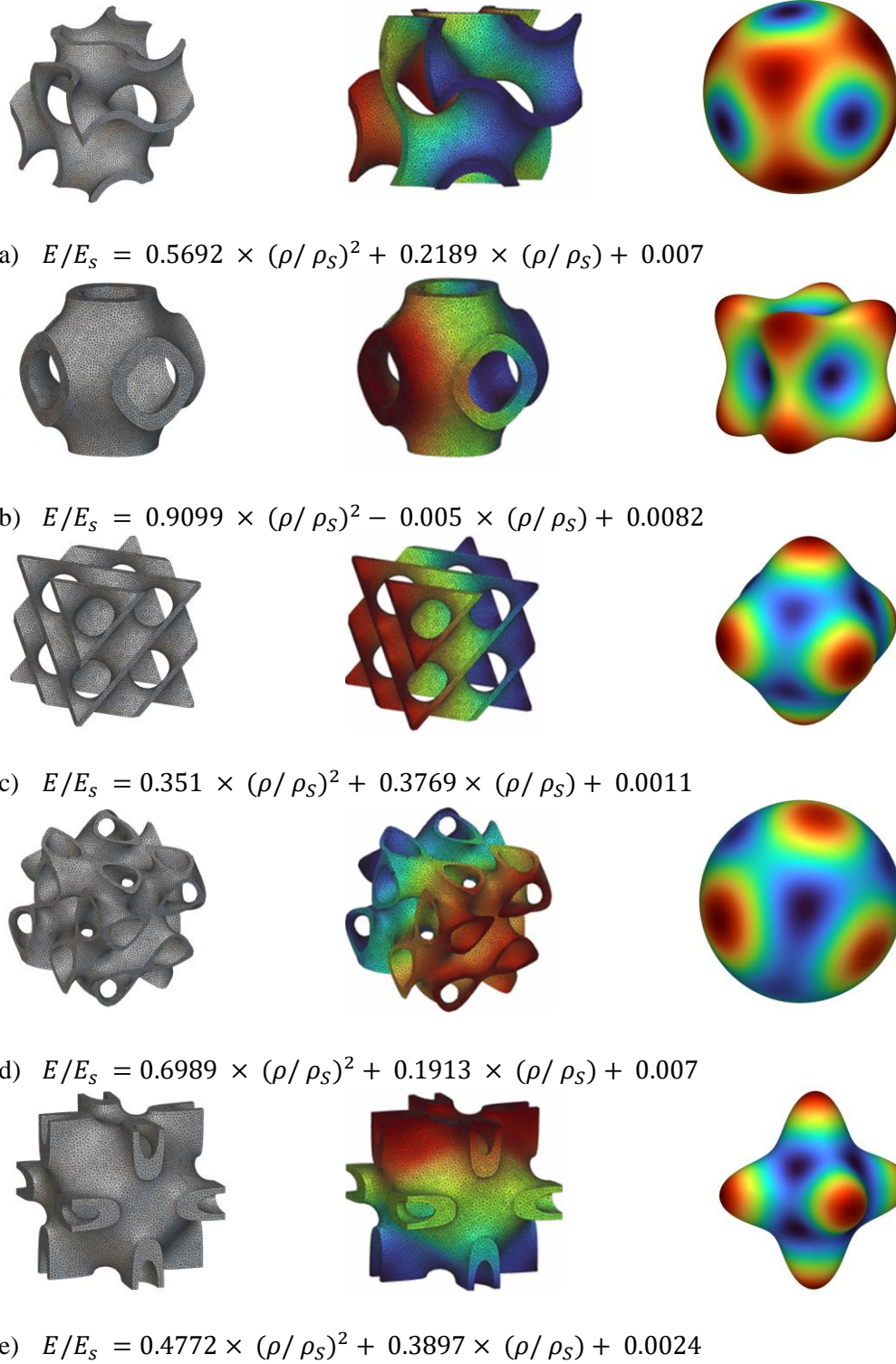


Figure 5.4 Calculated expression from curve fitting for each TPMS type; a) Gyroid, b) Schwarz, c) Diamond, d) Split, e) Neovius

5.1.1 Numerical analysis of TPMS units

The parametric modelling approaches are the Unit Cell Design Based on Mathematical Algorithm (a unit cell), Unit Cell Design Based on Topology Optimization (uniform raster of 5×5), Non-Uniform Lattice Structure Based on Structural Optimization (raster of 5×5), Non-Uniform Lattice Structures Based on Functional Gradient Design, and Design with a hybrid geometry. The results from Figure 5.5 indicate that the non-uniform Gyroid lattice, optimized by structural optimization with thickness variation, has the most uniform stress distribution. On the other hand, in the Diamond structure, the most neutral stress distribution is observed in the hybrid Diamond/Neovius structure, although some stress concentration in the transitional region is inevitable.

In the context of stiffness, a noticeable trend emerges when considering different material configurations to achieve an identical final relative density: in the case of a uniform lattice, the Diamond structure exhibits 20-40% higher stiffness than the Gyroid structure. Furthermore, when it comes to non-uniform lattices, the Diamond structure has a 10-20% higher stiffness than its counterpart with a uniform lattice at the same relative density. The introduction of graded and hybrid structures generally contributes to isotropy in two orthogonal directions, but there is significant anisotropic behaviour in the third direction. With grading and hybridization, more material is directed into the lower unit cells, resulting in a less stiff top structure and a stiffer lower structure.

The numerical analysis of the periodic design reveals that non-uniformity does not necessarily bring structural advantages. In the case of the Gyroid structure, a uniform periodicity coupled with a structural optimization of the wall thickness mitigates the stress concentrations. In the Diamond structure, on the other hand, a uniform cell size leads to the lowest deformation along the height, while a slight structural optimization of the wall thickness does not result in a uniform stress distribution.

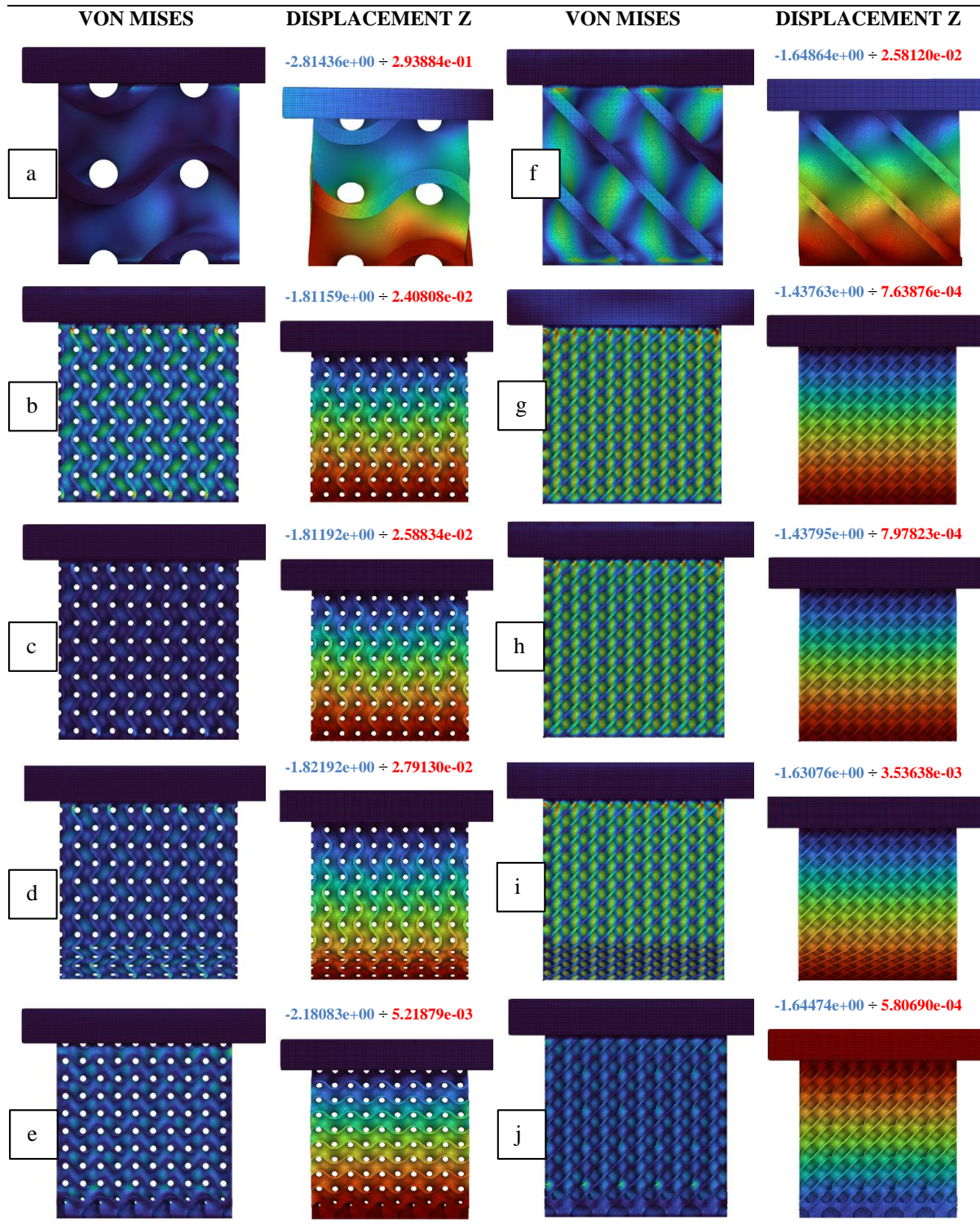


Figure 5.5 Parametric design of: a) Gyroid Unit Cell: Math Algorithm (1 cell), b) Gyroid Unit Cell: Topology Optimization (5×5 raster), c) Gyroid Non-Uniform Lattice: Structural Optimization (5×5 raster), d) Gyroid Non-Uniform Lattice: Functional Gradient Design e) Gyroid with Neovius Hybrid Geometry; f) Diamond Unit Cell: Math Algorithm (1 cell), g) Diamond Unit Cell: Topology Optimization (5×5 raster), h) Diamond Non-Uniform Lattice: Structural Optimization (5×5 raster), i) Diamond Non-Uniform Lattice: Functional Gradient Design and j) Diamond with Neovius Hybrid Geometry

To achieve a more uniform directional modulus of elasticity, the concept of designing graded and hybrid structures, i.e. Gyroid/Neovius and Diamond/Neovius structures, was applied. At low volume fractions, the connection between the parent structures in hybrid structures may not be properly established. This is another limitation of the research. Despite attempts to achieve the best transition through parameter adjustments, a robust connection between the structures cannot be achieved at this relatively low volume fraction of 26%, which can lead to stress concentration and failure in this region.

Figure 5.6 shows the influence of different parametric design approaches on the modulus of elasticity and the anisotropy properties (the Zener ratio) at the same relative density. Numerical homogenization theory and FEA were used to investigate the correlation between the TPMS parameters and the elastic modulus/anisotropy properties. The results indicate that Gyroid and Diamond exhibit strong and weak directions along the diagonal and axial axes.

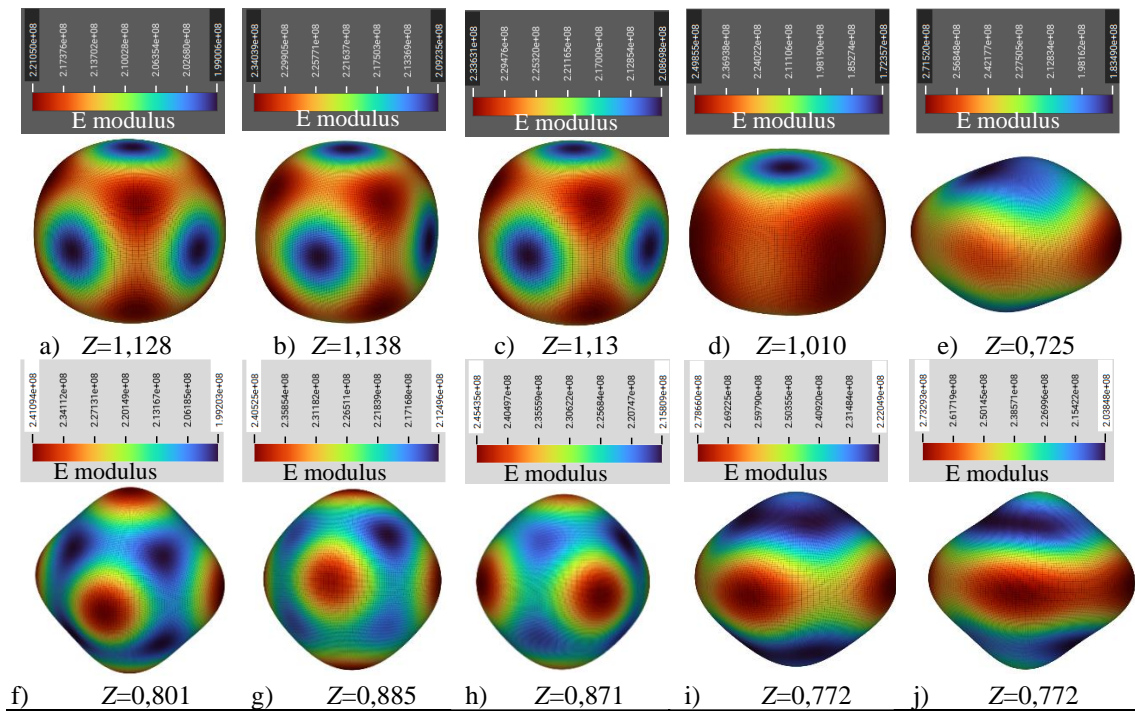


Figure 5.6 Anisotropy properties of sheet TPMS: a) Gyroid Unit Cell: Math Algorithm (1 cell), b) Gyroid Unit Cell: Topology Optimization (5×5 raster), c) Gyroid Non-Uniform Lattice: Structural Optimization (5×5 raster), d) Gyroid Non-Uniform Lattice: Functional Gradient Design e) Gyroid with Neovius Hybrid Geometry; f) Diamond Unit Cell: Math Algorithm (1 cell), g) Diamond Unit Cell: Topology Optimization (5×5 raster), h) Diamond Non-Uniform Lattice: Structural Optimization (5×5 raster), i) Diamond Non-Uniform Lattice: Functional Gradient Design and j) Diamond with Neovius Hybrid Geometry

The mechanical properties of Gyroid and Diamond lattice structures investigated using homogenization analysis reveal different behaviour, which can be attributed to different design strategies (Table 5.1). In their unit cell forms, both structures have isotropic moduli of elasticity,

with Gyroid exhibiting auxetic properties. Uniform material configurations slightly increase stiffness, while graded thickness leads to moderate variations. Graded unit structures lead to significant anisotropy and auxetic behaviour, and hybrid configurations further modify anisotropic properties. In summary, this illustrates how design decisions such as uniformity, grading and hybridization influence the mechanical responses of these lattice metamaterials, providing insights for tailored applications in structural engineering.

The homogenization analysis method is applied to investigate the mechanical properties of a TPMS unit cell, namely Gyroid and Diamond, based on the RVE method. The numerical homogenization method [172], which is integrated into the numerical analysis software Abaqus and nTopology, was used to calculate the effective stiffness matrix. Six load cases are applied to an RVE in the Homogenization analysis. For an orthotropic material, the stiffness matrix takes the following form (5.5):

$$\begin{Bmatrix} \sigma_{11} \\ \sigma_{22} \\ \sigma_{33} \\ \sigma_{23} \\ \sigma_{13} \\ \sigma_{12} \end{Bmatrix} = \begin{bmatrix} \frac{1 - \nu_{23}\nu_{32}}{E_2 E_3 \Delta} & \frac{\nu_{21} + \nu_{23}\nu_{31}}{E_2 E_3 \Delta} & \frac{\nu_{31} + \nu_{21}\nu_{32}}{E_2 E_3 \Delta} & 0 & 0 & 0 \\ & \frac{1 - \nu_{13}\nu_{31}}{E_1 E_3 \Delta} & \frac{\nu_{32} + \nu_{12}\nu_{31}}{E_1 E_3 \Delta} & 0 & 0 & 0 \\ & & \frac{1 - \nu_{12}\nu_{21}}{E_1 E_2 \Delta} & 0 & 0 & 0 \\ \text{sym} & \dots & & G_{23} & 0 & 0 \\ & & & & G_{13} & 0 \\ & & & & & G_{12} \end{bmatrix} \begin{Bmatrix} \varepsilon_{11} \\ \varepsilon_{22} \\ \varepsilon_{33} \\ 2\varepsilon_{23} \\ 2\varepsilon_{13} \\ 2\varepsilon_{12} \end{Bmatrix} \quad (5.5)$$

$$\begin{aligned} \Delta &= \frac{(1 - \nu_{12}\nu_{21} - \nu_{23}\nu_{32} - \nu_{13}\nu_{31} - 2\nu_{21}\nu_{32}\nu_{13})}{E_1 E_2 E_3} \\ E_2 &= E_3, G_{12} = G_{13}, \nu_{12} = \nu_{13}, \nu_{21} = \nu_{31}, \nu_{32} = \nu_{23}, \\ \nu_{21} &= \frac{E_2}{E_1} \nu_{12}, G_{23} = \frac{E_2}{2(1 + \nu_{23})}. \end{aligned} \quad (5.6)$$

The homogenization results from the stiffness tensor enable the extraction of the effective mechanical properties of the material. Depending on the FEA and software used, a TPMS unit cell is replaced by a solid volume of orthotropic or isotropic material or even by a 1D model so that the internal forces and displacements of the load-bearing elements can be calculated.

Table 5.1 Mechanical properties obtained from Homogenization Analysis

	E1	E2	E3	ν_{12}	ν_{13}	ν_{23}	G12	G13	G23
	[MPa]	[MPa]	[MPa]				[MPa]	[MPa]	[MPa]
GYROID									
unit cell	199.01	199.01	199.02	-0.45	-0.45	-0.45	85.68	85.68	85.66
uniform material	209.28	209.23	209.33	-0.43	-0.43	-0.43	91.67	91.62	91.63
graded thickness	208.79	208.70	209.02	-0.43	-0.43	-0.43	91.42	91.45	91.50

graded unit	231.27	230.94	172.36	-0.42	-0.49	-0.49	90.50	90.60	100.97
hybrid	244.06	245.76	191.49	-0.39	-0.43	-0.43	78.00	77.84	105.38
DIAMOND									
unit cell	241.10	241.09	241.03	-0.37	-0.37	-0.37	76.03	76.03	76.03
uniform material	238.80	238.76	240.53	-0.34	-0.34	-0.34	84.21	84.20	83.87
graded thickness	245.27	245.44	239.98	-0.35	-0.35	-0.35	85.00	84.97	85.07
graded unit	278.66	278.55	233.25	-0.35	-0.38	-0.38	85.30	85.25	97.50
hybrid	272.52	272.26	231.71	-0.34	-0.35	-0.35	78.09	78.04	98.97

5.1.2 Analytical analysis of TPMS units

The most important mechanical properties of TPMS structures include the modulus of elasticity, Poisson's ratio and anisotropy properties, in particular the Zener ratio — a dimensionless value used to quantify anisotropy in cubic crystals. The Zener ratio quantifies the degree to which a material deviates from isotropy, with a value of 1 indicating fully isotropic materials. The stiffness matrix constants C_{11} , C_{12} , and C_{44} can be used to estimate this value.

The relative density is generally considered to be the most important property of porous structures. The modulus of elasticity is influenced by the relative density (1 - porosity). The modulus of elasticity can be derived from compression tests as a function of the relative density of the unit [51,63,70,173,174].

Based on these semi-empirical formulations, the mechanical properties of porous structures can be evaluated directly using the relative density ρ_r ((5.7) [175]. Variations in the wall thickness inevitably led to variations in the relative density.

$$\begin{aligned} E^{\square}/E_s &= C_1(\rho^{\square}/\rho_s)^n = C_1\rho_r^n \\ \sigma_{pl}^{\square}/\sigma_{ys} &= C_2(\rho^{\square}/\rho_s)^m = C_2\rho_r^m \end{aligned} \quad (5.7)$$

where E^* and σ_{pl}^{\square} are modulus of elasticity and yield stress of porous structures, E_s and σ_{ys} are modulus of elasticity and yield stress of the original solid material, C_1 and C_2 are constants, ρ^{\square} and ρ_s are densities of porous and solid materials, m and n depend on the structure topology. The values of C_1 , C_2 , m and n can be obtained by numerous mechanical tests and data fitting.

Analytical expressions from [175] were used for the simple evaluation of mechanical properties. The power law model is simpler and often adequate for many applications. In contrast, the polynomial models from Figure 5.4 offers a more detailed representation.

The values of C_1 and n were determined by mechanical analysis and curve fitting, which allows direct evaluation of the mechanical performance of conventional porous structures based on relative density. However, within the same type of TPMS with different parameters C ,

porous structures with the same relative density do not necessarily have identical elastic modulus properties.

Table 5.2 Results for C_1 and n constants for each TPMS

	Gyroid	Schwarz	Diamond	Split	Neovius
E [MPa]	101.47	61.07	124.55	130.19	261.89
E/E_s	0.0676	0.0407	0.0830	0.0868	0.1746
E_s [MPa]	1500	1500	1500	1500	1500
ρ [%]	18.6	19.2	18.5	23.0	31.9
ρ_s [%]	100	100	100	100	100
C_1	4.1E-04	5.2E-04	4.1E-04	5.0E-04	4.6E-04
n	1.31	1.78	1.19	1.47	1.20
Accuracy [%]	96.20	93.18	98.43	97.87	99.21

5.2 Multilayer composite analysis

The analytical expressions (5.8)-(5.10) derived for the equivalent flexural stiffness $(EI)_{eq}$ of multi-layer composite beams, accommodate an arbitrary number of layers and material choices. Where, t_k represents the thickness of each ply, E_k represents the Young's modulus for isotropic and homogeneous materials and $(m_k - m_l)$ is the distance between the middle planes of the layers [176].

$$(EI)_{eq} = C_1 - \frac{B_{31}^2}{A_3} \quad (5.8)$$

$$A_3 = b \sum_{k=1}^n t_k E_k, C_2 = \frac{b^3}{12} \sum_{k=1}^n t_k E_k, C_{12} = 0, B_{32} = 0, \quad (5.9)$$

$$C_1 = \frac{b}{3} \sum_{k=1}^n (z_{k-1}^3 - z_k^3) E_k, B_{31} = \frac{b}{2} \sum_{k=1}^n (z_{k-1}^2 - z_k^2) E_k.$$

$$(EI)_{eq} = b \left[\sum_{k=1}^n \frac{t_k^3 E_k}{12} + \left(\sum_{k=1}^n t_k E_k \right)^{-1} \sum_{1 \leq k < l \leq n} t_k E_k \cdot t_l E_l \cdot (m_k - m_l)^2 \right] \quad (5.10)$$

$$m_k - m_l = \frac{t_k}{2} + t_{k+1} + \dots + t_{l-1} + \frac{t_l}{2}$$

The application supports the input of uniform line load. Furthermore, the dead load is automatically considered by algorithm (Figure 5.7), based on geometric characteristics and material selection. Deformation results are obtained with a limit of $L/250$. An error message is triggered if the slenderness exceeds $L/r > 50$, indicating that the element is too slender. To address this, users are advised to modify the density or cross-section of the structure. Here, r represents the gyration radius, which is the square root of the moment of inertia (I) divided by the effective area (A) of the TPMS type, L =buckling length. Additionally, the total weight of each element is calculated and included in the analysis (Table 5.3). Suggested densities based

on FEM analysis and existing literature on TPMS geometries [39,177] are as follows: Gyroid - 10% to 40%, Schwarz - 10% to 40%, Diamond - 10% to 40 %, Split - 20% to 40 %, and Neovius - 15% to 30%.

Table 5.3 Values for density and Young's modulus of chosen materials

Material	Density [kg/m ³]	Young modulus [MPa]
Unfilled plastic	1080	2000
Filled plastic	1500	5000
Concrete	2500	30000
Glass	2500	70000
Aluminium	2700	70000
Steel	7850	210000
Unidirectional FRP	2000	40000

The results of deflections are calculated using Bernoulli's equations for different types of beam configurations and buckling lengths, including simply supported beams, one-side fixed beams, both-side fixed beams, and cantilever beams. The interface of the calculator for computing multilayered beam and plate elements utilizing the TPMS core is illustrated in Figure 5.7. Full design process flow is shown in Figure 5.8.

The software interface includes the following input fields and results:

- TPMS: Gyroid
- TPMS size: 100 mm
- Relative density: 20 %
- Material: 3D printed plastic
- Static system: Simply supported beam
- Beam length: 2700 mm
- Beam width: 1000 mm
- Beam height: 200 mm
- Top flange: 2 mm
- Material top flange: Glass
- Bottom flange: 1 mm
- Material bottom flange: Unidirectional FRP
- Uniform design load $E_d = 5$ kN/m
- *Auto-calculation of self-weight

Results displayed in the calculator:

```

deflection = L / 1029.8192
deflection = 2.6218 mm
deflection ≤ L/250

Material mass summary:
3D printed plastic: 108.00 kg
Glass: 13.50 kg
Unidirectional FRP: 5.40 kg
    
```

Each TPMS geometry has its anisotropy factor. Gyroid and Split are almost 100% isotropic material while Schwarz, Diamond and Neovius are orthotropic material. The basic TPMS unit is selected as a representative volume element (RVE). According to the generalized Hooke's law, and Lamé constants in stiffness matrix, both elastic modulus and anisotropy properties can be obtained. Using statistical data from FEM analysis polynomial regression curve is used for determination of mechanical properties of each TPMS type. Analytical expressions for the effective bending stiffness of multilayered composite beams with an arbitrary number of layers and material selection are used.

Figure 5.7 Software interface

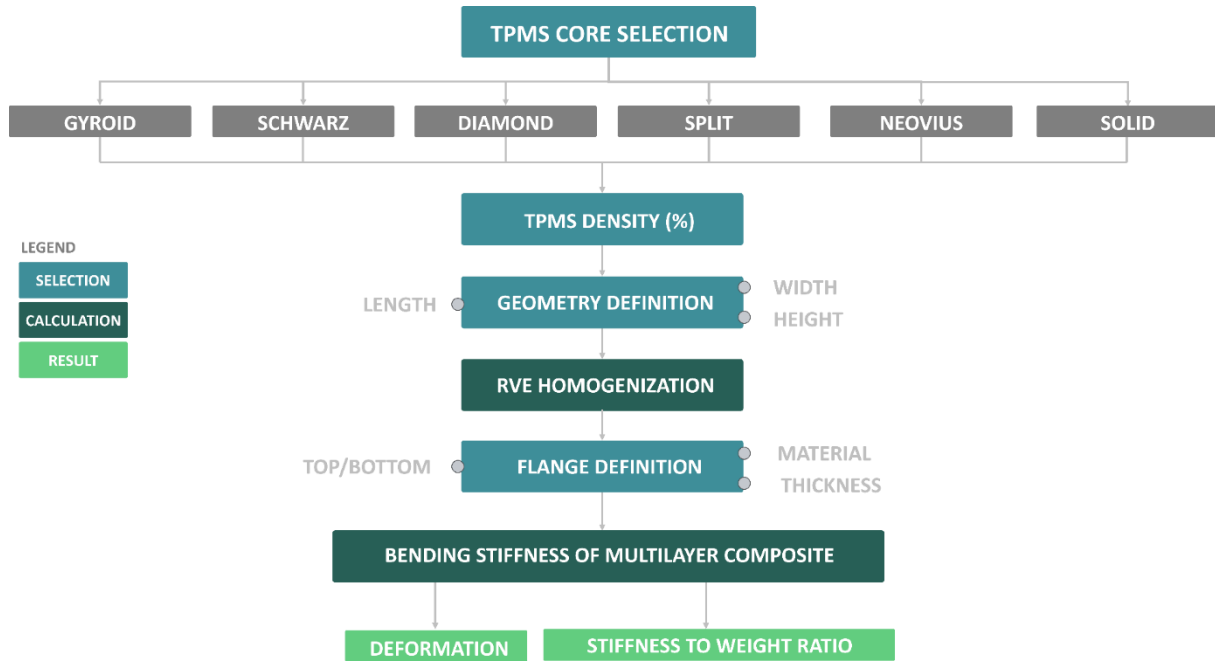


Figure 5.8 Design flowchart

The results of the multilayer composite analysis using different TPMS infill types and various thickness and material combinations for the flanges will be presented. The results, obtained through the calculation algorithm specifically designed for composites with TPMS infill, will be compared with the results from FEM analysis. Graphical representations and tables will showcase the findings, demonstrating a strong correlation and good overlap between the results obtained using the calculation algorithm and the FEM analysis for the evaluated composite structures. The graphical representation of TPMS is determined by the size of the mesh, which is an integer value indicating the resolution. In the case of a cube with a size of 100 mm and a certain resolution, the TPMS geometry can be represented in an implicit form that refers to a certain type of minimal surface in three-dimensional Euclidean space that maintains its shape when translated by a rank-3 lattice.

The FEA was executed using nTopology software. Parametric design methodologies were employed to define the geometries for the top and bottom flanges, as well as the bounding boxes for the core. The TPMS structure was also parametrically defined using mathematically defined equations for unit cells, and a rectangular lattice definition was employed to achieve a periodic multiplication of these units. Following the precise geometry definitions, meshing was carried out, contingent upon the TPMS wall thickness. Specifically, a Gyroid structure with a density of 15% and a mesh size of 5 mm was utilized, resulting in a mesh with over 1 million faces. Boundary conditions were established, wherein line displacement restraints were applied, and

a pressure equivalent to 5 kN/m^2 plus self-weight was defined on the top face of the top flange to simulate loading conditions.

In the next example, Figure 5.9 shows a beam with a length of 1 m and a Diamond infill with an external cross-sectional dimension of $10 \text{ cm} \times 20 \text{ cm}$ and an additional glass flange modelled as fully constrained to infill. All materials are defined as unfilled 3D printed plastic. The beam is subjected to a uniform load of 5 kN/m and its self-weight. The results demonstrate a 2.5% difference in deflection between the FEM results and those obtained through the proposed algorithm.

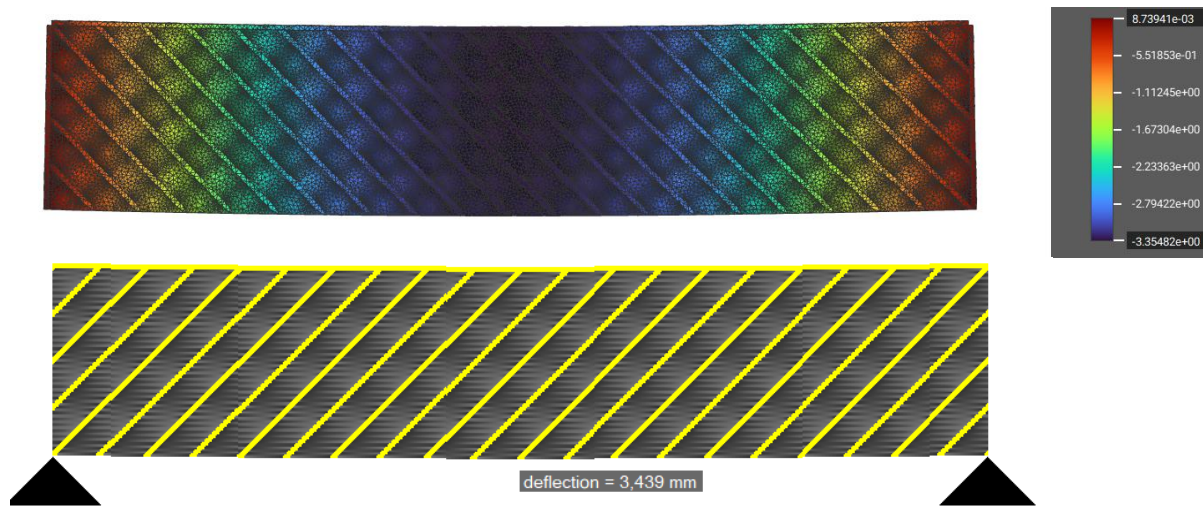


Figure 5.9 Comparison of results from FEM analysis and novel application for composite beams with TPMS infill

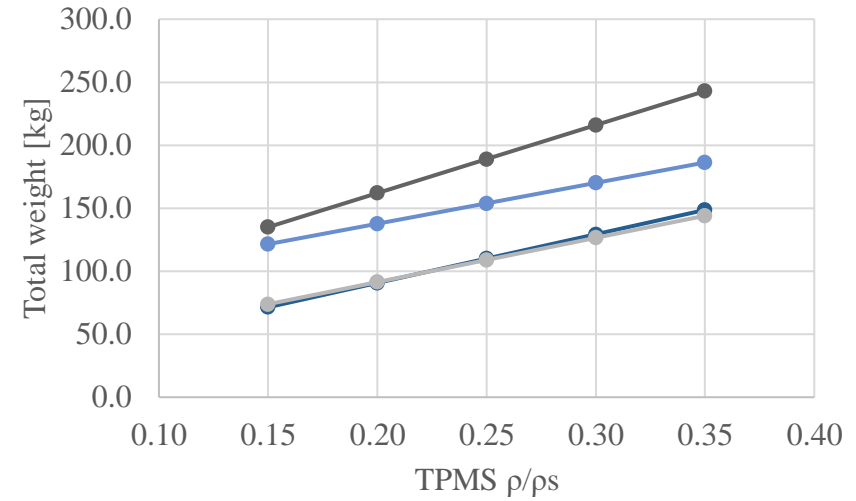
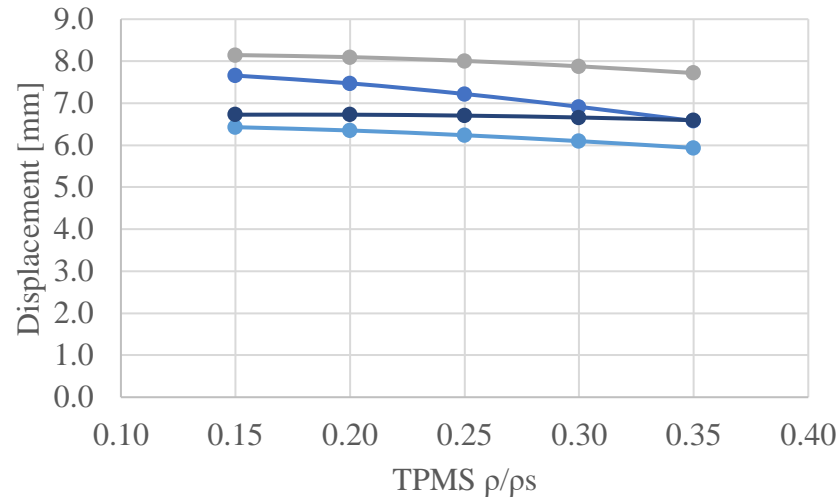
A more detailed analysis was conducted for a plate dimensions measuring $2.7 \times 1.0 \times 0.2 \text{ m}$, considering four different TPMS and different densities as presented in Table 5.4.

- a) Model 1 comprises of an unfilled 3D printed plastic composite with a total height of 200 mm and 10 mm top and bottom flanges.
- b) Model 2 consists of a set of filled 3D printed plastic TPMS with a total height of 110 mm, accompanied by 1 mm glass sheets that are additionally glued to the infill.
- c) Model 3 is composed of a 120 mm unfilled 3D printed TPMS, with a 10 mm concrete top layer and a 1 mm unidirectional GFRP (Glass Fiber Reinforced Polymer) component.
- d) Model 4 is constructed using a 100 mm filled 3D printed plastic TPMS, with top and bottom 0.5 mm steel sheets.

Table 5.4 Comparison of results for different TPMS, density of TPMS infill and for 4 models

Gyroid													
TPMS ρ/ρ_s	0.15		0.2		0.25		0.3		0.35		0.4		
Model	m [kg]	δ [mm]	m [kg]	δ [mm]	m [kg]	δ [mm]	m [kg]	δ [mm]	m [kg]	δ [mm]	m [kg]	δ [mm]	
1	135.0	7.4	162.0	6.9	189.0	6.7	216.0	6.4	243.0	6.1	270.0	5.8	
2	71.4	7.9	90.7	7.8	110.0	7.7	129.3	7.6	148.6	7.4	167.9	7.3	
3	121.5	6.2	137.7	6.1	153.9	6.0	170.1	5.8	186.3	5.7	202.5	5.5	
4	73.9	6.6	91.4	6.6	109.0	6.5	126.5	6.5	144.1	6.4	161.6	6.4	
Schwarz													
TPMS ρ/ρ_s	0.15		0.2		0.25		0.3		0.35		0.4		
Model	m [kg]	δ [mm]	m [kg]	δ [mm]	m [kg]	δ [mm]	m [kg]	δ [mm]	m [kg]	δ [mm]	m [kg]	δ [mm]	
1	135.0	7.7	162.0	7.5	189.0	7.2	216.0	6.9	243.0	6.6	270.0	6.2	
2	71.4	8.1	90.7	8.1	110.0	8.0	129.3	7.9	148.6	7.7	167.9	7.5	
3	121.5	6.4	137.7	6.4	153.9	6.2	170.1	6.1	186.3	5.9	202.5	5.8	
4	73.9	6.7	91.4	6.7	109.0	6.7	126.5	6.7	144.1	6.6	161.6	6.5	
Diamond													
TPMS ρ/ρ_s	0.15		0.2		0.25		0.3		0.35		0.4		
Model	m [kg]	δ [mm]	m [kg]	δ [mm]	m [kg]	δ [mm]	m [kg]	δ [mm]	m [kg]	δ [mm]	m [kg]	δ [mm]	
1	135.0	6.8	162.0	6.4	189.0	6.1	216.0	5.8	243.0	5.5	270.0	5.3	
2	71.4	7.7	90.7	7.5	110.0	7.4	129.3	7.2	148.6	7.1	167.9	6.9	
3	121.5	6.0	137.7	5.8	153.9	5.7	170.1	5.5	186.3	5.4	202.5	5.3	
4	73.9	6.5	91.4	6.4	109.0	6.4	126.5	6.3	144.1	6.2	161.6	6.1	
Split													
TPMS ρ/ρ_s	0.15		0.2		0.25		0.3		0.35		0.4		
Model	m [kg]	δ [mm]	m [kg]	δ [mm]	m [kg]	δ [mm]	m [kg]	δ [mm]	m [kg]	δ [mm]	m [kg]	δ [mm]	
1	135.0	7.0	162.0	6.7	189.0	6.4	216.0	6.0	243.0	5.7	270.0	5.3	
2	71.4	7.8	90.7	7.7	110.0	7.5	129.3	7.4	148.6	7.2	167.9	7.0	

3	121.5	6.1	137.7	6.0	153.9	5.8	170.1	5.7	186.3	5.5	202.5	5.3
4	73.9	6.5	91.4	6.5	109.0	6.4	126.5	6.4	144.1	6.3	161.6	6.2
Neovius												
TPMS ρ/ρ_s	0.15		0.2		0.25		0.3		0.35		0.4	
Model	m [kg]	δ [mm]	m [kg]	δ [mm]	m [kg]	δ [mm]	m [kg]	δ [mm]	m [kg]	δ [mm]	m [kg]	δ [mm]
1	135.0	6.7	162.0	6.4	189.0	6.0	216.0	5.7	243.0	5.4	270.0	5.1
2	71.4	7.7	90.7	7.5	110.0	7.3	129.3	7.1	148.6	6.9	167.9	6.7
3	121.5	6.0	137.7	5.8	153.9	5.6	170.1	5.5	186.3	5.3	202.5	5.1
4	73.9	6.5	91.4	6.4	109.0	6.3	126.5	6.2	144.1	6.2	161.6	6.1



● Model 1 ● Model 2 ● Model 3 ● Model 4

● Model 1 ● Model 2 ● Model 3 ● Model 4

Figure 5.10 left: graph displacement to TPMS infill density ratio; right: Total weight of structural system vs. TPMS infill density ratio

All models from Table 5.4 were evaluated for TPMS types Gyroid, Schwarz, Diamond, Split, and Neovius, considering six different TPMS densities: 15%, 20%, 25%, 30%, 35%, and 40% (Figure 5.10). According to the results Model 2 exhibits the lowest stiffness behaviour while maintaining a satisfactory deformation limit. It also has the lowest weight among the models. On the other hand, fully 3D printed Model 1 has the highest weight and an average stiffness compared to the other models. Model 3 demonstrates the highest stiffness but weighs 40% more than Model 2 and Model 4.

In the examples illustrated in Figure 5.11 a composite plate measuring $2.7 \times 1.0 \times 0.2$ m, and employing a TPMS Gyroid infill configuration, was compared to FEM analysis across four distinct models. Both the top and bottom flanges were modelled as tie constrained to the TPMS lattice. Comparable stiffness was obtained while varying the weight of the material. This entailed using different core heights (ranging from 100-200 mm) and top and bottom flanges made of glass, steel, concrete, thin steel, or 3D printed plastic. The infill material for the Gyroid was selected as either 3D printed filled (reinforced with glass fibre) or unfilled plastic. Difference in weight, 135 kg (Model 1), 71.42 kg (Model 2), 121.5 kg (Model 3), and 73.85 kg (Model 4), representing an almost 50% difference between Model 2 and Model 1 for the same stiffness. The potential for optimization of the strength-to-weight ratio lies in combining varied flange materials with the 3D printed core. The disparity in deformation obtained between the FEM model and the proposed algorithm is less than 2% for Model 2 and Model 4, while for Model 1 it is 8%, and for Model 3 it is 11%. This indicates that the quick estimation algorithm serves as an effective initialization for dimensions, materials, and structure, preparing the system for a detailed FEM analysis.

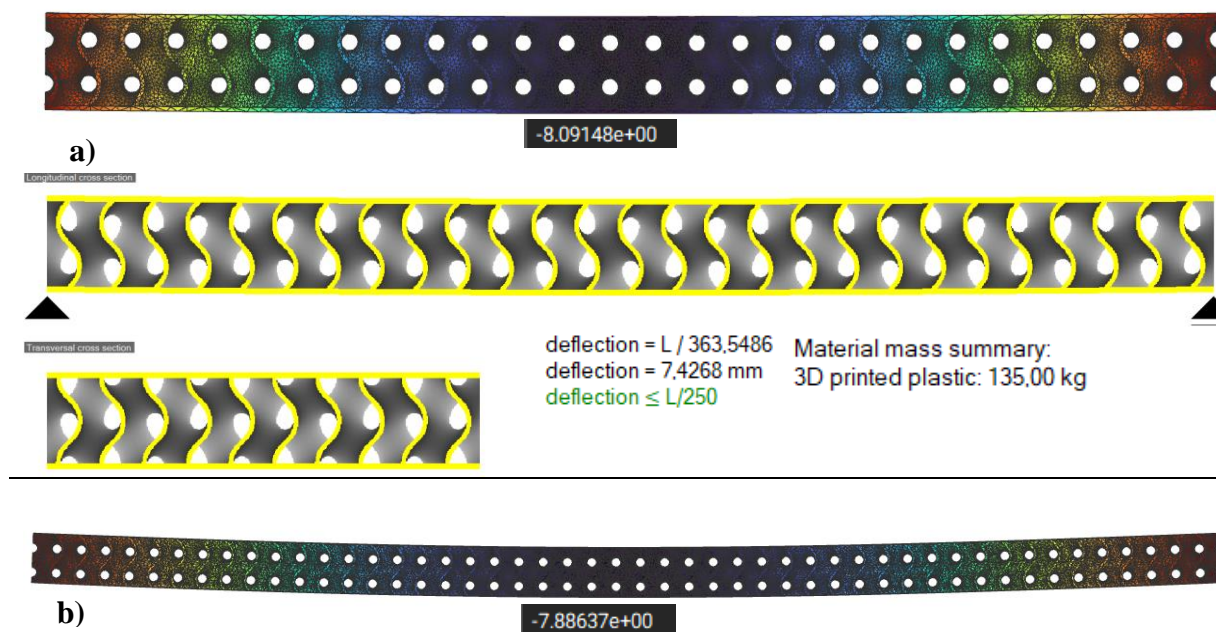




Figure 5.11 Optimised composite plate with 15% gyroid core - FEM and results from quick estimation algorithm: a) 200 mm core and top and bottom 10 mm flange from 3D printed unfilled plastic; b) 110 mm core from 3D printed filled plastic and 1 mm top and bottom glass flange; c) 120 mm core from 3D printed unfilled plastic, 10 mm top concrete and 1 mm bottom FRP flange; d) 100 mm core from 3D printed filled plastic and 0.5 mm top and bottom steel flange

The results suggest that the inclusion of thin metal, glass, or FRP sheets through gluing or welding to the 3D printed infill core can enhance the overall performance of the composite structure. This approach demonstrates potential applicability in various architectural structures, including glass facades, bridge decks, ceilings, wall panels, beams, and columns.

5.3 Thermo-mechanical analysis

Material Characterization and Qualification (MCQ) tool driven material model in the GENOA software [178] allows the definition of various parameters to characterize the behaviour of the composite. These parameters include the properties of the fibres and matrix, the volume fraction of the fibres and voids, the geometry of the fibres, the presence of manufacturing defects, and the criteria for failure. By inputting these parameters, the MCQ model provides valuable results, such as the properties of aligned plies, orientations through

thickness that are reversed, and the ability to account for nonlinear material behaviour. Upon completion of the full FEA and detection of damage in the composite, it is recommended that the fibre/matrix properties be updated.

Thermomechanical analysis is an important tool to understand the behaviour of structures during 3D printing. This paper presents a step-by-step process for performing thermomechanical analysis in 3D printing, including creating GCode, converting GCode to CSV format, creating an input file, performing thermal (TMg) analysis, and visualizing and post-processing the results.

The issue of air gaps in polymer 3D printing poses significant challenges in achieving optimal print quality and structural integrity. Air gaps refer to voids or empty spaces within the printed object, which can compromise its strength, functionality, and overall aesthetics. To identify potential air gaps in the structure, path coverage analysis was conducted. Path coverage analysis refers to the assessment of the print path or the GCode to identify the air gaps formed between the exterior contours and the infill. If there are air gaps predicted by path coverage, this indicated potential voids in the structure. Since path coverage analysis is mesh-dependent, engineers can change the mesh density or element type in areas of poor path coverage. Increasing the mesh density can improve the identification of potential voids and improve the accuracy of the FEM analysis.

In analysing the behaviour of 3D printed structures, a mapping procedure is used to combine the results of thermal analysis from 3D printing with the mesh from FEM analysis. This map is then used to create a combined void file in explicit format that contains information about the location and size of each void in the structure, as well as the temperature.

The mechanical analysis simulates the 3D printing process by applying the same conditions and thermal history as during the printing process. The degraded input file is used to model the presence of voids and their effects on the mechanical properties of the element.

The results of the mechanical analysis are stored in an output database (ODB) file format. The ODB file contains information about the deformation, stress, strain, and temperature.

The ODB file is then used to define the initial conditions for the stress analysis in service. In-service load analysis simulates the behaviour of the structure under the real loading conditions it will be subjected to during its lifetime.

Comparing the predicted load-displacement and stress-strain curves with experimental data from the machine test can help validate the accuracy of the analysis and identify areas where the model may need improvement. The iterative process of analysis and validation can

help engineers optimize the design of 3D-printed structures for better performance and reliability.

The steps in the analysis and optimization process to identify the effects of defects, voids, creep, manufacturing anomalies, and environmental conditions in 3D printing a TPMS 'unit' and bridge deck are as follows:

- Determine the key material properties and process parameters that affect the quality and performance of the design.
- Perform thermal-structural analysis to predict residual stress, distortion, heat-affected zone, delamination, and other potential problems resulting from the combined thermal and mechanical effects: (a) dogbone XY tension test; b) Bridge deck bending test; c) support zone compression test.
- Progressive failure/fracture analysis: use progressive failure analysis techniques to predict the type, location, and percentage contribution of each failure mode to fracture. This analysis helps identify potential areas of damage or failure and evaluate the structural integrity of printed components.
- Manufacturing optimization using computer algorithms to identify the ideal material combination, material distribution, and print direction orientation for optimal performance and structural integrity and export the optimized design parameters to software such as Rhinoceros and nTopology for further refinement and iteration. Full design process methodology is presented in Figure 5.12.

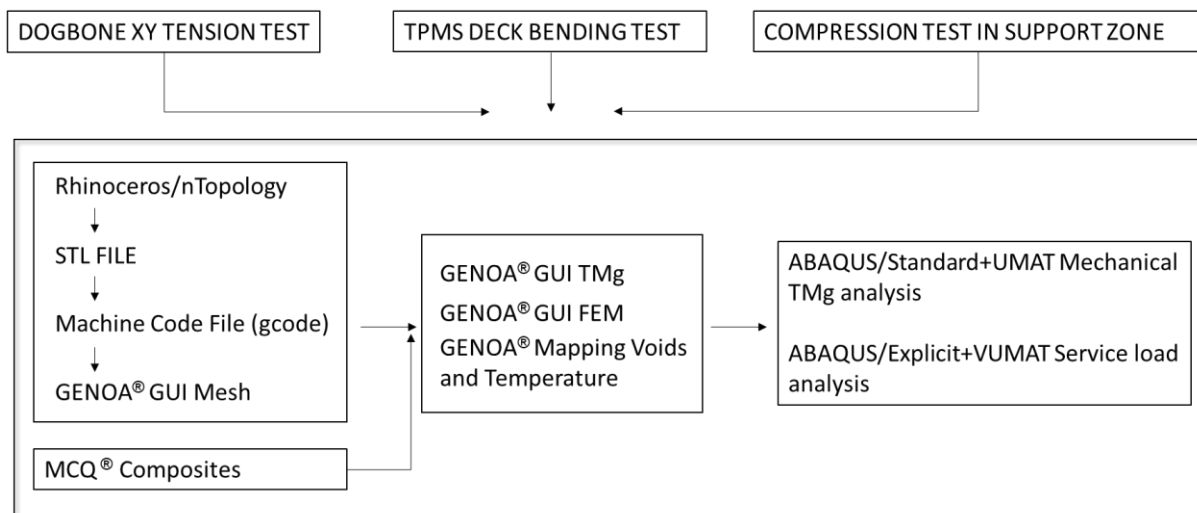


Figure 5.12 Flowchart of simulation approach

A digital engineering approach presented in this work enhances additive manufacturing by creating temperature-dependent material models, simulating tool paths, predicting cracks

and failure modes [179]. The standardized numerical model [88] includes building a geometry, meshing, slicing, assigning local material's references and running static or dynamic analysis. Additional parameters are included in this virtual simulation method, which is presented in this paper. Material card from the filament and the geometry from the G-code serve as input parameters. Thermal, mechanical, and service analysis are then carried out.

Virtual simulation analyses are used to predict material properties with minimal or no reliance on actual laboratory tests. The traditional method involves conducting laboratory tests to gather data on material behaviour and properties, which are then used to calibrate the numerical models. However, advancements in virtual simulation techniques and material modelling have made it possible to predict material properties and behaviour accurately without extensive laboratory testing. This approach reduces costs, time, and resource requirements while still providing reliable material calibration. The choice between these two approaches depends on factors such as the availability of test data, accuracy requirements, cost constraints, and the level of confidence in virtual simulation predictions. Virtual simulations involve testing the filament's material, which serves as an input parameter. Second input parameter is model geometry from the G-code. It is important to mention that predicting fractures in polymers is generally challenging, especially in the case of 3D printed polymers. The imperfections in the filament production, along with the imperfections in the printer's path, can be observed at both microscopic and macroscopic levels. For this reason, photos from Scanning Electron Microscopy (SEM) are used for the detailed visualization of the specimen's topography at a very fine scale.

To perform virtual simulations, tensile tests were also carried out on the specimens of the ASA filament. The specimen with a diameter of 1.75 mm was wound onto the metal spool at both ends in the testing machine, with a spool distance of 180 mm (Figure 5.13). Three specimens were tested under displacement rate of 0.3 mm/min. Although three specimens are insufficient for accurately drawing a representative mean curve, the results will be presented based on this limited number of specimens.

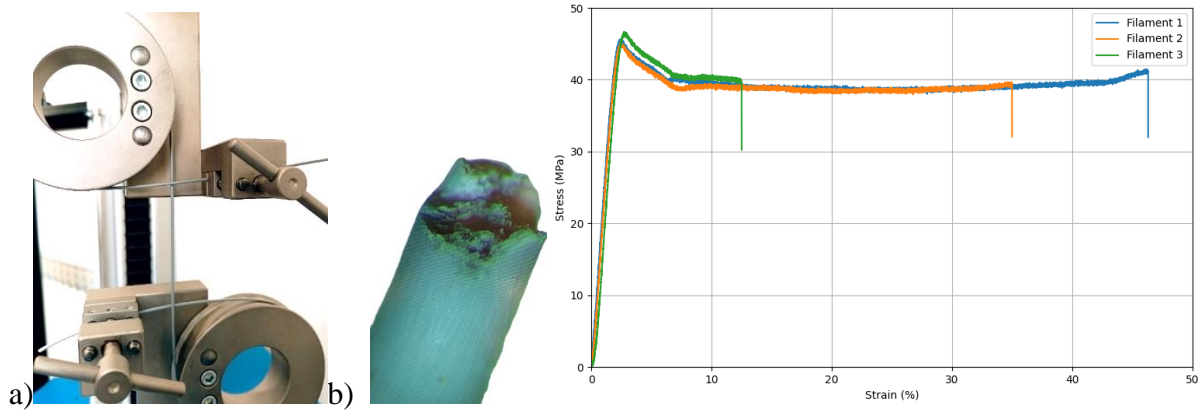


Figure 5.13: a) ASA filament tension test setup; b) Microscopic view of the fracture zone; c) stress-strain relationship obtained from the tensile test performed on the ASA filament specimen

3D printing has many applications, including the production of functional parts [138] and use as moulds [157]. The study by Talagani [4] shows a simulation method for AM used in the numerical simulation of a full-size 3D printed car. The MCQ for composite material is an innovative methodology that combines composite nano- and macromechanics. In the MCQ model, the mechanical properties, the volume fraction of voids, and the failure criteria were defined. As a result, nonlinear material behaviour was provided.

In the analysis of 3D printing, a mapping procedure is employed to combine the results of thermal analysis and FEA, generating files that contain information on void location, size, and temperature. FEA includes creating a regular rectangular mesh using a G-code from path generation software. The tool path is drawn through the background grid, and the elements for the FEM model are activated accordingly. Mechanical analysis is conducted to simulate the 3D printing process, accounting for the presence of voids and their effects on mechanical properties. During the dynamic service analysis, thermal profiles, deformations, and stresses are assigned to each finite element. The software programs for thermo-mechanical analysis utilize GENOA + ABAQUS/Standard + UMAT subroutine and for service analysis use GENOA + ABAQUS/Explicit + VUMAT subroutine. A full flowchart is presented in Figure 5.14.

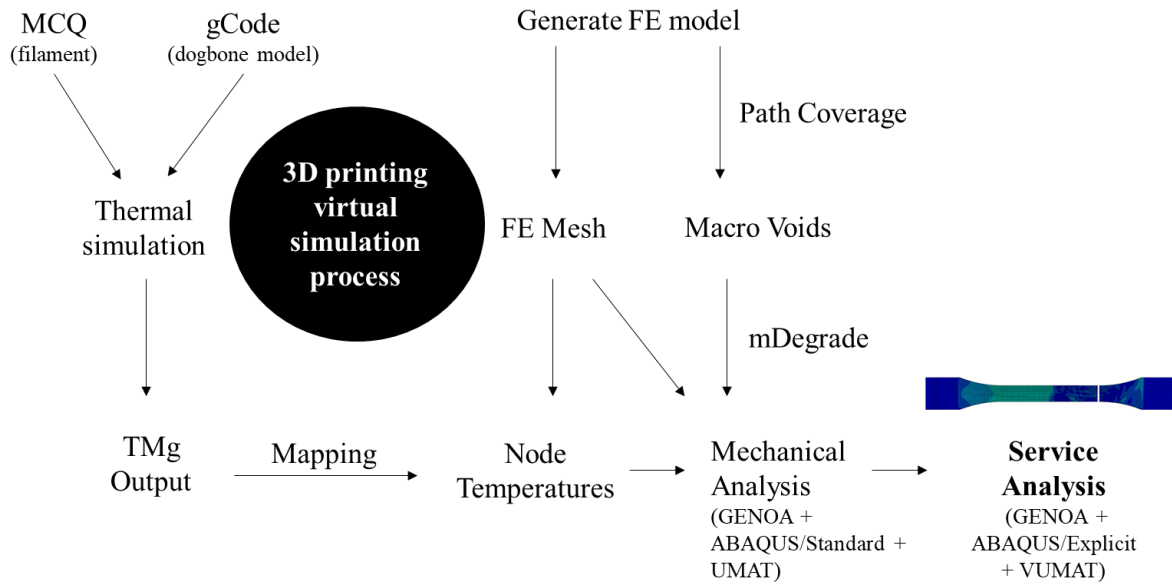


Figure 5.14 Virtual simulation flowchart

The results derived from thermomechanical and fracture analyses using the GENOA 3DP software [180] are showcased for the printing directions XY and ZX, introducing the possibility of a fully numerical simulation from the 3D printing process to fracture analysis, as shown in Figure 5.15.

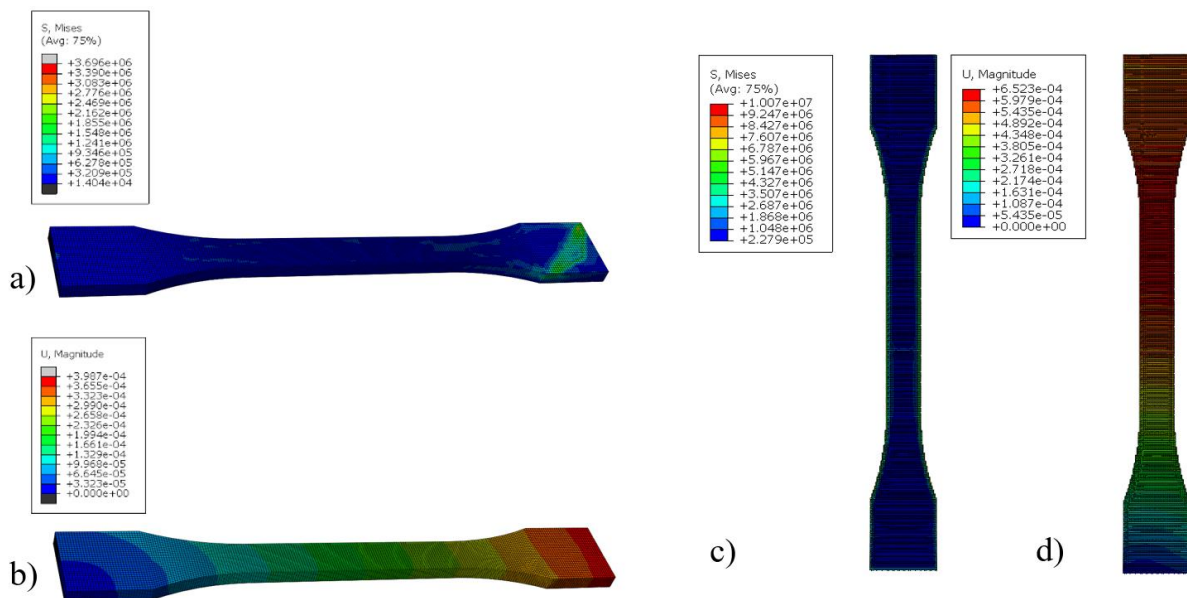


Figure 5.15 Mechanical analysis from Abaqus UMAT: a) Stress – von Mises XY print direction; b) Magnitude of displacement XY print direction; c) Stress – von Mises ZX print direction; d) Magnitude of displacement ZX print direction.

In Abaqus, explicit dynamic analysis was employed for the tensile test, with boundary conditions applied: one side had a restrained node set, while the other side's node set was subjected to uniaxial loading in the X-direction (Figure 5.16). Strain concentration and potential fracture zones, corresponding to the real tested specimens, are highlighted in Figure 5.17. Furthermore, Figure 5.18a demonstrates brittleness observed in the XY print direction, showing a slightly rougher cutting plane and some additional material tearing at the edge. In Figure 5.18b, a distinct brittle fracture is evident due to the perpendicular orientation of the layers to the load direction in the ZX print direction, with the fracture strictly following the cutting line where two layers meet. Figure 5.19 and Figure 5.20 present a comparison between the virtual simulations conducted for the XY and ZX print direction and the actual laboratory tests. The results demonstrate a strong correlation between the real testing and virtual simulation tests. Specifically, for the XY print direction, the average maximum stress from three specimens is 29.15 MPa, while the virtual simulations indicate 28.68 MPa, reflecting an accuracy of 98.39%. On the other hand, the results from the laboratory-tested specimens in the ZX direction exhibit significant dispersion. Despite this variance, the average from the laboratory test yields 21.24 MPa, whereas the virtual simulation provides 22.14 MPa, indicating a notable 95.93% overlap. The slope of the linear part closely resembles that of the ASA 3-2 specimen, although the strain has a 30% error for all three specimens in ZX direction.

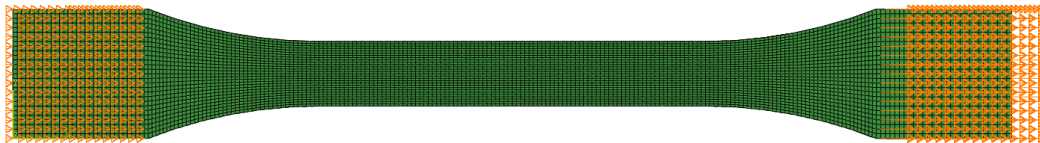


Figure 5.16 Boundary conditions for the tensile test simulation

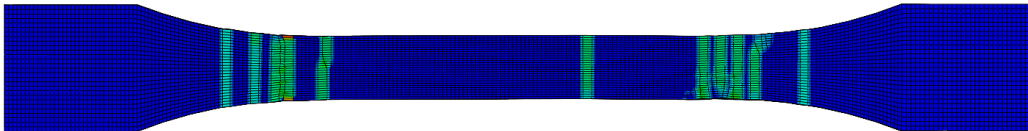


Figure 5.17 Strain concentration and potential fracture zones

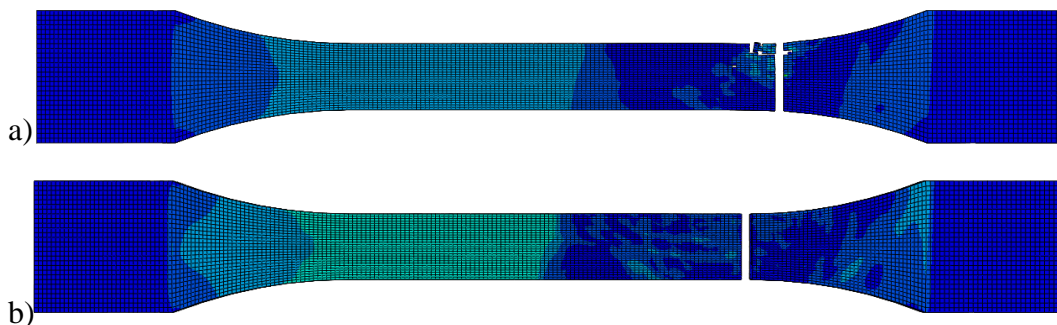


Figure 5.18 Dogbone brittle fracture: a) ASA XY print direction; b) ASA XZ print direction

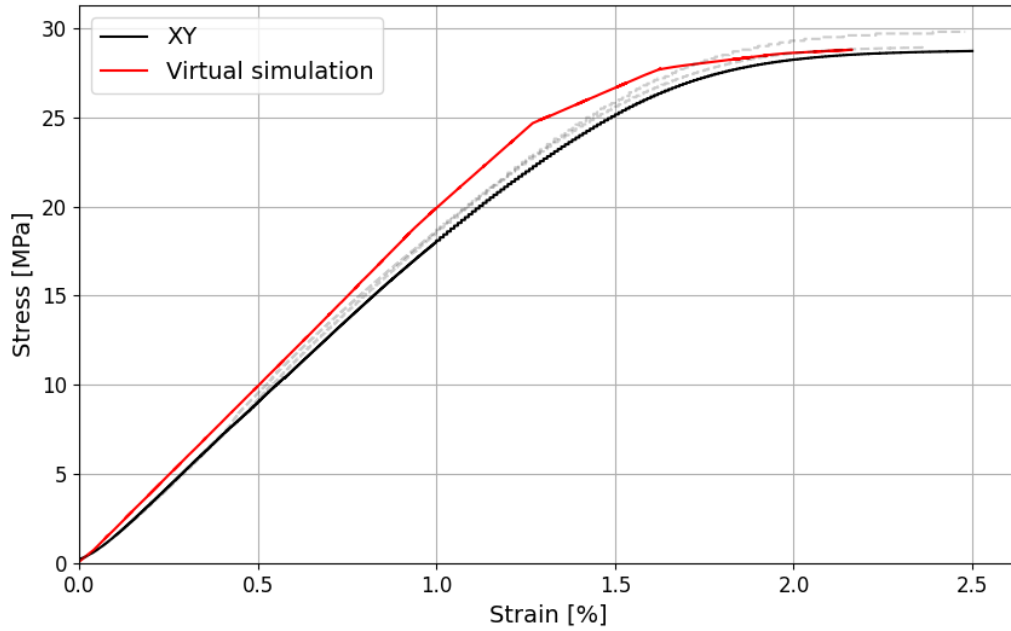


Figure 5.19 Comparison of Virtual Simulation Dynamic Analysis with the 3D printed tensile test in the XY print direction

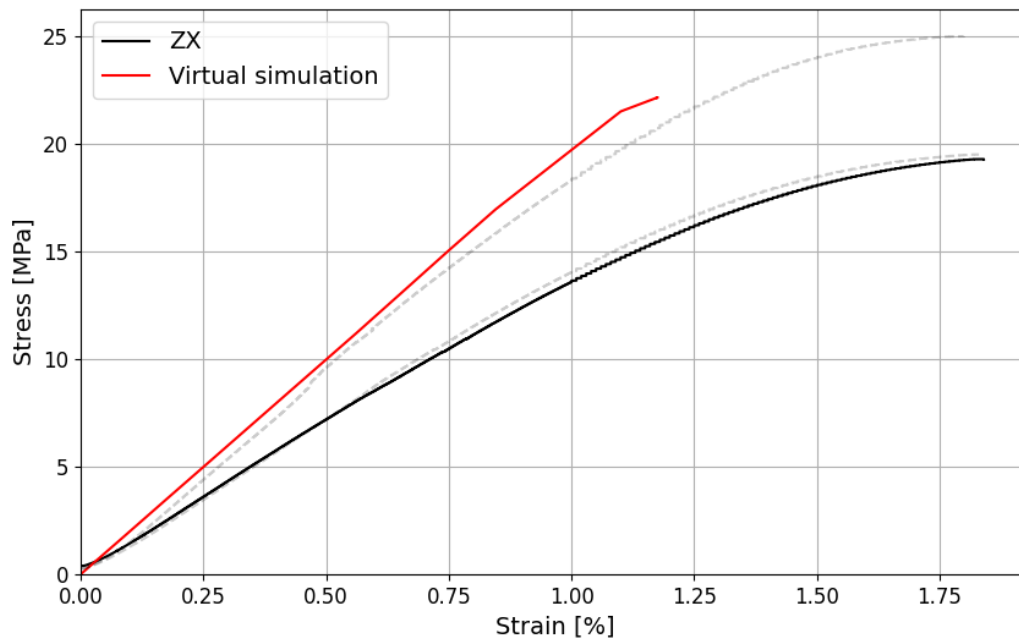


Figure 5.20 Comparison of Virtual Simulation Dynamic Analysis with the 3D printed tensile test in the ZX print direction

6 SPECIMEN DESIGN AND EXPERIMENTAL CAMPAIGN

6.1 TPMS units

The unit cells of five different TPMS structures (Gyroid, Schwarz, Diamond, Split and Neovius) were generated using a uniform parametric design based on a mathematical algorithm and manufactured using the FDM 3D printing process. The preparation for the 3D printing of the STL file of the mesh was conducted using GrabCAD slicer. Printing was carried out on the Stratasys F123 machine using grey ASA material with a bead width of 0.4 mm, a layer height of 0.15 mm and 100% infill. After completion of the printing process, a visual inspection of the samples revealed no issues. Deviations in the 3D cellular lattices, such as size effect problem [181] and the staircase effect, are minimized with a layer height of 0.15 mm, but remain visible. Due to the three-dimensionality of all geometries, there are overhangs that require the use of additional support material. These supports, polymer parts that are printed concurrently with the structure, provide essential support for the layers that would otherwise be deposited in empty spaces [170]. A secondary material was employed for the supports, which was subsequently removed by post-processing. The support material was also supplied by Stratasys Inc.

Compression tests were performed on TPMS units to determine the properties at failure. A cellular TPMS structure, defined as the minimal surface within a specified cube of dimensions 50×50×50 mm was employed. As already mentioned, the relative density of a TPMS element can be expressed as 1-porosity or the ratio of solid volume to the total volume of solid and air. Due to differences in surface area of the various types, a consistent density/mass ratio was achieved by adjusting the wall thicknesses (Table 6.1). For each TPMS type, laboratory tests were conducted with a relative density of 20% (Figure 6.1) and 40% (Figure 6.2).

Table 6.1 Properties of the 3D-printed TPMS samples

TPMS type	Relative density (%)	Wall thickness (mm)	Cross section area (mm ²)	Mass (g)
Gyroid_20	20	4.8	390	25.049
Gyroid_40	40	9.6	811	50.404
Schwarz_20	20	2.8	373	25.901
Schwarz_40	40	5.6	768	51.875
Diamond_20	20	4.0	368	25.046
Diamond_40	40	8.0	759	50.227
Split_20	20	3.6	438	25.466
Split_40	40	7.2	867	51.095
Neovius_20	20	0.8	402	24.443
Neovius_40	40	1.7	1052	50.706

All samples were constructed in an upright orientation and subjected to compression in the direction of construction. The units were loaded in compression using a universal static testing machine (Zwick/Roell Z600E) with a load cell capacity of ± 50 kN. The compressive load was applied evenly to the top surface of the unit using a hard and rigid plate. During loading, both the applied force and the vertical deflection were measured. All TPMS units were tested to failure. A strain rate of 1 mm/min was used under displacement control. The compressive strength of each sample was determined by dividing the maximum applied force by the total cross-sectional area.

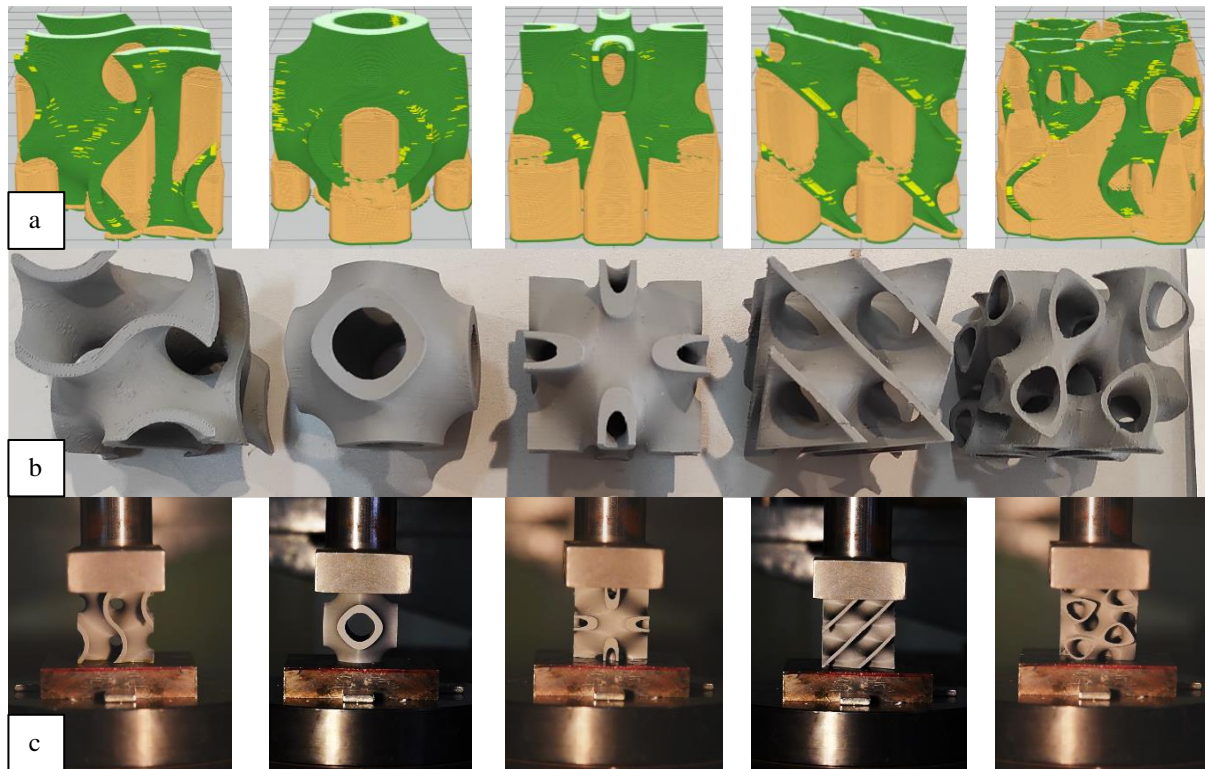


Figure 6.1 Five TPMS units (Gyroid, Schwarz, Neovius, Diamond and Split from left to right) with 20% relative density: a) Model preparation; b) 3D-printed part after removal of support material; c) laboratory test setup.

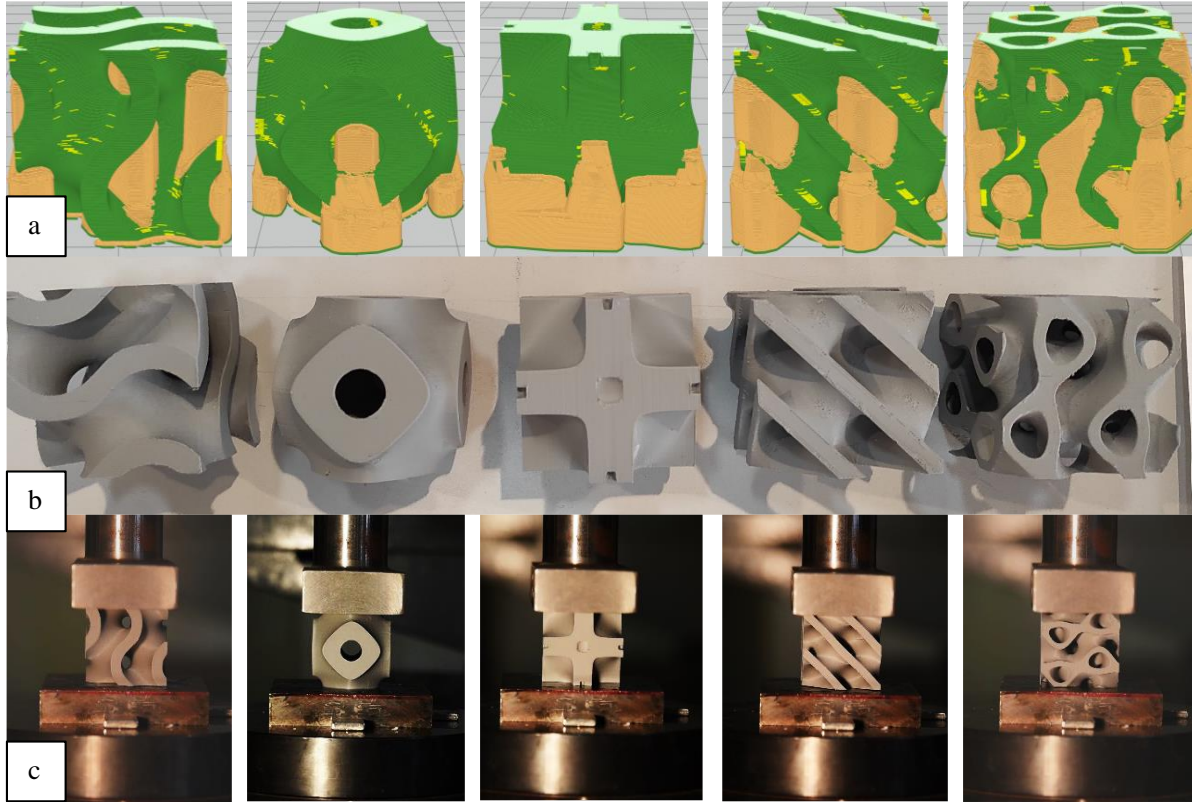


Figure 6.2 Five TPMS units (Gyroid, Schwarz, Neovius, Diamond and Split from left to right) with 40% relative density: a) Model preparation; b) 3D-printed part after removal of support material; c) laboratory test setup.

6.2 Composite sandwich panel with tempered glass face sheets

The stiffness of glass sheets is calculated for \bar{E}_f of 70 GPa, thickness t is 3 mm, and B and L represent the width and length, respectively, matching the dimensions of the sandwich panel at 300 mm and 810 mm. The stiffness of a standalone non-uniform Gyroid core subjected to uniaxial tension can be expressed [182] in Eq. (6.1):

$$K_c = \bar{E}_c \times \frac{(h - 2t)B}{L} = E_s \times g(r, l, \theta) \times \frac{(h - 2t)B}{L} \quad (6.1)$$

Here, \bar{E}_c represents the effective Young's modulus of the Gyroid core, and r, l , and θ stands for radius, length, and inclination angle of the Gyroid unit cell. The ratio of the stiffness K_f of the flange to the stiffness K_c of the core ranges from 45 to 120 which ensures that the face sheets effectively control the deformation of the core (Eq. (6.2)).

$$\frac{K_f}{K_c} = \frac{E_f \times \frac{tB}{L}}{\bar{E}_c \times \frac{(h - 2t)B}{L}} = \frac{\bar{E}_f}{\bar{E}_c} \frac{t}{(h - 2t)} \quad (6.2)$$

The three-point bending test was carried out using a Shimadzu AGS-X 100 kN universal testing machine in accordance with ASTM: C393 standards for flexural tests on sandwich structures. The specimen dimensions included a total length of 810 mm along the L-direction, a width of 300 mm in the W-direction, and a loading span of 740 mm between the supports. The supporting cylinders had diameters of 35 mm and the steel circular hollow section with 40 mm diameter was used as the loading cylinder. The specific influence of the cylinders was not investigated for the current model. To avoid direct contact of cylinders with glass component, rubber was placed at the contact zones. The accuracy of traverse speed is determined by measuring the traverse displacement over a specific time period at a constant speed of 2 mm/min using the TRAPEZIUM X software package (Figure 6.3).

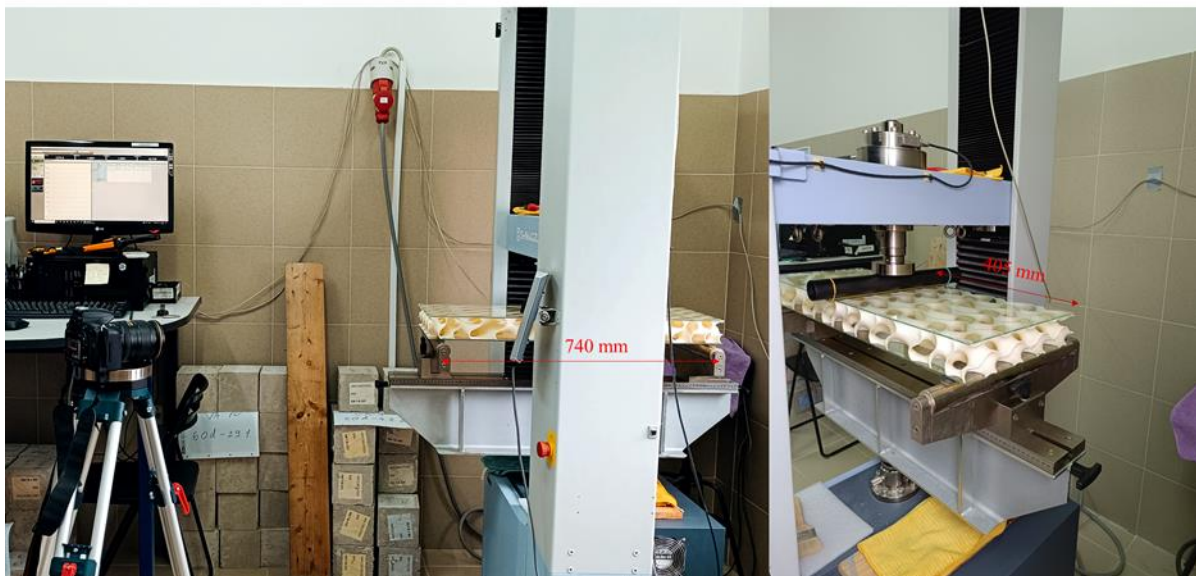
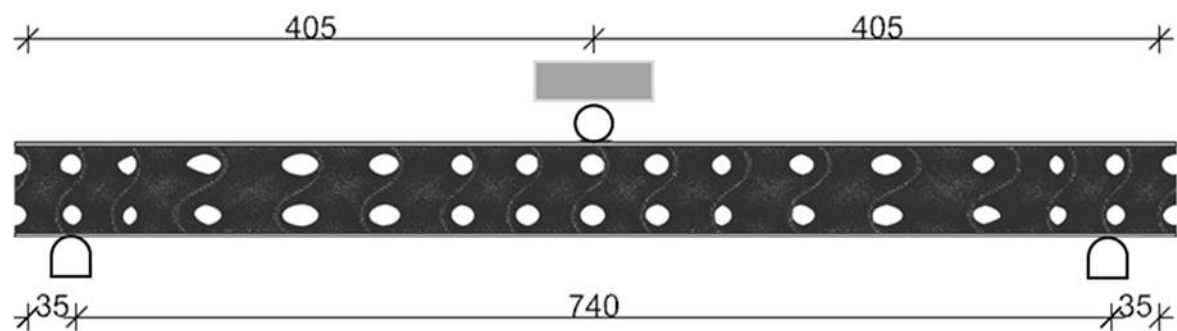


Figure 6.3 Three-point bending test – setup

6.3 Composite sandwich panel with GFRP face sheets

The top and bottom face sheet laminates were manufactured using unidirectional glass fibres weighing 430 g/m^2 produced by GIVIDI FABRIC S.R.L. The epoxy resin, Biresin® CR83-2, developed by Sika Technology AG, was used. Laminates with $[90/0]_s$ glass fibre orientation were produced via vacuum infusion and allowed to cure at room temperature for 24

hours. The same resin was used as the adhesive for bonding the core to the top and bottom laminates.

For the beam element measuring $440 \times 60 \times 60$ mm, a total of four-layer laminates were produced, resulting in a total thickness of 1.2 mm of top and bottom face sheets. Additionally, for the arch bridge, five-layer laminates were manufactured with a total thickness of 1.5 mm. Preliminary calculations for the multilayer composite were performed to ensure that the skin faces possessed sufficient stiffness to control the deformation of the core. The material properties of the laminates previously investigated in [183] were used.

The 3D printed specimens' experiments can be divided into three groups: first, the bending beam test of the standalone core simply supported beam measuring $440 \times 60 \times 60$ mm; second, the bending beam test of composite specimens consisting of a 3D printed core $440 \times 60 \times 60$ mm with top and bottom face sheets made from 1.2 mm thick GFRP sheets; and finally, the arch bridge composite with a 3D printed core and 1.5 mm thick GFRP face sheets.

The relative density of a TPMS element may be articulated as $1 - \text{porosity}$, or the proportion of solid volume to the combined volume of solid and air. To maintain homogeneity throughout the entire cellular structure, the unit size and wall thicknesses remain fixed at 6 mm, ensuring a consistent relative density of 20% across the entire volume.

One sample of core only and two samples of composite sandwich beam $440 \times 60 \times 60$ mm underwent bending tests at a constant displacement rate of 5 mm/min using a 50kN Walter + Bai AG electromechanical machine. Force and strain data were recorded, and DIC captured surface displacement for strain (Figure 6.4).

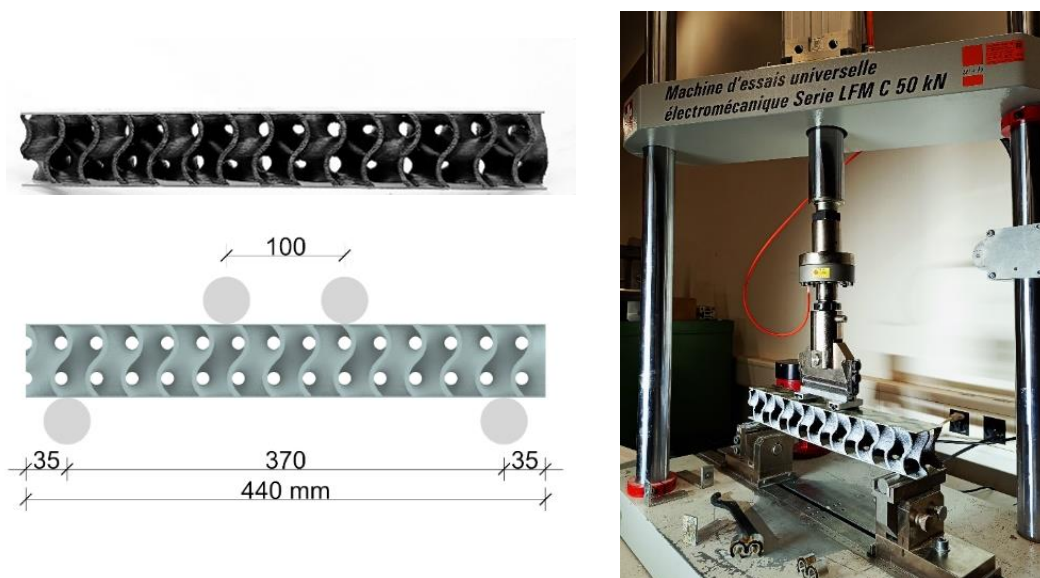


Figure 6.4 4-point bending test of beam samples

Analytical expressions in Eq. (5.10) derived for the equivalent flexural stiffness $(EI)_{eq}$ of multi-layer composite beams, accommodating an arbitrary number of layers and material choices were used.

First, finite element investigation was conducted on a single Gyroid unit measuring $60 \times 60 \times 60$ mm. The effective material properties of one unit were calculated using homogenization analysis [172]. Since the cellular structure is periodic and homogeneous, this Gyroid unit serves as the RVE for the entire structure. Initially, the stiffness matrix was established for six load cases. The perturbation of the volume-averaged stress in each load case contributed to a column of the Hooke's stiffness tensor. Homogenization analysis was performed within the nTopology software, and the resulting stiffness matrix was utilized for the calculation of orthotropic material properties (Table 6.2).

Table 6.2 Mechanical properties obtained from Homogenization Analysis

E11 [MPa]	E22 [MPa]	E33 [MPa]	ν_{12}	ν_{13}	ν_{23}	G12 [MPa]	G13 [MPa]	G23 [MPa]
220.45	220.43	220.45	-0.377	-0.377	-0.377	62.69	62.69	62.69

The process parameters set in the BLADE Slicer Software for the industrial BigRep PRO printer (Figure 6.5), used in large-format additive manufacturing, remain consistent for the bridge arch core structure, as outlined in Table 6.3. This research prioritized constructing a large model with maximum speed, hence employing a 1.0 mm diameter nozzle and a maximum layer height of 0.6 mm. The impact of these parameters on mechanical properties will be discussed in the Results section. Visual inspection post-printing revealed no issues with the samples. Acceptable deviations, such as the size effect problem [181] and the staircase effect, were observed in the 3D cellular lattices at the 0.6 mm layer height, although remaining visible.

Table 6.3 Process parameters for BigRep PRO

Build volume [mm]	1005 x 1005 x 1005
Printing speed [mm/s]	300 mm/s
Layer height [mm]	0.3 and 0.6
Line width [mm]	1.0
Infill angle	45°
Printing direction	XY
Printing temperature [°C]	230
Bed temperature [°C]	60
Duration of print 440×60×60	5 hours 33 minutes
Material consumption [g]	500
Duration of print 900×240×220	1day 23 hours 15 minutes
Material consumption [g]	2076
Support material consumption [g]	1128



Figure 6.5 Bigrep PRO printer built print space of 1005 x 1005 x 1005 mm.

Given the three-dimensional nature of Gyroid geometries, nearly all overhangs required no additional support material except for the arch bottom surface. However, no inside support material within the structure was necessary. The complete production process of the composite sandwich arch is illustrated in Figure 6.6 starting from after-print support removal, followed by the production of flanges using vacuum infusion placed on a timber frame formwork to obtain the required curvature. Finally, the fully assembled part contains top and bottom GRPF flanges and a 3D printed Gyroid core.



Figure 6.6 Production of the composite sandwich arch

7 NUMERICAL MODELLING

7.1 TPMS units

For the numerical analysis, the same geometry is used as for the samples tested in the laboratory with the dimensions $50 \times 50 \times 50$ mm and identical boundary conditions are simulated. The initial step in the analysis process was to create the geometry using the nTopology software. To ensure accurate results while maintaining computational efficiency, a mesh resolution of 1×1 mm was considered suitable.

For a detailed analysis, the complex mesh (over 1 million elements) was subjected to polygonization. The resulting STEP file from the Rhinoceros software was then imported into Abaqus for dynamic analysis. Rigid plates were positioned at the top and bottom of the AM model, with the reference points having restrained translational and rotational degrees of freedom. A displacement-controlled boundary condition was implemented at the top reference point.

To prevent self-penetration, the general contact settings were adjusted to include all surface pairs within the structure itself. In addition, a frictionless interaction property between the plates and the TPMS unit was created to allow sliding. The material model was defined as an elastic-plastic material for the dynamic analysis and supplemented with ductile fracture properties to identify potential fracture zones. Prior to this analysis, uniaxial tensile tests were performed on 3D-printed dogbone specimens printed in three different directions. The aim of these tests was to determine the non-linear mechanical properties of the 3D-printed ASA material as well as the modulus of elasticity.

The analysis was based on the premise that the tensile test covers all factors resulting from the production process. In order to simplify the calculation of these intricate geometries, this approach was validated.

Comparing the predicted load-displacement and stress-strain curves with the experimental data from the laboratory tests can help to verify the accuracy of the analysis and identify areas where the model may need to be improved. This iterative process of analysis and validation can help engineers optimize the design of 3D printed structures for better performance and reliability.

7.2 Composite sandwich panel with tempered glass face sheets

The preliminary design of the required core height was analytically calculated using parameters derived from curve fitting as described in [160]. After that, a 3D model was generated in nTopology software using parametric design. Finally, the mesh file determined by a minimum wall thickness of 3×3 mm was exported for the fracture analysis in Abaqus. This mesh comprises a total of 1,659,896 face elements. Exceeding this number of elements significantly increases computational time. Therefore, the model was analysed by recreating it with both denser and less dense meshes until satisfactory convergence of results and computational time was achieved.

To explore the influence of geometric parameters on the bending characteristics of a sandwich plate with a 3D-printed core, FEA was conducted using ABAQUS/Explicit, with the goal of reproducing the three-point bending test. In FEA, an elastic-plastic constitutive model was applied to the ASA-graded Gyroid core, while an elastic constitutive model was employed for the glass sheet panels. In the Abaqus definition of contact properties between the glass sheets and the 3D printed lattice core, a penalty-based formulation was used for the tangential behaviour, with a friction coefficient set to 1 (indicating full contact), and the normal behaviour was defined as 'hard contact'.

The boundary conditions were configured to restrict only vertical displacement while allowing free horizontal movement. The load was applied through vertical displacement at the midpoint of the top glass plate. This setup aimed to simulate a displacement rate of 2 mm/min, effectively replicating the conditions observed during the laboratory test.

Figure 7.1 illustrates representative three-dimensional finite element models of the sandwich panel, showcasing glass sheets and a 3D-printed core. The FEA was utilized to validate the observed ductile failure mode in the three-point bending experimental test. Material parameters were carefully considered for accuracy, and the mesh size was set at 3×3 mm to capture intricate details in the analysis.



Figure 7.1 Material model set for FEM analysis of the sandwich panel with 3D printed core.

Alternatively, the mechanical parameters of the graded Gyroid core can be determined through the Homogenization analysis method using an RVE of one unit cell. The Homogenization analysis sets up six load cases on an RVE. Each load case involves applying a unit perturbation to one component of the volume-averaged engineering strain, while keeping all other components constant at zero [171]. Subsequently, the perturbation of the volume-averaged stress for each load case contributes to a column of the Hooke's stiffness tensor.

After choosing the TPMS type and size, multiplication was done in a rectangular cell map to fit the total plate dimensions. The TPMS sandwich core is characterized as non-uniform, with unit cell parameters derived from the stress point map obtained through a three-point bending test on a solid structure. Considering the implementation of graded topology into the design of this specific sandwich core, the core was divided into five segments. A unit size of $100 \times 70 \times 60$ mm (presented as Material_01 and Material_01_R* in Figure 7.2) was applied to the edges and middle section, while a less dense geometry with a unit size of $130 \times 70 \times 60$ mm (presented as Material_02 and Material_02_R* in Figure 7.2) was used for the remaining two segments.

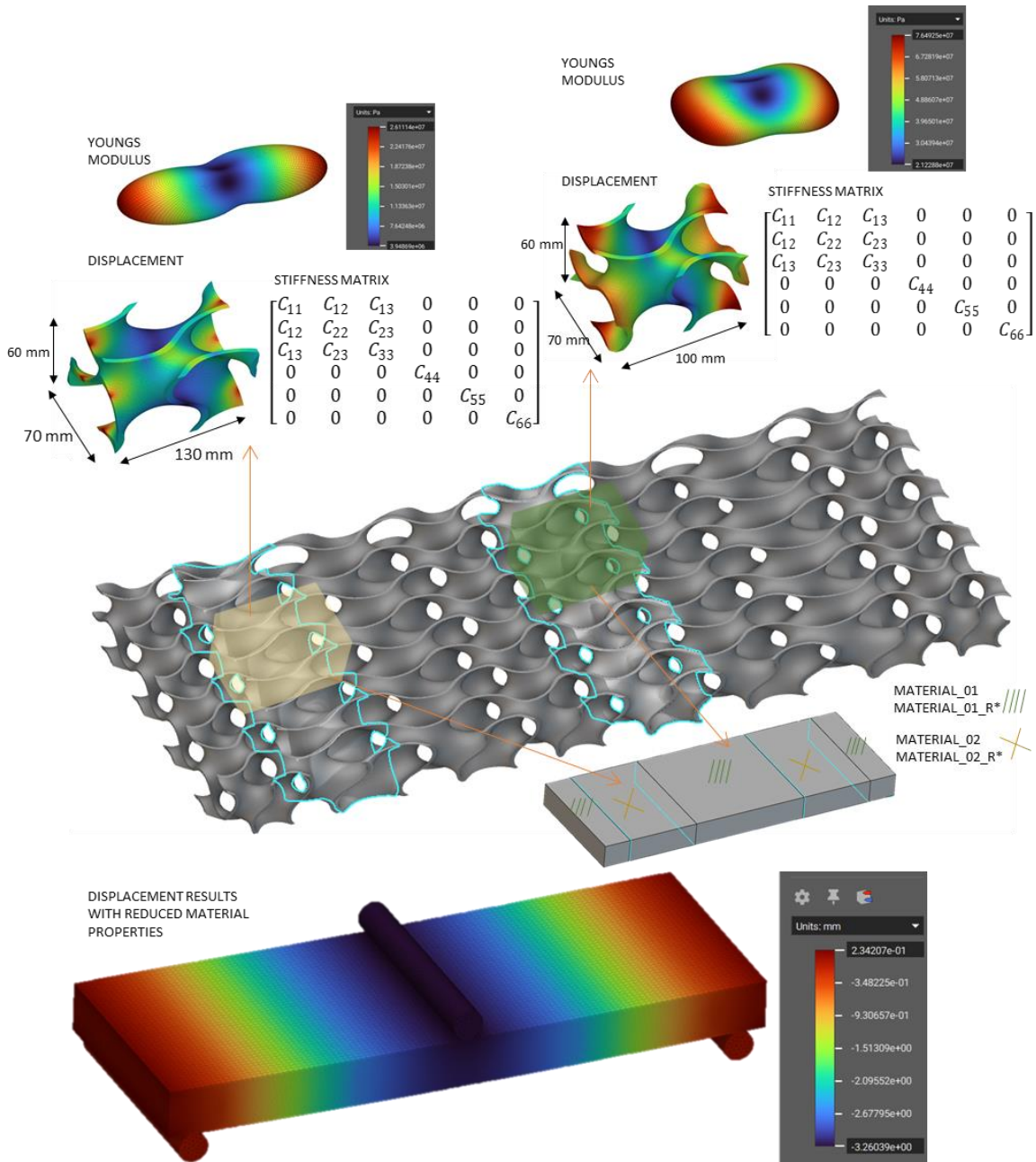


Figure 7.2 Design process flow

The objective was to attain the desired global sandwich stiffness by iteratively adjusting the properties of the reduced material in Homogenization analysis (Material_01_R* and Material_02_R*) until the results aligned with the laboratory test, which subjected the structure to a total load of 3 kN, resulting in a deformation of 3.3 mm.

7.3 Composite sandwich panel with GFRP face sheets

Finite Element Models were developed to simulate the performance of 3D printed structural components presented in Figure 7.3. The first model simulates the behaviour of the “core only” beam featuring a uniform periodic Gyroid cellular structure. This model served as validation for an isotropic elastic-plastic material model calibrated from the results of tensile tests on 3D-printed dogbone specimens. The second model simulates the performance of the “sandwich beam” while the third one that of the “arch beam” specimen. It is assumed that this material model definition can be applied for the analysis of larger 3D printed components with satisfactory result output.

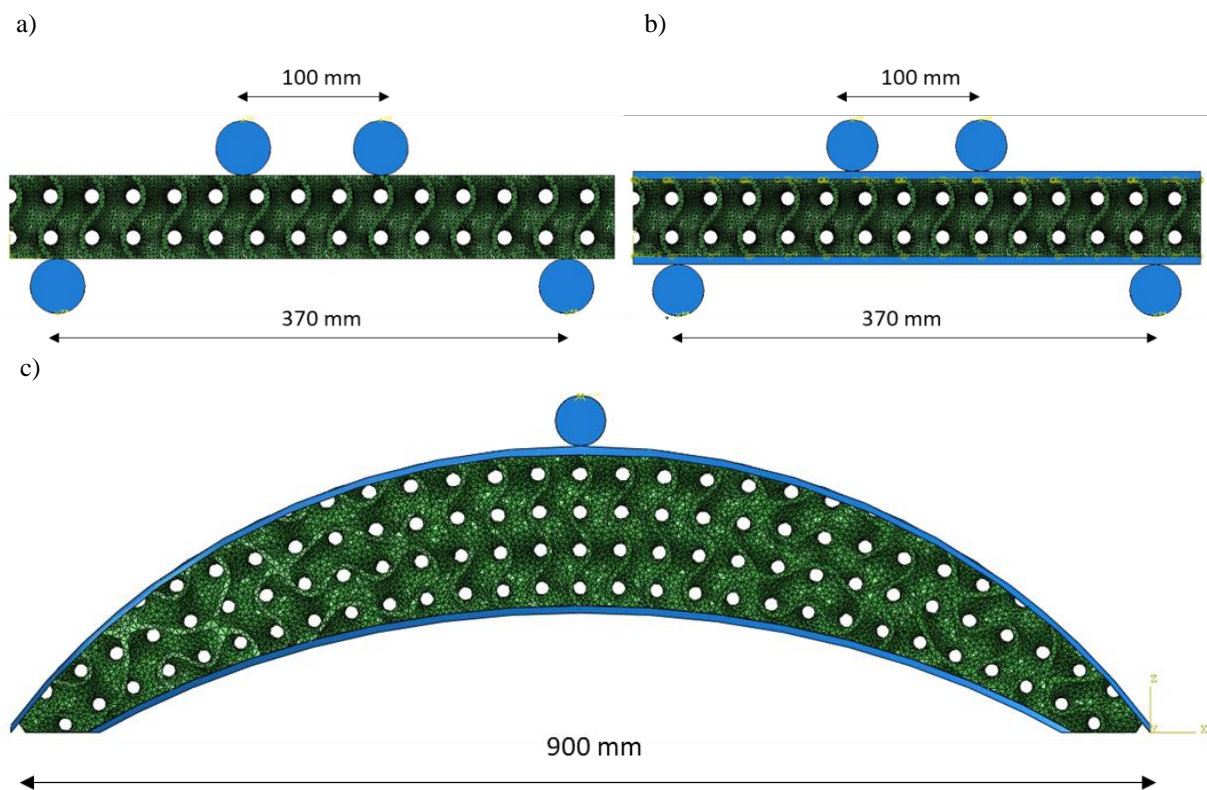


Figure 7.3 Finite element models: a) Core only; b) Sandwich beam; c) Arch beam

All 3D models were created in nTopology software using parametric design. Subsequently, the mesh files, configured with a minimum wall thickness of 3×3 mm, were exported for fracture analysis in Abaqus. This mesh comprises a total of 70,603 nodes for the sandwich core. Exceeding this node count significantly increases computational time. Consequently, the models underwent analysis with both denser and coarser meshes until achieving satisfactory convergence of results and computational efficiency.

The “sandwich beam” utilizes the same core geometry as “core only” and the same boundary conditions (a simply supported beam). This periodic homogeneous cellular core structures were chosen to be 3D printed with repeatable building block units measuring $60 \times 60 \times 60$ mm, resulting in a total beam size of $440 \times 60 \times 60$ mm. Following the validation of the appropriate material model through the analysis of “core only” and “sandwich beam” will be defined with the same core isotropic elastic plastic material model.

To enhance stiffness while preserving the lightweight nature of the structural system, “sandwich beam” introduces a composite sandwich system using top and bottom thin GFRP sheets bonded to the core structure. However, due to the mesh resolution of the thin face sheets, computational time increased to capture the composite behaviour. To address this, equivalent material properties were utilized and applied to the thicker face sheets, ensuring that the same stiffness is maintained as with the thinner GFRP sheets.

The boundary conditions for “core only” and “sandwich beam” were configured to restrict only vertical displacement while allowing unrestricted horizontal movement. Four-point bending was achieved using two rollers positioned 50 mm away from the midpoint. This setup was tailored to simulate a displacement rate of 5 mm/min, faithfully replicating the conditions observed during laboratory testing.

“Arch beam” maintains the core building block geometry of $60 \times 60 \times 60$ mm, yet it showcases an outer shape with a curved and variable cross-section inspired by the Da Vinci Bridge, with overall dimensions of $900 \times 240 \times 220$ mm. The boundary conditions for “arch beam” were established by constraining all horizontal and rotational movement at both edges. The identical setup for simulating a displacement rate of 5 mm/min was applied here as well.

8 COMPARISON OF EXPERIMENTAL AND NUMERICAL RESULTS

8.1 TPMS units

Some general conclusions on the mechanical properties of TPMS under compressive loading are drawn by researchers in other fields. When testing Diamond and Gyroid structures, higher values of elongation at break occur. In general, high stiffness and strength is observed for the Schwarz structure, while the Neovius structure shows better energy absorption [39]. Therefore, the most appropriate TPMS structure can be selected considering the project requirements.

Production using the FDM process is shown in Figure 8.1a and Figure 8.2a for five TPMS units with a relative density of 20% and 40% respectively. The hot polymer that emerges from the extruder and covers the cooler layers below is displayed with temperatures in Celsius. For ASA material, the steel bed temperature is maintained at 100°C and the extrusion temperature for the steel nozzle is set at 250°C. The thermal profile assigned to each element based on the G-code coordinates is subjected to a non-linear heat transfer analysis. This non-linearity results from temperature-dependent material properties and non-linear boundary conditions, whereby the film coefficient can be a function of the surface temperature. The temperature field calculation incorporates conduction, boundary convection and boundary radiation.

Unlike some other additive manufacturing technologies, FDM technology does not allow the layers to overlap during printing, resulting in a structure with inherent air gaps or voids. The toolpath for FDM also showed the possibility of air gaps in small features of the cellular structure (Figure 8.1b and Figure 8.2b). These voids are simulated using the virtual simulation tool GENOA from Alphastar [180].

The compression test, performed at a uniform strain rate with a fixed steel plate, revealed a noteworthy observation: an almost flat plane within the structure is recognized as the most compressed area (Figure 8.1c and Figure 8.2c). When the ASA material is subjected to a high load during compression tests, a clear indication of regions under significant stress is the whitening of the material. It is assumed that the fracture during compression originates from weak regions between the layers of the structure, which spread and interconnect throughout the cell, eventually leading to cell failure. As compression continues, the deformed cells come together, causing stress to increase until the next fracture occurs. However, a plateau was

observed in structures with low volume fractions, which is due to a lower interlocking of the compressed structure, which in turn is attributed to a lower material density.

The numerical fracture analysis from the Abaqus simulation accurately reproduces the real test results, as depicted in Figure 8.1d and Figure 8.2d, for all TPMS geometries, with the exception of Schwarz_40, where a vertical fracture plane occurred instead of a horizontal one. With anisotropic materials such as Schwarz and Neovius, distinct failure modes are evident such as sudden and catastrophic failure (fragmentation in the case of Schwarz). In contrast, more isotropic materials (Gyroid, Diamond, and Split) display a different behaviour. After the initial failure (in the horizontal plane), the walls are further crushed, which enhances their safety for use in load-bearing structures. In all TPMS samples, failure occurs in the horizontal plane at the interfaces between the layers, indicating the known challenges [184] in the bead contact zones. After the initial failure at the contact zone between the beads, buckling of the walls at a relative density of 20% enlarged the crack zones between numerous beads. In Gyroid, Diamond and Split with a relative density of 40%, the wall buckling was reduced due to the thicker walls, leading to further failure of the TPMS walls orthogonal to the print direction, accompanied by a whitening of the surrounding area typical of polymer materials.

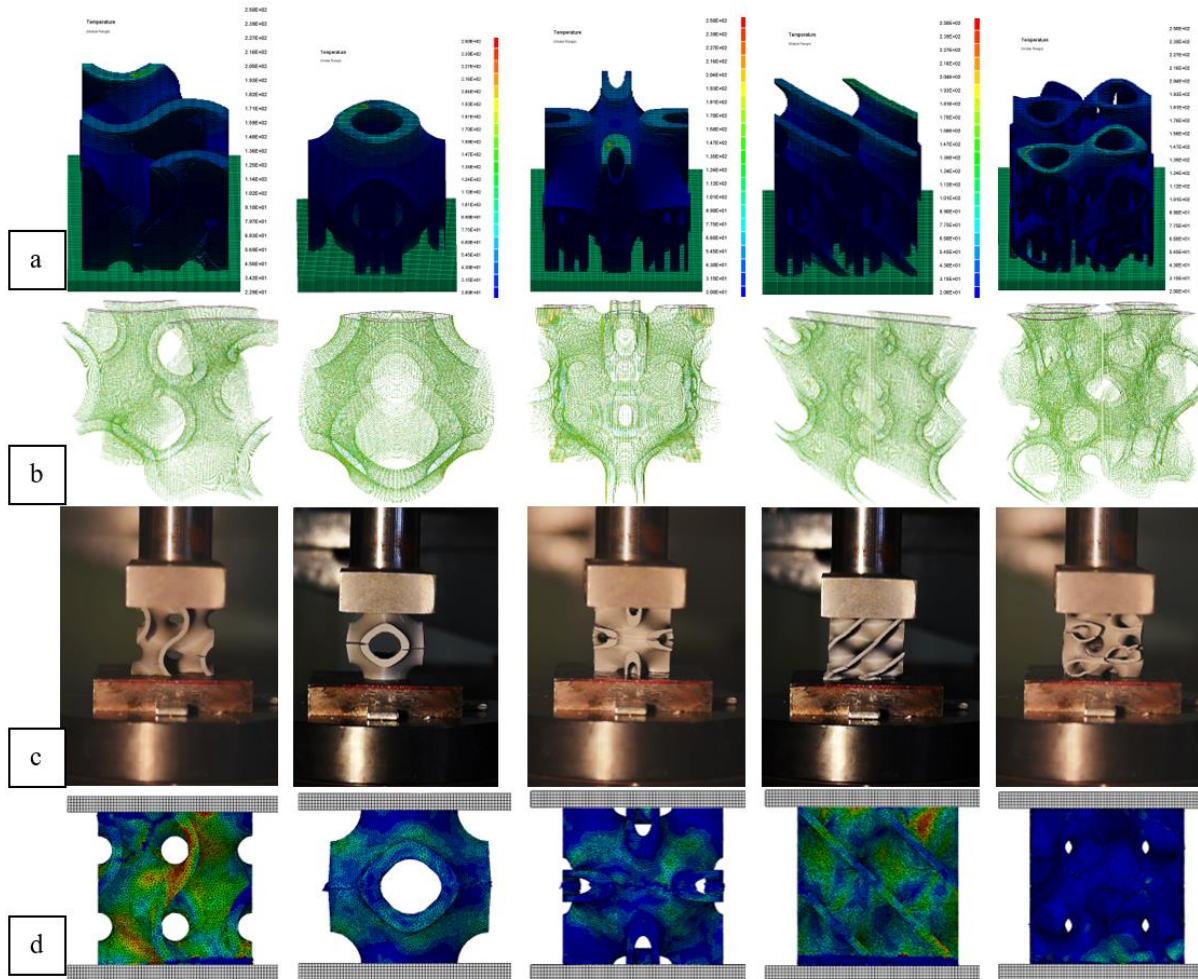


Figure 8.1 TPMS unit cells (Gyroid, Schwarz, Neovius, Diamond and Split from left to right) with 20% relative density: a) Thermal analysis; b) Void from toolpath error; c) Compression test failure modes; d) Abaqus dynamic failure analysis

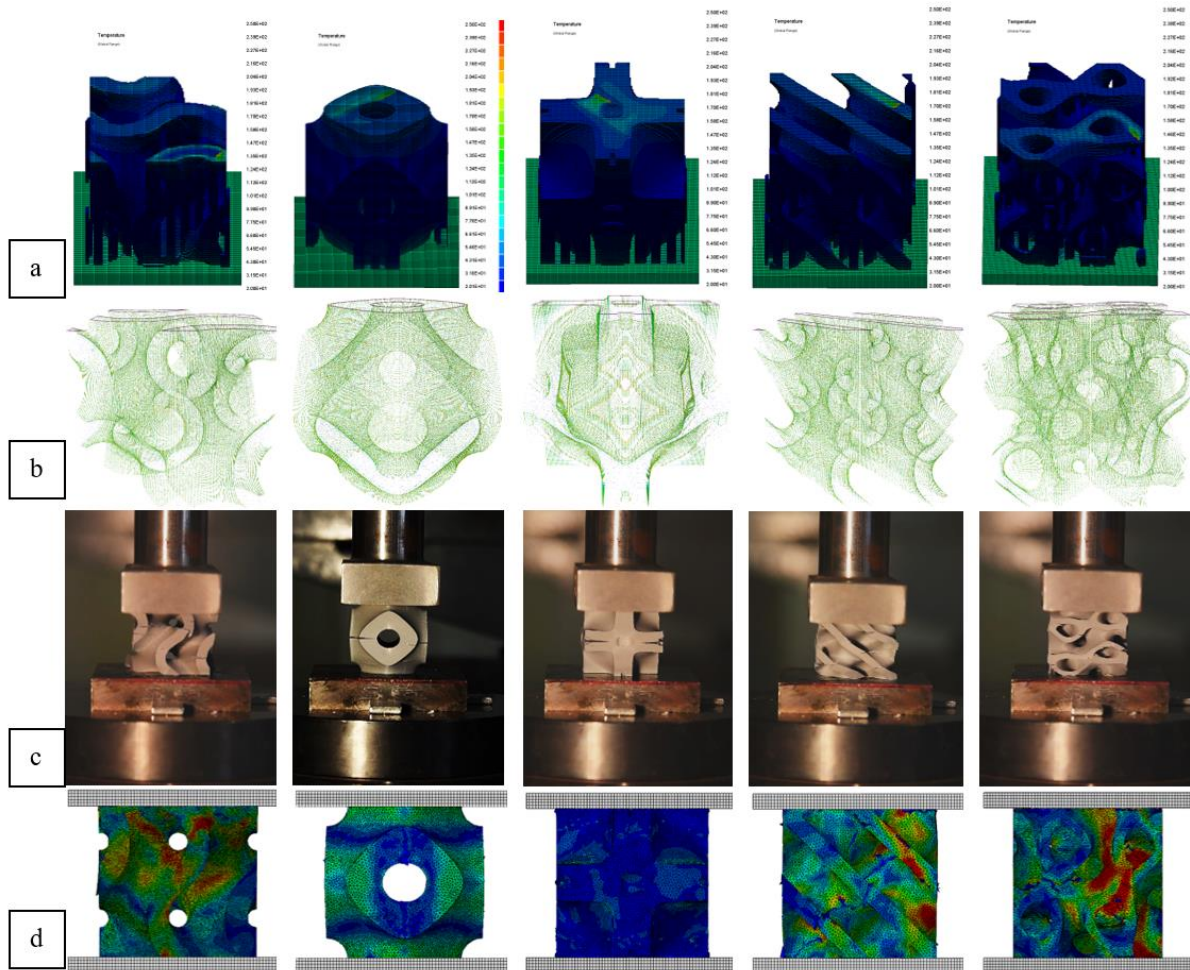


Figure 8.2 TPMS unit cells (Gyroid, Schwarz, Neovius, Diamond and Split from left to right) with 40% relative density: a) Thermal analysis; b) Void from toolpath error; c) Compression test failure modes; d) Abaqus dynamic failure analysis

The failure modes observed under uniaxial compression are explained in Figure 8.3, where a parallel is drawn with the behaviour of timber, where beads can be compared with grains. Four failure modes are identified: tension perpendicular to the bead interface, wall buckling, shear and crushing. In the context of the TPMS samples tested, the more isotropic geometries (Gyroid, Diamond and Split) with lower relative density (20%) exhibited a combination of wall buckling and tension perpendicular to the bead interface. As the force increased, the buckling of the walls increased, causing cracks to propagate in the interlayers.

In TPMS structures with a relative density of 20%, but with a more anisotropic behaviour (Schwarz and Neovius), tension perpendicular to the bead interface and crushing occurred, accompanied by a sudden material rupture. In TPMS structures with a higher relative density (40%) but with a more isotropic behaviour (Gyroid, Diamond and Split), together with the anisotropic Neovius structure, tension perpendicular to the bead interface, reduced wall buckling due to thicker walls and shear occurred. The denser Schwarz structure exhibited the

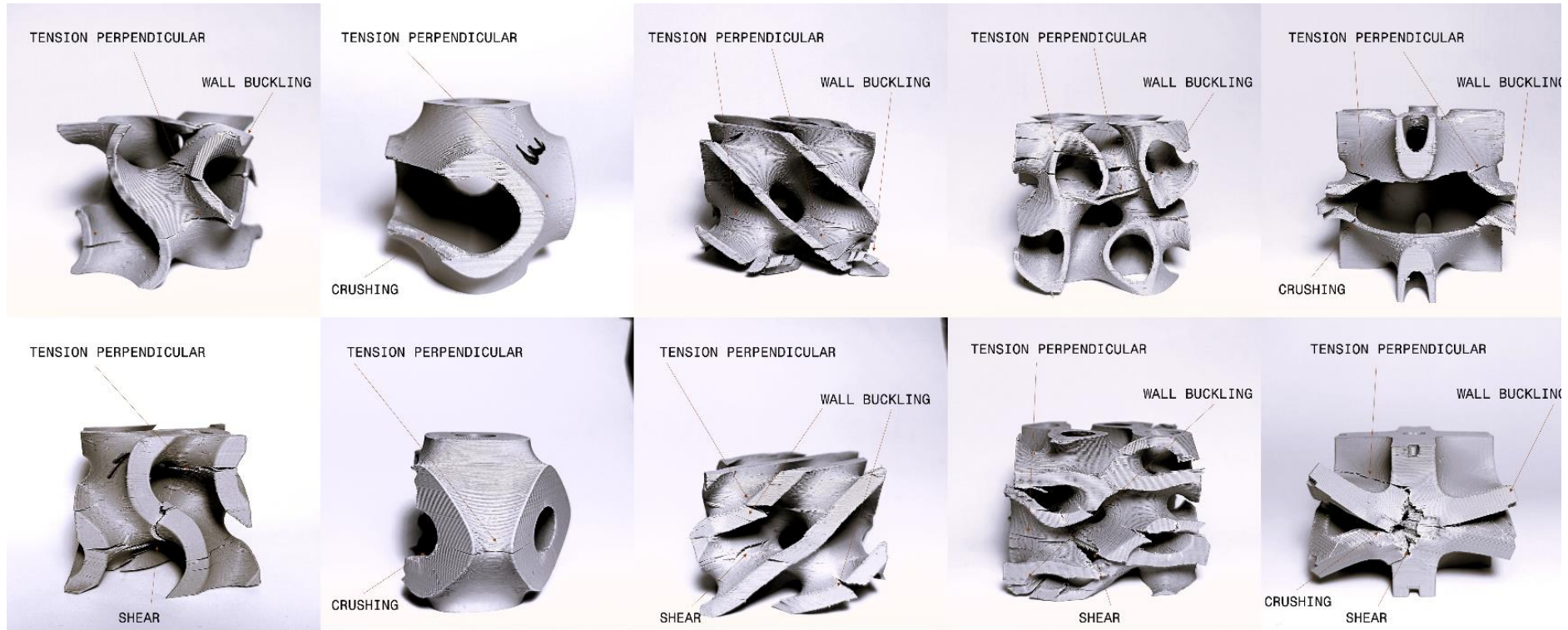


Figure 8.3 Failure modes of TPMS units under compressive load (Gyroid, Schwarz, Diamond, Split and Neovius from left to right)

same failure modes as its lighter counterpart (tension perpendicular and crushing), while the Neovius structures exhibited significant wall buckling, tension perpendicular and crushing at both 20% and 40% relative density.

Force and displacement diagrams for the three samples of each geometry and density (20% and 40%) are illustrated in Figure 8.4 and compared with the dynamic/explicit finite element analysis (FEA) model with an elastic-plastic material model.

In the elastic region, all TPMS structures exhibited uniform deformation. As anticipated, the Diamond structure proved to be superior in terms of compressive force, with maximum values of 8.36 kN at a relative density of 20% and 20.10 kN at a relative density of 40%.

As expected, the force was lowest for the Schwarz structure, with minimum values of 1.55 kN and 9.48 kN, before brittle fracture occurred at both 20% and 40% relative density. Another isotropic geometry, Neovius, proved to be the best performer under uniaxial compression loading, closely following Diamond with 7.78 kN and 18.75 kN, for relative density values of 20% and 40% respectively. Notably, Diamond exhibited the greatest elongation before significant failure occurred. Gyroid and Split, both isotropic materials, are proving to be advantageous for applications such as mechanical and tissue engineering, with Gyroid resembling the structure of human bones. Although Split exhibits superior properties, its large surface area may not be the best choice for structural applications that require long printing times and a large number of finite elements. Gyroid, on the other hand, was considered in further parametric design due to its promising characteristics and appealing visual aesthetics.

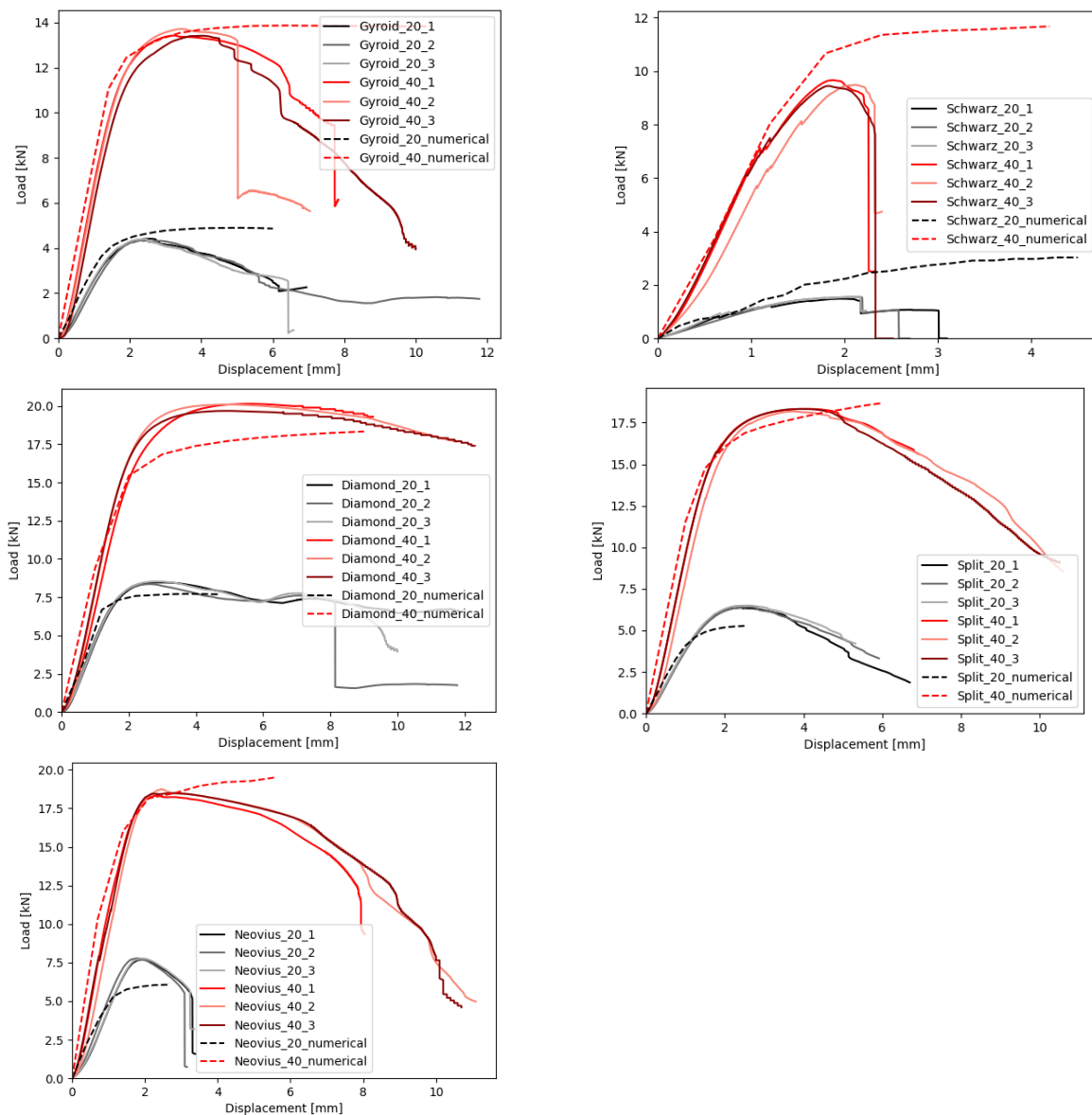


Figure 8.4 Compressive load-displacement diagrams for five TPMS geometries

8.2 Composite sandwich panel with tempered glass face sheets

Detailed FEM analysis in Abaqus using an elastic-plastic isotropic material model, concluded that the sandwich decks were expected to exhibit higher performance than the provided test results. The material properties were most likely affected by the manufacturing process. To address this, a reduction in material properties was calculated using homogenization analysis and presented as MATERIAL_01_R* and MATERIAL_02_R* in Table 3. Structural analysis was conducted on the solid using substitute reduced material properties, and dynamic explicit analysis was performed in Abaqus on the sandwich structure with 3D TPMS geometry, utilizing the reduced elastic-plastic isotropic material model. The iterative process resulted in the adjusted material model that align better with bending test.

To assess the bending performance of sandwich panels with 3D printed TPMS core, specifically designed for future large-scale bridge decks, a scaled gyroid structure with a total core height of 60 mm and 3 mm thick top and bottom flanges was chosen for the scaled prototype. The investigation involved a three-point bending test, and the corresponding force displacement curves are illustrated in Figure 8.5.

Observing the force-displacement curve it is evident that the load rapidly reached its peak within a limited displacement range. Following the peak, there was a noticeable decline in force, leading to an propagated plateau characterized by a stable increase in both load and deformation. Consequently, the force-displacement curve can be delineated into three phases:

1. **Pre-failure phase:** This stage represents a portion of the force/displacement curve from the beginning until the first peak force, during which the load increases steadily.
2. **Failure phase:** The certain walls with less dense material developing open cracks in horizontal plane between print beads. In this phase, perpendicular tension between print beads became dominant.
3. **Post-failure phase:** After failure occurred, a composite exhibited steady increase in both load and displacement. It finishes in a sudden, brittle fracture occurring in the top glass due to compression and shear failure in the core walls throughout the entire core height.

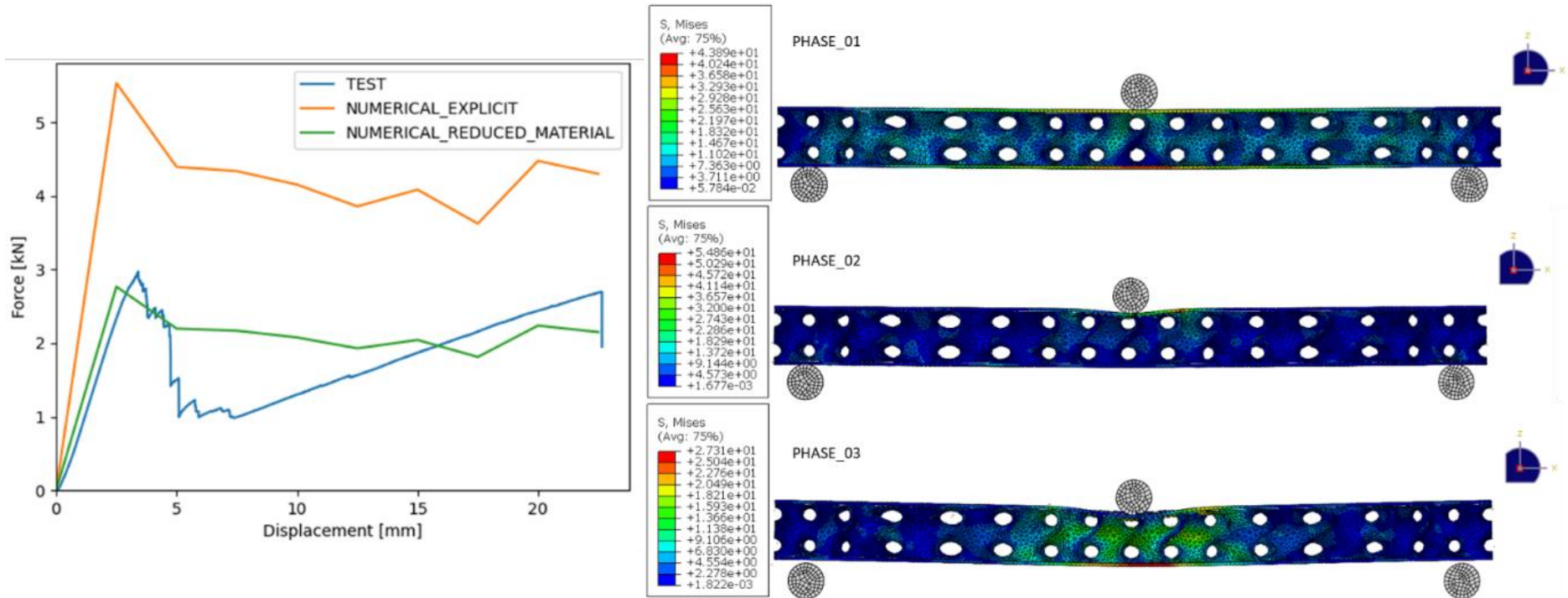


Figure 8.5 Three-point bending test results and comparison with the FEA

Considering the print direction and other printing parameters, such as layer height and bead width and the fact the larger part required longer time to print, it resulted in a substantial reduction in bending stiffness from the initial conditions where the 3D print was assumed to be isotropic. The peak force, $F_{\max} = 3000$ N, was likely induced by a lack of a connection between infill walls and outer print walls that led to increased voids and inadequate bonding of the 3D printed material (Figure 8.6).

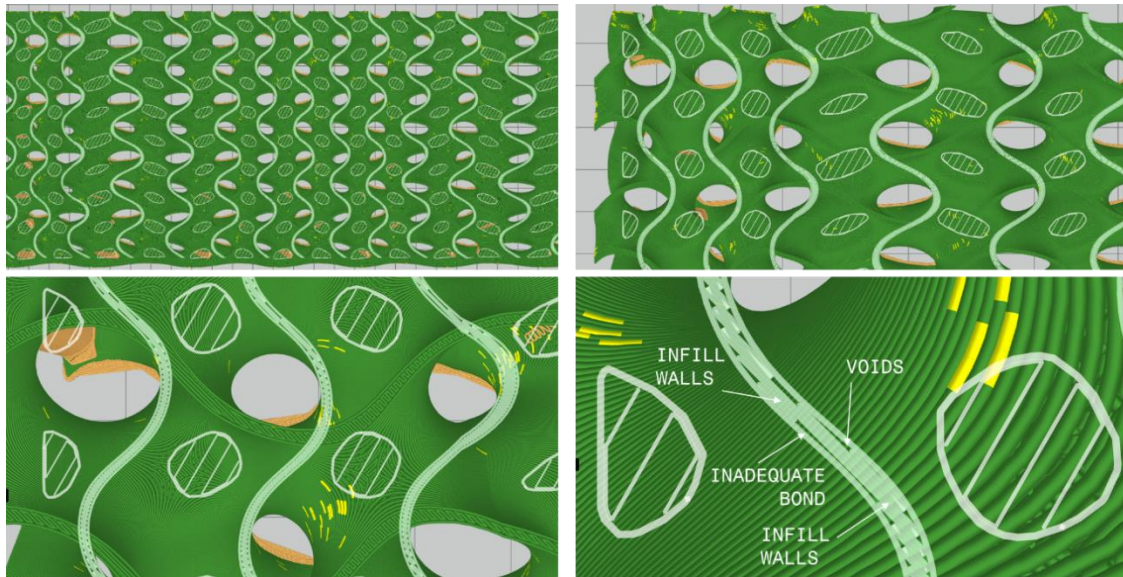


Figure 8.6 3D printing toolpath from GrabCAD slicer

The extension of cracks between beads, initially caused by voids within the 3D printed material, led to the brittle failure of the top glass flange and shear failure of the core walls in the middle. The strong link between the glass flanges and the gyroid structure stopped the glass from deforming. As the compression stress increased, it resulted in the glass being crushed, leading to an immediate failure of the core. Consequently, the bottom flange took over the entire load from the machine.

The fracture behaviour of the 3D sandwich panel under bending load was effectively captured using FEA, employing an elastic-plastic isotropic material model derived from tensile tests conducted on 3D printed dogbone samples, with printing direction aligned in the ZX.

Analysing the snapshots from the bending test in Figure 8.7, three phases of the force/displacement curve can be recognized, along with categorized failure modes of the 3D printed core: tension perpendicular to the print beads and shear; and failure modes of the top glass sheet: crushing under compression.



Figure 8.7 Snapshots from bending test by phases

However, for a more detailed analysis of 3D printed parts, it is recommended to create a thermo-mechanical model. Once the thermo-mechanical model is developed (Figure 8.8), incorporating toolpath data and material input, the results regarding stress and deformation serve as inputs for structural analysis under service loading conditions. The thermo-mechanical analysis simulates the 3D printing process by applying the same conditions and thermal history as during 3D printing process. The new input file incorporates the presence of voids and temperature on the mechanical properties of the element.

The results of the mechanical analysis are stored in an Abaqus ODB file format, containing information about deformation, stress, strain, and temperature. This ODB file is then used to define the initial conditions for stress analysis during service. In-service load analysis simulates the behaviour of the structure under the actual loading conditions it will face during its lifetime. In the future, a more comprehensive analysis that includes dynamic analysis in Abaqus, using the VUMAT subroutine for material definition, will be pursued.

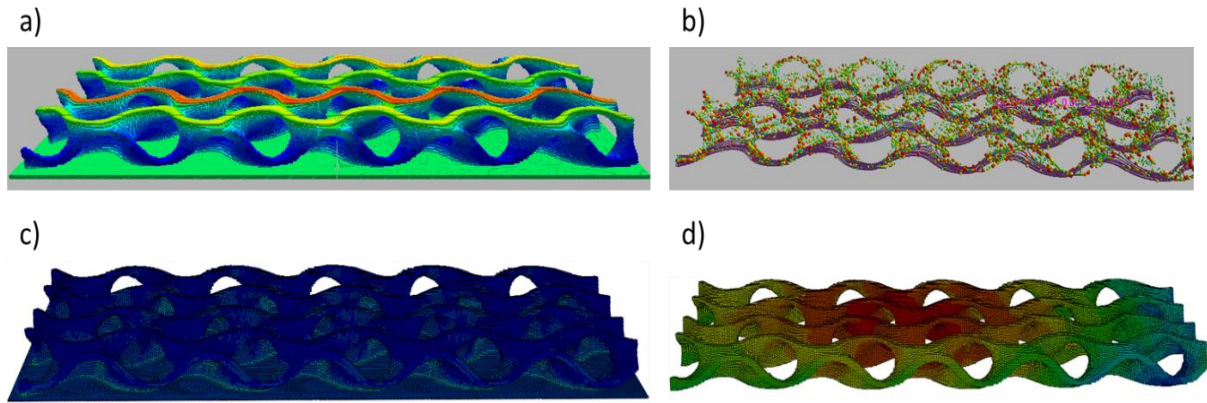


Figure 8.8 Detail finite element analysis in GENOA AlphaSTAR software: a) Thermal analysis– temperature; b) Macro-void resulting from toolpath errors; c) Mechanical analysis – von Mises; d) Mechanical analysis – displacements.

8.3 Composite sandwich panel with GFRP sheets

Due to the complexity of the geometry of the three-dimensional core structure, the results were statistically analysed using data obtained from 2D VIC measurements. The flat faces were observed to form edge walls at the front and back of the model. Although damage may occur in other parts of the structure, it is concluded that these walls will ultimately deform most. For statistically interpreting the obtained results, the “core only” and “sandwich beam” were divided into three zones based on beam height (top, bottom, and middle), and into three zones based on beam length (support, midspan, and intermediate). In “arch beam”, the area of interest was the middle span. Thus, for the height, the zones were divided into top and bottom, along with two middle zones. For the length, the analysis focused on the nodes directly under the applied force, as well as the intermediate nodes transitioning from direct force.

Displacement data measured from DIC tests were plotted against the beam length, with different colours assigned to the top (blue), bottom (grey), and middle (green) nodes. Various markers were used to distinguish nodes at the support (square), middle (circle), and intermediate (triangle) positions. The results were plotted for a total of 39 nodes across all test time intervals, with opacity introduced to represent different time intervals. Deformation curves were plotted both at the point of failure and after the failure stage.

Another set of plots was generated for the stress-strain curves, which includes stress vs. strain along the X-axis and Y-axis, first and second principal stress vs. first principal strain and shear stress vs. shear strain, Using DIC strain data and the mechanical properties obtained from the material model calibration, the stresses were calculated.

8.3.1 Core only

The displacement in 13 Gyroid walls was plotted, with three nodes representing each wall (top, middle, and at the cross-section bottom). This results in a total of 39 nodes being plotted in Figure 8.9. Additionally, for each node, the results were plotted for time intervals of 5 seconds. The latter time interval was graphically presented with reduced colour opacity. The three deformation curves connecting the top nodes (blue line), middle nodes (green line) and bottom nodes (grey) are drawn for the results at failure (continuous lines) and after failure (dashed lines). The deformation curve at failure shows relatively uniform load propagation across the top, middle, and bottom nodes. After failure occurred, reverse displacement orientation is observed on the left (the deformation curve connecting the top nodes is deformed the most) and right sides of the beam (the deformation curve connecting the bottom nodes is deformed the most). Additionally, excessive deformation in the mid-span is observed from the top nodes, indicating wall breakage at that location.

Regarding shear stress and strain presented in Figure 8.10, the maximum shear stress recorded stands at 15.76 MPa, with shear strain of 1.19%. These results, observed for the data collected right before the failure, suggest the following failure mechanisms: compression stress perpendicular to the material deposition during the 3D printing process causes interlayer crack opening, while an increase in compressive stress prolongs cracks, leading to shear failure in the same zone.

The stress and strain results for “core only” are presented in Figure 8.11. In the direction parallel to the material deposition (σ_x), the analysis reveals a maximum tensile stress of 6.48 MPa and a strain of 0.21% in the bottom cross-section near the support, with other zones also indicating similar tensile stress levels. Additionally, a maximum compression stress of 8.97 MPa and a compressive strain of 0.29% are observed in the bottom cross-section in the middle of the span. In the direction perpendicular (σ_y) to the material deposition, a maximum tensile stress of 13.27 MPa and tensile strain of 0.43% are observed at the cross-section middle in the middle of the span, while a maximum compression stress of 37.99 MPa and compressive strain of 1.23% are recorded at the cross-section bottom in the middle of the span.

The analysis indicates that both the first principal stress (tension) and second principal stress (compression) predominantly occur at the bottom cross-section in the middle of the span. In terms of first principal stress (σ_1), the analysis reveals a value of 16.09 MPa and a strain of 0.52%. Moving to second principal stress (σ_2), the data highlights a value of 63.05 MPa and a strain of 2.05%.

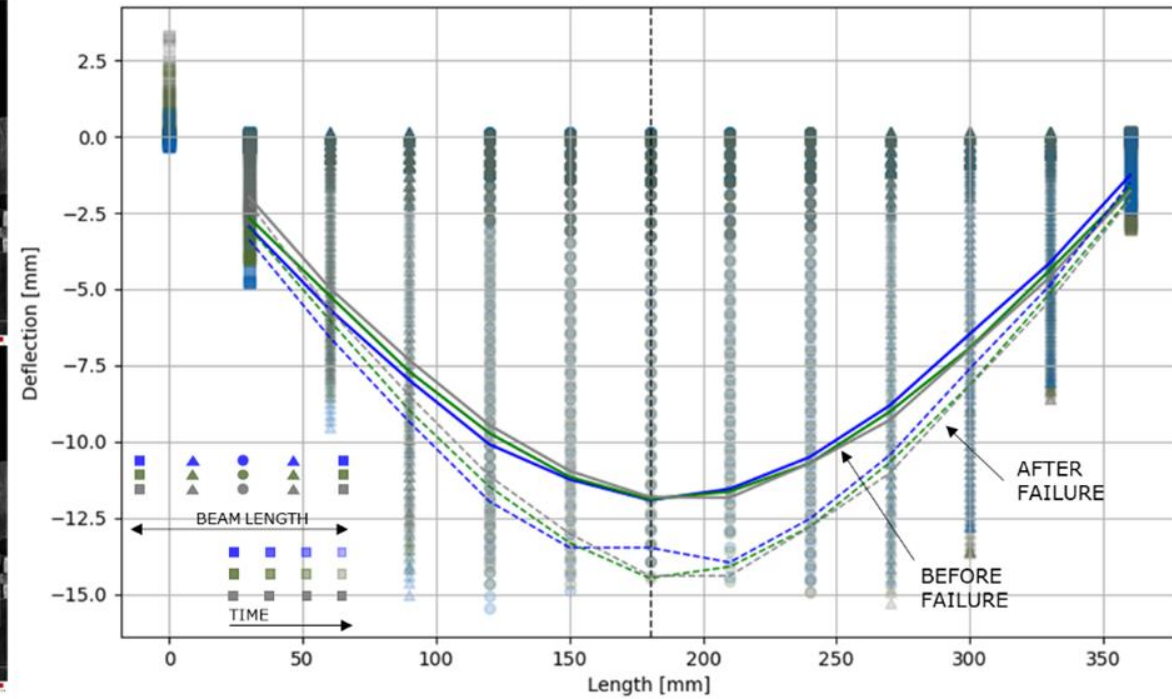
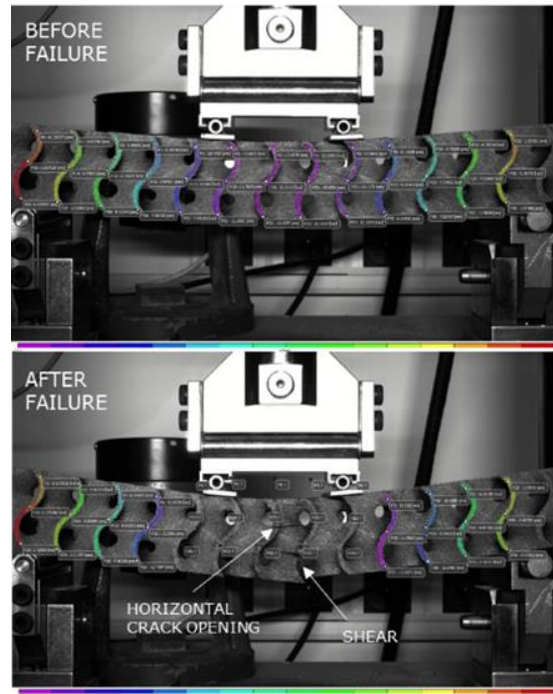


Figure 8.9 Core only: Displacement

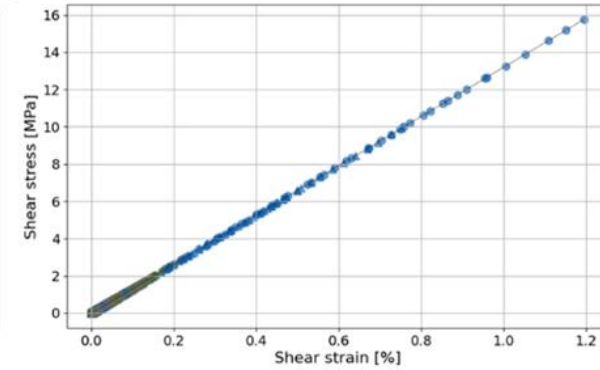
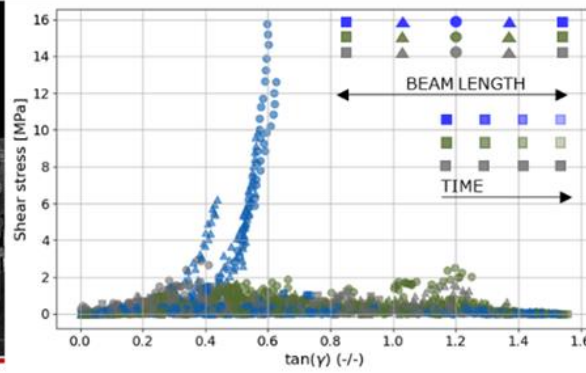
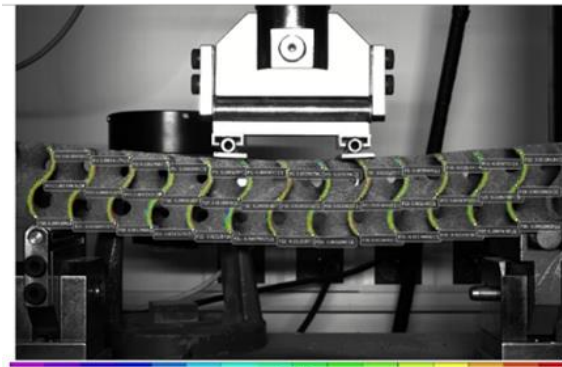


Figure 8.10 Core only: Shear stress vs. strain

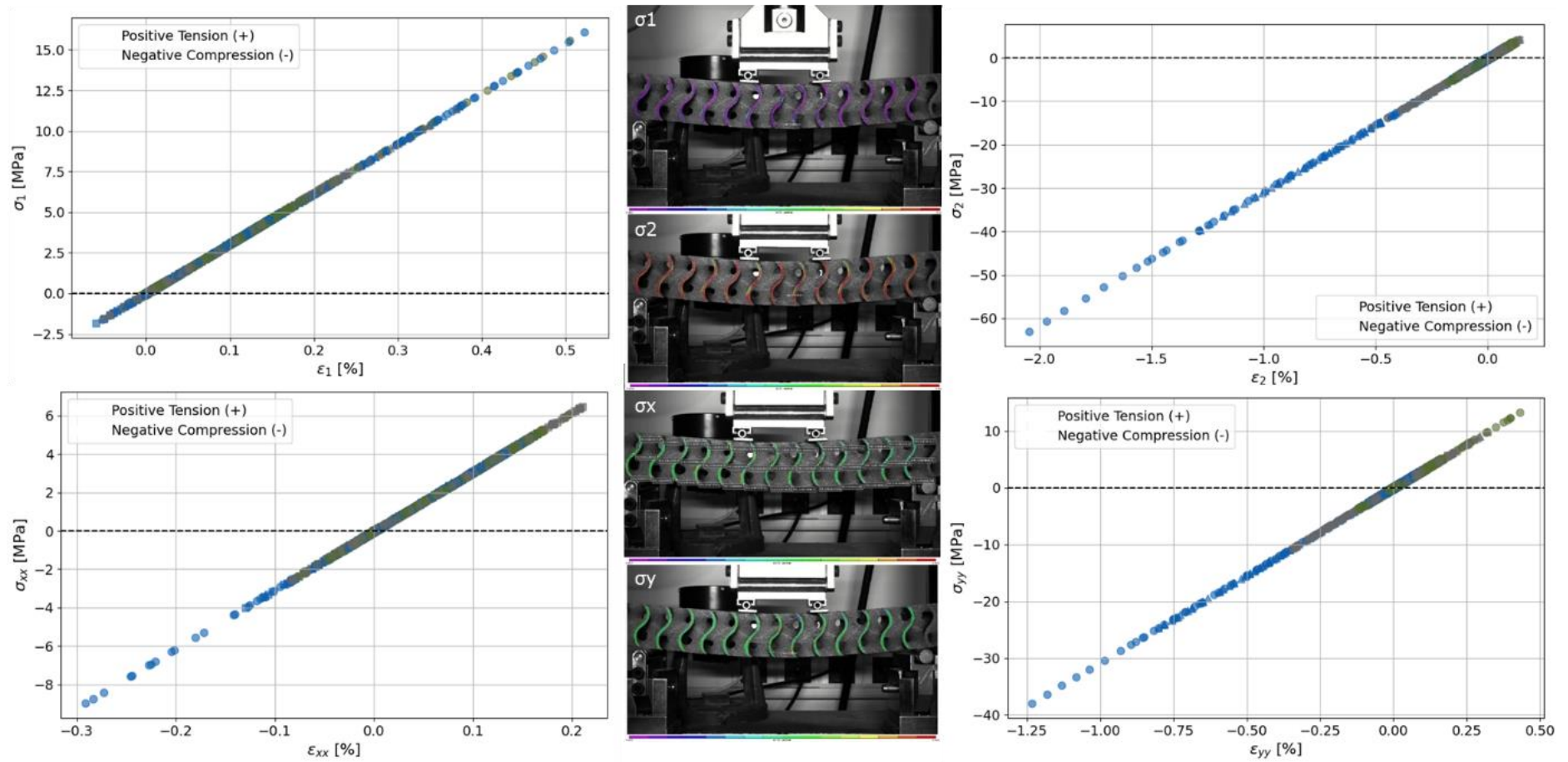


Figure 8.11 Core Only: First principal stress vs. strain, second principal stress vs. strain, stress vs. strain in x direction (parallel to material deposition), stress vs. strain in y direction (orthogonal to material deposition)

8.3.2 Sandwich beam

As expected, due to the addition of the composite face sheets, the “sandwich beam” shows higher stiffness compared to the “core only” specimen by four times. Observing the deformation curves (Figure 8.12) connecting the top nodes (blue line), middle nodes (green line), and bottom nodes (grey) both at the point of failure (continuous lines) and after failure (dashed lines), it is notable that a wider range of nodes in the middle deformed uniformly before failure. However, after failure occurred under the right roller, reverse displacement orientation is observed on the left side (the deformation curve connecting the top nodes is deformed the most) and the right side of the beam (the deformation curve connecting the bottom nodes is deformed the most). Additionally, excessive deformation is observed along the mid-span towards the support walls, indicating shear wall breakage at that location.

Considering shear stress and strain (Figure 8.13), it's apparent that the cross-section middle near support experiences a maximum shear stress of 3.54 MPa, along with a maximum shear strain of 0.27%, indicating localized stress concentrations in that area. These results observed on the composite sandwich beam for the data collected right before the failure, conclude following failure mechanisms: In the absence of interlayer crack opening, a brittle failure occurs in the compressed area at the load introduction, followed by instantaneous shear propagation towards the support zone. Consequently, delamination of the face sheets from the core occurs in the support zone, resulting in the highest final compression in this zone.

Examining the principal stress, a maximum tensile stress of 17.79 MPa is found at the cross-section bottom in the middle of the span, coinciding with a maximum tensile strain of 0.58%. For second principal stress the analysis unveils a maximum compression stress of 18.16 MPa at the cross-section middle near support, accompanied by a maximum compression strain of 0.59%. Results for stresses and strain (Figure 8.14) indicate that in the direction parallel to the material deposition (σ_x), the top cross-section in the intermediate span experiences a maximum tensile stress of 5.20 MPa, with a strain of 0.17%, while other middle span sections generate comparable tensile stress levels. Meanwhile, at the top cross-section near support, a maximum compressive stress of 4.52 MPa and a compressive strain of 0.15% are observed. On the other hand, in the direction perpendicular to the material deposition (σ_y), the bottom cross-section in the middle of the span bears a maximum tensile stress of 17.50 MPa, contrasting with a maximum compression stress of 14.40 MPa at the cross-section middle near support. This stress distribution is complemented by a tensile strain of 0.57% and a compressive strain of -0.47% at their respective nodes.

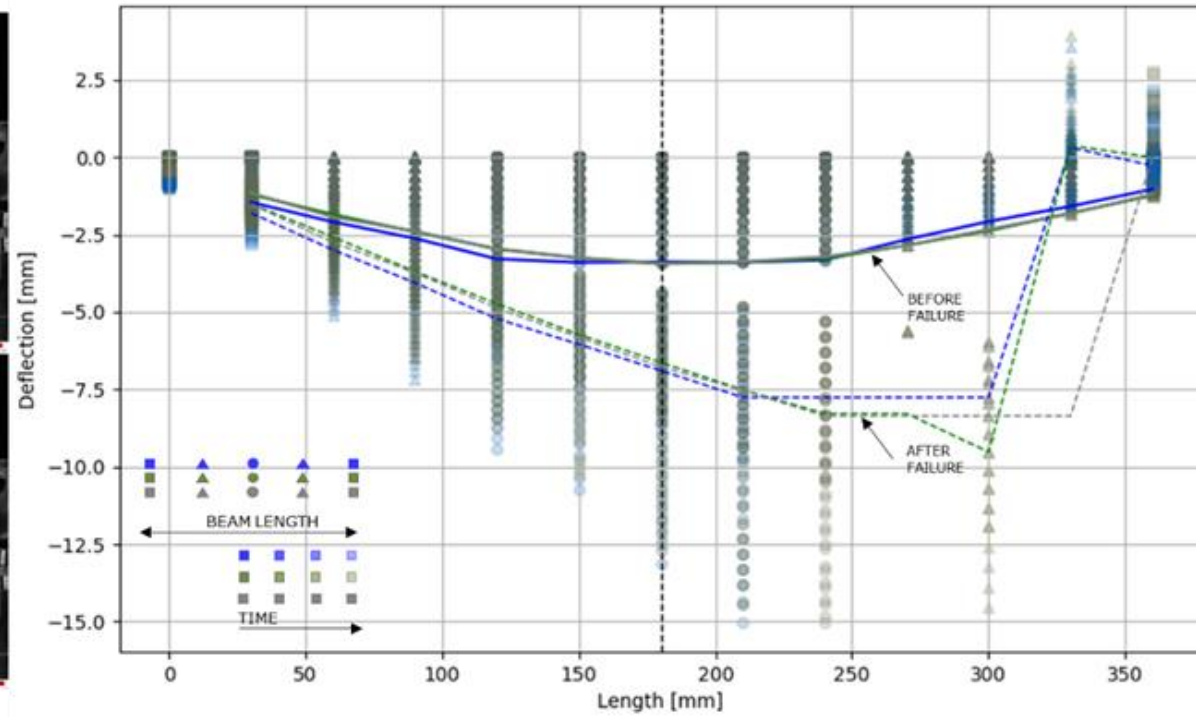
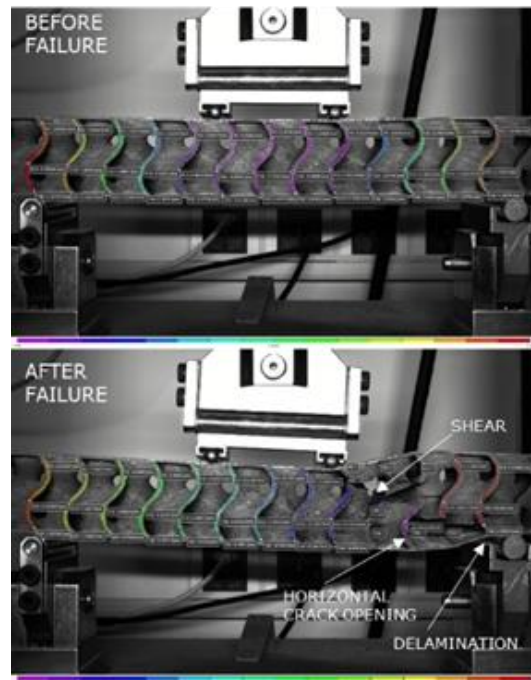


Figure 8.12 Sandwich beam: Displacement

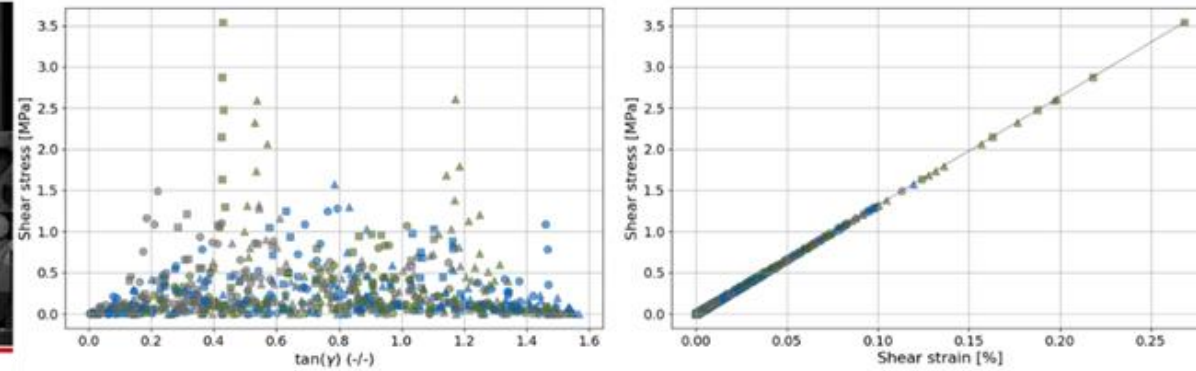


Figure 8.13 Sandwich beam: Shear stress vs. strain

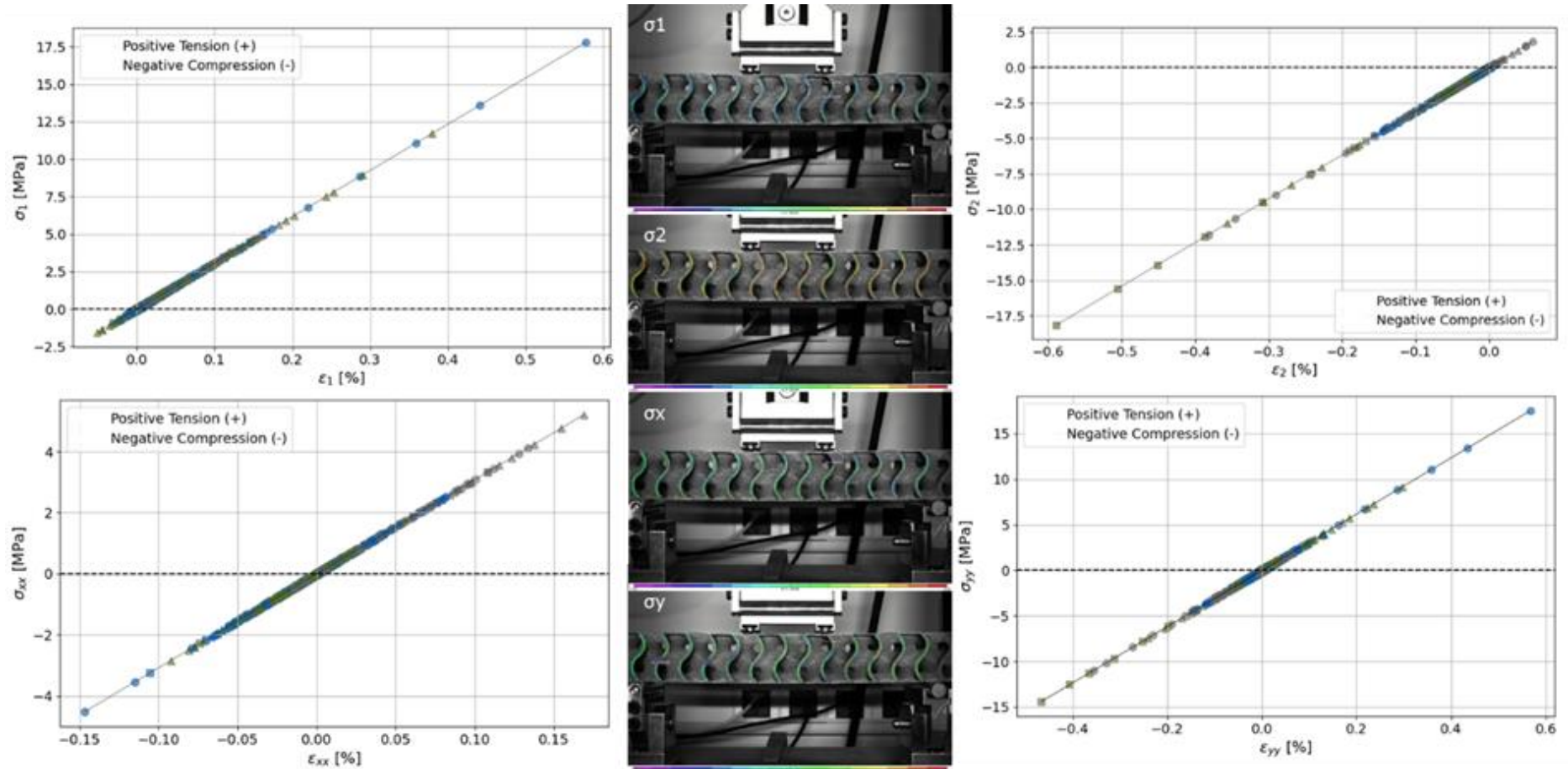


Figure 8.14 Sandwich beam: First principal stress vs. strain, second principal stress vs. strain, stress vs. strain in x direction (parallel to material deposition), stress vs. strain in y direction (orthogonal to material deposition)

8.3.3 Arch beam

The failure mode observed in “arch beam” significantly compromised the overall performance of the arch structure. Initially, crushing occurred at the top cross-section near the load location, subsequently propagating to neighbouring walls on the right (Figure 8.15).

Regarding shear stress and strain (Figure 8.16), the maximum shear stress recorded stands at 11.51 MPa, and the maximum shear strain is observed at 0.87%, both occurring at the top cross section in the middle of the arch span. The results obtained from the composite arch beam, based on the data collected just before failure, lead to the following conclusions regarding failure mechanisms: Firstly, a horizontal interlayer crack develops in the top cross-section due to tension perpendicular to the material deposition direction, followed by rapid delamination of the top face sheet from the core, along with brittle shear failure occurring in the top cross-section under load.

The stress and strain characteristics of “arch beam” are illustrated in Figure 8.17. In the direction parallel to the material deposition (σ_x), the analysis reveals a maximum tensile stress of 14.09 MPa and strain 0.46%, and a maximum compression stress of 4.40 MPa and strain 0.14%. Both stresses are observed predominantly at nodes located in the bottom cross section in the middle of the arch span for tensile stress and in the top cross section in the middle of the arch span for compressive stress. The maximum tensile strain is recorded at 0.46% while the maximum compressive strain is noted at 0.14%, both occurring at the bottom cross section in the middle of the arch span.

In the direction perpendicular to the material deposition, significantly higher stresses are observed, with a maximum tensile stress of 109.49 MPa and a maximum compression stress of 57.07 MPa. The maximum tensile strain is recorded at 3.55%, and the maximum compressive strain at 1.85%, with both occurring at the top cross section in the middle of the arch span for tensile stress and the lower middle cross section in the intermediate arch span for compressive stress.

Regarding the first principal stress/strain (ϵ_1), a maximum tensile stress of 115.86 MPa and a maximum tensile strain of 3.76% are observed, both occurring at the top cross section in the middle of the arch span. Moving to the second principal stress (ϵ_2), a maximum compression stress of 63.51 MPa and a maximum compression strain of 2.06% both occurring at the lower middle cross section in the intermediate arch span.

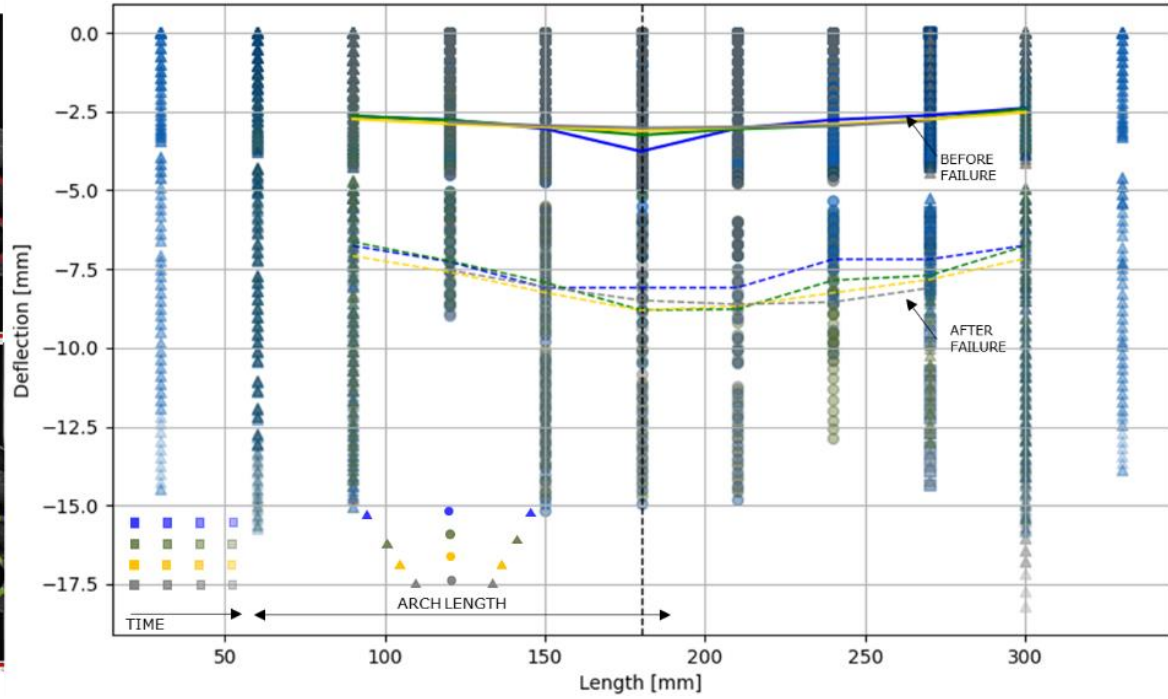
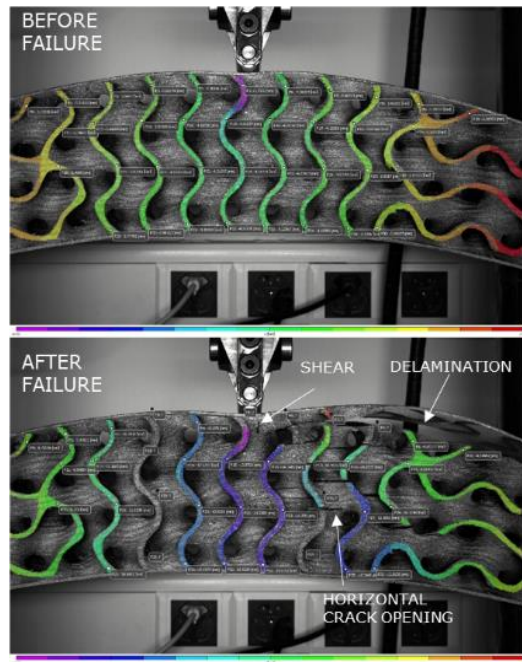


Figure 8.15 Arch beam: Displacement

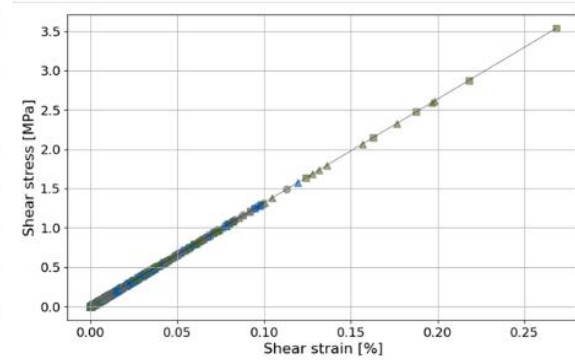
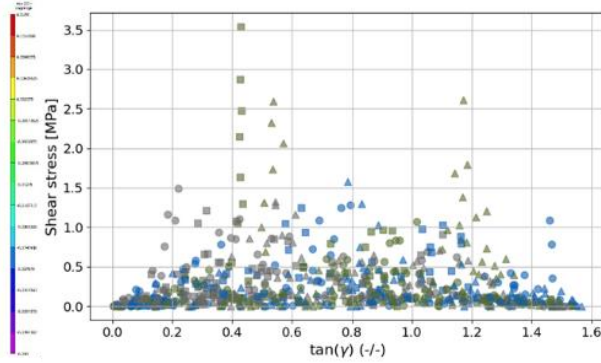
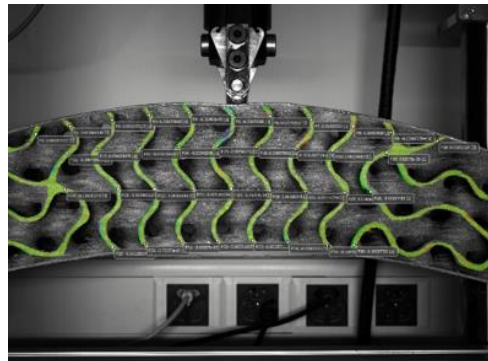


Figure 8.16 Arch beam: Shear stress vs. strain

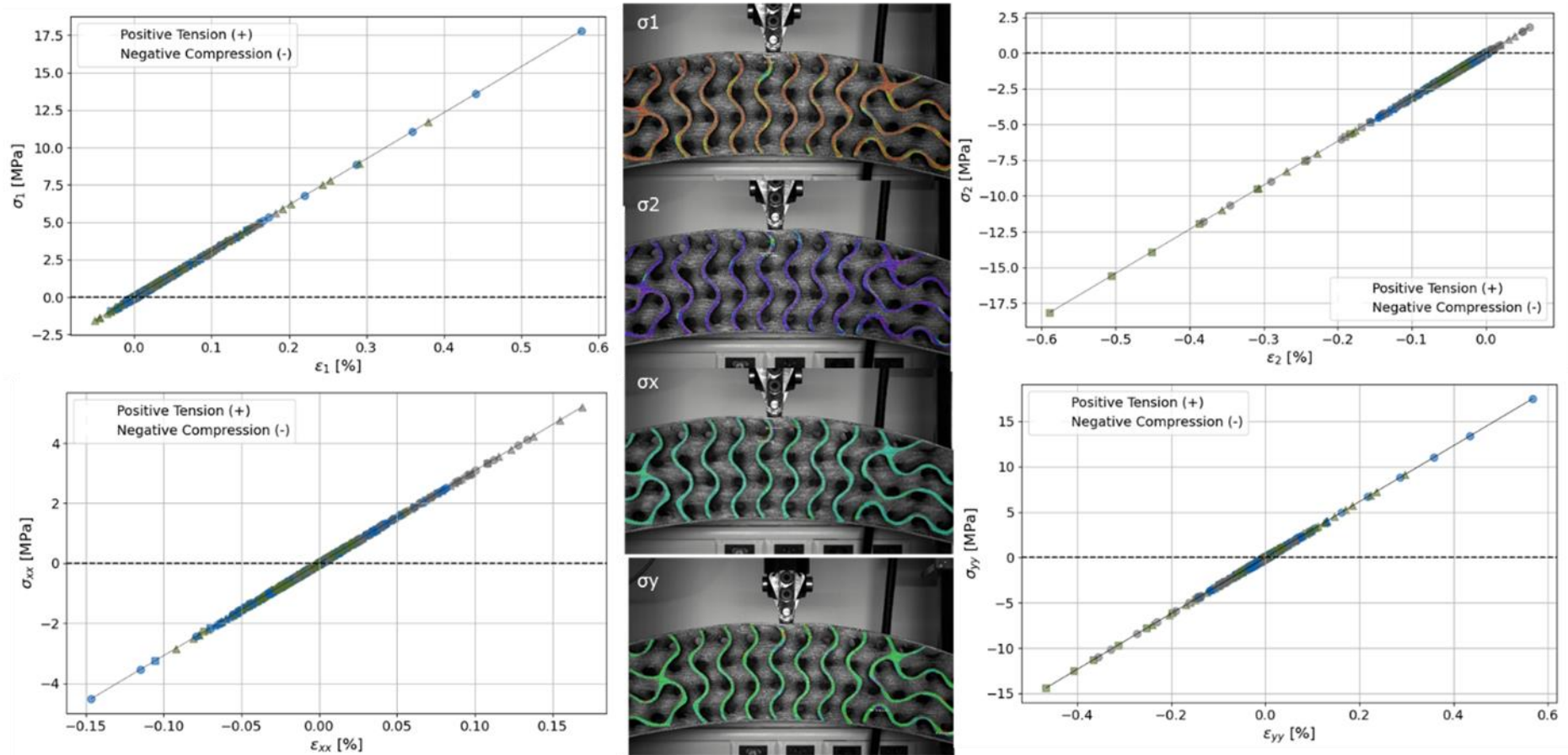


Figure 8.17 Arch beam: First principal stress vs. strain, second principal stress vs. strain, stress vs. strain in x direction (parallel to material deposition), stress vs. strain in y direction (orthogonal to material deposition)

8.3.4 Finite element models

The results from fracture analysis performed in Abaqus are presented in Figure 8.18. The material model was validated through FEM analysis on “core only” and it was determined that the XY print direction with a print layer height resolution of 0.6 mm was the most suitable. This choice also aligns with the print parameters of cellular structure (in the XY direction) and the layer thickness of 0.6 mm.

The “sandwich beam” was analysed and compared with two sandwich beam samples tested under bending. The analysis and laboratory tests demonstrated that the stiffness of “sandwich beam” and “arch beam” increased due to the manufacturing process of sandwich composite, which involved gluing the core to the face sheets with Biresin® CR83-2, that consequently impregnated into the zone of the top and bottom cross sections. These models successfully detected structural stiffness and identified failures occurring in the support zone through FEA (Figure 8.18). The analysis proved consistent with initial analytical calculations, which indicated that the face sheets have sufficient stiffness to control core deformation. The impressive finding is that “sandwich beam”, compared to “core only”, exhibits a nearly seven-fold increase in load-bearing capacity, and four times higher stiffness. With a relatively small increase of 25% in the total weight of the structure.

The 3-point bending test in “arch beam” that has uniform cellular periodicity of the core induced a concentrated force only in the middle top section which resulted in crushing of the thin lattice walls (Figure 8.19). Since the height of the cross sections was two times higher than in “sandwich beam” the system showed redundant behaviour. Nevertheless, the potential of the topology-optimized arch structures with cellular metamaterials should be further investigated, focusing on making smaller adjustments in core geometry to introduce more material into stress-concentrated zones. The FEA model successfully captured phenomena such as crushing, and delamination of the top face sheet compared to the testing. However, the lack of post-behaviour and crack propagation inside the 3D printing model should be addressed with a more detailed analysis that incorporates the thermal mechanical model of the 3D printing process.

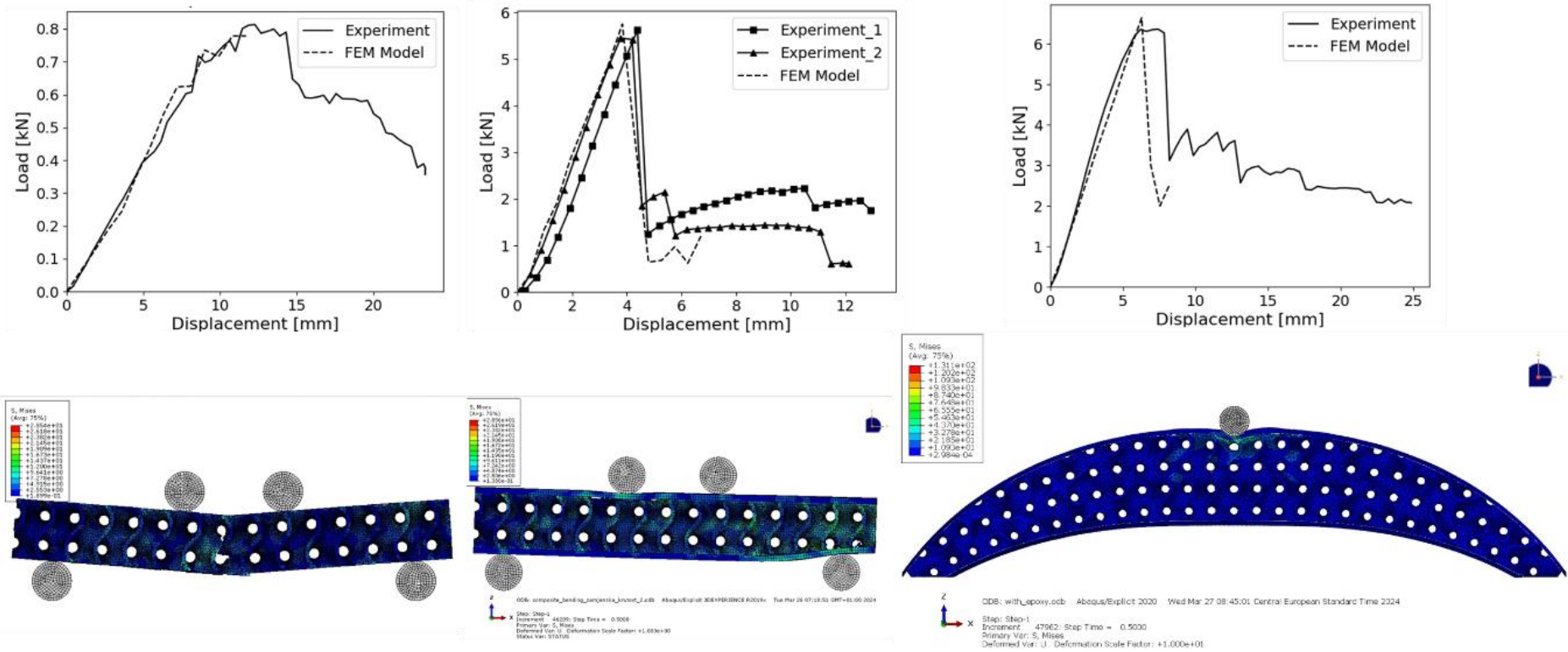


Figure 8.18 Comparison of load vs. displacement: FEM and experimental data for “core-only”, “sandwich beam”, and “arch beam”

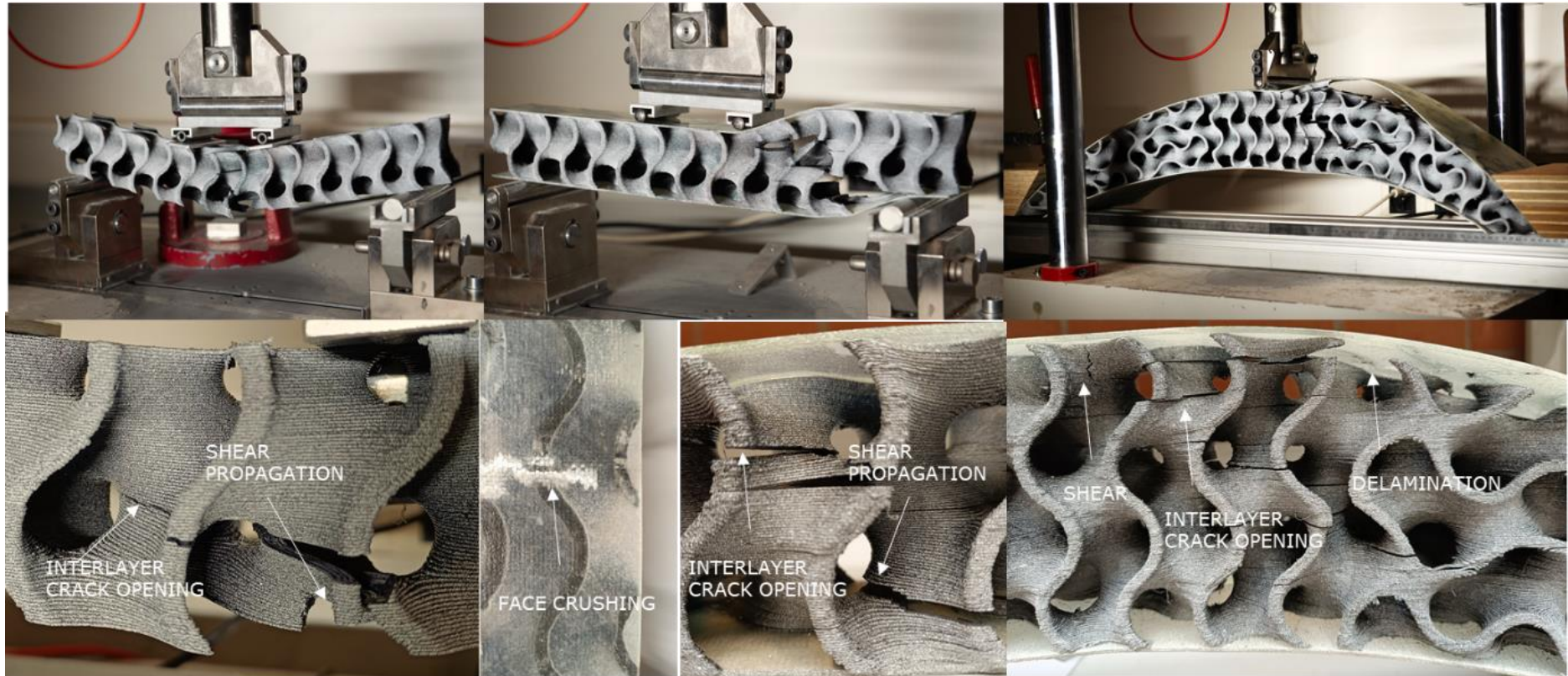


Figure 8.19 Failure modes detected for: “core only”; “sandwich beam”, “arch beam”

9 DISCUSSION

In this section, the results presented in the main chapters of the doctoral thesis are interpreted. Firstly, the findings from preliminary studies conducted on bridge decks with both 2D and 3D core geometries are discussed. Following the promising results of bridge decks with 3D core geometries, FDM materials were selected. The mechanical properties of the 3D-printed materials were then determined by tensile tests, considering the printing direction and print resolutions.

The detailed experimental and numerical investigations included compression tests on thirty samples of TPMS units with different morphologies and densities. Following validation, further parametric analysis and the development of design approaches for load-bearing elements were explored.

Finally, two novel structural systems produced and tested in the laboratory are discussed: a) a novel bridge deck with tempered glass face sheets and a topology-optimized core defined using a mathematical gradation algorithm; and b) a sandwich panel with a uniform TPMS core and irregular external volume bonded to GFRP face sheets.

9.1 PRELIMINARY INVESTIGATION OF COMPOSITE BRIDGE DECKS WITH LATTICE STRUCTURES

In a preliminary study, the finite element modelling of FRP bridge decks made of pultruded profiles and sandwich panels was performed in Abaqus. Typical infill geometries (rectangular, triangular, trapezoidal and honeycomb) were used, with two different materials for each infill, namely a quasi-isotropic material and a cross-ply laminate. The objective of this research was to analyse the effects of the arch shape and infill configuration of the bridge deck on the overall stiffness when compared to a flat bridge deck. In pultruded decks, hexagonal and triangular infill configurations show higher bending stiffness than rectangular ones, while honeycomb is the best configuration in sandwich panels. When comparing pultruded decks and sandwich panels under uniform load, pultruded profiles with longitudinal cavities are stiffer. There are research possibilities for finding new infill configurations, especially in TPMS infill geometries that could vary in density and cross-sectional height. The results justify the use of 3D printing technology and polymeric filament that allow variations in the shape and infill cell configuration of the bridge structure. Form finding could reduce the material cost of retaining

the structural integrity. The preliminary results showed there is a potential for future material and system investigation in TPMS cellular lattices for structural applications.

9.2 MECHANICAL CHARACTERIZATION OF 3D PRINTED MATERIAL

ASA, known for its excellent outdoor properties in FDM production, exhibits consistent mechanical properties, including modulus of elasticity, tensile strength, and elongation at break, in the XY and XZ directions. However, it displays significantly lower mechanical properties in the ZX direction, emphasizing the material's anisotropic nature. The result is as expected, as the load is aligned perpendicular to the layers. Moreover, there is a notable increase in result variability in the ZX direction when comparing virtual simulations with physical testing. These findings underscore the importance of considering material anisotropy and optimizing printing parameters to ensure consistent and reliable 3D-printed ASA components while addressing variability challenges in specific directions.

The thermo-mechanical analysis on ASA material has successfully demonstrated the correlation between theoretical predictions derived from a virtual simulation model and the outcomes of physical tensile tests on ASA material printed in three orthogonal directions. By utilizing ASA filament material and G-code geometry as input parameters, a comprehensive thermal analysis was conducted to simulate the influence of several factors on the quality of 3D-printed parts. This dynamic service analysis considered factors such as residual stresses from thermal model and void detection resulting from toolpath errors.

Employing FEA simulations, virtual testing, and a minimal amount of laboratory testing to validate the material model significantly streamlines and alleviates the financial burden associated with the 3D printing process. This research not only contributes to advancing our understanding of material behaviour in additive manufacturing but also underscores the practical utility of simulation methodologies in optimizing the production of high-quality 3D-printed components.

The second material investigation concerned the carbon-reinforced polymer material HI_TEMP CF, which was analysed for the three print directions (XY, XZ and ZX) and two print resolutions (0.3 and 0.6 mm). Consistent fracture modes were detected at different print resolutions within the same print direction. Significant differences were found in load capacity and strain deviations, especially noticeable in the specimens printed in the XY direction.

9.3 ANALYSIS APPROACHES

This doctoral thesis offers insight into detailed and simplified design methods through analytical formulations for rapid assessment of TPMS lattice's mechanical performance. These methods utilize statistically processed databases with numerical simulations and laboratory tests. Such an approach is promising for the integration of metamaterials into structural engineering as a preliminary design method that precedes the complex computational design process.

A calculation algorithm combining RVE Homogenization analysis and multilayer composite analysis with varied material selections was developed. The results obtained from these analyses exhibited a significant agreement with the FEM analysis, validating the accuracy of the proposed algorithm. The presented algorithm proves to be a valuable tool for the rapid estimation of composite sandwich panels and beams under the serviceability limit state (SLS), a critical factor in assessing their structural integrity. By incorporating TPMS infill and various flange materials, this approach offers new opportunities for designing and optimizing composite sandwich panels with bioinspired 3D printed infill cores. This combination allows for the exploration of different material combinations, layer thicknesses, TPMS selections, and structural systems, providing quick results in terms of achieving the desired stiffness-to-weight ratio of sandwich panels.

Different parametric designs for lattice structures were investigated as well. Various model configurations, including uniform and non-uniform lattice structures, graded designs, and hybrid geometries, provide valuable insights. The hybrid Diamond/Neovius structure shows a neutral stress distribution, although with some concentration in transitional regions. On the other hand, the Gyroid structure achieves a neutral stress distribution as the wall thickness increases in higher stress zones. It is concluded that non-uniformity brings no structural advantages when the comparison is made for the fixed weight parameter. The introduction of graded and hybrid structures contributes to isotropy but introduces notable anisotropic behaviour in the third direction.

9.4 TPMS UNITS

The exploration of TPMS metamaterials on a macro scale encompassed parametric designs, design approaches and laboratory tests of five different TPMS geometries, each tested at two different values of relative density (20% and 40%).

Compression tests reveal distinct failure modes, with anisotropic structures (Schwarz and Neovius) experiencing sudden catastrophic failure, while more isotropic structures (Gyroid, Diamond and Split) show enhanced safety due to the prolonged failure without catastrophic scenarios. Understanding the observed failure modes, including tension, wall buckling and shear, highlights the superior compression resistance of the Diamond structure compared to others. Both Diamond and Gyroid are identified as promising choices for various mechanical applications. However, caution is advised regarding anisotropic structures such as Neovius and Schwarz, as there is a risk of sudden structural failure.

9.5 COMPOSITE SANDWICH WITH TEMPERED GLASS FACE SHEETS

A parametrically designed plate with an auxetic core, 3D printed from polymeric material, and homogeneous top and bottom glass sheets were investigated. A numerical approach was proposed on two levels: a simplified approach with homogenization analysis that defines the three-dimensional geometry as orthotropic material with a substitute stiffness matrix, and a detailed FEM analysis using an elastic-plastic material model. To enhance accuracy, 3D printing parameters were integrated into the Finite Element Analysis (FEA), through elastic-plastic material model and homogenization analysis. The graded parametric design was introduced in sandwich panels. Core stiffness ratio and face sheet stiffness was analysed separately before integrating it into the composite.

Homogenization analysis approach has been validated with satisfactory results through comparison of FEM analysis on TPMS structure with TPMS substitute material properties. For structural analysis in software that does not utilize detailed FEM analysis and to reduce computational time for the design of complex TPMS structures, this method has been proposed. The implementation of this approach in future designs of large-scale TPMS structures or for preliminary analysis before conducting detailed FEM analysis would be beneficial.

The bending stiffness of the sandwich panel and the shear stiffness of the 3D printed core could be enhanced in future investigations through various measures. These may include adopting a higher resolution in 3D printing or using a larger nozzle diameter, incorporating denser material (since in this prototype only 10% of the core volume was filled with the Gyroid structure), and considering thicker walls for the Gyroid structure.

9.6 COMPOSITE SANDWICH WITH GFRP FACE SHEETS

The final investigation focused on composite sandwich elements comprising a Gyroid core and thin top and bottom faces made from GFRP sheets. Initially, the material characteristics were examined for the CF reinforced polymeric 3D printing material through tensile tests on dogbone specimens in three orthogonal printing directions and with two different layer thickness. Subsequently, the static bending response was investigated for the simply supported “core only”, “sandwich beam” and a fixed “arch beam”. The effect of the FDM additive manufacturing process was assessed by observing the fracture of the core material, which was then compared with the FEA model using the isotropic elastic material model. The following conclusions are drawn:

- Consistent fracture modes were detected across different print resolutions within the same print direction. Significant differences were found in load capacity and strain deviations, especially noticeable in specimens printed in the XY direction. Notably, while other print directions and resolutions showed similar stress/strain curves, specimens printed at both layer resolutions (0.3 mm and 0.6 mm) displayed a considerable decrease of approximately 30% in mechanical properties compared to the values listed in the technical data sheets.
- The bending test conducted on “core only” revealed that the XY print direction with a print layer height resolution of 0.6 mm emerged as the most suitable option. This selection is consistent with both the print parameters of the cellular structure (in the XY direction) and the layer thickness of 0.6 mm. FEM analysis employing the specified material model, yielded consistent results with the laboratory tests, demonstrating identical stiffness and failure modes. This alignment suggests that compression stress perpendicular to the material deposition during the 3D printing process induces interlayer delamination and crack opening, while the increased compression stress prolongs and exacerbates shear failure within the middle span.
- The stiffness characteristics of “sandwich beam”, particularly concerning displacement, exhibited a significant increase in stiffness when measuring a 3 mm displacement in the middle span, compared to “core only” by four times. These findings, observed in the composite sandwich beam data collected right before failure, shed light on the failure mechanisms: In scenarios where interlayer crack opening is absent, a brittle failure manifests in the compressed area during load introduction, followed by rapid shear propagation towards the support zone. Subsequently, delamination of the face sheets

from the core occurs in the support zone, resulting in the highest final compression in this region.

- The failure mode observed in “arch beam” shows horizontal interlayer crack development in the top cross-section due to tension perpendicular to the material deposition direction, followed by rapid delamination of the top face sheet from the core and brittle shear failure in the top cross-section under load. While the analysis on “arch beam” utilized the same material definition as “sandwich beam”, the 3-point bending test induced a concentrated force only in the middle top section, leading to the crushing of the thin lattice walls.

Using statistical interpretation to analyse the failure mechanisms of complex 3D geometries was analysed through DIC measurement and FEM analysis. This indicated that failure mechanisms of three-dimensional geometries can be predictable, with predominant shear failure but with robustness that shows promise for future load-bearing applications. Therefore, composite sandwiches with stochastic core structures result in a very brittle failure mode.

10 CONCLUSIONS

After both the experimental and numerical modelling campaign were conducted, the most significant conclusions are drawn as follows:

- Preliminary analysis has shown that TPMS bridge decks exhibit a stiffness increase of 40-60% compared to traditional FRP decks, while maintaining the same material properties. Considering new materials with reduced material properties caused by the manufacturing process (residual stresses, warpage, heat-affected zones, delamination, etc., are common problems in the production of 3D-printed parts), introducing topology optimization can effectively address these challenges while still demonstrating an enhancement in stiffness.
- Both materials (with and without fibre reinforcement) exhibit a decrease in mechanical properties in the ZX direction, highlighting the material's anisotropic nature resulting from the manufacturing process. This outcome was expected, considering that the tension load was aligned perpendicular to the layers.
- The 3D printed material with carbon fibres exhibited significantly higher mechanical properties compared to the unreinforced ASA material, despite ASA having a much finer print resolution (0.15 mm) compared to 0.3 mm and 0.6 mm for the CF material. The CF material was much stiffer but also more brittle, showing almost no ductility in all print directions.
- After validation through the FEM fracture analysis, it was determined that, for FDM printers, the elastoplastic material model derived from the tensile test conducted in the XY print direction proved to be the most suitable for beams undergoing bending. This choice is supported by the toolpath movement in the XY direction within one layer and moving for the specified layer height along the Z-axis.
- Compression tests conducted on TPMS units revealed diverse failure modes, distinguishing between anisotropic and more isotropic behaviours. Anisotropic structures like Schwarz and Neovius display sudden catastrophic failure, whereas Gyroid, Diamond, and Split, with greater isotropy, demonstrate propagated failure without catastrophic events, enhancing safety. Analysis of observed failure modes, including tension, wall buckling, and shear, highlights Diamond's superior compression resistance compared to others. Consequently,

Diamond and Gyroid emerge as promising options for various load bearing applications.

- A calculation algorithm developed within this dissertation combines RVE Homogenization and multilayer composite analysis with diverse material choices, demonstrating strong alignment with FEM analysis. This tool proves invaluable for estimating the bending stiffness of composite sandwich panels and beams. By integrating TPMS infill and a variety of flange materials, it creates opportunities for enhancing the optimization of composite sandwich panels.
- The FEM analysis, integrating thermo-mechanical analysis on 3D printed parts, validated the correlation between numerical predictions from virtual simulations and physical tests. By defining the material and geometry input parameters for the comprehensive thermal analysis, factors affecting 3D-printed part quality, such as residual stresses and void detection due to toolpath errors, are predicted with high accuracy. Despite the notable increase in computational time, this tool proves invaluable for future prototyping, minimizing trial and error approaches.
- The sandwich beam showed approximately a four-time increase in stiffness and seven times load bearing capacity increase compared to the non-sandwich system with a 3D printed lattice structure alone.
- The findings from the composite sandwich beam with GFRP face sheets and tempered glass sheets reveal similar failure modes. In the innovative bridge deck system, featuring a low-density topology optimized TPMS core and tempered glass face sheet, failure occurred with cracks developing between print layers, resulting in brittle failure of the top glass flange and shear failure of the core walls.
- The difference between these two sandwich systems lay in the significantly higher bending stiffness of tempered glass compared to the core, and the GFRP sheets compared to their core. The fixed bond between the glass flanges and the Gyroid structure prevented glass deformation, resulting in brittle fracture as compression stress intensified. In contrast, the GFRP face sheets exhibited only local crushing while maintaining their integrity. After unloading, the sandwich with GFRP composite returned almost to its initial position, while the sandwich with tempered glass, due to the glass fracture, was irreversible.

10.1 Research hypothesis verification

In this chapter, the hypotheses are discussed, based on the outcomes of the experimental tests and the numerical modelling campaign.

H1: Diamond and Gyroid TPMS structures are the most applicable for load-bearing structural elements.

Five different TPMS geometries and two different densities were tested in the laboratory and compared with numerical analysis. The initial comparison was drawn based on the densities. In TPMS structures with a relative density of 20%, but with a more anisotropic behaviour (Schwarz and Neovius), tension perpendicular to the bead interface and crushing occurred, accompanied by a sudden material rupture. In TPMS structures with a higher relative density (40%) but with a more isotropic behaviour (Gyroid, Diamond and Split), together with the anisotropic Neovius structure, tension perpendicular to the bead interface, reduced wall buckling due to thicker walls and shear occurred. The denser Schwarz structure exhibited the same failure modes as its lighter counterpart (tension perpendicular and crushing), while the Neovius structures exhibited significant wall buckling, tension perpendicular and crushing at both 20% and 40% relative density.

The comparison drawn from the TPMS morphologies is as follows. The Diamond structure exhibited superior compressive force, reaching maximum values of 8.36 kN at 20% relative density and 20.10 kN at 40% relative density. Conversely, the Schwarz structure demonstrated the lowest force, with minimum values of 1.55 kN and 9.48 kN before brittle fracture occurred at both densities. Neovius, another isotropic geometry, performed well under uniaxial compression loading, closely following Diamond with 7.78 kN and 18.75 kN for 20% and 40% relative densities, respectively. Diamond also exhibited the greatest elongation before significant failure. Gyroid and Split, both isotropic materials, offer advantages in terms of isotropic behaviour and high mechanical performance. While Split's large surface area may not be suitable for applications requiring long printing times and a large number of finite elements.

Based on the aforementioned statements, Diamond and Gyroid are most suitable for load-bearing structural elements and were further considered in parametric design due to their promising attributes and appealing aesthetics.

H2: A topology-optimized structure using a TPMS structure leads to uniform stress distribution, resulting in material and cost savings.

The stress distribution within the TPMS cellular structure was initially analysed numerically at the level of TPMS units and subsequently as part of a sandwich structure. Considering the results obtained on TPMS units, which confirmed Hypothesis 1, Diamond and Gyroid emerged as the most favourable geometries. Diamond exhibited superior compressive behaviour and Gyroid was chosen for further analysis due to its isotropic properties and smaller surface area compared to Split. Neovius, with favourable uniaxial compressive properties, is examined within a hybrid material configuration. Various lattice configurations including unit cell designs based on mathematical algorithms and topology optimization, as well as non-uniform lattice structures based on structural and functional gradient designs, and hybrid geometries, were examined. The analysis indicates that the non-uniform Gyroid lattice optimized by structural optimization demonstrates the most uniform stress distribution. Conversely, the hybrid Diamond/Neovius structure shows the most neutral stress distribution in the Diamond structure, along with some stress concentration in the transitional region. In terms of stiffness, the Diamond structure consistently exhibits higher stiffness than the Gyroid structure across different material configurations at identical relative densities. Additionally, the introduction of graded and hybrid structures contributes to isotropy in two orthogonal directions, but significant anisotropic behaviour remains in the third direction. Structural optimization, achieved by changes in wall thickness, results in the most uniform stress distribution. However, while gradation in unit size may not neutralize stresses, it does offer other structural advantages.

In preliminary numerical analysis on sandwich decks with TPMS core topology optimization was applied to the Gyroid deck to reduce overall weight. The Gyroid unit was modelled with a 500x500x500 mm grid, with wall thickness varying from 10 to 50 mm based on von Mises stress values from static analysis of the solid. The optimized TPMS gyroid deck was 80% lighter than the solid and 57% lighter than the uniform TPMS gyroid deck, with only 18% higher deformation. Additionally, with the same total volume but double the weight and a 50% degradation in modulus of elasticity, the stiffness of the optimized structure increases by 23%, with neutral stress distribution throughout the deck.

Following the results of numerical analysis confirming Hypothesis 2, the research extended to experimental investigation. The Gyroid, with its isotropic properties, high specific bending stiffness, and interconnected pores enabling light transmission throughout the

structure, was chosen as the core structure for manufacturing scaled prototypes of sandwich bridge deck panels. Two sandwich systems were proposed within this dissertation. The first prototype consisted of an ASA material topology optimized Gyroid core, incorporating combined unit size gradation and wall thickness adjustments based on stress distribution. The core was additively manufactured and then bonded to tempered glass flanges to create the sandwich system. The second prototypes comprised a carbon fibre-reinforced polymer with a uniform cellular lattice in a flat, simply supported beam, and a uniform cellular lattice in an arched, fixed beam, with outer geometry inspired by the Da Vinci bridge design. Even though the preliminary analysis, modelled with isotropic material, showed promising neutral stress distribution within the entire TPMS core structure, the inevitable anisotropy from the filament material at the microscale and anisotropy from the FDM production process observed at the mesoscale led to premature failure. This failure initiated from interlayer crack opening and propagated into shear failure of the core walls. This anisotropy was successfully incorporated into the FEM using an elastic-plastic material definition.

The overall conclusion is that topology optimized TPMS cellular structures theoretically exhibit uniform stress distribution. However, due to 3D printing, residual stresses and porosity are introduced. This becomes more significant when considering the size-effect, which will be inevitable for larger-scale 3D printed objects requiring fast production. The topology optimization through controlled material redistribution can significantly impact the normalization of stress distribution and increase the load-bearing capacity, thereby proving the H2 hypothesis.

Understanding of the 3D printing material and 3D printing process is essential for the 3D printed part's failure mechanisms prediction. High bending stiffness and robustness of sandwich decks with TPMS cellular core shows promise for future load-bearing applications.

10.2 Scientific contribution of proposed research

Based on the experimental testing of the material, the mechanical properties of the 3D printed material (100% infill) were determined, taking into account the direction and quality of the printing. Based on the test results, the material model was calibrated and further used in the numerical analysis. As many parts and products will be manufactured using additive manufacturing in the future, testing of 3D-printed items is essential for comprehensive product design and possible future standardization. Testing materials produced by additive manufacturing is key to understanding how materials work and how designs can be improved for more reliable products.

There is a lack of research on large 3D printed parts, particularly in TPMS cellular structures, whose implementation is evident primarily in tissue engineering and mechanical engineering at a much smaller and finer level of detail compared to architectural and structural components. Therefore, this research represents an innovation in structural design, introducing organic structures through mathematically controlled parameters.

This research has validated several design approaches that bring TPMS lattices to practical applications. After the detailed FEM analysis was validated through laboratory tests, simplified design approaches were proposed, including a fast estimation algorithm developed within this dissertation.

Homogenization of mechanical properties for TPMS lattices with different porosity was performed in nTopology and Abaqus software. The laboratory tests were validated through detailed FEM analysis on 3D printed TPMS units. A TPMS unit is considered as a new material with a different stiffness matrix, which is determined in a homogenization analysis. Applying the new material properties to the solid body will result in a faster analysis that can be performed in any software for structural analysis.

The use of TPMS geometries, especially in load-bearing sandwich structures will lead to a great improvement in structural properties while increasing visual attractiveness.

Topology optimization of structural elements using parametric TPMS geometry was performed to achieve uniform stress distribution. The final results lead to an optimal shape and geometry applicable to a specific project, regardless of standard structural shapes and based on the chosen material. Additive manufacturing will be the production process that removes all obstacles to producing complex geometries.

10.3 Recommendations for future research

In structural engineering, the potential applications of 3D printing for mechanical metamaterials are vast, yet few studies have explored this area extensively, leaving ample room for innovation and further research. In following example, a non-uniform lattice structure, optimized structurally, was applied to a solid square panel wall fixed on four sides. This involved a parametric design utilizing a scalar field derived from a stress point map. Figure 10.1 showcases the Gyroid and Schwarz walls with varying TPMS relative density and an outer glass surface.

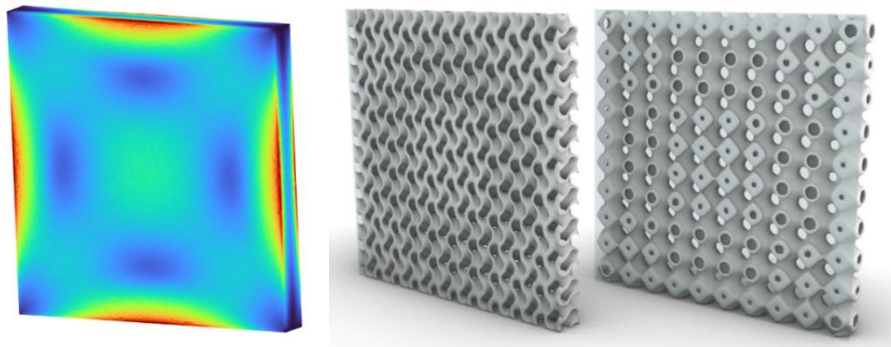


Figure 10.1 Panel wall with non-uniform lattice structure based on structural optimization

Based on the conducted theoretical evaluation, the knowledge obtained experimentally and numerically, the following recommendations are given for future research:

- Introduction of bio composite material into 3D printing is recommended.
- Exploration of various TPMS morphologies within sandwich systems and investigation of their application in other structural components such as insulation and load-bearing walls, columns, frames, and domes are suggested.
- Development of new non-stochastic cellular core structures with higher levels of ductility, load-bearing capacity, and stiffness, while maintaining relatively high porosity and low mass.
- Further investigation into topology-optimized arch structures with cellular metamaterials.
- The production process of full-scale load-bearing elements using a robotic arm FDM should be considered and further investigated.
- It is advisable to gather data through the monitoring of novel sandwich bridge systems to enhance the scope of data collection throughout their service life.
- Software development with design capabilities incorporating the 3D printing process and 3D printed materials is encouraged.



The design freedom afforded by additive manufacturing can revolutionize architecture and structural design, leading to material and cost savings, faster production, lighter and more organic structures, attractive designs, and overall, more sustainable construction practices. Therefore, further research in this field is imperative, and the education of future architects and engineers can play a crucial role in accelerating the adoption of advanced technologies and materials in civil engineering and architecture.

REFERENCES

- [1] I. Gibson, D. Rosen, B. Stucker, *Additive Manufacturing Technologies; 3D Printing, Rapid Prototyping, and Direct Digital Manufacturing*, 2015.
- [2] Z. Li, Z. Chen, X. Chen, R. Zhao, Multi-objective optimization for designing porous scaffolds with controllable mechanics and permeability: A case study on triply periodic minimal surface scaffolds, *Compos. Struct.* 333 (2024) 117923. <https://doi.org/10.1016/j.compstruct.2024.117923>.
- [3] J.M. Jafferson, H. Sharma, Design of 3D printable airless tyres using NTopology, *Mater. Today Proc.* 46 (2021) 1147–1160. <https://doi.org/10.1016/j.matpr.2021.02.058>.
- [4] M.R. Talagani, S. Dormohammadi, R. Dutton, C. Godines, H. Baid, F. Abdi, V. Kunc, B. Compton, S. Simunovic, C. Duty, L. Love, B. Post, C. Blue, Numerical simulation of big area additive manufacturing (3D printing) of a full size car, *SAMPE J.* 51 (2015) 27–36.
- [5] A.H. Alami, A. Ghani Olabi, A. Alashkar, S. Alasad, H. Aljaghoub, H. Rezk, M.A. Abdelkareem, Additive manufacturing in the aerospace and automotive industries: Recent trends and role in achieving sustainable development goals, *Ain Shams Eng. J.* 14 (2023) 102516. <https://doi.org/10.1016/j.asej.2023.102516>.
- [6] R. Hedayati, *3D Printing for Space Habitats : Requirements , Challenges , and Recent Advances*, (2023).
- [7] P. Kyvelou, C. Buchanan, L. Gardner, Numerical Modelling of the World ’ s First Metal 3D Printed Bridge, *5* (2022). <https://doi.org/10.1002/cepa.1728>.
- [8] L. Stepinac, A. Skender, D. Damjanović, J. Galić, Frp pedestrian bridges—analysis of different infill configurations, *Buildings* 11 (2021) 1–16. <https://doi.org/10.3390/buildings11110564>.
- [9] *3D Printed Bridge*, (2019). <https://polymaker.com/3d-printed-bridge/>.
- [10] A. Akman, A. Sadhu, Recent Development of 3D-Printing Technology in Construction Engineering, *Pract. Period. Struct. Des. Constr.* 29 (2024). <https://doi.org/10.1061/PPSCFX.SCENG-1278>.
- [11] J.-J. Cabibihan, A. Gaballa, F. Fadli, M. Irshidat, E. Mahdi, N. Bitoria, Z. Mansour, H. Abdulrazak, A guided approach for utilizing concrete robotic 3D printing for the architecture, engineering, and construction industry, *Constr. Robot.* 7 (2023) 265–278. <https://doi.org/10.1007/s41693-023-00103-9>.
- [12] Q. Chen, Y. Gao, L. Ding, C. Zhou, W. Han, Y. Zhou, Y. Shi, Genetic Algorithm–Based

- Multiobjective Optimization for 3D Printable Design of a Double-Shell Lunar Habitat Structure, *J. Aerosp. Eng.* 36 (2023) 1–20. <https://doi.org/10.1061/jaeeez.aseng-4755>.
- [13] G. Serin, M. Kahya, H.O. Unver, N. Durlu, A REVIEW OF ADDITIVE MANUFACTURING TECHNOLOGIES Production of Ti-6Al-4V Alloys Used in Aerospace Industry by Additive Manufacturing View project Deep Learning for Intelligent Manufacturing View project, (2018).
- [14] A. Jipa, M. Bernhard, B. Dillenburger, M. Meibodi, M. Aghaei-Meibodi, 3D-Printed Stay-in-Place Formwork for Topologically Optimized Concrete Slabs, 2016 TxA Emerg. Des. + Technol. (2016) 96–107. [internal-pdf://0960461026/Jipa-2017.pdf%0Ahttps://www.research-collection.ethz.ch/443/handle/20.500.11850/237082](https://www.research-collection.ethz.ch/443/handle/20.500.11850/237082).
- [15] I. Maskery, N.T. Aboulkhair, A.O. Aremu, C.J. Tuck, I.A. Ashcroft, Compressive failure modes and energy absorption in additively manufactured double gyroid lattices, *Addit. Manuf.* 16 (2017) 24–29. <https://doi.org/10.1016/j.addma.2017.04.003>.
- [16] M. Mansour, K. Tsongas, D. Tzetzis, A. Antoniadis, Mechanical and Dynamic Behavior of Fused Filament Fabrication 3D Printed Polyethylene Terephthalate Glycol Reinforced with Carbon Fibers, *Polym. - Plast. Technol. Eng.* 57 (2018) 1715–1725. <https://doi.org/10.1080/03602559.2017.1419490>.
- [17] T.A.M. Salet, Z.Y. Ahmed, F.P. Bos, H.L.M. Laagland, Design of a 3D printed concrete bridge by testing*, *Virtual Phys. Prototyp.* 13 (2018) 222–236. <https://doi.org/10.1080/17452759.2018.1476064>.
- [18] C. Daniel R, E. Sudhagar P, Evaluation of transverse shear properties of various 3D-printed bioinspired modified honeycomb core: Numerical and experimental study, *Mech. Based Des. Struct. Mach.* 0 (2023) 1–25. <https://doi.org/10.1080/15397734.2023.2200819>.
- [19] I. Maskery, A. Hussey, A. Panesar, A. Aremu, C. Tuck, I. Ashcroft, R. Hague, An investigation into reinforced and functionally graded lattice structures, *Ultrasonics ...* (2022) 106705. <https://doi.org/10.1177/ToBeAssigned>.
- [20] E. Cuan-Urquizo, R. Guerra Silva, Fused Filament Fabrication of cellular, lattice and porous mechanical metamaterials: a review, *Virtual Phys. Prototyp.* 18 (2023). <https://doi.org/10.1080/17452759.2023.2224300>.
- [21] H. Guo, J. Xu, S. Zhang, G. Yi, Build orientation optimization based on weighted analysis of local surface region curvature, *Appl. Sci.* 11 (2021) 1–20. <https://doi.org/10.3390/app11010304>.

- [22] N. Hack, W. Lauer, S. Langenberg, F. Gramazio, M. Kohler, Overcoming repetition: Robotic fabrication processes at a large scale, *Int. J. Archit. Comput.* 11 (2013) 285–300. <https://doi.org/10.1260/1478-0771.11.3.285>.
- [23] A. Paolini, S. Kollmannsberger, E. Rank, Additive manufacturing in construction: A review on processes, applications, and digital planning methods, *Addit. Manuf.* 30 (2019). <https://doi.org/10.1016/j.addma.2019.100894>.
- [24] S. Besklubova, M.J. Skibniewski, X. Zhang, Factors Affecting 3D Printing Technology Adaptation in Construction, *J. Constr. Eng. Manag.* 147 (2021). [https://doi.org/10.1061/\(ASCE\)CO.1943-7862.0002034](https://doi.org/10.1061/(ASCE)CO.1943-7862.0002034).
- [25] A. Nega, D. Gedafa, A Review of the Application of Artificial Intelligence, Remote Sensing, and 3D Printing for the Sustainability of Civil Infrastructure, in: *ASCE Inspire 2023*, American Society of Civil Engineers, Reston, VA, 2023: pp. 123–132. <https://doi.org/10.1061/9780784485163.015>.
- [26] N. Strömberg, A new multi-scale topology optimization framework for optimal combinations of macro-layouts and local gradings of TPMS-based lattice structures, *Mech. Based Des. Struct. Mach.* 0 (2022) 1–18. <https://doi.org/10.1080/15397734.2022.2107538>.
- [27] Q.Q. Liang, Y.M. Xie, P.S. Grant, OPTIMAL TOPOLOGY DESIGN OF BRACING SYSTEMS FOR MULTISTORY STEEL FRAMES, (2000) 823–829.
- [28] O. Al-Ketan, R. Rowshan, R.K. Abu Al-Rub, Topology-mechanical property relationship of 3D printed strut, skeletal, and sheet based periodic metallic cellular materials, *Addit. Manuf.* 19 (2018) 167–183. <https://doi.org/10.1016/j.addma.2017.12.006>.
- [29] Y. Han, W.F. Lu, A novel design method for nonuniform lattice structures based on topology optimization, *J. Mech. Des.* 140 (2018) 1–10. <https://doi.org/10.1115/1.4040546>.
- [30] Z. Wang, Y. Zhang, A. Bernard, Lightweight porous support structure design for additive manufacturing via knowledge-based bio-inspired volume generation and lattice configuration, *Virtual Phys. Prototyp.* 17 (2022) 894–918. <https://doi.org/10.1080/17452759.2022.2090015>.
- [31] Z. Zhang, Y. Li, W. Zhou, X. Chen, W. Yao, Y. Zhao, TONR: An exploration for a novel way combining neural network with topology optimization, *Comput. Methods Appl. Mech. Eng.* 386 (2021). <https://doi.org/10.1016/j.cma.2021.114083>.
- [32] L.J. Gibson, Biomechanics of cellular solids, *J. Biomech.* 38 (2005) 377–399.

- <https://doi.org/10.1016/j.jbiomech.2004.09.027>.
- [33] S.H. Siddique, P.J. Hazell, H. Wang, J.P. Escobedo, A.A.H. Ameri, Lessons from nature: 3D printed bio-inspired porous structures for impact energy absorption – A review, *Addit. Manuf.* 58 (2022) 103051. <https://doi.org/10.1016/j.addma.2022.103051>.
- [34] J. Zhang, X. Chen, Y. Sun, J. Yang, R. Chen, Y. Xiong, W. Hou, L. Bai, Design of a biomimetic graded TPMS scaffold with quantitatively adjustable pore size, *Mater. Des.* 218 (2022) 110665. <https://doi.org/10.1016/j.matdes.2022.110665>.
- [35] Y. Yang, Q. Zhu, W. Wang, X. Peng, Structure bionic design method oriented to integration of biological advantages, (2021).
- [36] L.J. Gibson, M.F. Ashby, Cellular solids: Structure and properties, *J. Biomech.* 22 (1989) 397. [https://doi.org/10.1016/0021-9290\(89\)90056-0](https://doi.org/10.1016/0021-9290(89)90056-0).
- [37] P. Zhang, J. Toman, Y. Yu, E. Biyikli, M. Kirca, M. Chmielus, A.C. To, Efficient design-optimization of variable-density hexagonal cellular structure by additive manufacturing: Theory and validation, *J. Manuf. Sci. Eng. Trans. ASME* 137 (2015) 41–45. <https://doi.org/10.1115/1.4028724>.
- [38] W. Gao, Y. Zhang, D. Ramanujan, K. Ramani, Y. Chen, C.B. Williams, C.C.L. Wang, Y.C. Shin, S. Zhang, P.D. Zavattieri, The status, challenges, and future of additive manufacturing in engineering, *CAD Comput. Aided Des.* 69 (2015) 65–89. <https://doi.org/10.1016/j.cad.2015.04.001>.
- [39] J. Feng, J. Fu, X. Yao, Y. He, Triply periodic minimal surface (TPMS) porous structures: from multi-scale design, precise additive manufacturing to multidisciplinary applications, *Int. J. Extrem. Manuf.* 4 (2022) 022001. <https://doi.org/10.1088/2631-7990/ac5be6>.
- [40] X. Zhang, L. Jiang, X. Yan, Z. Wang, X. Li, G. Fang, Revealing the apparent and local mechanical properties of heterogeneous lattice: a multi-scale study of functionally graded scaffold, *Virtual Phys. Prototyp.* 18 (2023). <https://doi.org/10.1080/17452759.2022.2120406>.
- [41] B. Khoshnevis, D. Hwang, K.-T. Yao, Z. Yeh, Mega-scale fabrication by contour crafting Behrokh Khoshnevis, *Int. J. Ind. Syst. Eng.* 1 (2006) 301–306.
- [42] N. Strömberg, A new multi-scale topology optimization framework for optimal combinations of macro-layouts and local gradings of TPMS-based lattice structures, *Mech. Based Des. Struct. Mach.* 0 (2022) 1–18. <https://doi.org/10.1080/15397734.2022.2107538>.
- [43] D. Sharma, S.S. Hiremath, Additively manufactured mechanical metamaterials based on

- triply periodic minimal surfaces: Performance, challenges, and application, *Mech. Adv. Mater. Struct.* 29 (2022) 5077–5107. <https://doi.org/10.1080/15376494.2021.1948151>.
- [44] L. Han, S. Che, An Overview of Materials with Triply Periodic Minimal Surfaces and Related Geometry: From Biological Structures to Self-Assembled Systems, *Adv. Mater.* 30 (2018). <https://doi.org/10.1002/adma.201705708>.
- [45] L. Han, S. Che, An Overview of Materials with Triply Periodic Minimal Surfaces and Related Geometry: From Biological Structures to Self-Assembled Systems, *Adv. Mater.* 30 (2018). <https://doi.org/10.1002/adma.201705708>.
- [46] M. Rezapourian, I. Jasiuk, M. Saarna, I. Hussainova, Selective laser melted Ti6Al4V split-P TPMS lattices for bone tissue engineering, *Int. J. Mech. Sci.* 251 (2023) 108353. <https://doi.org/10.1016/j.ijmecsci.2023.108353>.
- [47] B. Castanie, C. Bouvet, M. Ginot, Review of composite sandwich structure in aeronautic applications, *Compos. Part C Open Access* 1 (2020). <https://doi.org/10.1016/j.jcomc.2020.100004>.
- [48] W. Lee, D.Y. Kang, J. Song, J.H. Moon, D. Kim, Controlled Unusual Stiffness of Mechanical Metamaterials, *Sci. Rep.* 6 (2016) 1–7. <https://doi.org/10.1038/srep20312>.
- [49] C. Wu, C. Chen, C. Cheeseman, Size Effects on the Mechanical Properties of 3D Printed Plaster and PLA Parts, *J. Mater. Civ. Eng.* 33 (2021). [https://doi.org/10.1061/\(ASCE\)MT.1943-5533.0003787](https://doi.org/10.1061/(ASCE)MT.1943-5533.0003787).
- [50] Y. Tang, Y.F. Zhao, A survey of the design methods for additive manufacturing to improve functional performance, *Rapid Prototyp. J.* 22 (2016) 569–590. <https://doi.org/10.1108/RPJ-01-2015-0011>.
- [51] O. Al-Ketan, R. Rowshan, R.K. Abu Al-Rub, Topology-mechanical property relationship of 3D printed strut, skeletal, and sheet based periodic metallic cellular materials, *Addit. Manuf.* 19 (2018) 167–183. <https://doi.org/10.1016/j.addma.2017.12.006>.
- [52] C. Lin, G. Wen, H. Yin, Z.P. Wang, J. Liu, Y.M. Xie, Revealing the sound insulation capacities of TPMS sandwich panels, *J. Sound Vib.* 540 (2022). <https://doi.org/10.1016/j.jsv.2022.117303>.
- [53] P. Sengsri, H. Fu, S. Kaewunruen, Mechanical Properties and Energy-Absorption Capability of a 3D-Printed TPMS Sandwich Lattice Model for Meta-Functional Composite Bridge Bearing Applications, *J. Compos. Sci.* 6 (2022) 71. <https://doi.org/10.3390/jcs6030071>.
- [54] B. Liu, J. Feng, Z. Lin, Y. He, J. Fu, Controllable three-dimension auxetic structure

- design strategies based on triply periodic minimal surfaces and the application in hip implant, *Virtual Phys. Prototyp.* 18 (2023). <https://doi.org/10.1080/17452759.2023.2170890>.
- [55] S.K. Patiballa, G. Krishnan, On the design of three-dimensional mechanical metamaterials using load flow visualization, *Mech. Based Des. Struct. Mach.* 50 (2022) 442–467. <https://doi.org/10.1080/15397734.2020.1719506>.
- [56] J. Mahdinejad Gorji, G. Payganeh, R. Moradi-Dastjerdi, Mechanical and energy absorption behavior of an innovative high-performance auxetic structure, *Mech. Based Des. Struct. Mach.* 0 (2023) 1–20. <https://doi.org/10.1080/15397734.2023.2177863>.
- [57] N. Novak, M. Borovinšek, O. Al-Ketan, Z. Ren, M. Vesenjak, Impact and blast resistance of uniform and graded sandwich panels with TPMS cellular structures, *Compos. Struct.* 300 (2022). <https://doi.org/10.1016/j.compstruct.2022.116174>.
- [58] G. Liu, X. Zhang, X. Chen, Y. He, L. Cheng, M. Huo, J. Yin, F. Hao, S. Chen, P. Wang, S. Yi, L. Wan, Z. Mao, Z. Chen, X. Wang, Z. Cao, J. Lu, Additive manufacturing of structural materials, *Mater. Sci. Eng. R Reports* 145 (2021) 100596. <https://doi.org/10.1016/j.mser.2020.100596>.
- [59] S. Vijayavenkataraman, L. Zhang, S. Zhang, J.Y.H. Fuh, W.F. Lu, Triply periodic minimal surfaces sheet scaffolds for tissue engineering applications: An optimization approach toward biomimetic scaffold design, *ACS Appl. Bio Mater.* 1 (2018) 259–269. <https://doi.org/10.1021/acsabm.8b00052>.
- [60] R. Miralbes, D. Ranz, F.J. Pascual, D. Zouzas, M. Maza, Characterization of additively manufactured triply periodic minimal surface structures under compressive loading, *Mech. Adv. Mater. Struct.* 29 (2022) 1841–1855. <https://doi.org/10.1080/15376494.2020.1842948>.
- [61] W. Yang, J. An, C.K. Chua, K. Zhou, Acoustic absorptions of multifunctional polymeric cellular structures based on triply periodic minimal surfaces fabricated by stereolithography, *Virtual Phys. Prototyp.* 15 (2020) 242–249. <https://doi.org/10.1080/17452759.2020.1740747>.
- [62] C. Peng, K. Fox, M. Qian, H. Nguyen-Xuan, P. Tran, 3D printed sandwich beams with bioinspired cores: Mechanical performance and modelling, *Thin-Walled Struct.* 161 (2021) 107471. <https://doi.org/10.1016/j.tws.2021.107471>.
- [63] S.Z. Khan, S.H. Masood, E. Ibrahim, Z. Ahmad, Compressive behaviour of Neovius Triply Periodic Minimal Surface cellular structure manufactured by fused deposition modelling, *Virtual Phys. Prototyp.* 14 (2019) 360–370.

- <https://doi.org/10.1080/17452759.2019.1615750>.
- [64] A. Romero, M. Piovan, C. Mainetti, D. Stechina, S. Mendoza, H. Martín, C. Maggi, Tensile properties of 3d printed polymeric pieces: Comparison of several testing setups, *Ing. e Investig.* 41 (2021) 1–8. <https://doi.org/10.15446/ing.investig.v41n1.84467>.
- [65] I. Mahapatra, R. Velmurugan, R. Jayaganthan, Enhanced Flexural Performance of Diamond Latticed Triply Periodic Minimal Surface Sandwich Panels, *Adv. Eng. Mater.* (2023). <https://doi.org/10.1002/adem.202300813>.
- [66] Q. Ma, M.R.M. Rejab, J.P. Siregar, Z. Guan, A review of the recent trends on core structures and impact response of sandwich panels, *J. Compos. Mater.* 55 (2021) 2513–2555. <https://doi.org/10.1177/0021998321990734>.
- [67] T. Krolikowski, R. Knitter, M. Stachnik, Thermo-mechanic tests using 3d printed elements, *Procedia Comput. Sci.* 159 (2019) 2551–2559. <https://doi.org/10.1016/j.procs.2019.09.430>.
- [68] J. Nguyen, S. in Park, D. Rosen, Heuristic optimization method for cellular structure design of light weight components, *Int. J. Precis. Eng. Manuf.* 14 (2013) 1071–1078. <https://doi.org/10.1007/s12541-013-0144-5>.
- [69] J. Zhang, H. Huang, G. Liu, H. Zong, C. Zhang, Stiffness and energy absorption of additive manufactured hybrid lattice structures, *Virtual Phys. Prototyp.* 16 (2021) 428–443. <https://doi.org/10.1080/17452759.2021.1954405>.
- [70] O. Al-Ketan, A. Soliman, A.M. AlQubaisi, R.K. Abu Al-Rub, Nature-Inspired Lightweight Cellular Co-Continuous Composites with Architected Periodic Gyroidal Structures, *Adv. Eng. Mater.* 20 (2018). <https://doi.org/10.1002/adem.201700549>.
- [71] Y.M. Xie, X.Y. Yang, Q.Q. Liang, G.P. Steven, O.M. Querin, Evolutionary structural optimization, 2002. <https://doi.org/10.1007/978-1-4471-0985-3>.
- [72] M.P. Bendsøe, A. Ben-Tal, J. Zowe, Optimization methods for truss geometry and topology design, *Struct. Optim.* 7 (1994) 141–159. <https://doi.org/10.1007/BF01742459>.
- [73] G.I.N. Rozvany, M. Zhou, T. Birker, Generalized shape optimization without homogenization, *Struct. Optim.* 4 (1992) 250–252. <https://doi.org/10.1007/BF01742754>.
- [74] A. Aremu, I. Ashcroft, R. Wildman, R. Hague, C. Tuck, D. Brackett, The effects of bidirectional evolutionary structural optimization parameters on an industrial designed component for additive manufacture, *Proc. Inst. Mech. Eng. Part B J. Eng. Manuf.* 227 (2013) 794–807. <https://doi.org/10.1177/0954405412463857>.
- [75] A.E.F. Athanasiadis, M.A. Dias, M.K. Budzik, Can confined mechanical metamaterials replace adhesives?, *Extrem. Mech. Lett.* 48 (2021) 101411.

- <https://doi.org/10.1016/j.eml.2021.101411>.
- [76] J. Hu, S. Wang, Y. Wang, F. Li, Z. Luo, A lightweight methodology of 3D printed objects utilizing multi-scale porous structures, *Vis. Comput.* 35 (2019) 949–959. <https://doi.org/10.1007/s00371-019-01672-z>.
- [77] D.W. Abueidda, M. Elhebeary, C.S. (Andrew) Shiang, S. Pang, R.K. Abu Al-Rub, I.M. Jasiuk, Mechanical properties of 3D printed polymeric Gyroid cellular structures: Experimental and finite element study, *Mater. Des.* 165 (2019) 12–14. <https://doi.org/10.1016/j.matdes.2019.107597>.
- [78] Y. Mu, Y. Jin, H. Ji, W. Wang, S. Zou, C. Zhang, J. Du, Mechanical properties of a novel hierarchical cellular structure architected with minimal surfaces and Voronoi-tessellation, *Compos. Struct.* 325 (2023) 117610. <https://doi.org/10.1016/j.compstruct.2023.117610>.
- [79] M. Wan, D. Hu, H. Zhang, B. Pi, X. Ye, Crashworthiness study of tubular lattice structures based on triply periodic minimal surfaces under quasi-static axial crushing, *Compos. Struct.* 327 (2024) 117703. <https://doi.org/10.1016/j.compstruct.2023.117703>.
- [80] C. Pan, Y. Han, J. Lu, Design and optimization of lattice structures: A review, *Appl. Sci.* 10 (2020) 1–36. <https://doi.org/10.3390/AP10186374>.
- [81] H. Nguyen-Xuan, K.Q. Tran, C.H. Thai, J. Lee, Modelling of functionally graded triply periodic minimal surface (FG-TPMS) plates, *Compos. Struct.* 315 (2023) 116981. <https://doi.org/10.1016/j.compstruct.2023.116981>.
- [82] V. Birman, G.A. Kardomateas, Review of current trends in research and applications of sandwich structures, *Compos. Part B Eng.* 142 (2018) 221–240. <https://doi.org/10.1016/j.compositesb.2018.01.027>.
- [83] J. Smardzewski, Experimental and numerical analysis of wooden sandwich panels with an auxetic core and oval cells, *Mater. Des.* 183 (2019) 108159. <https://doi.org/10.1016/j.matdes.2019.108159>.
- [84] X. Gao, M. Zhang, Y. Huang, L. Sang, W. Hou, Experimental and numerical investigation of thermoplastic honeycomb sandwich structures under bending loading, *Thin-Walled Struct.* 155 (2020) 106961. <https://doi.org/10.1016/j.tws.2020.106961>.
- [85] X. Wang, Z. Yuan, Accurate stress analysis of sandwich panels by the differential quadrature method, *Appl. Math. Model.* 43 (2017) 548–565. <https://doi.org/10.1016/j.apm.2016.11.034>.
- [86] K. Magnucki, E. Magnucka-Blandzi, Generalization of a sandwich structure model: Analytical studies of bending and buckling problems of rectangular plates, *Compos.*

- Struct. 255 (2021) 112944. <https://doi.org/10.1016/j.compstruct.2020.112944>.
- [87] L. Stepinac, A. Skender, D. Damjanović, J. Galić, Frp pedestrian bridges—analysis of different infill configurations, *Buildings* 11 (2021) 1–14. <https://doi.org/10.3390/buildings11110564>.
- [88] C. Godines, S. DorMohammadi, F. Abdi, M. Villa Montero, D. Huang, L. Minnetyan, Damage tolerant composite design principles for aircraft components under static service loading using multi-scale progressive failure analysis, *J. Compos. Mater.* 51 (2017) 1393–1419. <https://doi.org/10.1177/0021998316671575>.
- [89] C. Peng, K. Fox, M. Qian, H. Nguyen-Xuan, P. Tran, 3D printed sandwich beams with bioinspired cores: Mechanical performance and modelling, *Thin-Walled Struct.* 161 (2021) 107471. <https://doi.org/10.1016/j.tws.2021.107471>.
- [90] A.W. Alshaer, D.J. Harland, An investigation of the strength and stiffness of weight-saving sandwich beams with CFRP face sheets and seven 3D printed cores, *Compos. Struct.* 257 (2021) 113391. <https://doi.org/10.1016/j.compstruct.2020.113391>.
- [91] P. Sengsri, H. Fu, S. Kaewunruen, Mechanical Properties and Energy-Absorption Capability of a 3D-Printed TPMS Sandwich Lattice Model for Meta-Functional Composite Bridge Bearing Applications, *J. Compos. Sci.* 6 (2022). <https://doi.org/10.3390/jcs6030071>.
- [92] C. Lin, G. Wen, H. Yin, Z.P. Wang, J. Liu, Y.M. Xie, Revealing the sound insulation capacities of TPMS sandwich panels, *J. Sound Vib.* 540 (2022). <https://doi.org/10.1016/j.jsv.2022.117303>.
- [93] I. Mahapatra, R. Velmurugan, R. Jayaganthan, Enhanced Flexural Performance of Diamond Latticed Triply Periodic Minimal Surface Sandwich Panels, *Adv. Eng. Mater.* (2023). <https://doi.org/10.1002/adem.202300813>.
- [94] L. He, T. Li, D. Zhong, H. Tao, Y. Peng, S. Chen, Blast Resistance in Sandwich Structures Based on TPMS, *Buildings* 13 (2023) 2835. <https://doi.org/10.3390/buildings13112835>.
- [95] D. Laskowska, T. Szatkiewicz, B. Bałasz, K. Mitura, Mechanical Properties and Energy Absorption Abilities of Diamond TPMS Cylindrical Structures Fabricated by Selective Laser Melting with 316L Stainless Steel, *Materials (Basel)*. 16 (2023). <https://doi.org/10.3390/ma16083196>.
- [96] M. Diamantopoulou, C.C. Roth, T. Tancogne-Dejean, C.M. Lauener, D. Mohr, Ceramic/polymer microlattices: Increasing specific energy absorption through sandwich construction, *Extrem. Mech. Lett.* 53 (2022) 101708.

- <https://doi.org/10.1016/j.eml.2022.101708>.
- [97] T.A. Schaedler, W.B. Carter, Architected Cellular Materials, *Annu. Rev. Mater. Res.* 46 (2016) 187–210. <https://doi.org/10.1146/annurev-matsci-070115-031624>.
- [98] World Trade Organization Technical Barriers to Trade (TBT) Committee, C393/C393M – 20, 2006. <https://doi.org/10.1520/C0393>.
- [99] Z.-H. Wen, D.-W. Wang, L. Ma, Sound transmission of composite sandwich panel with face-centered cubic core, *Mech. Adv. Mater. Struct.* 28 (2021) 1663–1676. <https://doi.org/10.1080/15376494.2019.1700433>.
- [100] M.R.M. Rejab, W.J. Cantwell, The mechanical behaviour of corrugated-core sandwich panels, *Compos. Part B Eng.* 47 (2013) 267–277. <https://doi.org/10.1016/j.compositesb.2012.10.031>.
- [101] L. Yang, L. Sui, Y. Dong, X. Li, F. Zi, Z. Zhang, S. Yang, J. Yang, L. Wu, Quasi-static and dynamic behavior of sandwich panels with multilayer gradient lattice cores, *Compos. Struct.* 255 (2021) 112970. <https://doi.org/10.1016/j.compstruct.2020.112970>.
- [102] P. Huang, Q. Gao, X. Su, Z. Feng, X. Sun, G. Zu, Effect of Core Density on the Three-Point Bending Performance of Aluminum Foam Sandwich Panels, *Materials (Basel)*. 16 (2023) 7091. <https://doi.org/10.3390/ma16227091>.
- [103] J.F. Davalos, P. Qiao, X. Frank Xu, J. Robinson, K.E. Barth, Modeling and characterization of fiber-reinforced plastic honeycomb sandwich panels for highway bridge applications, *Compos. Struct.* 52 (2001) 441–452. [https://doi.org/10.1016/S0263-8223\(01\)00034-4](https://doi.org/10.1016/S0263-8223(01)00034-4).
- [104] G. Liao, Z. Li, Y. Cheng, D. Xu, D. Zhu, S. Jiang, J. Guo, X. Chen, G. Xu, Y. Zhu, Properties of oriented carbon fiber/polyamide 12 composite parts fabricated by fused deposition modeling, *Mater. Des.* 139 (2018) 283–292. <https://doi.org/10.1016/j.matdes.2017.11.027>.
- [105] N. Kladovasilakis, P. Charalampous, K. Tsongas, I. Kostavelis, D. Tzetzis, D. Tzovaras, Experimental and computational investigation of lattice sandwich structures constructed by additive manufacturing technologies, *J. Manuf. Mater. Process.* 5 (2021). <https://doi.org/10.3390/JMMP5030095>.
- [106] J. Smits, Fiber-Reinforced Polymer Bridge Design in the Netherlands: Architectural Challenges toward Innovative, Sustainable, and Durable Bridges, *Engineering* 2 (2016) 518–527. <https://doi.org/10.1016/J.ENG.2016.04.004>.
- [107] R. Sonnenschein, K. Gajdosova, I. Holly, FRP Composites and their Using in the Construction of Bridges, *Procedia Eng.* 161 (2016) 477–482.

- <https://doi.org/10.1016/j.proeng.2016.08.665>.
- [108] L. Ascione, J.-F. Caron, P. Godonou, K. van Ijsselmuijden, J. Knippers, J. Mottram, M. Oppe, M. Gantriis Sorensen, J. Taby, L. Tromp, PROSPECT FOR NEW GUIDANCE IN THE DESIGN OF FRP Support to the implementation, harmonization and further development of the Eurocodes, 2016. <https://doi.org/10.2788/22306>.
- [109] T. Kišiček, M. Stepinac, T. Renić, I. Hafner, L. Lulić, Strengthening of masonry walls with FRP or TRM, *Gradjevinar* 72 (2020) 937–953. <https://doi.org/https://doi.org/10.14256/JCE.2983.2020>.
- [110] F. Jin, P. Feng, L. Ye, Study on dynamic characteristics of light-weight FRP footbridge, in: *Adv. FRP Compos. Civ. Eng. - Proc. 5th Int. Conf. FRP Compos. Civ. Eng. CICE 2010*, 2011: pp. 173–176. https://doi.org/10.1007/978-3-642-17487-2_37.
- [111] V. Mara, *Fibre reinforced polymer bridge decks : Sustainability and a novel panel-level connection*, (2014).
- [112] H.W. Gürtler, *Composite Action of Frp Bridge Decks Adhesively Bonded To Steel Main Girders Par*, Lausanne, EPFL, 2004.
- [113] C.E. Bakis, L.C. Bank, V.L. Brown, E. Cosenza, J.F. Davalos, J.J. Lesko, A. Machida, S.H. Rizkalla, T.C. Triantafillou, *Fiber-Reinforced Polymer Composites for Construction - State-of-the-Art Review, Perspect. Civ. Eng. Commem. 150th Anniv. Am. Soc. Civ. Eng.* (2003) 369–383. [https://doi.org/10.1061/\(asce\)1090-0268\(2002\)6:2\(73\)](https://doi.org/10.1061/(asce)1090-0268(2002)6:2(73)).
- [114] V. Mara, R. Haghani, *Review of FRP decks: Structural and in-service performance*, *Proc. Inst. Civ. Eng. Bridg. Eng.* 168 (2015) 308–329. <https://doi.org/10.1680/bren.14.00009>.
- [115] P. Alagusundaramoorthy, I.E. Harik, M. Asce, C.C. Choo, *Structural Behavior of FRP Composite Bridge Deck Panels*, 11 (2006) 384–393.
- [116] G. Camata, P.B. Shing, *Static and fatigue load performance of a gfrp honeycomb bridge deck*, *Compos. Part B Eng.* 41 (2010) 299–307. <https://doi.org/10.1016/j.compositesb.2010.02.005>.
- [117] T. Keller, M. Schollmayer, *Plate bending behavior of a pultruded GFRP bridge deck system*, *Compos. Struct.* 64 (2004) 285–295. <https://doi.org/10.1016/j.compstruct.2003.08.011>.
- [118] P.K. Majumdar, Z. Liu, J.J. Lesko, T.E. Cousins, *Performance Evaluation of FRP Composite Deck Considering for Local Deformation Effects*, *J. Compos. Constr.* 13 (2009) 332–338. [https://doi.org/10.1061/\(asce\)cc.1943-5614.0000008](https://doi.org/10.1061/(asce)cc.1943-5614.0000008).
- [119] T. Keller, Y. Bai, T. Vallé, *Long-term performance of a glass fiber-reinforced polymer*

- truss bridge, J. Compos. Constr. 11 (2007) 99–108.
[https://doi.org/10.1061/\(ASCE\)1090-0268\(2007\)11:1\(99\)](https://doi.org/10.1061/(ASCE)1090-0268(2007)11:1(99)).
- [120] M. Gabler, J. Knippers, Improving fail-safety of road bridges built with non-ductile fibre composites, Constr. Build. Mater. 49 (2013) 1054–1063.
<https://doi.org/10.1016/j.conbuildmat.2012.10.015>.
- [121] M. Kulpa, T. Siwowski, M. Rajchel, L. Wlasak, Design and experimental verification of a novel fibre-reinforced polymer sandwich decking system for bridge application, J. Sandw. Struct. Mater. 23 (2021) 2326–2357.
<https://doi.org/10.1177/1099636220909756>.
- [122] T. Siwowski, M. Kulpa, M. Rajchel, P. Poneta, Design, manufacturing and structural testing of all-composite FRP bridge girder, Compos. Struct. 206 (2018) 814–827.
<https://doi.org/10.1016/j.compstruct.2018.08.048>.
- [123] FiberCore europe, (n.d.). <https://www.fibercore-europe.com/en/>.
- [124] J. Smits, The Art of Bridge Design, 2019.
- [125] T. Keller, H. Gürtler, Design of hybrid bridge girders with adhesively bonded and compositely acting FRP deck, Compos. Struct. 74 (2006) 202–212.
<https://doi.org/10.1016/j.compstruct.2005.04.028>.
- [126] T. Keller, H. Gürtler, Quasi-static and fatigue performance of a cellular FRP bridge deck adhesively bonded to steel girders, Compos. Struct. 70 (2005) 484–496.
<https://doi.org/10.1016/j.compstruct.2004.09.028>.
- [127] I. Kreja, On geometrically non-linear FEA of laminated FRP composite panels, Shell Struct. Theory Appl. - Proc. 10th SSTA 2013 Conf. 3 (2014) 33–42.
<https://doi.org/10.1201/b15684-7>.
- [128] BD 90/05 Design of FRP Bridges and Highway Structures, Des. Man. Roads Bridg. Highw. Struct. Approv. Proced. Gen. Des. 1 (2005) 21.
- [129] A. J. Leggatt, GRP and buildings: A Design Guide for Architects and Engineers, 1984.
- [130] C. Bilim, İ.F. Kara, A.F. Ashour, Flexural Behavior of Hybrid Frp-Concrete Bridge Decks, Turkish J. Eng. 3 (2019) 206–217. <https://doi.org/10.31127/tuje.554075>.
- [131] D.W. Abueidda, R.K. Abu Al-Rub, A.S. Dalaq, D.W. Lee, K.A. Khan, I. Jasiuk, Effective conductivities and elastic moduli of novel foams with triply periodic minimal surfaces, Mech. Mater. 95 (2016) 102–115.
<https://doi.org/10.1016/j.mechmat.2016.01.004>.
- [132] G. Allen, nTopology Modeling Technology, 2020.
- [133] W. Frącz, G. Janowski, R. Smusz, M. Szumski, The influence of chosen plant fillers in

- PHBV composites on the processing conditions, mechanical properties and quality of molded pieces, *Polymers* (Basel). 13 (2021). <https://doi.org/10.3390/polym13223934>.
- [134] M.A. Vigil Fuentes, S. Thakur, F. Wu, M. Misra, S. Gregori, A.K. Mohanty, Study on the 3D printability of poly(3-hydroxybutyrate-co-3-hydroxyvalerate)/poly(lactic acid) blends with chain extender using fused filament fabrication, *Sci. Rep.* 10 (2020) 1–12. <https://doi.org/10.1038/s41598-020-68331-5>.
- [135] R. Blok, J. Smits, R. Gkaidatzis, P. Teuffel, Bio-Based Composite Footbridge: Design, Production and In Situ Monitoring, *Struct. Eng. Int.* 29 (2019) 453–465. <https://doi.org/10.1080/10168664.2019.1608137>.
- [136] V. Cabreira, R.M.C. Santana, Effect of infill pattern in fused filament fabrication (FFF) 3D printing on materials performance, *Rev. Mater.* 25 (2020) 1–9. <https://doi.org/10.1590/s1517-707620200003.1126>.
- [137] F. Calignano, D. Manfredi, E.P. Ambrosio, S. Biamino, M. Lombardi, E. Atzeni, A. Salmi, P. Minetola, L. Iuliano, P. Fino, Overview on additive manufacturing technologies, *Proc. IEEE* 105 (2017) 593–612. <https://doi.org/10.1109/JPROC.2016.2625098>.
- [138] J. Gardan, Additive manufacturing technologies: State of the art and trends, *Int. J. Prod. Res.* 54 (2016) 3118–3132. <https://doi.org/10.1080/00207543.2015.1115909>.
- [139] Y.Y. Aw, C.K. Yeoh, M.A. Idris, P.L. Teh, W.N. Elyne, K.A. Hamzah, S.A. Sazali, Influence of Filler Precoating and Printing Parameter on Mechanical Properties of 3D Printed Acrylonitrile Butadiene Styrene/Zinc Oxide Composite, *Polym. Technol. Mater.* 58 (2019) 1–13. <https://doi.org/10.1080/03602559.2018.1455861>.
- [140] J. Qureshi, A Review of Fibre Reinforced Polymer Structures, *Fibers* 10 (2022) 4–6. <https://doi.org/10.3390/fib10030027>.
- [141] Y. Sun, W. Tian, T. Zhang, P. Chen, M. Li, Strength and toughness enhancement in 3d printing via bioinspired tool path, *Mater. Des.* 185 (2020) 108239. <https://doi.org/10.1016/j.matdes.2019.108239>.
- [142] S. Sharafi, M.H. Santare, J. Gerdes, S.G. Advani, A review of factors that influence the fracture toughness of extrusion-based additively manufactured polymer and polymer composites, *Addit. Manuf.* 38 (2021) 101830. <https://doi.org/10.1016/j.addma.2020.101830>.
- [143] E. Padovano, M. Galfione, P. Concialdi, G. Lucco, C. Badini, Mechanical and thermal behavior of ultem® 9085 fabricated by fused-deposition modeling, *Appl. Sci.* 10 (2020) 1–15. <https://doi.org/10.3390/app10093170>.

- [144] I.M. Daniel, Yield and failure criteria for composite materials under static and dynamic loading, *Prog. Aerosp. Sci.* 81 (2016) 18–25. <https://doi.org/10.1016/j.paerosci.2015.11.003>.
- [145] J. Shi, L. Zhu, L. Li, Z. Li, J. Yang, X. Wang, A TPMS-based method for modeling porous scaffolds for bionic bone tissue engineering, *Sci. Rep.* 8 (2018). <https://doi.org/10.1038/s41598-018-25750-9>.
- [146] D.M. Sánchez, M. de la Mata, F.J. Delgado, V. Casal, S.I. Molina, Development of carbon fiber acrylonitrile styrene acrylate composite for large format additive manufacturing, *Mater. Des.* 191 (2020) 108577. <https://doi.org/10.1016/j.matdes.2020.108577>.
- [147] D. Moreno-Sanchez, A. Sanz de León, D. Moreno Nieto, F.J. Delgado, S.I. Molina, Basalt Fiber Composites with Reduced Thermal Expansion for Additive Manufacturing, *Polymers (Basel)*. 14 (2022). <https://doi.org/10.3390/polym14153216>.
- [148] S. Ding, B. Zou, P. Wang, H. Ding, Effects of nozzle temperature and building orientation on mechanical properties and microstructure of PEEK and PEI printed by 3D-FDM, *Polym. Test.* 78 (2019) 105948. <https://doi.org/10.1016/j.polymertesting.2019.105948>.
- [149] E.M. Agaliotis, B.D. Ake-Concha, A. May-Pat, J.P. Morales-Arias, C. Bernal, A. Valadez-Gonzalez, P.J. Herrera-Franco, G. Proust, J.F. Koh-Dzul, J.G. Carrillo, E.A. Flores-Johnson, Tensile Behavior of 3D Printed Polylactic Acid (PLA) Based Composites Reinforced with Natural Fiber, *Polymers (Basel)*. 14 (2022). <https://doi.org/10.3390/polym14193976>.
- [150] H. Alzyod, P. Ficzer, Material-Dependent Effect of Common Printing Parameters on Residual Stress and Warpage Deformation in 3D Printing: A Comprehensive Finite Element Analysis Study, (2023).
- [151] D.A. Roberson, A.R. Torrado Perez, C.M. Shemelya, A. Rivera, E. MacDonald, R.B. Wicker, Comparison of stress concentrator fabrication for 3D printed polymeric izod impact test specimens, *Addit. Manuf.* 7 (2015) 1–11. <https://doi.org/10.1016/j.addma.2015.05.002>.
- [152] V.B. Mohan, D. Bhattacharyya, Mechanical, electrical and thermal performance of hybrid polyethylene-graphene nanoplatelets-polypyrrole composites: a comparative analysis of 3D printed and compression molded samples, *Polym. Technol. Mater.* 59 (2020) 780–796. <https://doi.org/10.1080/25740881.2019.1695272>.
- [153] M. Mansour, K. Tsongas, D. Tzetzis, Measurement of the mechanical and dynamic

- properties of 3D printed polylactic acid reinforced with graphene, *Polym. Technol. Mater.* 58 (2019) 1234–1244. <https://doi.org/10.1080/03602559.2018.1542730>.
- [154] M. Khosroupour Arabi, N. Kordani, 3D-printing of Continuous Fiber: A review of processes, materials and properties, *Polym. Technol. Mater.* 62 (2023) 1525–1559. <https://doi.org/10.1080/25740881.2023.2222793>.
- [155] M.A. Caminero, J.M. Chacón, I. García-Moreno, G.P. Rodríguez, Impact damage resistance of 3D printed continuous fibre reinforced thermoplastic composites using fused deposition modelling, *Compos. Part B Eng.* 148 (2018) 93–103. <https://doi.org/10.1016/j.compositesb.2018.04.054>.
- [156] A. Roschli, K.T. Gaul, A.M. Boulger, B.K. Post, P.C. Chesser, L.J. Love, F. Blue, M. Borish, Designing for Big Area Additive Manufacturing, *Addit. Manuf.* 25 (2019) 275–285. <https://doi.org/10.1016/j.addma.2018.11.006>.
- [157] B.K. Post, P.C. Chesser, R.F. Lind, A. Roschli, L.J. Love, K.T. Gaul, M. Sallas, F. Blue, S. Wu, Using Big Area Additive Manufacturing to directly manufacture a boat hull mould, *Virtual Phys. Prototyp.* 14 (2019) 123–129. <https://doi.org/10.1080/17452759.2018.1532798>.
- [158] D. Moreno Nieto, V. Casal López, S.I. Molina, Large-format polymeric pellet-based additive manufacturing for the naval industry, *Addit. Manuf.* 23 (2018) 79–85. <https://doi.org/10.1016/j.addma.2018.07.012>.
- [159] L. Stepinac, J. Galić, A. Skender, FRP DECK SYSTEM USING TPMS LATTICE STRUCTURE, in: 11th Int. Conf. Fiber-Reinforced Polym. Compos. Civ. Eng. (CICE 2023), Rio Janeiro, 24-26 July 2023, 2023. <https://doi.org/10.5281/zenodo.8066199>.
- [160] L. Stepinac, J. Galić, M. Binički, Fast estimation of bending stiffness in sandwich-structured composites with 3D printed TPMS core, *Mech. Adv. Mater. Struct.* 0 (2023) 1–10. <https://doi.org/10.1080/15376494.2023.2267551>.
- [161] ISO 527-2 Plastics - Determination of tensile properties, 2012 (2012).
- [162] B. (China), HI-TEMP CF bigrep filament, n.d.
- [163] EN ISO 178:2019 Plastics - Determination of flexural properties, (2019).
- [164] K. Suzuki, N. Kikuchi, Shape and topology optimization by a homogenization method, *Am. Soc. Mech. Eng. Appl. Mech. Div. AMD* 115 (1990) 15–30.
- [165] J. Feng, B. Liu, Z. Lin, J. Fu, Isotropic porous structure design methods based on triply periodic minimal surfaces, *Mater. Des.* 210 (2021) 110050. <https://doi.org/10.1016/j.matdes.2021.110050>.
- [166] C. Peng, P. Marzocca, P. Tran, Triply periodic minimal surfaces based honeycomb

- structures with tuneable mechanical responses, *Virtual Phys. Prototyp.* 18 (2023). <https://doi.org/10.1080/17452759.2022.2125879>.
- [167] S. Khaleghi, F.N. Dehnavi, M. Baghani, M. Safdari, K. Wang, M. Baniassadi, On the directional elastic modulus of the TPMS structures and a novel hybridization method to control anisotropy, *Mater. Des.* 210 (2021) 110074. <https://doi.org/10.1016/j.matdes.2021.110074>.
- [168] W.E. Lorensen, H.E. Cline, Marching cubes: A high resolution 3D surface construction algorithm, *Proc. 14th Annu. Conf. Comput. Graph. Interact. Tech. SIGGRAPH 1987* 21 (1987) 163–169. <https://doi.org/10.1145/37401.37422>.
- [169] T. Maconachie, R. Tino, B. Lozanovski, M. Watson, A. Jones, C. Pandelidi, A. Alghamdi, A. Almalki, D. Downing, M. Brandt, M. Leary, The compressive behaviour of ABS gyroid lattice structures manufactured by fused deposition modelling, *Int. J. Adv. Manuf. Technol.* 107 (2020) 4449–4467. <https://doi.org/10.1007/s00170-020-05239-4>.
- [170] L. Germain, C.A. Fuentes, A.W. van Vuure, A. des Rieux, C. Dupont-Gillain, 3D-printed biodegradable gyroid scaffolds for tissue engineering applications, *Mater. Des.* 151 (2018) 113–122. <https://doi.org/10.1016/j.matdes.2018.04.037>.
- [171] Smith M., ABAQUS/Standard User's Manual, Version 6.9. Providence, RI: Dassault Systèmes Simulia Corp, 2009., (n.d.).
- [172] G.P. Steven, Homogenization of multicomponent composite orthotropic materials using FEA, *Commun. Numer. Methods Eng.* 13 (1997) 517–531. [https://doi.org/10.1002/\(sici\)1099-0887\(199707\)13:7<517::aid-cnm74>3.3.co;2-c](https://doi.org/10.1002/(sici)1099-0887(199707)13:7<517::aid-cnm74>3.3.co;2-c).
- [173] D.W. Lee, K.A. Khan, R.K. Abu Al-Rub, Stiffness and yield strength of architected foams based on the Schwarz Primitive triply periodic minimal surface, *Int. J. Plast.* 95 (2017) 1–20. <https://doi.org/10.1016/j.ijplas.2017.03.005>.
- [174] C.N. Kelly, J. Francovich, S. Julmi, D. Safranski, R.E. Guldberg, H.J. Maier, K. Gall, Fatigue behavior of As-built selective laser melted titanium scaffolds with sheet-based gyroid microarchitecture for bone tissue engineering, *Acta Biomater.* 94 (2019) 610–626. <https://doi.org/10.1016/j.actbio.2019.05.046>.
- [175] J. Feng, J. Fu, C. Shang, Z. Lin, B. Li, Sandwich panel design and performance optimization based on triply periodic minimal surfaces, *CAD Comput. Aided Des.* 115 (2019) 307–322. <https://doi.org/10.1016/j.cad.2019.06.007>.
- [176] M. Birsan, D. Pietras, T. Sadowski, Determination of effective stiffness properties of multilayered composite beams, *Contin. Mech. Thermodyn.* 33 (2021) 1781–1803. <https://doi.org/10.1007/s00161-021-01006-2>.

- [177] M. Al Khalil, N. Lebaal, F. Demoly, S. Roth, A design and optimization framework of variable-density lattice structures for additive manufacturing, *Mech. Adv. Mater. Struct.* 29 (2022) 4711–4725. <https://doi.org/10.1080/15376494.2021.1936704>.
- [178] alphastarcop.com, (n.d.). <http://alphastarcop.com/genoa-3dp-simulation/>.
- [179] R. Hajiha, K. Reichelderfer, H. Baid, C. Godines, F. Abdi, Part performance of FDM printed Nylon 12CF Bracket for Cost-Effective Ground Support Equipment, *CAMX 2019 - Compos. Adv. Mater. Expo* (2020). <https://doi.org/10.33599/nasampe/c.19.0818>.
- [180] AlphaSTAR Corporation, (n.d.). <https://alphastarcop.com/> (accessed June 21, 2023).
- [181] N. Gan, Q. Wang, Topology optimization design for thermal buckling criterion with the size effect, *Mech. Based Des. Struct. Mach.* 51 (2023) 4894–4911. <https://doi.org/10.1080/15397734.2021.1981378>.
- [182] Y.C. Jeong, K. Kang, Mechanical design of a convex-deformable polymer plate, *Mater. Des.* 231 (2023) 112083. <https://doi.org/10.1016/j.matdes.2023.112083>.
- [183] J. Fan, A.P. Vassilopoulos, V. Michaud, Mode I fracture of thick adhesively bonded GFRP composite joints for wind turbine rotor blades, *Compos. Struct.* 327 (2024) 117705. <https://doi.org/10.1016/j.compstruct.2023.117705>.
- [184] C.E. Duty, V. Kunc, B. Compton, B. Post, D. Erdman, R. Smith, R. Lind, P. Lloyd, L. Love, Structure and mechanical behavior of Big Area Additive Manufacturing (BAAM) materials, *Rapid Prototyp. J.* 23 (2017) 181–189. <https://doi.org/10.1108/RPJ-12-2015-0183>.

CURRICULUM VITAE

Lucija Stepinac was born on 1 October 1990 in Livno, Bosnia and Herzegovina. She completed Ljudevit Gaj primary school in 2005 and attended Josip Jelačić grammar school, from which she graduated in 2009. In 2010, she enrolled in the undergraduate programme at the Faculty of Civil Engineering at the University of Zagreb. She completed her studies in 2012 with a bachelor's degree in civil engineering. After that, she continued her education at the Faculty of Civil Engineering at the University of Zagreb, where she enrolled in the graduate/master's programme specializing in structural engineering. In 2014, she obtained her master's degree in the field of structural engineering and successfully defended her master's thesis entitled "Structural design of a multi-storey steel building".

From 2014 she worked as a structural engineer for companies: KP Konstrukcije, Gavin & Doherty Geosolutions, Dublin and VERTIV.

Since March 2018, she has been working as a research and teaching assistant at the Section of building structures, Department of Architectural Technology and Building Science, Faculty of Architecture, University of Zagreb. She participates in the teaching, research and professional activities of the department. As a lecturer, she is involved in several courses at the undergraduate and graduate level. She worked on the project entitled "Development of double façade with a hermetically sealed cavity (H-CCF)", Faculty of Architecture, University of Zagreb and KFK d.o.o. - a project funded by the EU Regional Development Fund (KK.01.2.1.02.0218). In her scientific work, she has published 4 research papers, 3 papers are currently under review and she has participated in 6 conferences. She extended her research at the EPFL University in Switzerland, which was funded by the Croatian Science Foundation under grant number MOBDOK-2023-4242.

She has been enrolled in the postgraduate doctoral programme at the Faculty of Civil Engineering, University of Zagreb since October 2019. Her research proposal entitled "Characterisation and modelling of additively manufactured polymeric TPMS lattices for structural application" was approved in November 2022. The approval was granted by a committee which included her mentor assoc. prof. Ana Skender, second mentor full prof. Josip Galić, full prof. Domagoj Damjanović, assoc. prof. Marko Bartolac, and asst. prof. Davor Andrić.

LIST OF PUBLISHED WORKS BY THE AUTHOR

1) Journal papers – Scientific Papers

Stepinac, Lucija; Galić, Josip; Vassilopoulos, Anastasios

Experimental and numerical investigation of an additively manufactured sandwich composite bridge deck utilizing gyroid building blocks. // Composite Structures.

doi: 10.1016/j.compstruct.2024.118304

Stepinac, Lucija; Zovko, Ivana; Galić, Josip

Exploring Mechanical Behavior and Design Optimization of Sandwich Panels with 3D Printed Auxetic Core: A Numerical and Experimental Study. // Journal of Sandwich Structures and Materials (UNDER REVIEW)

Stepinac, Lucija; Skender, Ana; Damjanović, Domagoj; Galić, Josip

Study on TPMS metamaterials: parametric designs, laboratory tests and numerical analysis for macro-scale structural applications. // Mechanics Based Design Of Structures And Machines (UNDER REVIEW)

Stepinac, Lucija; Galić, Josip; Binički, Marin

Fast estimation of bending stiffness in sandwich structured composites with 3D printed TPMS core // Mechanics of advanced materials and structures, 0/2013(2023), 0; str. 1-10.

doi:10.1080/15376494.2023.2267551

Galić, Josip; Stepinac, Lucija; Bošnjak, Antonia; Zovko, Ivana

Influence of PVB Interlayer Mechanical Properties on Laminated Glass Elements Design in Dependence of Real Time-Temperature Changes // Polymers, 14 (2022), 20; 1-25

doi:10.3390/polym14204402

Stepinac, Lucija; Skender, Ana; Damjanović, Domagoj; Galić, Josip

FRP Pedestrian Bridges - Analysis of Different Infill Configurations // Buildings, 11 (2021), 11; 564, 14 doi:10.3390/buildings11110564

Stepinac, Lucija; Galić, Josip; Vukić, Hrvoje; Haiman, Miljenko

Pregled istraživanja djelovanja požara u AB elementima i procjena stanja AB konstrukcije nakon požara // Građevinar : časopis Hrvatskog saveza građevinskih inženjera, 73/2021 (2021), 7/2021; 509-522 doi:10.14256/JCE.3196.2021

2) Knjige i priručnici:

Josip Galić, Hrvoje Vukić, Davor Andrić, Lucija Stepinac

Tehnike popravaka i pojačanja zidanih zgrada, 2023. Sveučilišni priručnik (recenzirani),
Arhitektonski fakultet Sveučilišta u Zagrebu; ISBN 978-953-8042-82-9 (tiskano)

3) Papers in Conference Proceedings – Scientific Papers in Conference Proceedings

Stepinac, Lucija; Galić, Josip

Parametarsko projektiranje i dokazivanje materijalnog modela za 3D ispis konstrukcije mosta.
// 9. Sabor Hrvatskih Graditelja. Cavtat, Hrvatska, 2024

Stepinac, Lucija; Marrey, Mallikharjun; Baid, Harsh; Cantarutti, Andrea; Galić, Josip

Structural design and mechanical performance analysis of a full-scale 3D-printed bridge deck
using GENOA 3DP Virtual Simulation Tool. // Thematic Conference on the Mechanical
Response of Composites – COMPOSITES, Trapani, Sicilija, 12.-14.09.2023.

Stepinac, Lucija; Galić, Josip; Ana Skender

FRP deck system using TPMS lattice structure. // 11th International Conference on Fiber-
Reinforced Polymer (FRP) Composites in Civil Engineering (CICE 2023), Rio, Brazil, 2023
23.-26.07.2023

Stepinac, Lucija; Zovko, Ivana; Galić, Josip

Evaluating Mechanical Properties of Laminated Glass Under Pure Shear Using 3D RVE
Analysis. // International Scientific Conference on Glass Facades, Zagreb, Hrvatska,
23.05.2023.

Veršić, Zoran ; Galić, Josip ; Binički, Marin ; Stepinac, Lucija

Factors in a Sustainability Assessment of New Types of Closed Cavity Facades //
International Journal of Social, Education, Economics and Management Engineering. 2022.
str. 3-3

Andrić, Davor; Galić, Josip; Stepinac, Lucija

Opportunities for Design and Construction of Pneubotic Structures in Architecture //
Organization, Technology & Management in Construction 2022, Cavtat, Hrvatska, 21-
24.09.2022.

Galić, Josip; Andrić, Davor; Stepinac, Lucija; Vukić, Hrvoje

Built Heritage in the 2020 Earthquakes in Zagreb and Petrinja, Croatia: Experience and
Consequences // 17th International Conference on Studies, Repairs and Maintenance of
Heritage Architecture – STREMAH 2021, Southampton, UK - online, 25-27.05.2021.

Stepinac, Lucija; Andrić, Davor; Galić, Josip

Earthquake Architecture in Earthquake Prone Areas // International Symposium on Durrës
Earthquakes and Eurocodes, Tirana, Albania, 22-23.09.2020.